UNDERSTANDING AND PREVENTING LIFETIME FAILURE IN LITHIUM-ION BATTERIES

by

Roby Gauthier

Submitted in partial fulfilment of the requirements
for the degree of Doctor of Philosophy

at

Dalhousie University
Halifax, Nova Scotia
August 2021

TABLE OF CONTENTS

LIST OF TABLES

LIST OF FIGURES

ABSTRACT

Researchers are rushing to improve the lifetime, energy density, and cost of lithium-ion batteries as their production grows to match increasing demand. They can achieve these goals by finding new electrolyte additives that increase long-term cycling performance or/and increase high voltage performance. They can also try to understand the mechanisms happening inside the cells to gain new knowledge that helps them in their quest. In this spirit, the first project consisted of studying a new family of electrolyte additives, the dioxazolone family. Dioxazolones with different functional groups were studied using long-term cycling, high-temperature storage, and other techniques to figure out if they would bring any advantage to the industry. Then, a second project was built to study a group of cells that cycled through different depth of discharge, C-rates, and temperature. Long-term cycling, dV/dQ analysis, thickness growth measurements, ultrasonic transmission mapping, X-ray CT scans, and other techniques were used to better understand the mechanisms that happen inside these cells. In the end, valuable knowledge was gained that would allow researchers to have a better intuition of the failure mechanisms happening inside cells.

LIST OF ABBREVIATIONS USED

A : Variable, depending on the depth of discharge, describing capacity fade.

A_0 : Constant related to A and representing lithium inventory loss at the negative electrode.

AG : Artificial graphite.

B_0 : Constant related to A and representing the capacity fade due to storage failure.

B3LYP : Becke, 3-parameter, Lee–Yang–Parr exchange-correlation functional.

C : Constant to fit to ΔV data.

C, C_1, C_2 : Capacitance of a capacitor.

CC : Constant current step.

CCCV : Constant current step followed by a constant voltage step.

CMC/SBR : carboxymethylcellulose/styrene-butadiene rubber.

CPE : Constant phase element.

Crate / C-rate : In general, a C-rate of 1/x (C/x) correspond to a current that charge the cell in x hours. For example, a C-rate of 0.1 (often written as C/10) correspond to a current that charge the cell in 10 hours.

CT : Computed tomography.

CV : Constant voltage step.

c : Speed of sound in a material.

$d(\Delta G_{solv})$: Difference in solvation free energy of a lithium cation in water versus in a battery.

D : Constant to fit to ΔV data.

DEC : Diethyl carbonate.

DFT : Density functional theory.

DMC : Dimethyl carbonate.

DMI : 1,3-Dimethyl-2-imidazolidinone.

DOD : Depth of discharge (decimals).

DTA : Differential thermal analysis.

DTD : 1,3,2-dioxathiolane-2,2-dioxide or ethylene sulfate.

E^0 : Reduction or oxidation potential of a redox reaction.

E^0_{SHE}(abs) : Absolute potential of the standard hydrogen electrode.

E^0_{SLE}(ref) : Relative potential of the standard lithium electrode versus E^0_{SHE}(abs) in water.

E : Total energy.

E_{elec} : Electronic energy.

E_{ref} : Lithium reference potential in a battery electrolyte.

e : Elementary charge.

EC : Ethylene carbonate.

EDG : Electron donating group.

EIS : Electrochemical impedance spectroscopy.

EMC : Ethyl methyl carbonate.

EWG : Electron withdrawing group.

E_{xc} : Exchange-correlation energy.

F : Faraday constant.

f : Frequency.

FEC : Fluoroethylene carbonate.

G : Gibbs free energy.

H : Enthalpy.

I/NI : With or without an impedance term.

IEFPCM : Integral equation formalism polarizable continuum model.

LC : Lower cutoff cells.

LCV : Lower cutoff voltage

LFO : Lithium difluorophosphate.

LFP : Lithium iron phosphate.

LuAG : $Lu_3Al_5O_{12}$:Ce.

M : One or a mixture of transition metals (Ni, Co, Mn).

M : A random molecule.

m : Electron mass.

m_{p0} : Initial active positive electrode mass.

m_p : Active positive electrode mass.

m_n : Active negative electrode mass.

MAGE : Measuring Archimedes' gas expansion apparatus.

MMDS : Methylene methyl disulfonate.

n : Electron density.

n : Cycle number.

n : Number of electrons being used during a redox reaction.

n : Constant of a CPE.

NCA : Lithium nickel cobalt aluminium oxide.

NG : Natural graphite.

NMC : Lithium nickel manganese cobalt oxide.

NMC622 : $LiNi_{0.6}Mn_{0.2}Co_{0.2}O_2$.

NMR : Nuclear magnetic resonance.

PCM : Polarizable continuum model.

PDO : 3-phenyl-1,4,2-dioxazol-5-one.

PES : Prop-1-ene-1,3-sultone.

pFDO : 3-(4-fluorophenyl)-1,4,2-dioxazol-5-one.

pMODO : 3-(4-methoxyphenyl)-1,4,2-dioxazol-5-one.

pNDO : 3-(4-nitrophenyl)-1,4,2-dioxazol-5-one.

PVDF : Polyvinylidene fluoride.

Q_o : Initial discharge capacity.

Q : Discharge capacity.

Q : Constant of a CPE.

Q_A, Q_B : Capacity stored on surface A and B of the graphite electrode.

Q_{cv} : Impedance related capacity gain during the constant voltage step.

Q_P : Positive electrode active mass loss in mAh.

Q_{SEI} : Lithium inventory loss.

q_n : Capacity of the reference negative electrode voltage curve.

q_p : Capacity of the reference positive electrode voltage curve.

R, R_0, R_1, R_2 : Resistance of a resistor.

R_{ct} : Diameter of the semi-circle in EIS.

$\vec{r}$: Position vector 1.

$\overrightarrow{r'}$: Position vector 2.

S_A, S_B : Surface area of area A and B of the graphite electrode.

SEI : Solid electrolyte interface.

SEM : Scanning electron microscope.

SOC: State of charge.

t : Time.

t_1 : A specific time.

T : Coefficient of transmission of ultrasonic wave.

T_s : Kinetic energy of the non-interacting electron systems.

TTSPi : tris(trimethylsilyl) phosphite.

UC : Upper cutoff cells.

UCV : Upper cutoff voltage.

UHPC : Ultra-high precision cycling.

UTM : Ultrasonic transmission mapping.

VC : Vinylene carbonate.

VC211 : 2% VC + 1% MMDS + 1% TTSPi.

V_n : Reference negative electrode voltage versus Li^+/Li.

V_p : Reference positive electrode voltage versus Li^+/Li.

v_{eff} : Kohn-Sham potential.

v_{ext} : External potential (Nuclear potential).

Z, Z_1, Z_2 : Electric or acoustic impedance.

α : Constant to fit.

Δ_0, δ_{n0} : Initial relative slippage.

Δ : Relative slippage.

ΔG^0 : Gibbs free energy of a redox reaction.

ΔQ_{cal} : Capacity loss due to storage failure.

ΔV_0 : Value of ΔV at t = 0 hour.

ΔV : Difference between the average charge voltage and the average discharge voltage.

$\delta/\delta n$: Functional derivative.

δ_n : Absolute slippage of the negative electrode.

δ_p : Absolute slippage of the positive electrode.

ε : Permittivity.

ε_i : Kohn-Sham orbital energies.

ρ: Density of a material.

ρ_A, ρ_B : Capacity surface density.

τ, τ^* : Characteristic time of lithium-ions diffusion.

ω : Angular frequency.

φ_i: Kohn-Sham orbitals.

ACKNOWLEDGEMENTS

I would like to acknowledge my supervisor, Dr. Jeff Dahn which made this work possible. His curiosity and passion for science and discovery, as well as his vast amount of knowledge and work ethic was a constant source of inspiration and it helped to build the scientist that I am today. I would like to acknowledge Tesla, NSERC and Dalhousie University for their financial support during this degree.

I would also like to acknowledge my colleagues who helped make this work even more impactful. I would like to thank David Hall for his mentorship. He helped me in the transition from theoretical research to experimental research and also helped me learn more chemistry and scientific rigor. I would also like to thank all co-authors of this work: David Hall, Katherine Lin, Jazmin Baltazar, Toren Hynes, Aidan Luscombe, Toby Bond, Michael Bauer, Michel Johnson, Jessie Harlow, and Alex Louli.

Finally, I would like to acknowledge my family and friends who supported me socially and emotionally through this work. I would like to especially thank my immediate family, Izzy Gallant, Zeynep Oziskender, Julie Bossé, Maryjo Valcourt and Josée Leblanc for their support.

CHAPTER 1 INTRODUCTION

1.1 MOTIVATION

Electric vehicles and grid energy storage would not be the same today without the presence of lithium-ion batteries. Their high energy density, lifetime performance and low cost made this possible, but to further support the current rapid growth of these industries, their performance and cost must further improve. To achieve this, researchers can choose two approaches: the trial-and-error approach to improvement or the theoretical/systematic approach to improvement. This thesis uses these two approaches to achieve this goal.

1.2 SCOPE OF THIS WORK

The goal of this work is to better understand and improve the long-term performance of lithium-ion batteries. Like mentioned above, one of the first methods that can be used to achieve this is by trial-and-error, which in this work is done by trying different electrolyte additives. Electrolyte additives are added individually or as a blend with other additives to the electrolyte of multiple lithium-ion cells and the capacity retention of these cells are measured as a function of cycle number. One can then choose the cell that performed the best, from which we can deduce the best additive or additive blend. One can also try to learn from this trial-and-error process, so that the next iteration is inspired by the results of the first. The second method is the theoretical/systematic approach to improvement. In that method, we try to understand why a specific cell performs better than another by using different experimental and theoretical techniques. For example, we can compare a specific theoretical model to experimental results or scan/analyze a cell using ultrasonic transmission mapping (UTM), X-ray computed tomography scans (X-ray CT), differential

thermal analysis (DTA), dV/dQ analysis and other techniques. UTM and X-ray CT allow non-invasive structural study of the cell, while DTA allow non-invasive study of the electrolyte and dV/dQ analysis allow to determine the degradation mechanisms that occurred inside the cell as well as their intensity.

Let us now briefly describe the content of each chapter of this thesis. Chapter 2 will introduce the science of lithium-ion cell. Chapter 3 will explain the experimental and theoretical techniques that were used in this work. Chapter 4 will describe the first part of this work, which used new electrolyte additives by trial-and-error to find an additive or an additive blend that was able to improve capacity retention. The new electrolyte additives tested were from the dioxazolone family of molecules. Chapter 5 will describe the second part of this work, which used a large matrix of cells cycling over different state of charge ranges, temperatures, and currents. The capacity versus time data from these cells were then fitted to a theoretical model. The cells were analyzed fully during and after cycling to better understand the failure mechanisms that occurred inside these cells. Chapter 6 will give a final discussion and conclusion.

CHAPTER 2 THE SCIENCE OF A LITHIUM-ION CELL

2.1 THE LITHIUM-ION CELL

A lithium-ion cell consists, in the uncharged state, of a graphite negative electrode and a lithium transition metal oxide positive electrode, like lithium nickel manganese cobalt oxide (NMC). Figure 2.1 shows that each electrode is coated on a current collector. The negative electrode is coated on copper, while the positive electrode is coated on aluminum. Aluminium is chosen at the positive electrode since the metal is corrosion resistant at high voltage due to the presence of a natural protective layer of alumina at the surface, while copper is chosen at the negative electrode since it does not alloy with lithium. A binder (e.g. polyvinylidene fluoride) and an electric conductor (e.g. carbon black) are mixed with the active materials before coating them on the current collectors using a solvent such as n-methyl pyrrolidone.[1,2] The two electrodes are separated by an electrolyte and a polyethylene or polypropylene separator. The electrolyte consists of a mixture of a salt, solvents, and some additive(s).

Figure 2.2 a) shows a photograph of the lithium-ion 402035-size pouch cells used in the current work. The energy of the battery is stored in the jelly roll, which is situated at the bottom of 2.2 a), while the upper part of 2.2 a) shows the gas bag of the pouch cell (gas produced in the jelly roll moves to this bag). Figure 2.2 b) show a cross-section of the jelly roll, where one can see multiple positive electrode and negative electrode layers spiraling one around the other.

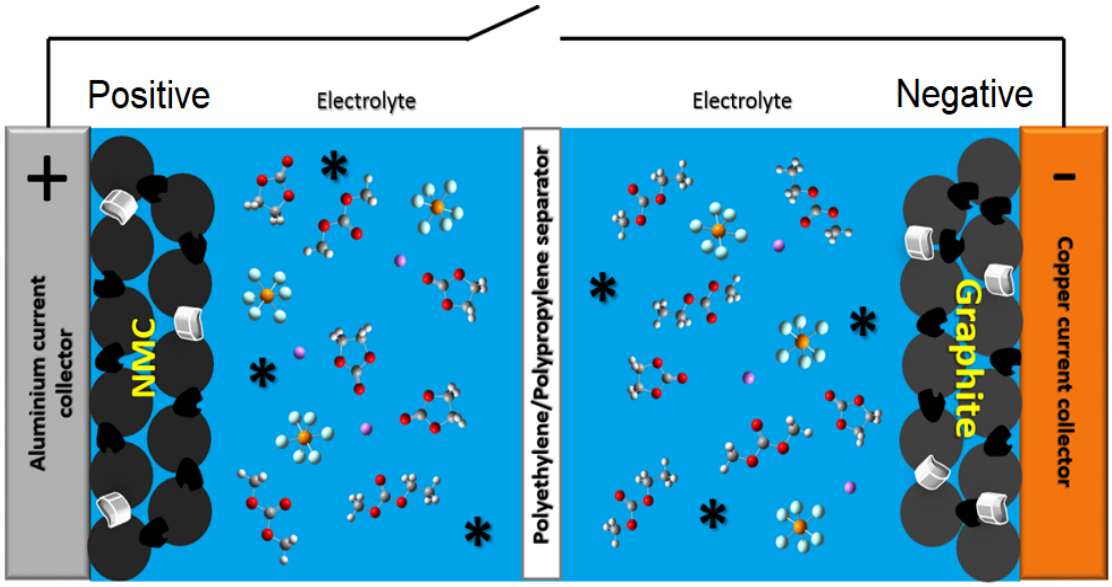

Figure 2.1: Simplified illustration of a lithium-ion cell in its pristine state. As an example, the electrolyte in the figure contains $LiPF_6$ as the salt and a mixture of the three solvents: ethylene carbonate, ethyl methyl carbonate and dimethyl carbonate. The stars represent an additive, the circles represent the active material particles, the white particles represent the binder, and the black particles represent the carbon black.

Figure 2.2 c) shows an expanded view of Figure 2.2 b) to see more detail. Finally, Figure 2.2 d) shows an expanded view of Figure 2.2 c). In this last view, we can see 1) the aluminum current collector (gray line), 2) the NMC active particles, 3) the copper current collector (white line), 4) the graphite active particles and 5) the separator. Note that the NMC and graphite active particles are present on both sides of their respective current collectors.

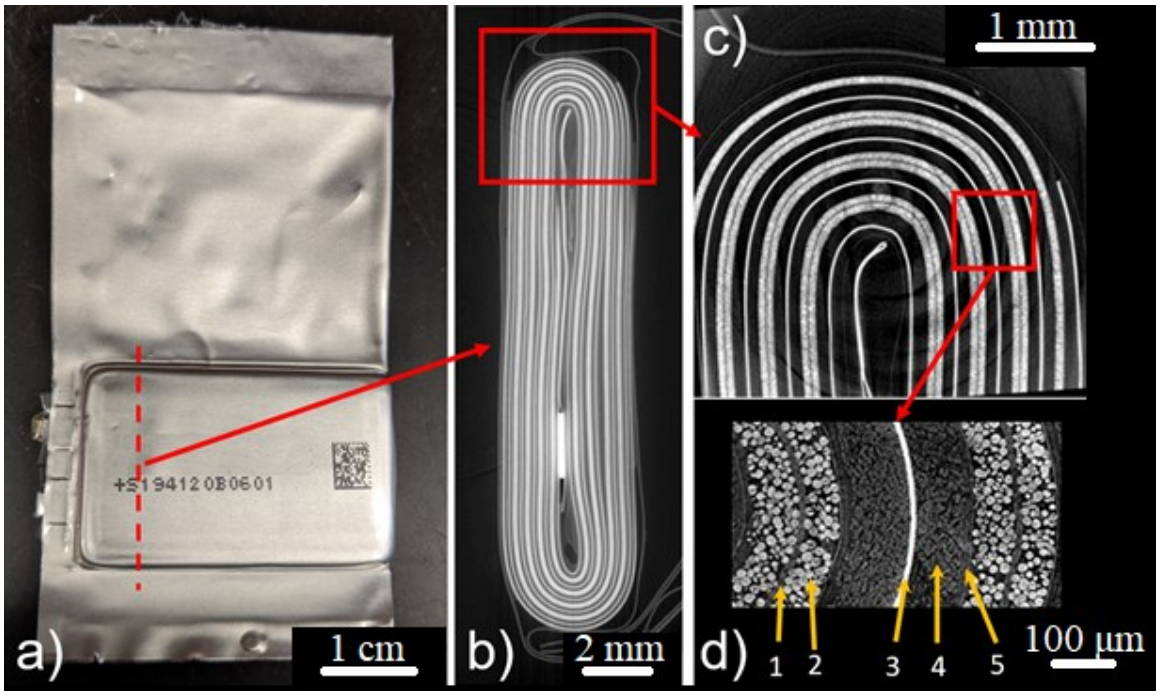

Figure 2.2: In this figure we can see**,** a) a typical pouch cell used in this work, b) a cross section of the jelly roll and c), d) expanded views of the jelly roll. d) shows 1) the aluminum current collector (gray line), 2) the NMC active particles, 3) the copper current collector (white line), 4) the graphite active particles and 5) the separator. CT-scans courtesy of Toby Bond.

The active materials of the positive and negative electrode, like NMC (Figure 2.3 b)) and graphite (Figure 2.3 c)), are intercalation compounds. This means that both compounds are made of parallel sheets in such a way that lithium atoms can be inserted between those sheets. Graphite is made of flat graphene sheets, while NMC is made of "thick sheets". The sheets in NMC are made of transition metal oxide octahedra (see Figure 2.3 b)). Oxygen atoms are present at each vertex of the octahedra, and a transition metal (Ni, Mn, Co) is present at the center of each octahedron. In the uncharged state, lithium atoms are present between the NMC sheets like a sandwich (Figure 2.3 b)). When a lithium-ion cell is charged, the lithium atoms inside the NMC electrode lose electrons due to the applied potential and the resulting lithium ions diffuse to the graphite electrode through the

electrolyte and separator. They then intercalate inside the graphite structure. To complete the circuit, electrons are added to the intercalated lithium ions. In the charged state, graphite becomes $LiC_{6,}$[3] while $LiNi_{0.6}Mn_{0.2}Co_{0.2}O_2$ (NMC622) loses most of its lithium. Throughout, both electrodes stay electrically neutral. The exact opposite occurs during discharge.

Figure 2.3 a) shows three potential curves: the potential curve of a full lithium-ion cell, of a graphite/Li half-cell and a NMC/Li half-cell plotted versus capacity (capacity corresponds to the amount of charge stored). In this case the full cell was a pouch cell and the electrodes for the half-cells (coin cells) were extracted from an identical pouch cell. If a full lithium-ion cell is charged from a cell voltage of 1.5 V to 4.3 V, during this process the potential of the graphite electrode (potential versus lithium metal as a reference electrode, V vs. Li/Li^+) decreases from ~1.5 V vs. Li/Li^+ to ~0.080 V vs. Li/Li^+, following the curve in Figure 2.3 a), while the NMC electrode has an increase in potential from ~3.0 V vs. Li/Li^+ to ~4.38 V vs. Li/Li^+. The difference between the half-cell potential curves gives the full cell potential curve.

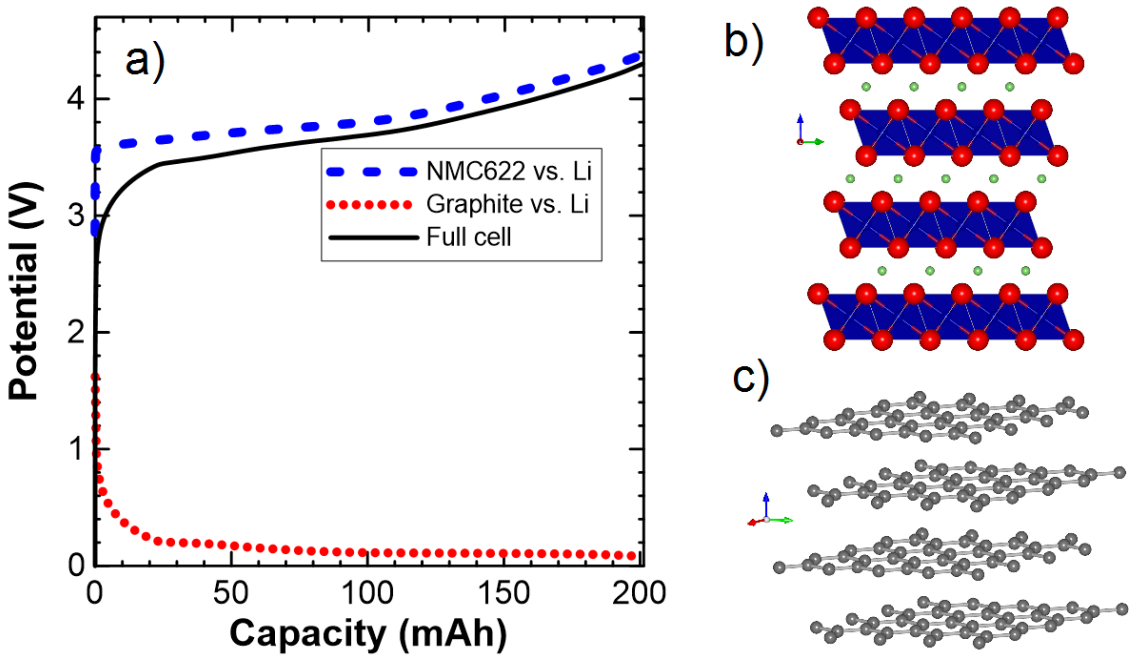

Figure 2.3: a) shows potential-capacity curve of a 200 mAh full lithium-ion cell (continuous black line) and the respective graphite/Li (blue dotted line) and $LiNi_{0.6}Mn_{0.2}Co_{0.2}O_2$ (NMC622)/Li potential-capacity curves (red dashed line). b) shows the crystalline structure of $LiMO_2$, where M is a transition metal or a mixture of transition metals (e.g. Ni, Mn, Co). In the case of a mixture of Ni, Mn and Co, the crystalline structure is called NMC. This structure corresponds to a fully discharged/pristine positive electrode. c) shows the crystalline structure of graphite. This structure corresponds to a fully discharged negative electrode.

Figure 2.4 a) shows a representation of the extremity of an unrolled jelly roll. As shown in the figure, the anode (negative electrode) has a larger area than the cathode (positive electrode). The extra width of the negative electrode is called the overhang, while the extra length of the negative electrode is called the overlap. The overhang and the overlap are vital parts of the battery, since without them misalignment of the positive and negative electrodes could result in lithium plating at the closest edge of the negative electrode.[4,5] Since the overhang and overlap are not facing the positive electrode, they do not get lithiated during the beginning of the first charge of the battery. However, if one were to put the cell in open circuit condition at the end of the first charge, lithium ions would diffuse

from the region of the negative electrode that directly faces the positive electrode to these overlap and overhang regions, as shown in Figure 2.4 b) and 2.4 c). Since the color of graphite changes with its lithium concentration, one can easily see the evolution of this diffusion as a function of time. In fact, graphite goes from black to dark blue/grey to red (LiC_{12}) to gold (LiC_6) as more and more lithium intercalates inside its structure. This color change results from an increase in charge carrier concentration and Fermi energy caused by electron doping from lithium. As a result, intraband (Drude) and interband transitions are affected.[6] Figure 2.5 a) shows a graphite electrode that was fully charged for the first time (formation) and then stored for 2 days. We can see a fully charged region (gold region) with a lithium depleted overhang (black/red region). Note that the overhang region is fully black (without any red) **immediately** after formation, 2 days before Figure 2.5 a) was taken (not shown in the Figure 2.5). After 6 days, the overhang completely turns red in b) and after 36 days it almost completely turns gold in c), showing that lithium-ions diffuse from the charged region to the overhang region. The entire electrode would turn gold if given enough time. Note that each subfigure corresponds to a different graphite electrode that was stored at different time. In general, this means that during cycling, the overhang and overlap regions can act as a sink or a source of lithium-ions, depending on the average state of charge (SOC) of the main section of the graphite electrode (the region directly facing the positive electrode) and the SOC of the overhang and overlap.

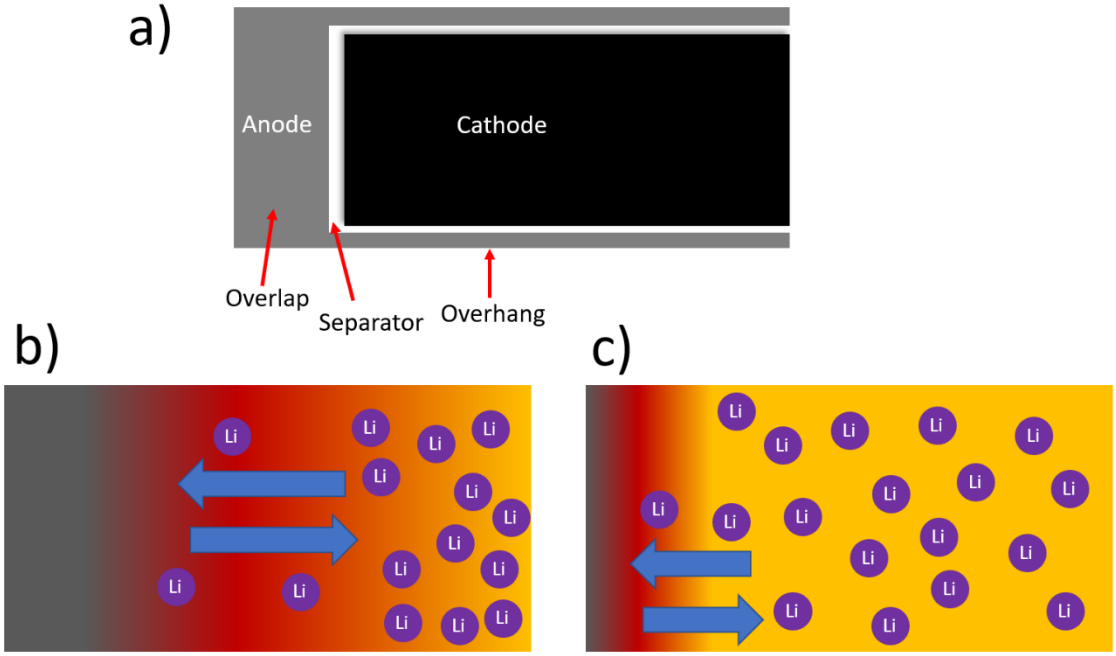

Figure 2.4: a) define the anode overlap and overhang of the negative electrode, while b) and c) show the diffusion of lithium-ions from/to the main section of the graphite electrode that is facing the cathode to/from the overhang or overlap. Similarly, this diffusion can occur in the opposite direction when the SOC of the overlap/overhang is higher than the main section of the graphite electrode. Colors are also shown to indicate that graphite changes color from gold to red to dark gray as the electrode is delithiated.

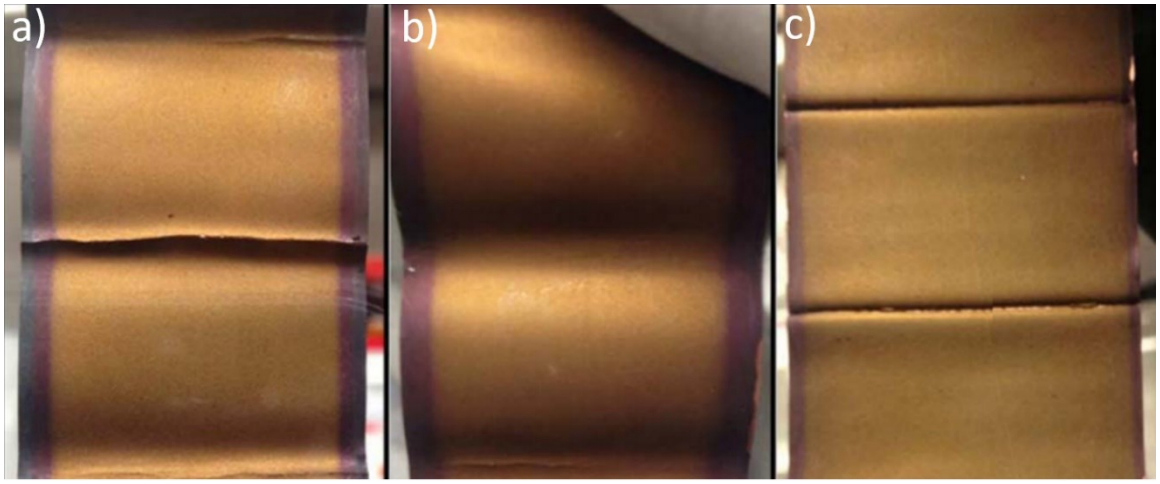

Figure 2.5: a) shows a fully charged graphite electrode 2 days after it was taken off the charger, b) shows the second graphite electrode 6 days after it was taken off and c) a third one after 36 days. Picture adapted from Gyenes et al.[5]

2.2 NEGATIVE ELECTRODE

The most used negative electrode in lithium-ion batteries is the graphite electrode. Graphite is usually preferred to other electrodes (i.e., lithium metal, metal alloys, lithium titanate, silicon-based electrodes) because of its combined stability and high specific capacity of 372 mAh/g. Graphite can be mined (natural graphite, NG) or synthesized in the laboratory by heating organic compounds at high temperature (artificial graphite, AG). Note that cells that contain artificial graphite usually perform better than cells that contain natural graphite due to the smaller irreversible volume expansion that they experience during cycling as a result of SEI growth.[7]

Figure 2.6 a) shows the voltage versus capacity, V(Q), of a graphite half-cell. One can see that the V(Q) curve has many points where the value of the slope rapidly changes and plateaus where the slope is almost zero. These regions of the curve are related to a specific arrangement of lithium atoms inside the graphite structure or to a specific transition between these different arrangements. These specific arrangements of lithium atoms inside the graphite structure are called stages and stage 1 to stage 4, including pure graphite (C_6) are shown in Figure 2.6 b). In b), the horizontal lines represent graphene sheets, while the purple circles represent lithium atoms. In a), we can see stage 1 at around ~372 mAh/g and stage 2 at ~185 mAh/g. The plateau between these two points represents the stage 2 to stage 1 transition. Between ~80 mAh/g to ~185 mAh/g one can see another plateau that is due to the stage 2L to stage 2 transition. The difference between stage 2L and stage 2 is that in stage 2L the Li atoms are dispersed randomly in the plane (L = liquid), while in stage 2 the Li atoms are arranged in an orderly fashion. Then, from 0 mAh/g to ~80 mAh/g, we have

the graphite to stage 4 transition, the stage 4 to stage 3 transition and the stage 3 to stage 2L transition, as shown in a).

During the first charge of the battery, a passivating film named the solid electrolyte interface (SEI) forms over the active particles of the negative electrode (the visual readers can have a look at Figure 2.12 for an illustration of the SEI). This passivating film is formed due to the reduction of the electrolyte and protects the electrolyte from further reduction. A similar film is also formed at the positive electrode.

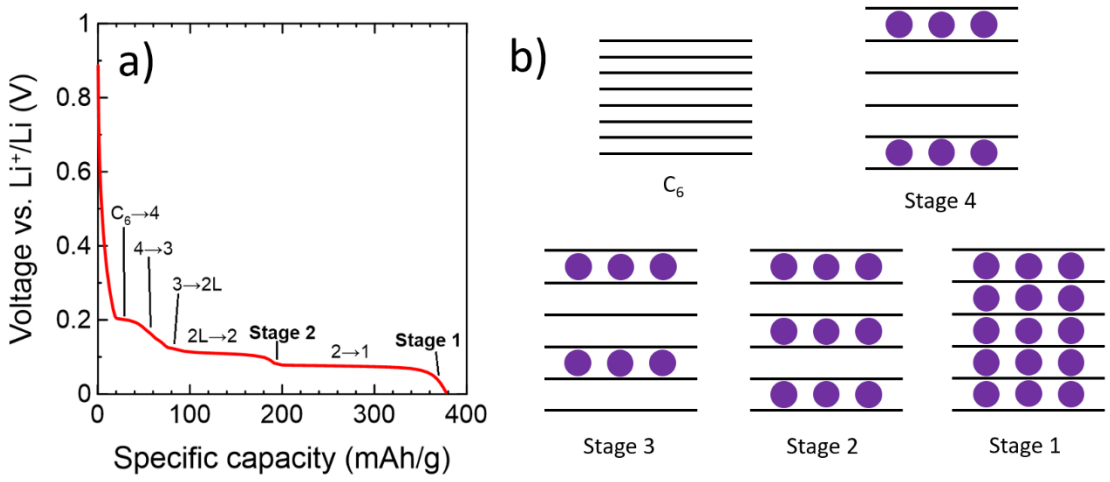

Figure 2.6: a) shows the voltage versus capacity curve of a graphite half-cell with the position of the different stages and stage transitions. b) shows what the different stages look like. The horizontal lines in b) represent graphene sheets, while the purple circles represent lithium atoms.

2.3 POSITIVE ELECTRODE

Many different types of positive electrodes exist. The most common type are $LiNi_{1-x-y}Mn_xCo_yO_2$ (where x = 0 to 1, y = 0 to 1 and x + y < 1; called NMC electrodes), $LiNi_{1-x-y}Co_xAl_yO_2$ (where x = 0 to 1, y = 0 to 1 and x + y < 1; called NCA electrodes) and $LiFePO_4$ (called LFP). While NMC and NCA electrodes have higher specific energy density than

LFP, LFP has improved safety compared to NMC and NCA electrodes. NCA electrodes have the worse safety. However, note that the safety and specific energy density of NMC and NCA electrodes also depends on the relative nickel content, as well as other parameters. The higher the nickel content in these electrodes, the higher the specific energy density and the lower the safety. The current work will focus on the $LiNi_{0.6}Mn_{0.2}Co_{0.2}O_2$ (NMC622) positive electrode, which shows a good compromise of high specific energy density, good safety, and good stability.

2.4 EXPANSION/CONTRACTION OF ACTIVE MATERIAL

The intercalation and deintercalation of lithium atoms from the graphite and NMC lattices causes repeated expansion and contraction of the graphite and NMC structures. As a result, these expansions can cause the SEI that surround these particles to crack and lose passivating ability and/or expansion can cause the graphite and NMC active particles to crack if the charge and discharge of the battery occurs at very high rate (>C/3). Note that a rate (i.e. C-rate) of C/x correspond to the rate/electric current it takes to charge or discharge the cell in x hours. As such, understanding these expansions and contractions is important to understand the lifetime performance of a cell.

Figure 2.7 a) shows the fractional volume change as a function of state of charge for graphite and NMC622 lattices. Here, 100% state of charge corresponds to a NMC622/graphite cell that is charged to 4.1 V. One can see a plateau (no volume change) for graphite between a state of charge of ~50% and ~90%. This plateau is due to the stage 2L to stage 2 transition, as shown in Figure 2.6 a). While graphite does expand outside the range of that transition. We also see that the graphite crystalline structure expands by 6%

over the full 100% SOC range (3.0 - 4.1 V), while the NMC622 crystalline structure contracts by 2% over the full range.

Figure 2.7 b) shows the pressure experienced by constrained NMC622/graphite cells as a function of state of charge at beginning of life. In that figure, we can see the stage 2L to 2 transition plateau again. However, we see a non-zero slope in the stage 2L to 2 transition region. This could be due to other effects like SEI growth, electrode stack deformation or active positive electrode particle cracking. Figures 2.7 c) and d) show the lattice parameter a and c as a function of lithium concentration inside NMC622. A line that indicates when the cell voltage is 4.1 V is indicated. Figures 2.7 a), c) and d) show that the decrease in the lattice parameter a is responsible for the contraction of the NMC622 particles during charging.

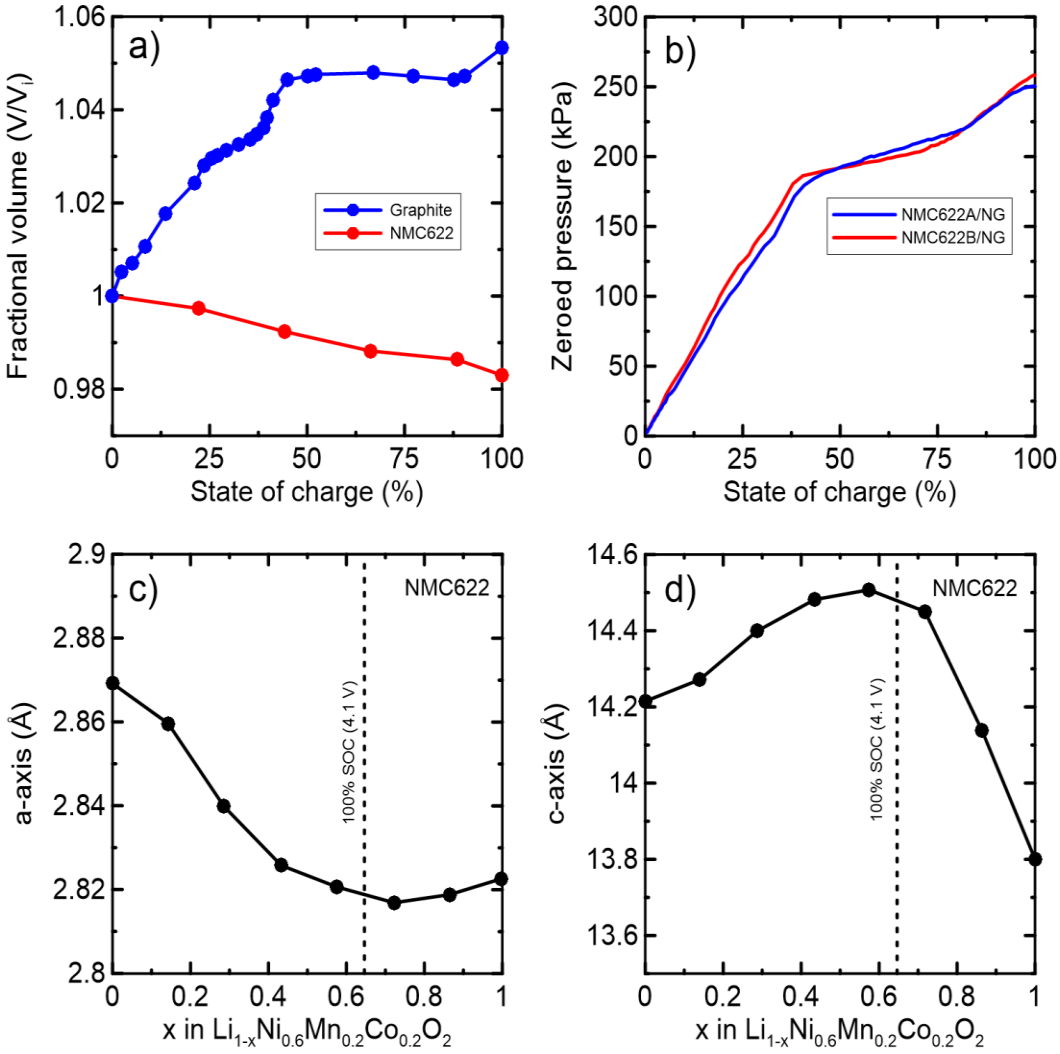

Figure 2.7: a) shows the fractional volume change of the primitive cell of graphite and NMC622 as a function of state of charge, b) shows the zeroed pressure change of a constrained NMC622/graphite pouch cells (with coating A or B on the positive electrode) as a function of state of charge, c) and d) show the change in a-axis and c-axis lattice parameters of NMC622 as a function lithium concentration inside the structure. For a) and b), a state of charge of 100% is the state of charge that occurs when the full-cell is at 4.1V. NMC622 data in a), c) and d) were digitized from Lee et al.[8] and graphite data in a) were digitized from Louli et al.[9]

2.5 ELECTROLYTE

Figure 2.8 shows some salts and solvents that are used in lithium-ion cells. $LiPF_6$ is the most commonly used salt in today's lithium-ion cells for the following reasons. While

$LiClO_4$ is less moisture sensitive than other salts like $LiPF_6$ and $LiBF_4$, the high oxidation state of chlorine in perchlorate (+7), compared to (+5) for $LiPF_6$ and $LiAsF_6$ and (+3) for $LiBF_4$, makes it a strong oxidant. As a result, the perchlorate anion can react violently with the organic solvent at high temperature, via a redox reaction, raising safety issues.[10] While $LiAsF_6$ has a slightly higher lithium ion conductivity in a mixture of EC and DMC (see Figures 2.8 e) and 2.8 f)) than $LiPF_6$, the production of As(III) species at the graphite electrode also raises safety issues due to their toxicity.[10] Furthermore, while $LiBF_4$ has better thermal stability than $LiPF_6$, the lower ionic conductivity of $LiBF_4$ in electrolytes makes it an unwanted salt for applications that require fast charge.[10,11] Although $LiClO_4$ and $LiAsF_6$ salts are not used in commercial cells due to the safety issues they bring, they have been used in laboratory tests in the past.[10] Table 2.1 shows the decomposition temperature and conductivity in EC/DMC for each salt as well as the oxidation state of the central atom of each salt.[10]

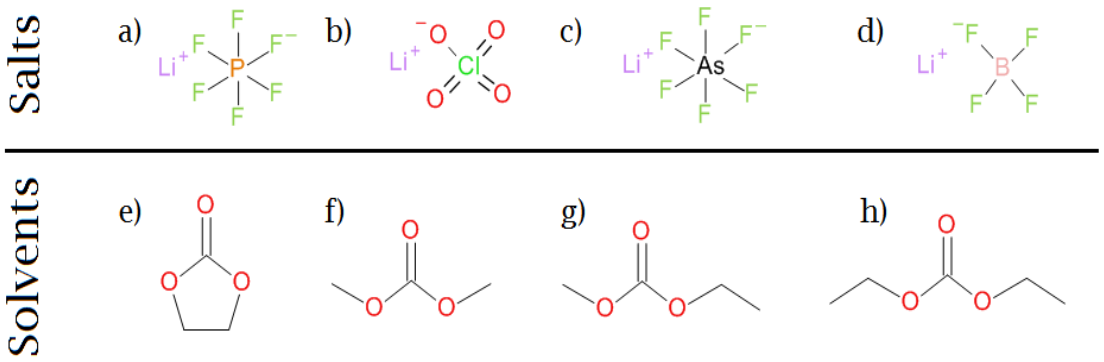

Figure 2.8: Some salts and solvents that can be used in lithium-ion battery electrolytes. In the first row, from left to right, some salts that can used in Li-ion batteries are shown: a) lithium hexafluorophosphate ($LiPF_6$), b) lithium perchlorate ($LiClO_4$), c) lithium hexafluoroarsenate ($LiAsF_6$) and lithium tetrafluoroborate ($LiBF_4$). In the second row, from left to right, the common solvents are shown: e) ethylene carbonate (EC), f) dimethyl carbonate (DMC), g) ethyl methyl carbonate (EMC) and h) diethyl carbonate (DEC).

Figures 2.8 e) - 2.8 f) show a range of different solvents used in lithium-ion batteries. Most often, these solvents are mixed to form a blend. The most common blends in our lab being EC:EMC 3:7, EC:DMC 3:7 and EC:EMC:DMC 25:5:70 (volume ratio).[12–14] These solvents are mixed for the reasons that follow. EC has a high permittivity, but a relatively high melting point (~36°C). The high permittivity of EC helps to dissolves the salt (e.g. $LiPF_6$), but EC needs to be melted beforehand, which is troublesome. To solve this problem, EC is mixed with a low melting point solvent like EMC, DMC or both. Not only does this lower the melting point of the mixed solvent, this also results in an electrolyte with lower viscosity and higher ionic conductivity, especially when DMC is present.[10,15,16] The relative percentage of each solvent can be optimized for the specific application in order to have an electrolyte with an appropriate viscosity, melting point and salt solubility.

Table 2.1: Decomposition temperature, lithium-ion conductivity, and oxidation state of the central atom for four different salts. The first two salts are common salt used today in commercial cells, while the last two are not used in commercial cells today, but they have been used in research in the past. The values of conductivity below are true at 1.0 M and 25°C.

	Decomposition temperature (°C)	**Conductivity in EC/DMC (S/cm)**	**Oxidation state of the central atom**
$LiPF_6$	~80	10.7	+5
$LiBF_4$	>100	4.9	+3
$LiAsF_6$	>100	11.1	+5
$LiClO_4$	>100	8.4	+7

2.6 REDUCTION AND OXIDATION

During charging, the negative electrode of a Li-ion battery becomes very reducing while the positive electrode becomes very oxidizing. Since the electrolyte is never perfectly immune to reduction and oxidation, especially during the first charge, it would get reduced at the negative electrode and oxidized at the positive electrode. As an example, let us consider the electrolyte 1.2M $LiPF_6$ EC:DMC (where 1.2M = 1.2 mol/L). Since EC is more easily reduced than DMC or even $LiPF_6$, it will reduce first. Past research[17] showed that the likely main reduction pathways of EC are the ones shown in Figures 2.9 and 2.10:

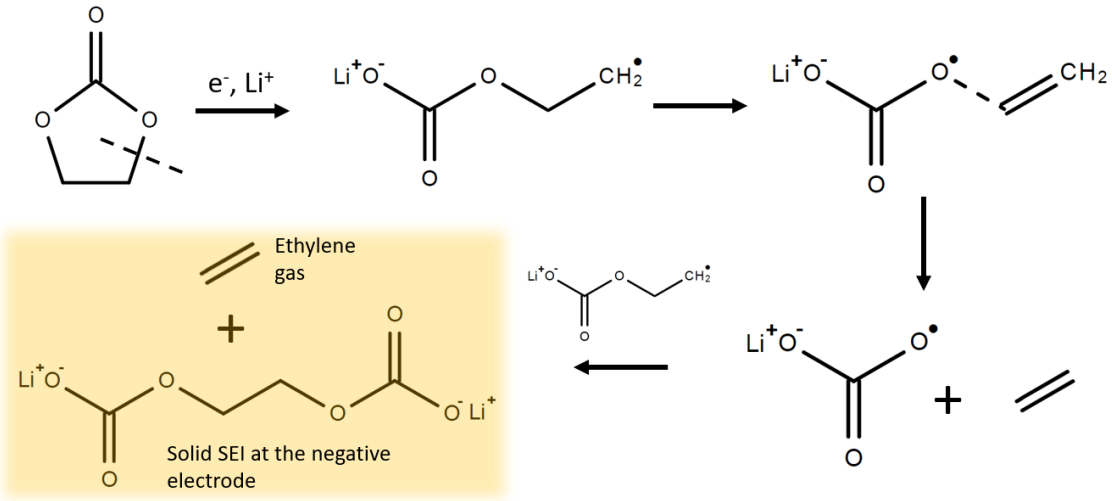

Figure 2.9: One electron reduction of EC. The result is ethylene gas and lithium ethylene dicarbonate. The shaded box shows the end products of the reduction.

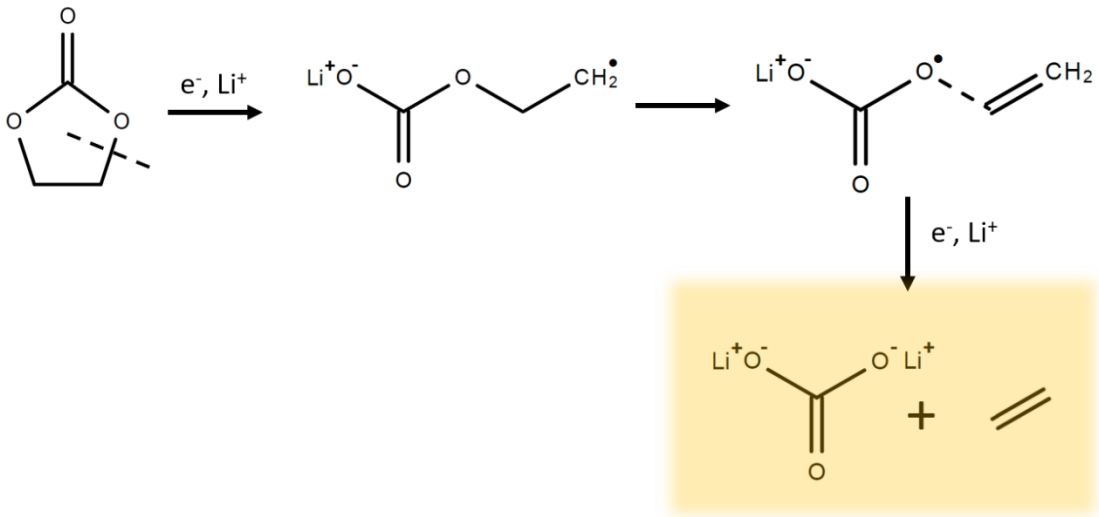

Figure 2.10: Two electron reduction of EC. The result is lithium carbonate and ethylene gas. The shaded box shows the end products of the reduction.

During this process, ethylene gas and the insoluble salts lithium carbonate and lithium ethylene dicarbonate are being produced. The salts deposit over the negative electrode surface to form the SEI and passivate the electrode against further reductions, like the reduction of DMC or more EC molecules. However, since the SEI has a high density of

lithium atoms, it still allows lithium conduction to occur through the SEI while passivation against further reduction occurs. We will see later that the SEI is however not perfect and side reactions, although they are at slower rate than before the passivation, can still occur.

2.7 ADDITIVES

The addition of a few percent of one or more additives to the electrolyte of lithium-ion cells has been shown to improve the cycling[18–24] and storage performance[20–22,24] of these cells. Note that cycling performance describes how often a battery can be charged and discharged before its discharge capacity decreases significantly, while storage performance describes how long a fully charged battery can stay in open-circuit conditions before its remaining capacity decreases significantly. Additives can improve cycling performance by reducing before EC, while forming a negative electrode SEI that is better at passivating against side reduction than the one formed by EC. Additives can also decrease oxidation and corrosion occurring at the positive electrode, resulting in better cycling and storage performance. Additives can also be used to improve safety (e.g. flame retardants).[25] Figure 2.11 shows a list of well known and new additives. At the top of Figure 2.11, one can see a list of the most studied additives: vinylene carbonate (VC),[18,21,23,24,26–28] ethylene sulfate (DTD),[14,19,22] propene sultone (PES)[22,29–31], lithium difluorophosphate ($LiPO_2F_2$; LFO)[23,32,33], fluoroethylene carbonate (FEC),[24,34–36] tris(-trimethyl-silyl)-phosphite (TTSPi)[37,38] and methylene methyl disulfonate (MMDS) [22,39]. At the bottom and middle right of the figure, one can see a list of some new or recently developed additives that were studied in this work: 3-phenyl-1,4,2-dioxazol-5-one (PDO), p-(4-fluorophenyl)-1,4,2-dioxazol-5-one (pFDO), p-(4-methoxyphenyl)-1,4,2-dioxazol-5-one (pMODO) and p-(4-

nitrophenyl)-1,4,2-dioxazol-5-one (pNDO). Note that the study of pFDO, pMODO and pNDO was motivated by the very good long-term cycling performance of the similar molecule PDO.[13] Similarly, the study of PDO itself was motivated by the good performance of 3-methyl-1,4,2-dioxazol-5-one (MDO) in propylene carbonate based electrolyte.[13,40] Many of the additives mentioned above contain a cyclic moiety and are polar due to the presence of carbonyl, sulfonate, or sulfate groups. However, two in Figure 2.11 are significatively different than the others: the phosphite ester TTSPi and the lithium salt $LiPO_2F_2$ (LFO).

2.8 DEGRADATION

Lithium-ion batteries are not perfect since they are prone to degradation which affects their performance. Many different types of degradation can occur, the main one being negative SEI growth. SEI growth caused by reduction of the electrolyte results in irreversible lithium inventory loss which causes capacity loss. Figure 2.12 shows SEI growth on a graphite particle for a bad electrolyte and a good electrolyte (with proper additive(s)). We can see that when the electrolyte contains the appropriate additive(s), the growth of the SEI can slow down drastically.

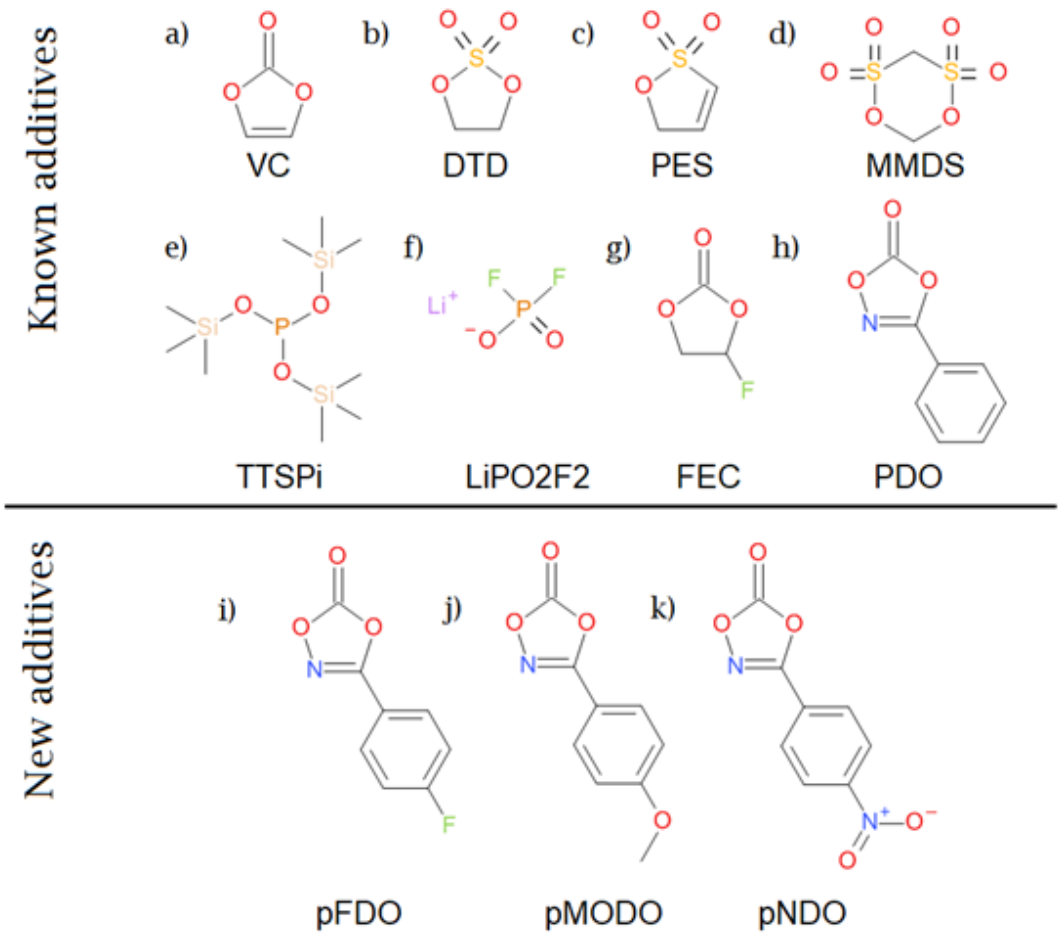

Figure 2.11: Figure showing some known and new electrolyte additives. In order from left to right and top to bottom: a) vinylene carbonate (VC), b) ethylene sulfate (DTD), c) propene sultone (PES), d) methylene methyl disulfonate (MMDS), e) tris(-trimethyl-silyl)-phosphite (TTSPi), f) lithium difluorophosphate (LiPO2F2; LFO), g) fluoroethylene carbonate (FEC), h) 3-phenyl-1,4,2-dioxazol-5-one (PDO), i) p-(4-fluorophenyl)-1,4,2-dioxazol-5-one (pFDO), j) p-(4-methoxyphenyl)-1,4,2-dioxazol-5-one (pMODO) and k) p-(4-nitrophenyl)-1,4,2-dioxazol-5-one (pNDO).

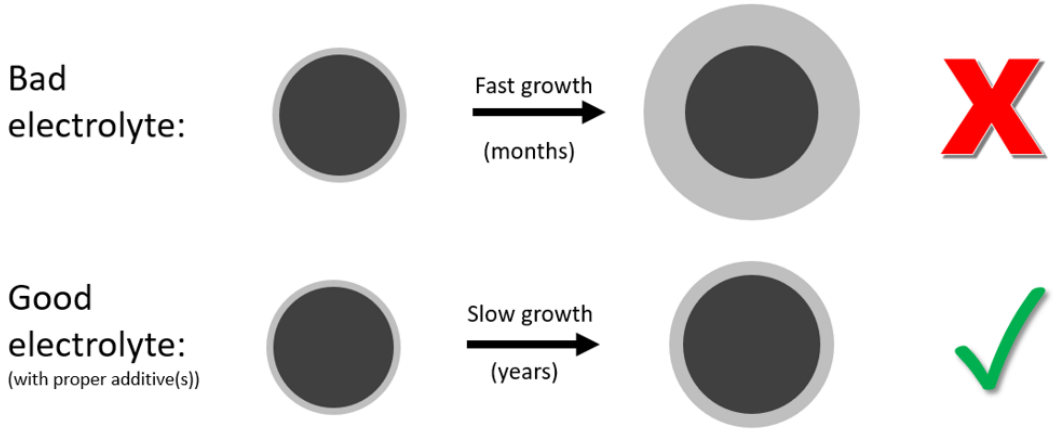

Figure 2.12: Growth of the SEI (gray) over a graphite particle (black) when the electrolyte is bad and when the electrolyte is good. Proper additives can slow down the growth of the SEI dramatically and improve the performance of the battery. Note that the SEI thicknesses shown here are not to scale: the diameter of a graphite particle is around 5 µm and the thickness of the SEI is around 20 nm.[41]

When a cell is cycled between a lower and upper cutoff voltage as a function of time as shown in Figure 2.13 a), the cell discharge capacity decreases as shown in Figure 2.13 b). The capacity fade in Figure 2.13 b) is mostly due to SEI growth. The growth of the SEI is generally assumed to be inversely proportional to the thickness of the SEI. This means that side reactions at the graphite electrode are diffusion limited. By solving the corresponding differential equation, one finds that the capacity of the battery as a function of time Q(t) can be predicted by:

$$Q(t) = Q_0\left(1 - A\sqrt{t}\right), \qquad (1)$$

where A is the rate of growth ($h^{-1/2}$), Q_0 is the initial capacity, A is a constant and t is the cycling time.

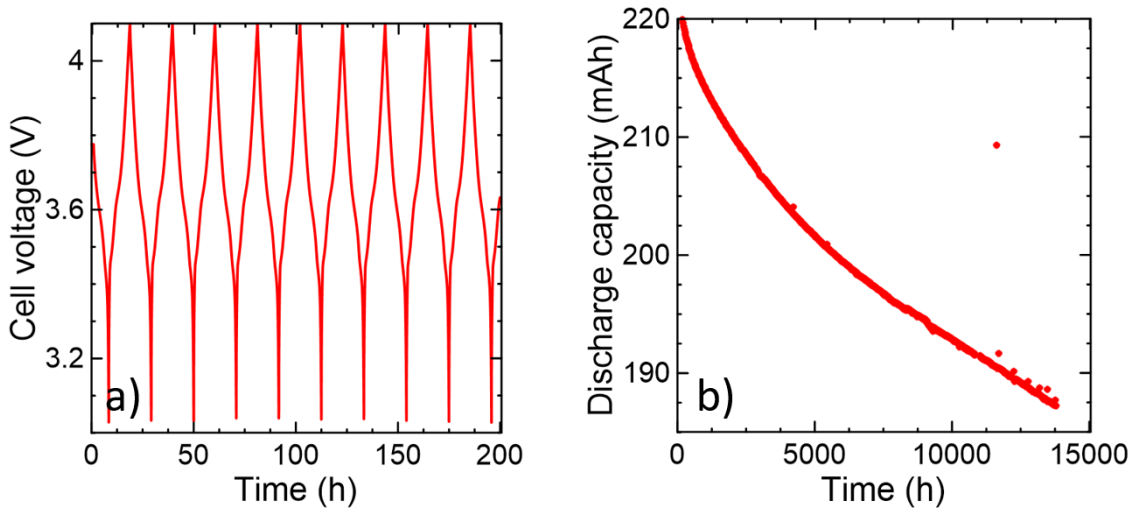

Figure 2.13: a) shows the voltage versus time during cycling of a cell and b) show the discharge capacity of that cell as a function of time for about 1.5 years of testing.

While equation (1) is valid under specific circumstances, it is not always valid. This is the case when the cell is charged at high current or when the cell impedance is high. Researchers can monitor the impedance of a cell using ΔV, which is the difference between the average charge voltage and the average discharge voltage. Figure 2.14 a) shows the voltage versus capacity graph of a cell during charge and discharge. It can be seen by eye that the average voltage during charge is higher than during discharge by ~ 0.1 V, so that $\Delta V \approx 0.1$ V in a). Note that ΔV is related to Ohm's law by $\Delta V \approx 2$ RI, where R is the DC resistance of the cell and I is the current. Figure 2.14 b) shows ΔV for the same cell as a function of cycling time and one can see that ΔV increases almost linearly as a function of time.

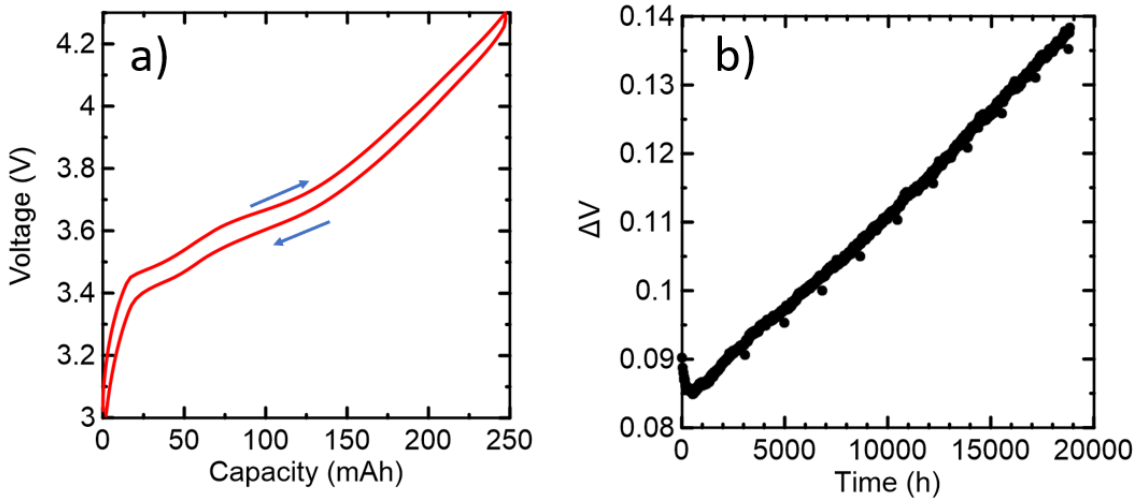

Figure 2.14: a) shows the voltage versus capacity curve during charge and discharge of a cell. The difference between the average charge and discharge voltage corresponds to ΔV. b) shows the evolution of ΔV as a function of cycling time for the same cell.

How does ΔV growth influence capacity loss during cycling? To better understand this, let us have a look at Figure 2.15. When cell impedance increases, the discharge voltage versus capacity Q(V) curve moves down by $(\Delta V - \Delta V_0)/2$, where ΔV_0 is the initial ΔV value. Figures 2.15 a) and b) show the effect of impedance growth on discharge Q(V) curves for two different lower cutoff voltages (LCV): 3.0 V and 3.77 V. In this example, exaggerated for clarity, we show three discharge Q(V) curves in both Figures 2.15 a) and b): The upper Q(V) curves are without impedance effects, the second have a ΔV growth of 0.1 V, and the lowest curves have a ΔV growth of 0.2 V. Due to the difference in slope of the V(Q) curve at 3.0 V versus at 3.77 V, we see that if a cell is discharged to 3.77 V without a constant voltage step, a much larger impedance related capacity loss can be seen than if the cell is discharged all the way down to 3.0 V. As a first order approximation, the resulting capacity loss is $\frac{1}{2}\frac{dQ}{dV}\Big|_L (\Delta V(t) - \Delta V_0)$. A similar reasoning can be applied to the constant current part of the charging Q(V) curve, which results in a capacity loss of $\frac{1}{2}\frac{dQ}{dV}\Big|_U (\Delta V(t) - \Delta V_0)$. A

$Q_{CV}(t)$ term is needed in the case of CCCV charging (CCCV charging means constant current charge to the upper cutoff voltage (UCV) and then maintain at that voltage until the current decrease below a certain value) but is unnecessary in the case of CC charging (CC charging means constant current charge to the upper cutoff voltage (UCV) without a constant voltage step). $Q_{CV}(t)$ correspond to the amount of capacity that is gained during the constant voltage step at top of charge as a function of time. A capacity gain can occur during this step since a constant voltage step allow more time for lithium-ions to intercalate inside the graphite electrode resulting in larger charge capacity. This term, like the impedance term, would not be needed if the diffusion of lithium-ion inside the cell was infinite.

Figure 2.15 c) shows $\frac{dQ}{dV}$ as a function of voltage during charge and discharge of the first cycle of a NMC622/graphite cell. A voltage shift between the charge and discharge $\frac{dQ}{dV}$ vs. V curves can be seen and this is caused by cell impedance. We can also see that a LCV of 3.0 V would result in a much lower impedance related capacity loss than a LCV of 3.4 V (around 18 times less). Note that impedance related capacity loss is reversible and can be recovered by switching to a lower cycling current, switching to voltage cutoffs with small dQ/dV values or lowering the cutoff current during the end of CCCV charging.

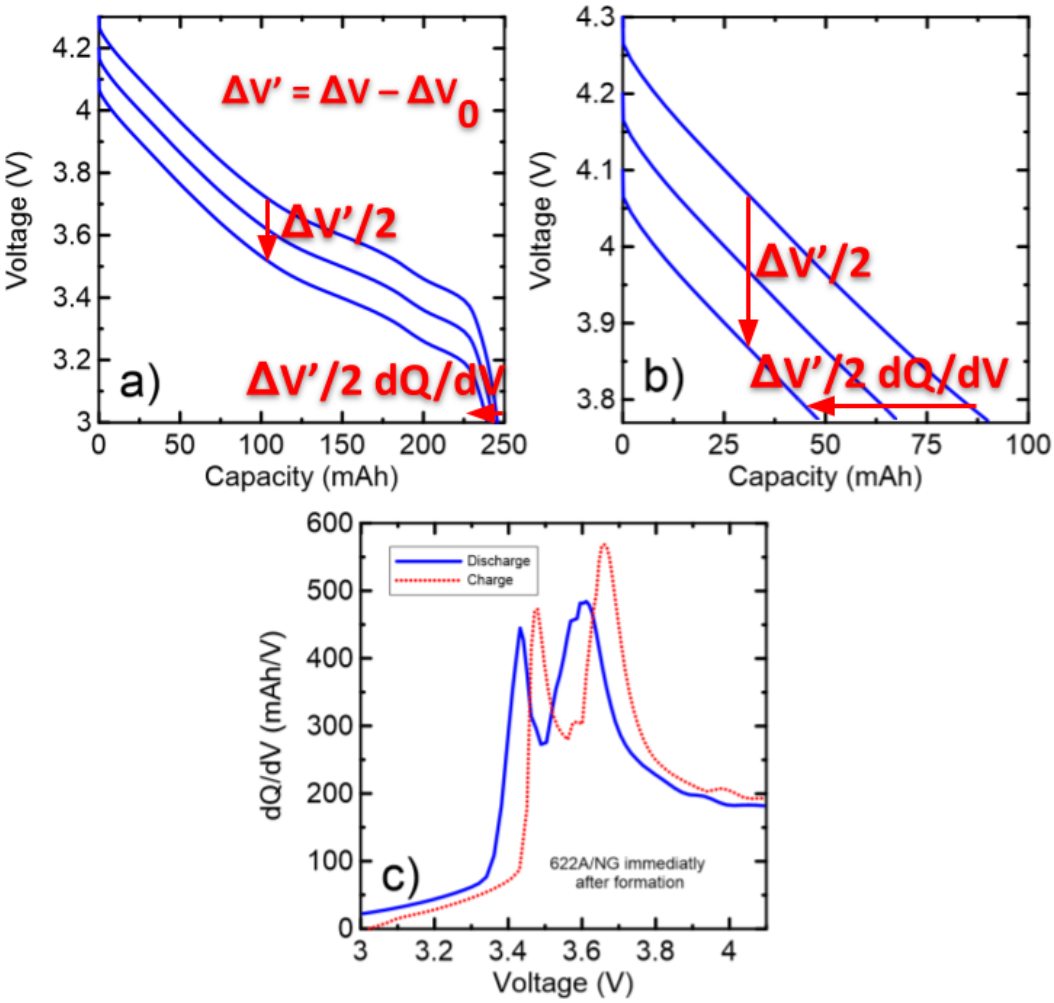

Figure 2.15: a) and b) shows the effect of impedance growth on discharge Q(V) curves for two different lower cutoff voltage (LCV): 3.0 V and 3.77 V. The slope of the Q(V) curve at the LCV has an impact on capacity loss. c) shows the derivative of the capacity with respect to voltage during charge and discharge of NMC622A/NG cells during the second charge/discharge cycle measured at C/20 and at 40°C. The shift between the two curves is mostly due to the non-zero value of ΔV which results in a ~0.1 V voltage shift.

This knowledge can be summarized into equations (2) and (3). The contribution to capacity loss from impedance is added to the contribution from SEI growth. The first is the charge capacity and the second is the discharge capacity:

$$Q_c(t) = Q_0\left(1 - A\sqrt{t}\right) - \frac{1}{2}\left.\frac{dQ}{dV}\right|_U (\Delta V(t) - \Delta V_0) + Q_{CV}(t) \quad (2)$$

$$Q_d(t) = Q_0\left(1 - A\sqrt{t}\right) - \frac{1}{2}\left(\left.\frac{dQ}{dV}\right|_L + \left.\frac{dQ}{dV}\right|_U\right) (\Delta V(t) - \Delta V_0) + Q_{CV}(t) \quad (3)$$

No term related to positive electrode active mass loss (i.e., how many positive electrode active particles lost electrical contact with the current collector; measured in grams) has been included in equations (2) and (3), since capacity loss mechanisms depend on whether the cell is anode limited or cathode limited. First, what is the meaning of a cell that is anode limited or cathode limited? To better understand the meaning of each, let us have a look at Figure 2.16.

Figure 2.16 a) illustrate a pristine cell using boxes and circles. Each circle represents a lithium atom and each box represent a site where lithium can be stored in graphite (blue), NMC (orange) or the SEI (green). In a pristine cell, most of the lithium atoms are present in the NMC electrode (~10% of the lithium atoms are present in the electrolyte as $LiPF_6$), the graphite electrode is empty and the SEI is not yet formed.

Figure 2.16 b) shows what happens after the first charge. The lithium atoms from the NMC electrode move through the electrolyte and intercalate inside graphite. During this process, some lithium reacts with the electrolyte to form the SEI. Then, the cell is discharged. If the cell is anode limited, the graphite electrode becomes empty of lithium before the NMC electrode becomes full of lithium. If the cell is cathode limited, the NMC electrode becomes full of lithium before the graphite electrode becomes empty of lithium.

Figure 2.16 c) shows an anode limited cell, while 2.16d) shows a cathode limited cell. Red lines in Figure 2.16 d) represent positive electrode active mass loss. If the cell loses more lithium due to SEI growth than lithium sites in the NMC electrode, the cell is anode limited and if the opposite is true the cell is cathode limited.

In the case where the cell is anode limited, the capacity loss due to SEI growth is larger than the capacity loss due to cathode mass loss and equations (2) and (3) are correct. However, in the case where the cell is cathode limited, the opposite is true and equations (2) and (3) need to be replaced with:

$$Q_c(t) = Q_0\left(1 - \frac{m_p(t)}{m_{p0}}\right) - \frac{1}{2}\left.\frac{dQ}{dV}\right|_U (\Delta V(t) - \Delta V_0) + Q_{CV}(t) \quad (4)$$

$$Q_d(t) = Q_0\left(1 - \frac{m_p(t)}{m_{p0}}\right) - \frac{1}{2}\left(\left.\frac{dQ}{dV}\right|_L + \left.\frac{dQ}{dV}\right|_U\right)(\Delta V(t) - \Delta V_0) + Q_{CV}(t)\,, \quad (5)$$

where m_{p0} is the initial positive active mass in gram and $m_p(t)$ is the positive active mass at time t.

Another mechanism that can affect capacity is diffusion from/to the overhang or overlap. Figures 2.17 a) and b) show these situations (the purple circles are lithium atoms). The rate of diffusion from one region to the other can be approximately calculated using a similar approach to Newton law of cooling. After defining $\Delta\rho_{OHL}$ in equation (6) has the difference in surface density of lithium-ion between the active area of the graphite electrode and the overhang/overlap region, a differential equation (7) is built from which we get equation

(8). From equation (8), we propose equation (9) which represents a more complete model for the discharge capacity. The overhang/overlap region has a capacity of $Q_{A,}$ a surface of S_A and a surface density of ρ_A and the active area of the graphite electrode has a capacity of $Q_{B,}$ a surface of S_B and a surface density of ρ_B.

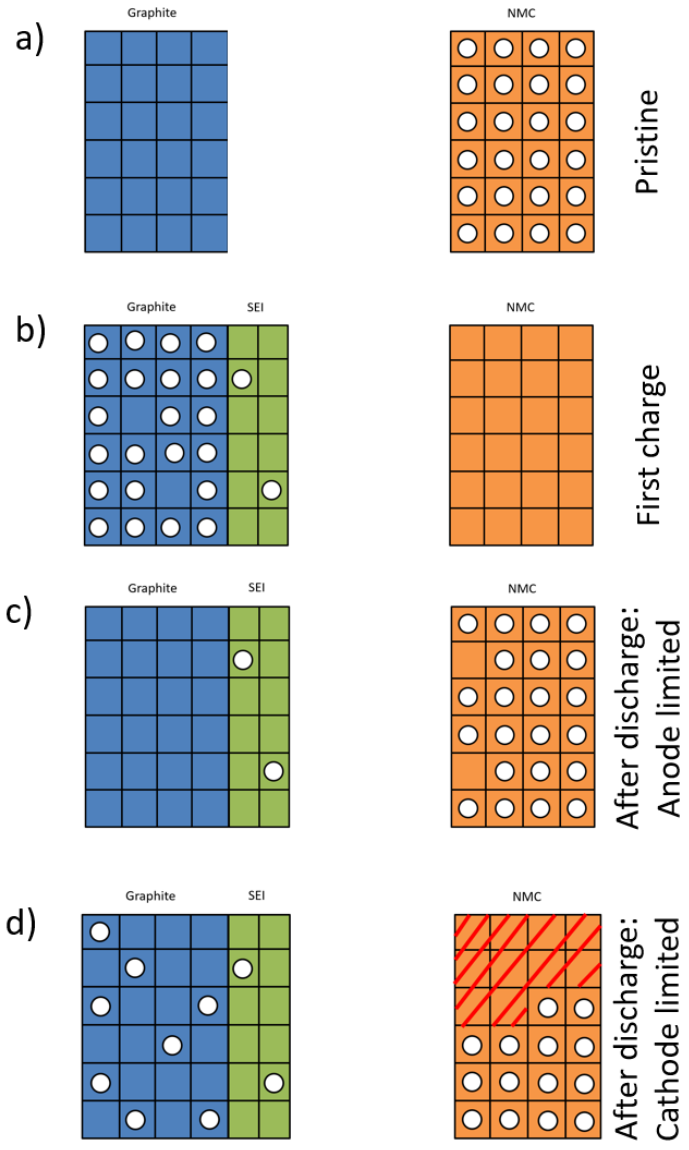

Figure 2.16: Model showing lithium atom (circles) and lithium sites (boxes) in the graphite electrode (blue), SEI (green) and the NMC electrode (orange). a) shows a

pristine cell, b) shows a cell after its first charging, c) shows an anode limited cell that was discharged after being charged and d) shows a cathode limited cell that was discharged after being charged. Red lines represent lithium sites that are no longer available because they became disconnected from the current collector.

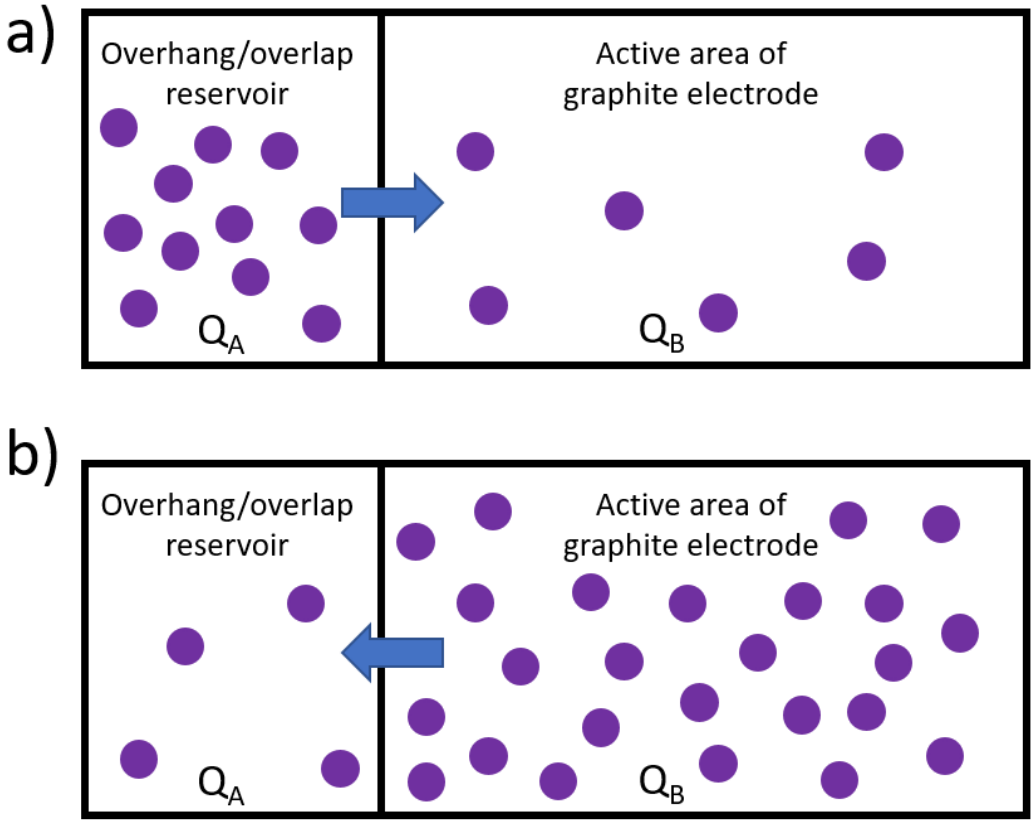

Figure 2.17: a) Diffusion of lithium atom from the overhang/overlap to the active area of the graphite electrode and b) diffusion of lithium atom from the active area of the graphite electrode to the overhang/overlap. The capacity in the overhang/overlap reservoir is represented by Q_A and the capacity in the active area of the graphite electrode is represented by Q_B. The overhang/overlap region has a surface of S_A and the active area of the graphite electrode has a surface of S_B.

$$\Delta\rho_{OHL} = \frac{Q_B}{S_B} - \frac{Q_A}{S_A} = \rho_B - \rho_A \tag{6}$$

$$\frac{d\Delta\rho_{OHL}}{dt} = -\frac{1}{\tau^*}\Delta\rho_{OHL} \tag{7}$$

$$\Delta\rho_{OHL}(t) = \Delta\rho_{OHL}(0)e^{-t/\tau^*} \tag{8}$$

$$Q_d(t) = Q_0\left(1 - A\sqrt{t}\right) - \frac{1}{2}\left(\left.\frac{dQ}{dV}\right|_L + \left.\frac{dQ}{dV}\right|_U\right)(\Delta V(t) - \Delta V_0) + Q_{CV}(t) \pm K\left(1 - e^{-t/\tau}\right) \quad (9)$$

2.9 SLIPPAGE AND ACTIVE MASS LOSS: EFFECT ON POTENTIAL VERSUS CAPACITY CURVES

Like Figure 2.3 a), Figure 2.18 a) shows the full-cell V(Q) and half-cell V(Q) curves of a pristine cell. However, what happen to those three curves when the cell degrades? Two degradation mechanisms can affect the half-cell V(Q) curves: lithium inventory loss and active mass loss. Figure 2.18 b) show the case where only lithium inventory loss occurs and no active mass loss occurs at any electrode. In that specific case, lithium inventory loss due to SEI growth is equivalent to slipping the negative electrode half-cell V(Q) curve forward as shown in Figure 2.18 b). For good reason, this action is called slippage. In Figure 2.18 b), 50 mAh of slippage has occurred due to SEI growth and as a result, the full-cell capacity decreased by the same amount (from 250 mAh to 250 – 50 = 200 mAh). Figures 2.18 c) and d) show cases where only positive electrode active mass loss occurs. In the present case, the positive electrode half-cell V(Q) curve is compressed in the x-axis direction to 66% of its initial capacity due to 33% of active mass loss. This results in a decrease in capacity from 250 mAh to ~170 mAh. In the case of c), the positive electrode active mass loss occurred when the active particles were full of lithium and in d) when the active particles were almost empty of lithium. Note that active mass loss can also happen at the negative electrode, but usually at a slower pace.

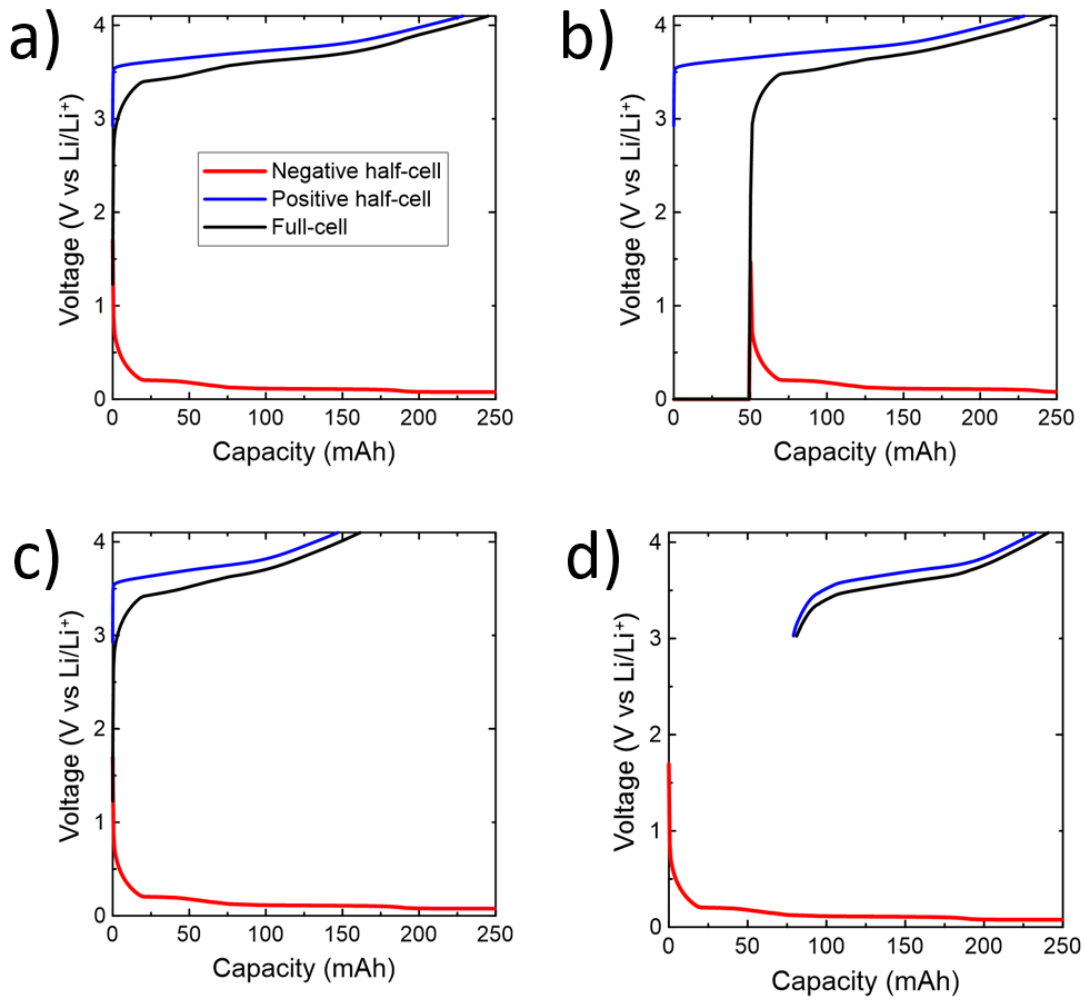

Figure 2.18: Full-cell and half-cell voltage versus capacity curve of a) a pristine NMC622/graphite cell. b) a hypothetical NMC622/graphite cell with 50 mAh of lithium inventory loss, but without any active mass loss and c) and d) a hypothetical NMC622/graphite cell with a 33% loss in positive electrode active mass loss, but without any lithium inventory loss. In the case of c), the positive electrode active mass loss occurred when the active particles were full of lithium and in d) when the active particles were almost empty of lithium.

2.10 WHAT IS RELATIVE SLIPPAGE AND HOW TO CALCULATE LITHIUM INVENTORY LOSS?

Relative slippage is the difference between the absolute slippage of the positive and negative half-cell V(Q) curve. It also corresponds to the amount of lithium atoms that were

irreversibly lost in the SEI relative to the number of lithium sites that were lost in the positive electrode due to loss of electric contact and is measured in mAh. If no loss of electric contact happens at the positive electrode (i.e., no positive active mass loss) than lithium inventory loss and relative slippage are equal, otherwise they are not. Figure 2.19 shows how we can calculate the lithium inventory loss due to SEI growth, Q_{SEI}, from the half-cell V(Q) curves when positive active mass loss does occur. We can see the full-cell, anode, and cathode half-cell V(Q) curves before and after long-term cycling, where the capacity of the full cell at top of charge has been fixed at the value from the formation cycle. Note that the formation cycle corresponds to the first charge/discharge of the battery. The half-cell V(Q) before long-term cycling were charged once (i.e., formation), which explain why the relative slippage at that point is not exactly zero (SEI growth occurs during the first cycle of charge and discharge).

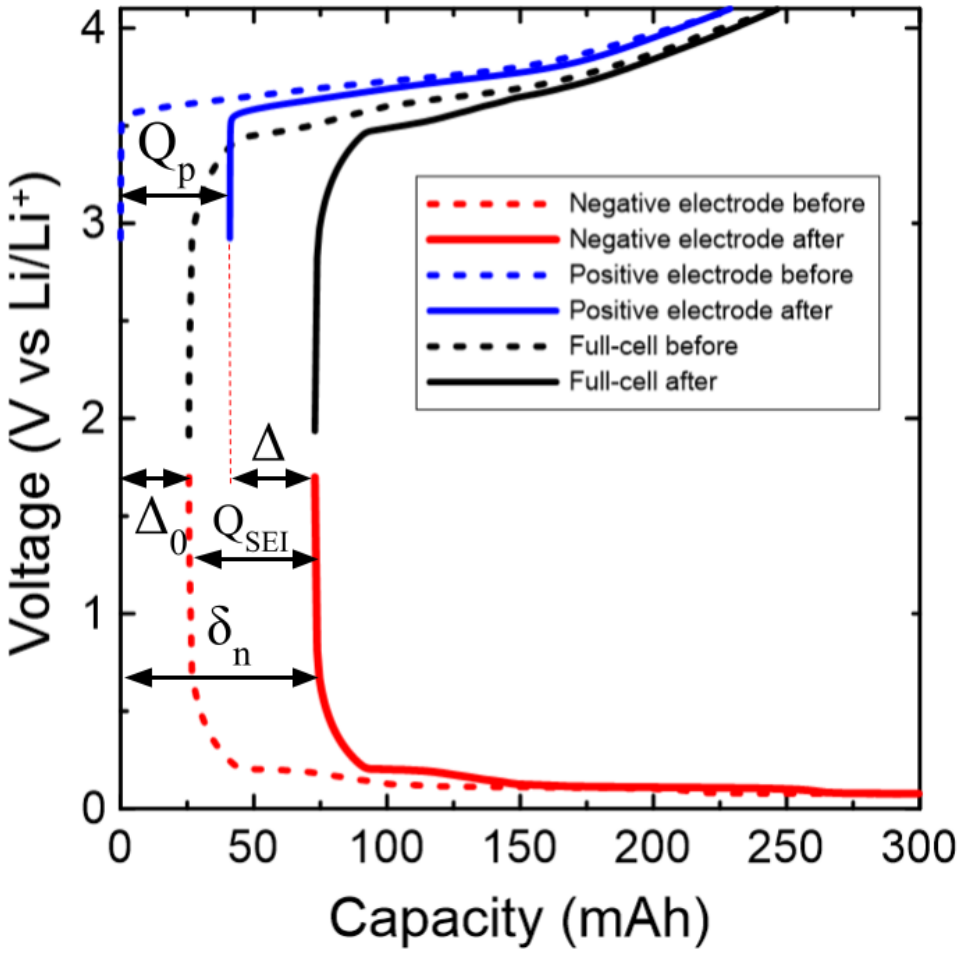

Figure 2.19: Positive and negative electrode half-cell V(Q) curves and full-cell V(Q) curves before cycling/after formation and after cycling.

From Figure 2.19, let us now calculate the lithium inventory loss of a cell that both had SEI growth at the negative electrode as well as positive active mass loss. From the figure, one can deduce that Q_{SEI} is equal to (where Q_p and Δ are also defined in equations (11) and (12)):

$$Q_{SEI} = (\Delta - \Delta_0) + Q_p = (\delta_n - \delta_{n0}) \quad (10)$$

$$Q_p = Q_0 (1 - m_p/m_{p0}) \quad (11)$$

$$\Delta = \delta_n - Q_p, \quad (12)$$

where Q_p is the capacity associated with positive active mass loss in mAh, δ_n is the absolute negative electrode slippage as defined in the figure, m_{p0} is the initial positive active mass in grams, m_p is the final positive active mass and δ_{n0} is δ_n before cycling/after formation, $\Delta = \delta_n - Q_p$ is the final relative slippage and $\Delta_0 = \delta_{n0}$ is the initial relative slippage. If the cell is anode limited, $\Delta > 0$ and if the cell is cathode limited, $\Delta < 0$.

2.11 dV/dQ ANALYSIS

To determine the principal cause of capacity loss of a cell, it is important to figure out the positive and negative electrode active mass and relative slippage of that cell before and after long-term cycling. It is possible to figure out the negative and the positive electrode active mass and the relative slippage between both electrode from the full-cell voltage versus capacity V(Q) curve when a library of positive electrode/Li and negative electrode/Li half-cell voltage versus capacity curves is available. dV/dQ analysis is used to accomplish this.[42] Knowing that the full-cell V(Q) curve is a combination of the positive electrode/Li and negative electrode/Li half-cell curves, we can fit those two curves with the appropriate coefficients to get the full cell curve and the coefficients can tell us information about the active masses and slippages of each electrode. Since taking the derivative of the V(Q) curve helps us to see its features more clearly, this fit is applied to the dV/dQ vs Q curve instead of the V(Q) curve. In the case that $V_p(q_p)$ is the reference positive electrode/Li half-cell voltage versus specific capacity curve and that $V_n(q_n)$ is the reference negative electrode/Li half-cell voltage versus specific capacity curve, the measured full-cell V(Q) can be fitted using equation (13):

$$\frac{dV(Q)}{dQ} = \frac{1}{m_p}\frac{dV_p}{dq_p} - \frac{1}{m_n}\frac{dV_n}{dq_n}, \quad (13)$$

where the specific capacity of the reference positive half-cell, q_p, and the reference negative hall-cell, q_n, are related to the capacity of the full-cell Q by equation (14):

$$Q = q_p m_p + \delta_p \; ; \; Q = q_n m_n + \delta_n \, , \quad (14)$$

where δ_p is the absolute positive electrode slippage.

Let us have a look at Figure 2.20 which shows the fitting process. The goal here is to fit the calculated dV/dQ curve (black line) to the measured dV/dQ curve (green line). Figure 2.20 a) show the dV/dQ curves of the half-cells and calculated full-cell in the case of zero slippage and when each electrode mass is 1 gram. The first step is to shift (i.e. slippage) the reference negative electrode dV/dQ curve to the left, as shown by the red arrow, in order to fit the calculated dV/dQ curve (black) to the experimental dV/dQ in the 20 mAh region. Figure 2.20 b) show the result of this first step. Then the next step is to adjust the positive electrode active mass by stretching the positive electrode half-cell dV/dQ curve, as show by the blue arrow. Figure 2.20 c) also show the result of this second step. Then, the positive electrode half-cell dV/dQ curve is shifted to the left, stretched again before an automatic fit is applied, as shown in Figure 2.20 c) to e). Figure 2.20 f) shows the result of all these steps. To have a better intuition of the impact that these steps have on the V(Q) curves, these operations are also applied to the reference negative and positive electrode V(Q) curve in Figures 2.21. Figure 2.21 f) shows the resulting half-cell curves that represent the voltage versus Li^+/Li curves of the positive and negative electrodes that fit the cell of interest the best.

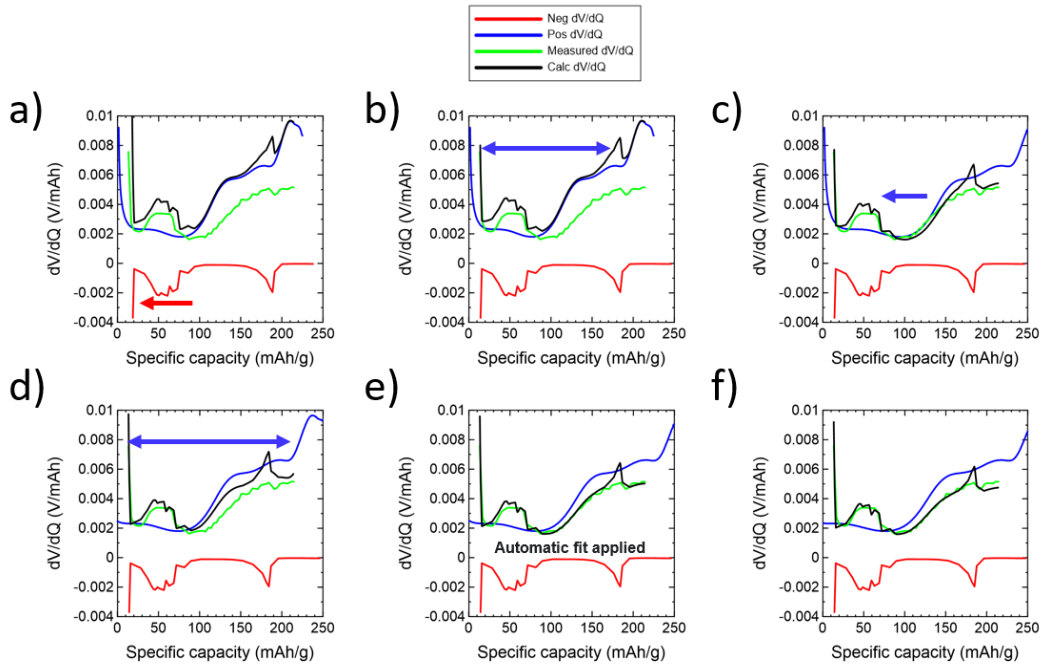

Figure 2.20: The process used to fit an experimental dV/dQ curve (green line) with a calculated dV/dQ curve (black line) that was calculated from negative electrode (red line) and positive electrode (blue line) dV/dQ reference curves.

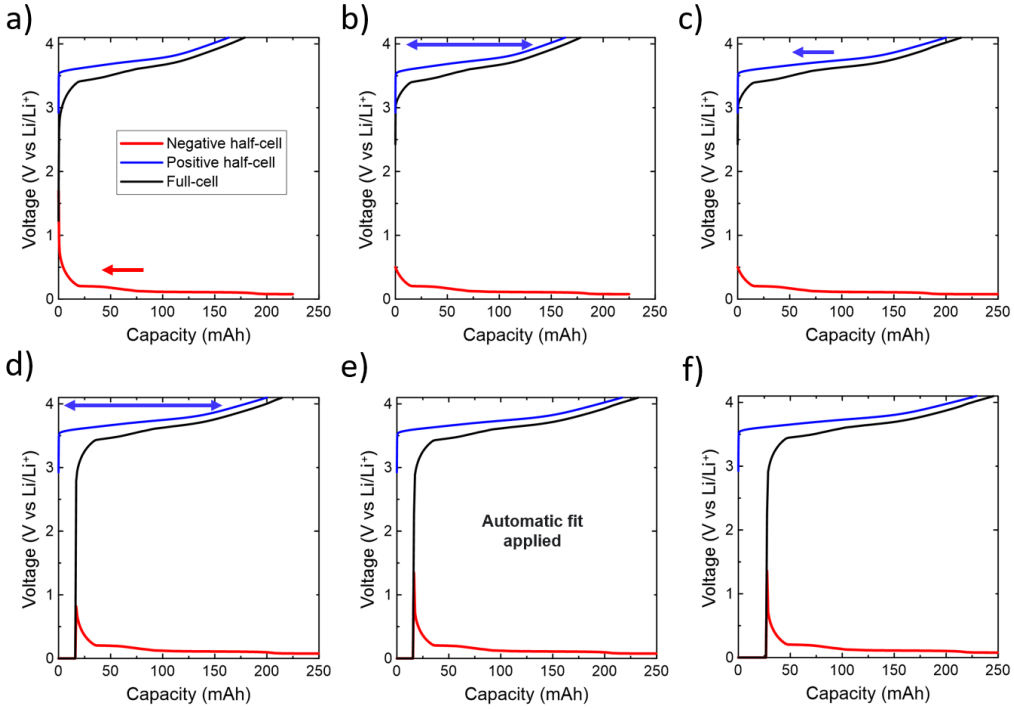

Figure 2.21: The same process as in Figure 2.20 was applied to the full-cell and hall-cell V(Q) curves to better see what the actions in Figure 2.20 mean for the V(Q) curves.

2.12 DENSITY FUNCTIONAL THEORY

Since many failure mechanisms can occur due to the reduction and oxidation of the electrolyte at the negative and positive, predicting these reduction and oxidation reactions becomes important to improve the stability of the electrolyte. Density functional theory is an interesting approach which allows one to predict the reduction and oxidation potentials of electrolyte components.

Density functional theory is a computational method used to solve the Schrodinger equation of an interacting electron system like an atom or a molecule. The theory is based on Hohenberg–Kohn theorems[43], which dictate that for a system of interacting electrons around an atomic nucleus (note that a functional is a function of a function, in this case the total energy is a function of the electron density function):

1. The total energy E is a unique functional of the electron density n, E[n].
2. The total energy functional E[n] reaches its lowest value at zero kelvin if the electron density n is the true ground state electron density.

If the exact functional E[n] of an interacting electron system is known, the Hohenberg-Kohn theorems allow us to calculate the total energy and the electron density of an atom/molecule using a self-consistent iterative approach. Unfortunately, the exact functional is not known.

In order to solve this problem, the interacting electronic system is replaced by a unique non-interacting electronic system called the Kohn-Sham system.[44] In this system, the electron interaction contributions are modeled by an external potential in such a way that the electron density and total energy of the Kohn-Sham system are the same as the original

interacting system. The governing equation of the Kohn-Sham system is the Schrodinger-like Kohn-Sham equation[44]:

$$\left(-\frac{\hbar^2}{2\mathrm{m}}\nabla^2 + v_{eff}(\vec{r})\right)\phi_i(\vec{r}) = \epsilon_i\phi_i(\vec{r}), \tag{155}$$

where ϕ_i are the Kohn-Sham orbitals, ε_i are the corresponding energies and v_{eff} is the Kohn-Sham potential:

$$\mathrm{v_{eff}}(\vec{\mathrm{r}}) = \mathrm{v_{ext}}(\vec{\mathrm{r}}) + \mathrm{e}^2\int\frac{\mathrm{n}(\overrightarrow{\mathrm{r'}})}{|\vec{\mathrm{r}}-\overrightarrow{\mathrm{r'}}|}\,\mathrm{d}\overrightarrow{\mathrm{r'}} + \frac{\delta\mathrm{E_{xc}[n]}}{\delta\mathrm{n}(\vec{\mathrm{r}})} \tag{16}$$

The first term corresponds to the nuclear potential, the second to the classical Coulomb potential for the electrons and the third to the exchange-correlation potential (a correction term), obtained from the functional derivative of the exchange-correlation energy. The physical meaning of the last term will be explained below. The Kohn-Sham orbitals can be calculated by solving the eigenvalue equation (15). Note that the Kohn-Sham orbitals do not have any physical meaning, however the corresponding total electron density does:

$$n(\vec{r}) = \sum_{i=1}^{N}|\phi_\mathrm{i}(\vec{\mathrm{r}})|^2 \tag{17}$$

Furthermore, the total energy of the Kohn-Sham system can be written as[44]:

$$E = \int v_{ext}(\vec{r})n(\vec{r})d\vec{r} + \frac{e^2}{2}\iint \frac{n(\vec{r})n(\overrightarrow{r'})}{\vec{r} - \overrightarrow{r'}} d\vec{r}d\overrightarrow{r'} + T_s[n] + E_{xc}[n]\,, \qquad (18)$$

where E is the total energy, v_{ext} is the external potential due to the nuclei, n is the electron density, r is the vector position, T_s is the kinetic energy of the non-interacting electron systems and E_{xc} is the exchange-correlation energy. The first term of equation (18) is the nuclei-electron interaction energy, and the second term is the classical Coulomb electron-electron interaction energy. The exchange-correlation energy is a combination of the exchange energy and correlation energy. The exchange energy is a correction that is added so that the final charge density respects the Pauli exclusion principle[45,46], while the correlation energy include effects like London dispersion[47].

Note that the functional $T_s[n]$ is unknown in terms of n, but it can be computed from the Kohn-Sham orbitals:

$$T_s[n] = \sum_{i=1}^{N} \int d\vec{r}\ \phi_i{}^*(\vec{r}) \left(-\frac{\hbar^2}{2\mathrm{m}}\ \nabla^2 \right) \phi_i(\vec{r}) \qquad (19)$$

The total energy of the system and the electron density is calculated by the following self-consistent iterative approach: First, the program starts with an initial guess for the electron density n(r). Second, the electron density is replaced in equation (16) and the resulting equation is replaced in equation (15). Third, a new electron density is calculated with (17) and the total energy is calculated using equation (18) and (19). Finally, the new electron density is replaced in equation (16) and the process is repeated until the total energy converges.[48]

For a specific DFT calculation, the form of $E_{xc}[n]$ depends on the choice of the user. In the case of the popular B3LYP hybrid functional[49], $E_{xc}[n]$ is a specific combination of the local exchange functional[46,50], local correlation functional of Vosko, Wilk, and Nusair[51], Becke exchange functional[52], Lee, Yang and Parr correlation functional[53] and a Hartree-Fock exchange correction.[49]

To calculate the absolute Gibbs free energy of a molecule, the partition function of the molecule is required. This can be done by first calculating the vibrational mode frequencies of the molecule, calculating the corresponding vibrational contribution to the partition function, and including the translation, electronic and rotational partition function contributions. Finally the Gibbs free energy can be calculated.[54]

2.13 CALCULATING REDUCTION/OXIDATION POTENTIALS OF A MOLECULE

A simple one electron reduction of a molecule M (a solvent or an additive) can sometimes occur at the graphite electrode according to the following reaction:

$$M + e^- + Li^+ \rightarrow LiM \tag{20}$$

Note that the resulting salt is often reactive and can form a dimer, a polymer or even decompose. In the case of a two electron reduction per molecule M, two electrons and two lithium cations will be present in the reactants and the product will be Li_2M, which can be reactive or not, depending on the nature of the molecule M.

Similarly, a simple one electron oxidation of a molecule M at the NMC cathode can occur following the reaction:

$$M - e^- \rightarrow M^+ \tag{21}$$

Here, in equation (20), the PF_6^- anion is generally not included due to its non-coordinating nature.[55] To obtain the reduction and oxidation potential of a molecule using equations (20) and (21), we first obtain the absolute Gibbs free energy of the atom/molecules M, Li^+, LiM and M^+ using the software, Gaussian, at standard state, for example. Note that the solvent surrounding the molecules is taken into account during these calculations using a polarizable continuum model (PCM), like the IEFPCM model.[56,57] A PCM model corrects the Gibbs free energy of a solvated atom/molecule by calculating the change in electrostatic energy that results from displacing the atom/molecule from a vacuum to a homogeneous continuum of dielectric constant ε. We can calculate the Gibbs free energy of reaction ΔG^0 for (20) and (21) by calculating the difference in absolute Gibbs free energy between the solvated products and the solvated reactants. From that, we can calculate E^0 and the corresponding potentials[58]:

$$E^0 = -\frac{\Delta G^0}{nF} - E_{ref}\,, \tag{22}$$

where n is the number of electrons transferred during the reactions, F is the Faraday constant and E_{ref} is the lithium (Li/Li^+) reference potential in the lithium-ion cell electrolyte. E_{ref} can be calculated from[58]:

$$E_{ref} = {E^0}_{SHE}(abs) + {E^0}_{SLE}(ref) + \frac{d(\Delta G_{solv})}{F}, \quad (23)$$

where the first term is the absolute potential of the standard hydrogen electrode (SHE), the second is the potential of the standard lithium electrode versus the SHE in an aqueous solution and $d(\Delta G_{solv})$ is the difference in solvation free energy of a lithium cation in water and of a lithium cation in the lithium-ion cell electrolyte (e.g. 1.2M $LiPF_6$ EC:EMC 3:7). The first term is around 4.281 V,[59] the second is -3.04 V_{SHE} [60] and the last term can be approximated using the Gaussian software via a polarizable continuum model (PCM).[58] We finally obtain E_{ref} = 1.44 V.[58]

2.14 ELECTROCHEMICAL IMPEDANCE SPECTROSCOPY (EIS)

Electrochemical impedance spectroscopy consists of applying a sinusoidal voltage of changing frequency from millihertz to kilohertz to the terminals of a cell. By measuring the amplitude and phase of the current response, the real part Re(Z) and imaginary part Im(Z) of the cell impedance Z can be calculated as a function of frequency and plotted. Those graphs are called Bode plots. The same data can be represented by plotting –Im(Z) versus Re(Z) instead. Those graphs are called Nyquist plots and are often used in the field of battery science.

To have a better intuition of what the Bode and Nyquist plots mean, let us consider the simple case of a parallel RC circuit. The impedance of this circuit is $Z= R/(1+i\omega RC)$, where R is the resistance of the resistor, C is the capacitance of the capacitor, i is the imaginary

number and ω is the angular frequency. Assuming that the resistance is R = 1 Ohm and that the capacitance is C = 0.1 mF, then the corresponding Bode and Nyquist plots are:

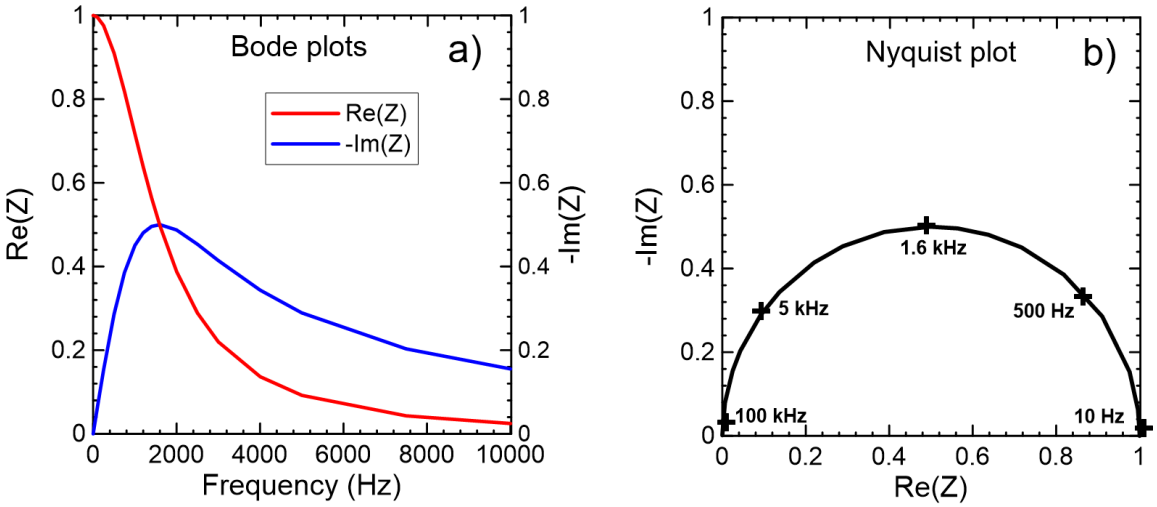

Figure 2.22: a) Bode plots and b) Nyquist plot of a parallel RC circuit. In a) the real part is in red, and minus of the imaginary part is in blue. In b), frequency is shown at five points in the plot.

The resulting Nyquist plot shown in Figure 2.22 b) is a semi-circle of diameter R and the frequency at the top of the semi-circle (when Re(Z) = Im(Z) = 0.5) is f=1/(2πRC). One can figure out that the maximum value of -Im(Z) vs. f and that the maximum slope of -Re(Z) vs. f in 2.22 a) is also occurring at the same frequency.

In the case of a cell, both electrode/electrolyte interfaces can be approximated by two parallel RC circuits in series themselves in series with a resistor, which represents the resistance of the electrolyte and electrodes. This circuit is shown in Figure 2.23. However, the capacitor in the RC circuits is better represented in this case by an imperfect capacitor, named a constant phase element (CPE). While the impedance of a capacitor is $Z = 1/[i\omega C]$, the impedance of a CPE is $Z = 1/[Q(i\omega)^n]$, where Q is a constant similar to C and n is a number between 0 and 1. When n = 1, we have a capacitor and Q = C and when n = 0, we

have a resistor, where the resistance is $R = Q^{-1}$.When we replace the capacitors by two CPE, the corresponding Nyquist plot is two imperfect semi-circles of different diameter both shifted to the right on the x-axis by R_0. Figures A.1 to A.4 show some experimental EIS Nyquist plots. We can see two imperfect semi-circles in Figures A.2 and A.4.

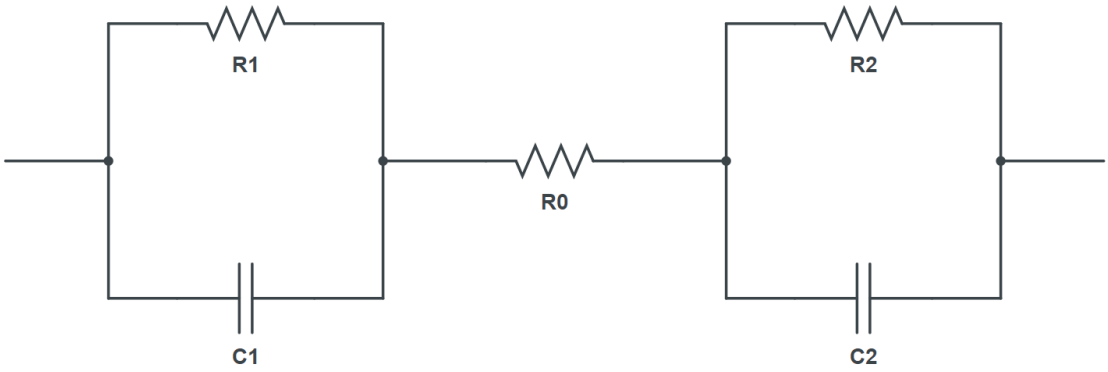

Figure 2.23: Equivalent circuit of a cell. Each parallel RC circuit represent an electrode/electrolyte interface. The resistor R_0 represents the resistance of the electrolyte and electrodes. In practice, the capacitors are replaced by constant phase elements. Other equivalent circuits can also be used.

2.15 ULTRASONIC TRANSMISSION MAPPING (UTM)

UTM consists of measuring the ultrasonic transmission of an object at many points on the surface of that object. The object is scanned in 2D space with an ultrasonic emitting transducer on the left of the object and the transmitted ultrasonic wave is measured on the right of the object with a receiving transducer. The transmission rate of an object to ultrasonic waves is given by:

$$T = \frac{4\,Z_1 Z_2}{(Z_1 + Z_2)^2}, \tag{24}$$

where Z_1 is the acoustic impedance of the surrounding media and Z_2 is the acoustic impedance of the object. Since the acoustic impedance of a gas is near 0.0004 MRayl and the acoustic impedance of liquid or solid materials are between 1 to 50 MRayl, the presence of gas in a cell can dramatically decrease its transmission to ultrasonic waves.[61] Note that the acoustic impedance of a material can be calculated using $Z = \rho c$, where ρ is the density of the material and c is the speed of sound in that material. All ultrasonic transmission mapping scans in this thesis were measured by Aidan Luscombe.

2.16 X-RAY COMPUTED TOMOGRAPHY (CT)

X-ray CT consists of shining a coherent and highly collimated X-ray beam at a rotating object. The transmitted X-rays are then measured as a function of the angle of rotation of the object. Using a computer program, the information can then be used to reconstruct the inside of the object. This imagery techniques has been used in the past in the battery field and as been very useful for monitoring the inside of cells in a non-destructive manner.[62–66] All X-ray CT scans shown in this thesis were measured by Toby Bond.

CHAPTER 3 EXPERIMENTAL AND THEORETICAL METHODS

3.1 POUCH CELL PREPARATION

$Li(Ni_{0.6}Mn_{0.2}Co_{0.2})O_2$ (NMC622)/graphite (gr) 402035-size pouch cells were received dry (i.e., with no electrolyte) from Li-Fun Technology (Zhuzhou, Hunan, China). This work utilized three different cell types, as shown in Table 3.1:

Table 3.1: List of cells used in this work for each project, as well as their formation capacity at C/20 and the voltage at which they were balanced. The letters A and B correspond the coating that was applied on the positive electrode. Coating A corresponds to an alumina coating, while coating B corresponds to a proprietary coating. If a cell is balanced at 4.4 V, it means that at 4.4 V, the capacity per unit of area of the positive and negative electrode are equal.

Project/Chapter	**Cell name**	**Balanced at**	**Formation capacity (at C/20)**
PDO project/Ch. 4	NMC622B/AG	4.4 V	~260 mAh (at 4.3 V)
DOD project/Ch. 5	NMC622A/NG	4.5 V	~250 mAh (at 4.1 V)
	NMC622B/NG	4.5 V	~250 mAh (at 4.1 V)

The NMC622 active materials used in this work were composed of conventional secondary spherical agglomerations (about 10 μm in diameter) of smaller (hundreds of nm) primary particles. Before cells were filled with electrolyte, they were cut open in an argon-atmosphere environment and dried under vacuum at 80°C for 14 hours. Detailed information about the pouch cells can be found in the Appendix (Tables A.1, A.2 and A.16).

3.2 ELECTROLYTE PREPARATION

This work used three types of control electrolytes in total and two control electrolyte types per project, as shown in Table 3.2:

Table 3.2: List of control electrolytes used in this work for each project, as well as the electrolyte additives that were added to each respective control electrolyte.

Project/Chapter	Control electrolyte	Additive(s) added
PDO project/Ch. 4	1.2M $LiPF_6$ EC:EMC:DMC 25:5:70	pFDO, pNDO or pMoDO with or without VC, DTD, LFO or MMDS
PDO project/Ch. 4	1.2M $LiPF_6$ EC:DMC 3:7	PDO with or without VC, DTD, LFO or MMDS
DOD project/Ch. 5	1.2M $LiPF_6$ EC:EMC 3:7	VC211
DOD project/Ch. 5	1.2M $LiPF_6$ EC:DMC 3:7	VC211

All solvent mixtures (EC:DMC 3:7, EC:EMC 3:7 and EC:EMC:DMC 25:5:70) were obtained from BASF and contained less than 20 ppm of water. $LiPF_6$ was obtained from Shenzhen Capchem and had a purity greater or equal to 99.9%. The VC211 ternary additive blend consists of 2 wt% VC (BASF, 99.5%, < 100 ppm water), 1 wt% TTSPi (Tokyo Chemical Industry Co., Ltd. (TCI), > 95.0%) and 1 wt% MMDS (Guangzhou Tinci Co. Ltd, 98.70%). 3-phenyl-1,4,2-dioxazol-5-one (PDO), *p*-(4-methoxyphenyl)-1,4,2-dioxazol-5-one (pMODO), *p*-(4-fluorophenyl)-1,4,2-dioxazol-5-one (pFDO) and *p*-(4-nitrophenyl)-1,4,2-dioxazol-5-one (pNDO) were synthesized by chemists in our lab. The

co-additives used in the PDO project were ethylene sulfate (DTD, Guangzhou Tinci Materials Tech. Co. Ltd., ≥98%), lithium difluorophosphate (LFO, Shenzhen CapChem Tech. Co. Ltd.), vinylene carbonate (VC, BASF, ≥99.8%), prop-1-ene-1,3-sultone (PES, Lianchuang Medical Chemistry Co., 98%) and methylene methyl disulfonate (MMDS, Guangzhou Tinci Materials Tech. Co. Ltd., 98.7%).

The cells were filled with electrolyte in an argon-atmosphere environment and then vacuum-sealed at a gauge pressure of −90 kPa and a sealing bar temperature of 165°C using a compact vacuum sealer (MSK-115A, MTI Corp.). All electrochemical measurements reported in this work were performed on a minimum of two replicate pouch cells, to ensure experimental precision.

3.3 FORMATION

Following filling with electrolyte, cells were maintained at 1.5 V and at room temperature for 24 h to allow time for the electrolyte to fully wet the electrodes. However, two 2% PDO and two 2% pNDO cells were wetted at 40.0 ± 0.1°C. The two 2% PDO cells were wetted at 1.5 V and 40.0 °C for 24h to confirm the volume of created gas during wetting in an in-situ gas apparatus. The two 2% pNDO cells were charged from open circuit potential (~0.1 V) to 3.2 V at C/20 and 40.0°C to confirm the DFT predicted reduction potential of pNDO. After initial volume measurement and wetting, all the other cells were then moved into temperature boxes at 40.0 ± 0.1°C and connected to a Maccor series 4000 battery tester for formation. First, cells were held at 1.5 V for 30 min to allow time for the temperature to stabilize and then they were charged at C/20 to 4.3 V. Cells were maintained at 4.3 V for

one hour and then discharged at C/20 to 3.8 V. The electrolyte of each cell reduced during the first charge to form the initial SEI on the graphite. Cells were degassed after formation and sealed again.

3.4 FULL CELL REFERENCE CURVE

To have a better idea of the amount of charge consumed by dioxazolone additives as well as vinylene carbonate (chapter 4) during cell formation via a capacity versus voltage Q(V) curve,graphite/Li and NMC622/Li half-cells were built. These cells were made to construct a differential voltage (dV/dQ) curve of a full cell that is free from reduction and oxidation contributions. The electrolyte used was 1.2M $LiPF_6$ EC:EMC 3:7 and the half-cells were cycled for 2 cycles at C/20. For the graphite/Li half-cell, the Q(V) data from the second cycle was used, while for the NMC622/Li half-cell, the Q(V) data from the first cycle was used. dV/dQ analysis was used to determine the active mass and capacity slippage of each full-cell electrode using established methods. [42,67–70] From the dV/dQ analysis, a full-cell capacity versus voltage Q(V) reference curve could be built, free from reduction and oxidation contributions.

3.5 ELECTROCHEMICAL IMPEDANCE SPECTROSCOPY (EIS)

EIS spectra were measured using a Bio-Logic VMP3 (Seyssinet-Pariset, France) using a sinusoidal amplitude of 10 mV over the frequency range 10 mHz – 100 kHz. Pouch cells were maintained at 10.0 ± 0.1°C in a wide range thermal chamber (Novonix, Canada) and

all cells had a voltage of 3.8 V during EIS measurements. In this work, R_{ct} represents the difference along the x-axis between the high and low frequency minima in the Nyquist plots. In the case where two semi-circles were present in the Nyquist plots, R_{ct} is defined here as the combined width of both semi-circles. The Nyquist plots of the most relevant electrolyte (the ones containing a dioxazolone compound with or without 1% DTD) can be found in the Appendix (Figures A.1-A.4).

3.6 HIGH TEMPERATURE STORAGE

Following formation and degassing, cells were placed in a temperature box at 40.0 ± 0.1°C and connected to a Maccor series 4000 battery tester. Two cycles at constant current (C/10) were executed between 2.8 V and 4.3 V starting with a discharge. At the end of the protocol, the voltage was held at 4.3 V for 24 h. Then the cells were transferred to 60.0 ± 0.1°C temperature boxes and connected to an automated storage system.[71] Finally, their open circuit voltages were measured every 6 hours for a period of 500 h.

3.7 LONG TERM CYCLING TESTS

PDO project (chapter 4)

Each relevant cell was placed in a temperature-controlled chamber at 40.0 ± 0.1°C and connected to a Neware battery cycler. The protocol used for long term cycling consisted of C/3 cycles between 3.0 V and 4.3 V using a CCCV charging profile (C/3 constant current to the top-of-charge, followed by a constant voltage step until the measured current

decreased to ≤ C/20) and a CC (C/3 constant current) discharge. A constant current C/20 cycle was performed every 50 cycles to assess what fraction of the capacity loss was due to cell impedance growth vs irreversible capacity losses.

DOD project (chapter 5)

48 cells were placed in a temperature-controlled chamber at 40.0 ± 0.1°C connected to a Neware battery cycler, while 48 cells were connected to a Neware battery cycler at room temperature (20 ± 2°C). 24 of the cells at 40°C were NMC622A/NG cells, while the rest were NMC622B/NG cells. The cells at room temperature were NMC622A/NG cells. The voltage ranges used for long-term cycling of each NMC622A/NG cell are summarized in Table 3.3 and the voltage ranges used for each NMC622B/NG cell are summarized in Table 3.4. Each voltage range is associated with an approximate depth of discharge (DOD) or SOC range.

Table 3.3: Voltage ranges applied to the NMC622A/NG cells. 18 cells are cycling for each voltage range. 12 cells at room temperature (20°C) and six cells at 40°C. This corresponds to 72 cells in total. These cells will be called fixed upper cutoff cells (UC cells).

	100% DOD 100-0% SOC	**~75% DOD** 100-25% SOC	**~50% DOD** 100-50% SOC	**~25% DOD** 100-75% SOC
Upper cutoff voltage	4.1 V	4.1 V	4.1 V	4.1 V
Lower cutoff voltage	3.0 V	3.495 V	3.6 V	3.77 V

Table 3.4: Voltage ranges applied to the NMC622B/NG cells. Six cells are cycling for each voltage range, for a total of 24 cells. All are at 40°C. These cells will be called fixed lower cutoff cells (LC cells).

	100% DOD **100-0% SOC**	**~75% DOD** **75-0% SOC**	**~50% DOD** **50-0% SOC**	**~25% DOD** **25-0% SOC**
Upper cutoff voltage	4.1 V	3.777 V	3.649 V	3.527 V
Lower cutoff voltage	3.0 V	3.0 V	3.0 V	3.0 V

For each voltage range, three pairs of UC or LC cells were cycled at three different C-rates: C/10, C/5, and C/3, except for the cells at 20°C. In the 20°C case, three quartets of UC cells were cycled at these three different C-rates. Quartets were used instead of doublets, since some data (100% SOC range checkup cycles) was missing before ~2000 hours of testing for the first doublets that cycled for a total of 20000 hours. As a result, a second doublet was cycled under the same conditions for ~7000 hours. The data was then combined to determine the resulting capacity loss over the full 20000 hours and to allow fitting. All NMC622A/NG cells that were not cycled using a full voltage range (3.0 V - 4.1 V) at C/10 had checkup cycles every 500 hours approximately, while all the equivalent NMC622B/NG cells had checkup cycles every 900 hours approximately. The checkup cycles consisted of full range cycles (3.0 V - 4.1 V) at C/10. Each cycle consisted of a CCCV charge and a CC discharge. A CCCV charge consists of a constant current (CC) charge from the lower cutoff voltage (LCV) to the upper cutoff voltage (UCV) followed

by a constant voltage (CV) hold at the UCV until the current decreased to C/20. A CC discharge consists of a constant current (CC) discharge from UCV to LCV.

3.8 ULTRA-HIGH PRECISION COULOMETRY (UHPC) CYCLING TESTS

Ultra-high precision cycling (UHPC) was performed using the UHPC chargers at Dalhousie University after the cells went through approximately 20000 h of long-term cycling.[72] The NMC622/graphite cells were cycled between 3.0 V and 4.1 V at C/40 on the UHPC charger at 40°C after an initial discharge from 3.8 V to 3.0 V.

3.9 DENSITY FUNCTIONAL THEORY (DFT)

All computational chemistry calculations were done using the Gaussian software package (G09.a02).[73] Geometry optimizations and thermochemistry calculations were done using the B3LYP functional at the 6-311++G(2df,2pd) level. To simulate solvation effects the integral equation formalism polarizable continuum model (IEFPCM)[56,57] was used with the dielectric constant (ε) of the electrolyte set to 20.[58,74] It is important to keep in mind that IEFPCM gives only an approximate representation of solvation effects and behaviors.[11] However, due to its balance of speed and accuracy, this model is here preferred over more computationally expensive approaches.[75–78] All optimized geometries were tested by normal mode analysis and have only positive (real) vibrational frequencies. Standard electrode potentials are reported relative to the standard lithium electrode in the same solution and were calculated as described previously, using E^{ref} = 1.44 V.[58,75] Thermal

contributions to the Gibbs free energy were calculated by normal mode analysis at room temperature (25°C).

Oxidation and reduction standard potentials of a molecule of interest M can be calculated using the method described in section 1.4 and by Self et al. [58] from the general formula for reduction (20) and oxidation (21). Optimized energies and molecular geometries are provided in the Appendix.

3.10 CELL THICKNESS MEASUREMENTS

The thickness of many of the pouch cells was measured in the center of the jelly roll region three times using a Mitutoyo linear gage. These three values were then averaged.

3.11 PRESSURE MEASUREMENTS

In-situ stack pressure measurements were performed using the apparatus detailed in Louli et al.[9] Pouch cells were volumetrically constrained within a rigid aluminum enclosure such that any volume expansion of the electrode stack would exert a force within the enclosure. The force within the enclosure was measured with subminiature load cells (LCKD-OMEGA Engineering) connected to DP25B-S-A (OMEGA Engineering) strain gauge panel meters. The load cells were fastened in the enclosure with the pouch cell, separated by a force distributing plate. The measured force was converted to kPa using the pouch cell area of 6 cm^2. For in-situ measurements, the pouch cells were connected to a Neware battery testing system and cycled at C/20 between 3.0 V and 4.1 V. The analog 0-10 V

output of the strain gauge panel meter was connected to an adjacent Neware channel to enable simultaneous electrochemical and pressure measurements from both the pouch cell and pressure sensor. These measurements were performed in a 40.0 ± 0.1°C temperature box. Finally, the initial pressure at a state of charge (SOC) of 0% was subtracted from the data, so that the "zeroed" pressure at a SOC of 0% was 0 kPa.

3.12 CELL VOLUME MEASUREMENTS (EX-SITU)

The change in volume of each cell was measured using Archimedes' principle. Cells after filling were suspended under an analytical balance (Shimadzu model AUW220D) by a metal wire and submerged in a beaker full of water and weighed. The process was repeated after formation to determine the volume of gas created during formation. The change in the volume of the cell was then calculated using the apparent change in mass due to the displacement of water, assuming the density of the water is ~1.00 g/mL. The cell weight under water was measured again after degassing and yet again after long term testing to determine the volume change during long term testing.

3.13 CELL VOLUME MEASUREMENTS (IN-SITU)

The evolution of gas during formation was measured using the measuring Archimedes' gas expansion (MAGE) apparatus as described previously.[79] All measurements using the MAGE were done at 40 ± 2°C, including the wetting of the cells. First the cells were wetted at 1.5 V for 24 h. The cells were then charged at a constant current (CC) of C/20 to 4.3 V.

Then the voltage was kept constant at 4.3V for 24h. CC charging at C/20 to 4.4 V and constant voltage of 4.4 V for 24 h followed. Finally, the cells were charged at C/20 to 4.5 V at CC and kept at that voltage for 24 h and then the cells went on open circuit condition.

3.14 MANUAL dV/dQ ANALYSIS

dV/dQ analysis was performed on V(Q) data obtained from UHPC cyclers using the method described in section 1.12 and using the software developed by H. Dahn et al.[42]

3.15 AUTOMATIC dV/dQ ANALYSIS

Long-term Neware cycling data was automatically analyzed using a program written using the MATLAB R2020a software.[80] In the case of cells with checkup cycles, only the checkup cycles were analyzed and the remaining main cycles were discarded by the program. The program operates similarly to the software developed by H. M. Dahn et al., however instead of using a nonlinear least squares fitting algorithm (Levenberg-Marquardt method) to fit the calculated dV/dQ vs. Q curve to the experimental dV/dQ vs. Q curve, the program developed in this work calculated Chi-square from the difference between the theoretical and experimental dV/dQ vs Q curves for **all** negative electrode slippage, positive electrode slippage, negative active mass and positive active mass values within a discrete 4D matrix and selected the electrode mass and slippage values corresponding to the smallest Chi-squared. From now on, this method will be called the dV/dQ matrix method. While the dV/dQ matrix method is more computationally expensive than the Levenberg-Marquardt method, it gave the authors a higher confidence in the results, since

the dV/dQ matrix method can help confirm that the global minimum has been found, if the matrix range is large enough. The automatic dV/dQ analysis was applied to the Neware data of a specific cell using the dV/dQ matrix method on N equally spaced cycles from 0 hour to ~20000 hours. The 4D matrix used for each cycle was a 150 x 75 x 10 x 5 matrix (positive electrode slippage precision x positive active mass precision x negative electrode slippage precision x negative active mass precision). When N = 6, the computational time for this matrix size was ~10 minutes per cell. The positive electrode slippage was scanned from -0.5 mAh to 75 mAh, the positive active mass was scanned from 0.9 g to 1.64 g, the negative electrode slippage was scanned from 0 mAh to -10 mAh and the negative active mass was scanned from 0.98 g to 1.08 g. The scanning range was guided by the results of manual dV/dQ vs. Q analysis. The program possesses a second mode which allows one to fix the negative electrode mass and negative electrode slippage to reasonable values. This is possible for our cells since these values do not seem to change dramatically when the program uses a 4D matrix (see Figure A.11). This allows the program to form an image from the matrix, which is now a 2D matrix, since the two additional dimensions are now fixed. To get a more interesting image, the negative value of the base 10 logarithm of the Chi-squared value was plotted instead of the Chi-squared value.

3.16 DIFFERENTIAL THERMAL ANALYSIS

Lithium-ion differential thermal analysis (Li-ion DTA) is a non-destructive method of probing the state of the electrolyte inside a Li-ion cell. This method, first developed by Day et al, involves cooling the cell down to a cryogenic setpoint where the electrolyte in the cell is entirely frozen, and tracking the temperature of the cell as it heats back to room

temperature at a constant, controlled rate.[81]

In this case, the lower setpoint was -100.0°C, while room temperature was 25°C. This range was chosen to cover the entire freezing regime of the electrolyte. As well, this range is entirely within the liquid phase of the reference cell, which in this case is 1.0 M $LiPF_6$ in methyl acetate. This is beneficial, as the reference cell will act very similarly to a sample cell that does not go through phase changes in the regime of interest. In all cases, the cells were cooled at a rate of 3.0 °C/min, held at the low temperature for ten minutes to allow for electrolyte temperature equilibration, and heated at 1.0 °C/min. The direct temperature signals of the sample and reference cells can then be compared to determine the temperatures at which the sample cell underwent phase changes. As these phase changes are sensitive to electrolyte composition, we can identify changes to the electrolyte by comparing DTA curves.

3.17 ULTRASONIC TRANSMISSION MAPPING

Ultrasonic transmission mapping was performed with an ultrasonic battery scanner (UBSC-LD50, Jiangsu Jitri-Hust Intelligent Equipment Technology Co., Ltd).[61] A pair of ultrasonic focus transducers (2 MHz frequency, 30 mm focal distance, customized from Shantou Institute of Ultrasonic Instruments Co., Ltd.) were positioned on either side of the cell. Transducers and cells were immersed in low viscosity silicone oil which serves as an ultrasonic coupling agent. The transducers were installed on a 2-dimensional motion system with a precision of 0.2 mm to perform progressive scanning. The ultrasonic signal was emitted by a transducer on one side of the cell and received by the transducer on the

other side. The driving source was a 200 V pulse signal with a pulse width of 250 ns, matching the 2 MHz ultrasonic transducer used here. The waveform of the transmitted signal was recorded with a collecting card. The peak-to-peak values of received transmission waves were converted into color heat maps to make pseudo color images. Cells were equilibrated at 3.8 V and degassed before the ultrasonic measurements were performed at 20ºC.

3.18 COMPUTED TOMOGRAPHY (CT) SCANS

CT scans were collected at the Canadian Light Source synchrotron facility on the Biomedical Imaging and Therapy Insertion Device beamline (BMIT-ID).[82] This beamline provides a coherent, highly-collimated, monochromatic x-ray beam with parallel geometry, allowing for enhanced contrast through propagation-based phase imaging. The use of monochromatic beam also minimizes the x-ray dose to the cell, as all incident photons contain sufficient energy to contribute to the acquired image. The high incident flux (3×10^{10} photons/cm^2·s) also allows for scans to be acquired many times faster than conventional CT, which limits artifacts from electrolyte motion. All scans were collected using a single-crystal LuAG ($Lu_3Al_5O_{12}$:Ce) scintillator paired with an optical camera. In this setup, the parallel x-ray projection image is optically magnified, as opposed to magnification using a conventional cone beam source. This makes micron-level imaging of larger objects such as pouch cells possible, as very small sample-to-source distances are not required.

Two different setups were used to image at different scales. A lower-resolution, high-

dynamic-range setup was used for imaging liquid electrolyte in the full cell, where a CCD camera (PCO 4000) with an effective pixel size of 8.9 μm was used with a monochromatic beam energy of 70 keV. Cells were scanned using 3000 projections (exposure time = 0.6 seconds) collected over a 180-degree range with the sample placed 40 cm from the detector. A higher-resolution setup was used to scan only the corner of the cells (for electrode thickness measurements) at a beam energy of 50 keV, where a high-magnification (5x) optical system (manufactured by Optique Peter) was used with an sCMOS camera (PCO Edge), providing an effective pixel size of 1.44 μm. 2500 projections were collected (exposure time = 1.0 seconds) with a sample-detector distance of 3 cm. All scans were reconstructed using the UFO-KIT software package using Paganin phase retrieval.[83] This technique processes the self-interference fringes present in synchrotron x-ray projections so that the contrast of the absorption image is enhanced using differences among the refractive indices of materials in the cell. After reconstruction, scans were manually aligned so that electrode planes were parallel to the image axes in the flat portions of the cell, with trilinear interpolation used for image resampling. Thickness measurements were taken manually by measuring the distance between surface planes at the high-contrast cathode/separator boundary.

CHAPTER 4 DIOXAZOLONE ELECTROLYTE ADDITIVES

4.1 INTRODUCTION

In a two-pronged effort to identify new electrolyte additives that improve capacity retention and to understand the relationship between chemical structure and additive performance, new electrolyte additives were synthesized by chemists in our lab for testing in lithium-ion cells. The electrolyte additives synthesized were from the dioxazolone family of molecules. This synthesis was motivated by previous investigations into other dioxazolones like 3-phenyl-1,4,2-dioxazol-5-one (PDO) and the structurally related electrolyte additive 3-methyl-1,4,2-dioxazol-5-one.[13,40] Three new compounds were considered in this work, based on the structure of PDO with the substitution of the para hydrogen on the phenyl moiety with methoxy, fluoro, or nitro functional groups (Figure 4.1). The compounds, synthesized by the one-pot method of Hynes et al.,[84] are 3-(4-methoxyphenyl)-1,4,2-dioxazol-5-one (pMODO), 3-(4-fluorophenyl)-1,4,2-dioxazol-5-one (pFDO) and 3-(4-nitrophenyl)-1,4,2-dioxazol-5-one (pNDO). These functional groups were chosen for their wide range in relative electron donating or electron withdrawing properties. Relative to the phenyl parent structure, methoxy is an electron donating group (edg), while fluoro and nitro are electron withdrawing groups (ewgs). Note that activating groups tend to donate electron density to the phenyl ring, while deactivating groups tend to withdraw electron density to the phenyl ring.

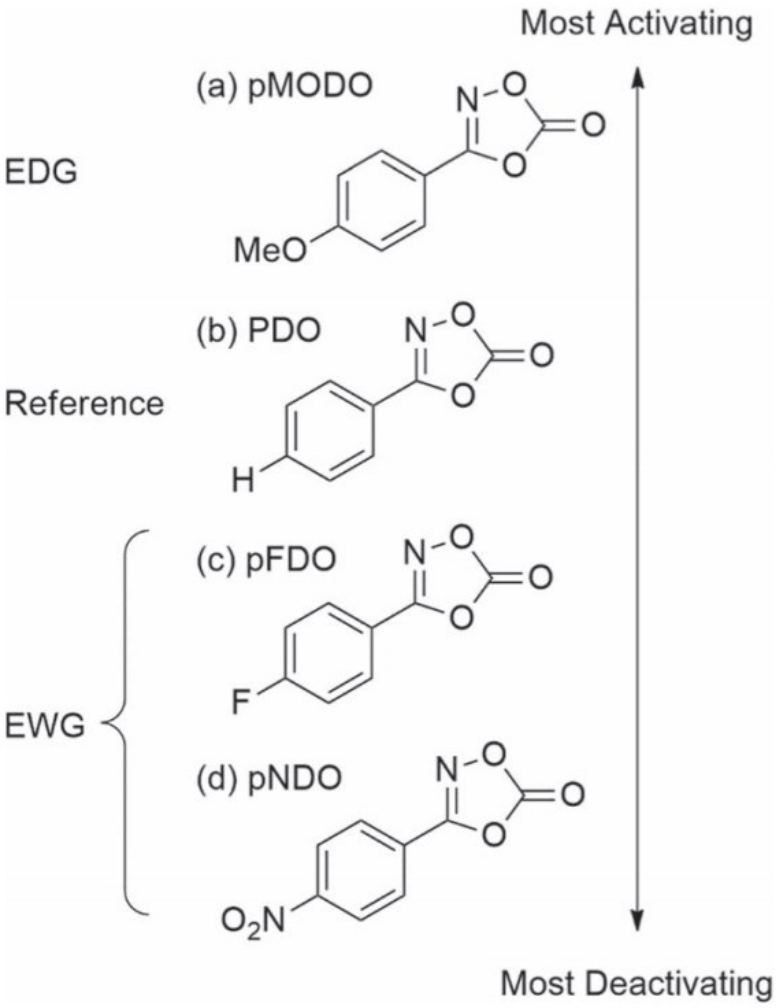

Figure 4.1: Molecular structures of (a) 3-(4-methoxyphenyl)-1,4,2-dioxazol-5-one (pMODO), (b) 3-phenyl-1,4,2-dioxazol-5-one (PDO), (c) 3-(4-fluorophenyl)-1,4,2-dioxazol-5-one (pFDO) and (d) 3-(4-nitrophenyl)-1,4,2-dioxazol-5-one (pNDO). The compounds are arranged by the relative activating or deactivating nature of the substituents at the para position of the phenyl moiety (EDG = electron donating group; EWG = electron withdrawing group).

4.2 REDUCTION AND OXIDATION

Electrolyte solutions were prepared with the three new additives and tested in NMC622/graphite (gr) pouch cells. It is useful to first examine the effects of any new electrolyte chemistry on the cell formation cycle, the first time a cell is charged. This is

because it is during this cycle that a SEI is formed at each electrode, directly affecting cell lifetime and performance. The differential capacity (dQ/dV versus voltage plots) of NMC622/gr cells prepared with PDO, pMODO, pFDO, and pNDO are compared with VC-containing and control (i.e., additive-free) electrolytes (Figure 4.2). In the absence of electrolyte additives, a reduction peak is observed at ~2.9 V, corresponding to the reduction of ethylene carbonate (EC) at the graphite electrode.[13] The differential capacity measured from VC-containing cells show the expected reduction peak at ~2.8 V, attributable to the electrochemical reduction of VC.[85] The absence of the EC reduction feature at ~2.9 V indicates that the SEI formed by VC reduction effectively passivated the graphite electrode surface.[18] Two reduction features were measured from PDO-containing cells at ~2.2V and ~2.5V, consistent with the reported formation behavior.[13] These peaks are also present in the differential capacity plots measured from cells prepared with pMODO and pFDO, whereas the cell with pNDO does not display any reduction features in the 2.0 – 3.2 V range. The EC reduction feature is suppressed but still present in PDO- and pMODO-containing cells, suggesting partial passivation of the graphite electrode. In contrast, the EC reduction peak is not present in cells made with pFDO or pNDO, indicating these additives are very effective at passivating the negative electrode surface. Since pNDO does not show any reducing peaks in the 2.0 – 3.2 V range, the passivation of the graphite electrode against EC reduction may seem contradictory. This apparent inconsistency will be discussed and explained later in the text.

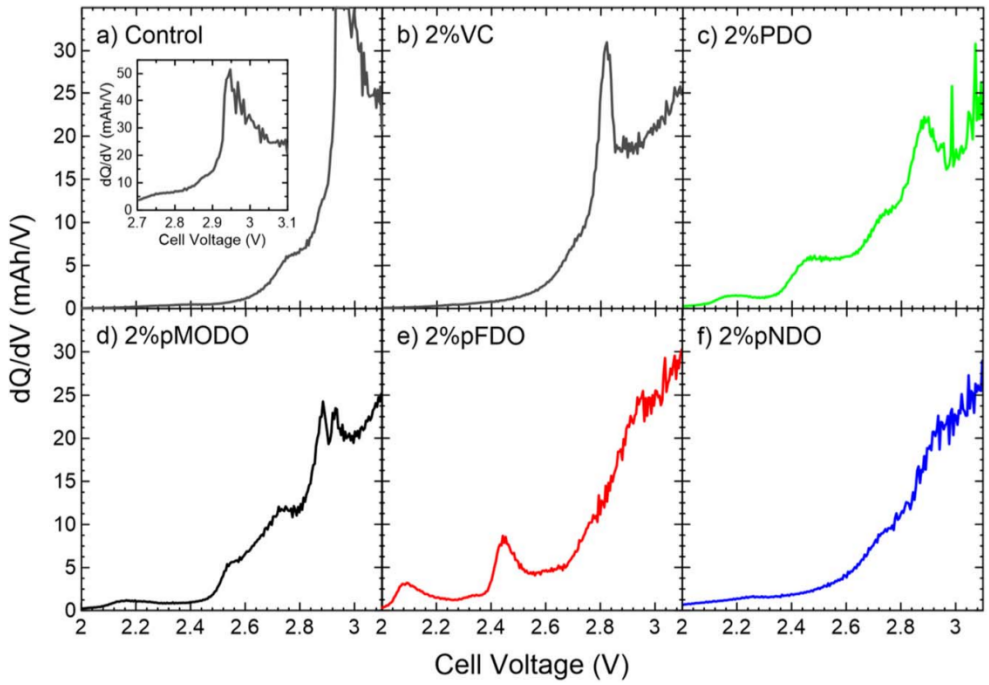

Figure 4.2: Differential capacity (dQ/dV) as a function of cell voltage during the formation cycle of NMC622/gr pouch cells measured at C/20 and 40.0 °C. Cells contained a) additive-free control electrolyte or b) 2% VC, c) 2% PDO, d) 2% pMODO, e) 2% pFDO, or f) 2% pNDO. Electrolytes contained 1.2 M $LiPF_6$ in EC:DMC 3:7 a) – c) or in EC:EMC:DMC 25:5:70 d) – f). The inset shows the reduction of EC in control cells.

DFT calculations are an attractive approach to predicting cell performance and understanding the passivation of the graphite electrode by pNDO. DFT calculations have been used by researchers to identify and understand the electrochemical reactions at both electrodes, especially to assign reduction features in dQ/dV graphs like the ones seen in Figure 4.2.[14,33,86–90] Table 4.1 shows DFT results for the absolute Gibbs free energies of the geometry-optimized additive species, including the products of one-electron oxidation or reduction. The corresponding standard potentials for oxidation and reduction were evaluated relative to the standard lithium electrode, according to an established method, which is also described in Section 2.14.[58,91]

Table 4.1: DFT-calculated absolute Gibbs free energies of unreacted, oxidized, and reduced pMODO, PDO, pFDO and pNDO in keV at 298.15 K. The Gibbs free energies of the reduced molecules were calculated for five different lithium atom sites (site 1–5) as illustrated in Figure 4.3. The oxidation potentials and reduction potentials are shown relative to the standard lithium electrode (Li/Li+). The corresponding cell voltages are also shown in the case of reduction assuming a NMC622 cathode material.

	pMODO	**PDO**	**pFDO**	**pNDO**
Unreacted (keV)	−19.12730	−16.01051	−18.71213	−21.57734
Oxidized (keV)	−19.12085	−16.00342	−18.70509	−21.56976
Reduced (keV)				
Li^+ at site 1	−19.33338	−16.21680	−18.91838	−21.78473
Li^+ at site 2	−19.33338	−16.21674	−18.91839	−21.78473
Li^+ at site 3	−19.33325	−16.21663	−18.91825	−21.78456
Li^+ at site 4	−19.33348	−16.21686	−18.91848	−21.78470
Li^+ at site 5	−19.33314	−16.21655	−18.91814	−21.78515
E_{ox} (V vs Li/Li^+)	5.01	5.65	5.61	6.14
$E_{red,1}$ (V vs Li/Li^+)	1.08	1.26	1.25	2.72
$E_{red,1}$ (V_{cell})	2.42	2.24	2.25	0.78

In the case of reduction, a lithium ion is involved in the structure and the Gibbs free energy is calculated for five different lithium-ion sites, as shown in Figure 4.3. The reduction potential can then be calculated using the lowest Gibbs free energy of the five sites. The cell voltages corresponding to the standard reduction potentials were calculated as described before.[92] Figure 2.3 can also be used to approximate the cell voltages from the standard reduction potentials (using the figure, we find that the cell voltage is approximately equal to 3.5 minus the standard reduction potential). The cell voltages at

which pFDO and PDO reduce are very similar (2.25 V and 2.24 V), while it is larger for pMODO (2.42 V) and much smaller for pNDO (0.78 V). As an example, the reduction product of PDO is shown in Figure A.10.

The calculated electrode potentials were then compared with the experimental features in the formation dQ/dV plots (Figure 4.2). For PDO, pMODO and pFDO, the two peaks present at ~2.2V and ~2.5V are very close and care must be taken in assigning these peaks to the DFT results. This is consistent with previously published results for PDO. Note that the slight difference in the results between the present work and the work by Hall et al. is attributable to their use of the double hybrid functional M06-2X, rather than the B3LYP functional used in the present work.[13] This difference does not affect the important conclusion that the DFT results are consistent with the experimental results for these three additives. The results shown in Figure 4.4 suggest that the peaks at ~2.5 V might be the ones matching the DFT results (the integrals of the peaks at ~2.2 V in Figure 2 are small). The ~2.5 V peaks and the DFT results also seem to follow the same trend (e.g. pMODO reduces at higher cell potential than the other dioxazolones). For pNDO, the DFT result suggests that it is very likely that pNDO reduces at a very low cell voltage (0.78 V), which explains why a peak cannot be seen in Figure 4.2. This could also explain the passivating nature of pNDO. Experimental results shown later will help to confirm this. The proposed first reduction product of pNDO is shown in Figure A.5.

The oxidation potential of all four molecules (pMODO, pDO, pFDO and pNDO) are between 5.0 – 6.5 V vs. Li/Li^+, pMODO having the smallest value and pNDO having the largest. While these potentials are smaller than the oxidation potentials of EC and EMC,

7.05 V vs. Li/Li^+ and 6.75 V vs. Li/Li^+, respectively,[92] it does not mean that oxidation will be the major mechanism at the cathode, as pseudo-combustion, the oxidation of the electrolyte by reactive oxygen species (e.g. singlet oxygen) released by the cathode at high voltage, can also occur.[58,93–95] However, oxidation and pseudo-combustion of an additive will not occur if all the additive molecules are immobilized at the graphite electrode as a reduction product, for example as an SEI component.

Capacity versus cell voltage curves of the other dioxazolones were compared to the reference curve in Figure 4.4. 2% VC is included in the figure as a comparison. Since this measurement is sensitive to any overpotentials, care is needed while comparing and interpreting these curves and the difference curves in Figure 4.4. The same applies for Figure 4.5. The corresponding capacity in mAh for a one, two and three electron(s) reduction for each additive was calculated and included in Figures 4.4 and 4.5 (see Table A.15 for the exact numbers and the molecular masses that were used). In Figure 4.4 a), the difference curve tells us that the reduction of 2% VC is about half an electron. While half an electron seems unexpected, this apparent oddity can be explained by two possible processes. The first is the passivation of the graphite electrode by half of the VC, while the other half does not reduce and stays in the electrolyte. The other is a one electron reduction of a VC molecule forming a radical, which can polymerize to poly(VC) without the use of further electrons, except during chain termination.[31,96] In reality, a mix of both phenomena likely happens at the same time. As such, the number of electrons deduced from Figures 4.4 and 4.5 should be seen as an apparent number of electrons that can help us deduce the real number of electrons per molecule used during each reduction. The difference between

the real and apparent number of electrons per molecule during reduction arises due to the passivation of the graphite electrode or due to polymerization.

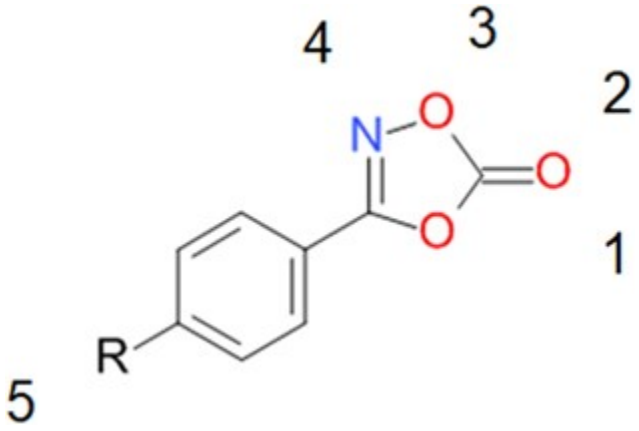

Figure 4.3: Illustration of the lithium-ion sites 1 to 5 used in the DFT-calculation to deduce the reduction potentials of all dioxazolones studied in this work. Each number indicates the position at which a lithium ion was placed to calculate the corresponding reduction potential. It is noted that each molecular geometry was optimized before the single point energy calculations were performed. In addition to the inclusion of a lithium-ion, an electron was transferred to the molecule before optimization to calculate the reduction potential of each dioxazolone.

If no passivation or polymerization were present, the real and apparent number of electrons would be equal. Note that the results found for 2% VC in Figure 4.4 a) are consistent with past work by Petibon et al.[97] However, the differences between Figure 4.4 a) and the results found by Wang et al.[24] are possibly due to differences in the graphite materials used (e.g. different specific surface area).

Since 2% PDO and 2% pMODO did not passivate the graphite electrode against EC reduction in Figures 4.2 c) and 4.2 d), it can be expected that the data in Figures 4.4 b) and

4.4 c) give a very good idea of the number of electrons used during the reduction of PDO and pMODO. As such, it is likely that one electron per molecule is used by those two additives during their reduction. It is difficult to explain the first peaks in the 2.2 V region in Figures 4.2 c) and 4.2 d). Since the used capacity in the 2.2 V region is low, those peaks may be due to impurities. However, those peaks could also be explained by an unknown mechanism. Further studies are needed to understand the peak in the 2.2 V region.

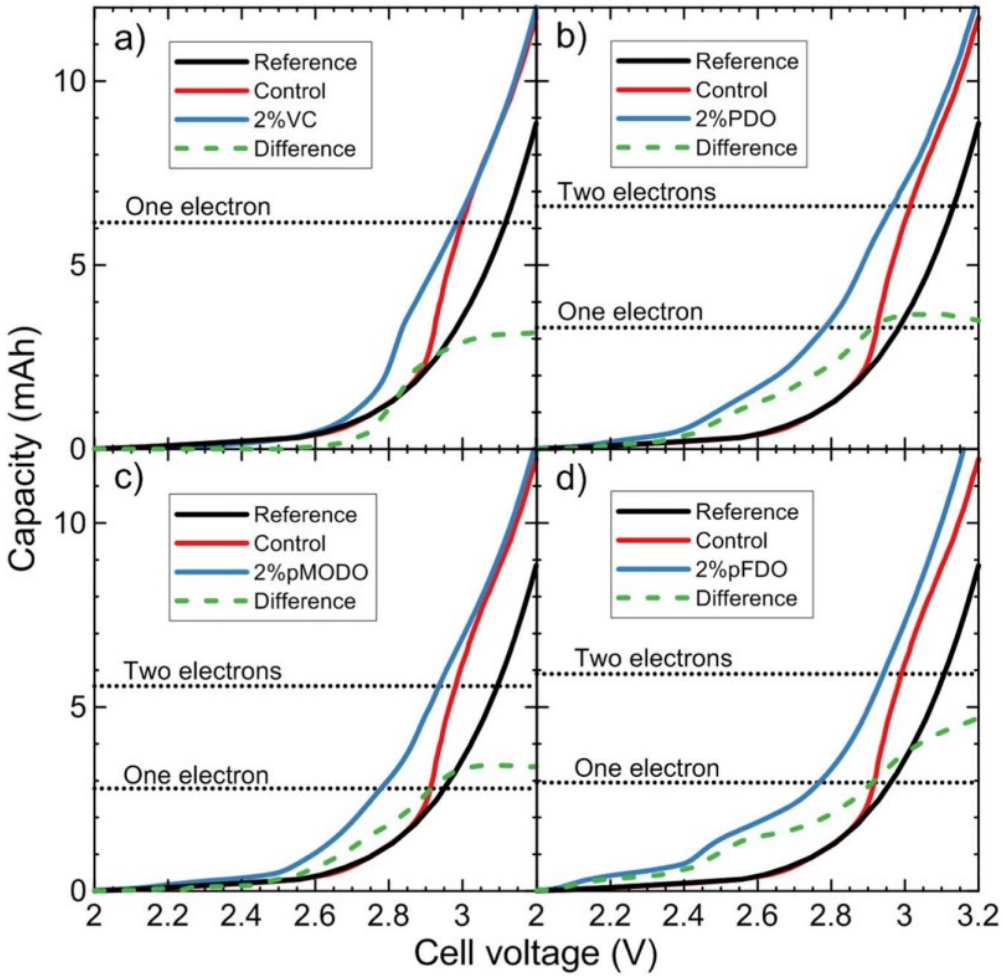

Figure 4.4: Capacity as a function of cell voltage of a) 2% VC, b) 2% PDO, c) 2% pMODO and d) 2% pFDO NMC622/gr pouch cell. The results are compared to those from a control cell and a full cell reference curve obtained from NMC622B/Li and Graphite/Li half-cells data as explained in the experimental methods section. The reference curve should show no features due to reduction of solvents or additives since the second cycle of the graphite

half-cell is used to create the reference curve. a) and b) used 1.2 M LiPF6 in EC:DMC 3:7 as the control electrolyte, while c) and d) used 1.2 M LiPF6 in EC:EMC:DMC 25:5:70 as the control electrolyte. The difference curve (green dashed curve) corresponds to the difference between the "electrolyte additive curve" (blue curve) and the reference curve (black curve).

Figure 4.2 e) shows that pFDO passivates the graphite electrode against EC reduction. Noting that the dashed curve in Figure A.12 (an extension of Figure 4.4 d) above 3.2 V) reaches a maximum of 5 mAh at a cell voltage of 3.3 V, it is possible that the reduction of 2% pFDO is in fact a two-electron process but does not reach 6 mAh because pFDO passivates the graphite electrode before all the pFDO can reduce. However, more studies are needed to confirm this and to propose a mechanism that agrees with all experimental data. Note that a peak is also present in the 2.2 V region for 2% pFDO in Figure 4.2 e). While the integral of that peak has a higher value in capacity than the equivalent peaks for 2% PDO and 2% pFDO, its true nature is also unknown.

In order to confirm the DFT prediction that pNDO reduces at 0.78 V, two 2% pNDO NMC622/gr cells were charged from 0.0 V to 3.2 V at C/20 and 40°C after a 15 minutes rest at the same temperature. Two control cells only containing 1.2 M $LiPF_6$ in EC:EMC:DMC 25:5:70 were also charged under the same conditions in order to make sure that any reduction peaks are indeed due to pNDO. The differential capacity (dQ/dV) results as a function of cell voltage are shown in Figure 4.5 a). Figure 4.5 b) shows the same data, but in a capacity versus voltage format. The 2.0 – 3.2 V region in Figure 4.5 a) shows results that are consistent with Figure 4.2. A peak at ~ 1.0 V with an onset at ~ 0.9 V in Figure 4.5 a), which is not present for the control cells, agrees with the DFT prediction. Further peaks are present in the 1.2 – 1.5 V regions, which are likely due to further reductions of pNDO.

To better understand the nature of these peaks, a DFT calculation and geometry optimization of pNDO with two lithium atoms describing a second reduction of pNDO, was performed. One lithium atom was placed in site 5 and the second in site 2 as indicated in Figure 4.3 and Figure A.6. These sites were chosen based on the free energies shown in Table 4.1 for each lithium site. Since sites 2 and 5 correspond to the ones that have the two lowest free energies for LipNDO, these sites were chosen for the second reduction of pNDO. It is found that the second reduction potential of pNDO is 1.75 V vs. Li/Li^+ which corresponds to a cell voltage of 1.75 V. This result provides a suggestive explanation of the peaks in the 1.2 – 1.5 V regions, within DFT errors. However, it can only explain one peak. The third peak may be due to a third reduction. At first, this may seem contradictory with Figure 4.5 b). However, the passivation of the graphite electrode by pNDO against EC reduction in Figure 4.5 a) is consistent with the possibility that some pNDO molecules may be still present in the electrolyte after the passivation. As a result, Figure 4.5 b) would underestimate the number of electrons used during the reduction of pNDO. Considering this possibility, DFT was used to calculate the third reduction of pNDO (lithium ions being present in sites 1, 2 and 5; these sites were chosen based on the free energies shown in Table 4.1 for each lithium sites). In this configuration, pNDO would likely decompose into lithium carbonate and a lithium p-nitrobenzonitrile radical according to our DFT results. Figures A.7 and A.8 show these DFT results. It is found, using DFT, that the third reduction potential of pNDO is 5.96 V vs. Li/Li^+, showing that this decomposition will happen immediately after the second reduction, further supporting this hypothesis. It is likely that the lithium carbonate then contributes to the negative SEI and that the lithium p-nitrobenzonitrile radical react further.

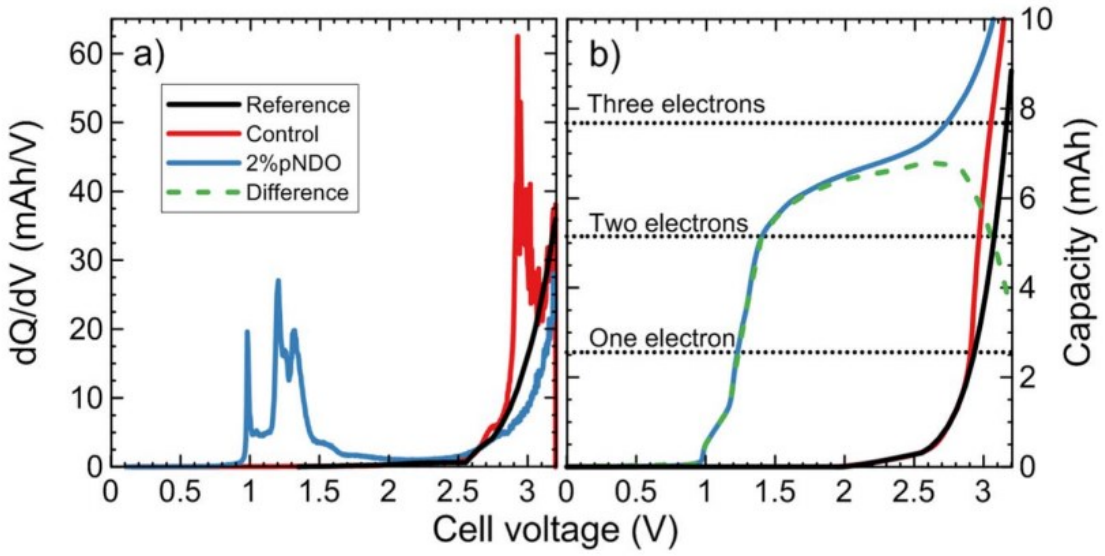

Figure 4.5: a) Differential capacity (dQ/dV) and b) capacity as a function of cell voltage of a control and a 2% pNDO NMC622/gr pouch cell. The cells are compared to the full cell reference curves obtained from NMC622B/Li and Graphite/Li half-cells data. Following an initial 15 min rest at 40 °C, the cells were charged at C/20 from 0 V to 3.2 V. In b), the difference curve (green dashed curve) corresponds to the difference between the "electrolyte additive curve" (blue curve) and the reference curve (black curve). The cells contained 1.2 M LiPF6 in EC:EMC:DMC 25:5:70 as the control electrolyte. The decrease in capacity above 2.7 V in b) for the difference curve could be due to an overpotential, since a shift is present in the same voltage range between the 2% pNDO data and the reference curves in a).

However, extensive experiments are needed to fully confirm this proposed pathway, which would comprise a complete study that is outside the scope of the present work. It is acknowledged that the accuracy of B3LYP methods is not fully known for such highly reduced compounds, which may have significant localization of charge density. Nonetheless the results of this analysis are expected to provide useful insight on reactivity trends.

4.3 CYCLING AND STORAGE

Figure 4.6 shows the long-term cycling data of cells prepared with the 3-R-1,4,2-dioxazol-5-one-based electrolyte additives. ΔV, shown in the lower panels of Figure 4.6, corresponds to the difference between the average charge and discharge voltage. ΔV is related to the impedance of the cells by Ohm's law. Figure 4.6, and the cycles to 90% summary in Figure 4.7 a), shows that when no co-additives are added, PDO is the best additive followed by pNDO, pMODO and pFDO. 2% X + 1% DTD blends also follow this trend. However, when LFO is added, pNDO is the best additive, followed by PDO, pMODO and pFDO. When MMDS is added, pNDO also shows good performance compared to the other dioxazolones, however MMDS has not been tested with PDO. When 2% VC is added, pNDO and pFDO have very similar performance, both are better than 2% pMODO + 2% VC and 2% PDO + 2% VC in terms of impedance growth (indicated by the slope of ΔV vs cycle number). They also perform very similarly to 2% VC without co-additives. Overall, the best cells in Figure 4.6 are 2% PDO + 1% DTD, followed by 2% pNDO + 1% DTD, 2% pNDO + 1% LFO and 2% pNDO + 1% MMDS.

The difference in performance between pFDO cells and PDO cells, especially when DTD is present, might be difficult to understand at first since DFT predicts similar reduction and oxidation potentials for these two additives in Table 4.1. Furthermore, Figure 4.2 shows that 2% PDO partially passivates the graphite electrode while 2% pFDO fully passivates it. This might seem contradictory to the data in Figure 4.6. A possible explanation could be that the reduction of pFDO produces soluble products or gases that negatively affect the performance of DTD by reacting with it and/or that negatively affects the positive

electrode, while the products of PDO reduction do not. pMODO could act similarly to pFDO, while not passivating the graphite electrode.

Figure 4.7 b) and c) shows 1% PDO + 2% DTD and 2% PDO + 1% DTD cells compared to some of the best cells ever tested in our lab in polycrystalline NMC622/gr cells. 2% VC and 1% LFO are also shown to help have an idea of the relative performance. By looking at Figure 4.7 b) and 4.7 c), 1% PDO + 2% DTD seems to be the best performing cell ever tested in our lab for this type of cell, closely followed by 0.5% PES + 1% VC + 1% MMDS (PES0511). While it may not be perfectly clear that 1% PDO + 2% DTD has a better performance than PES0511 in Figure 4.7 b), the difference in slope of both cells in Figure 4.7 c) make it clear that the ΔV of 1% PDO + 2% DTD does not grow as fast. A comparison of 1% PDO + 2% DTD and 2% PDO + 1% DTD shows that while they both seem to perform much better than 1% LFO in Figure 4.7 b), their difference in slope in Figure 4.7 c) is important.

In fact, the slope of 2% PDO + 1% DTD and 1% LFO are very similar after 500 cycles. Since 1% PDO + 2% DTD is shown to be better than 2% PDO + 1% DTD in Figure 4.7, none of the cells in Figure 4.6 are better than 1% PDO + 2% DTD.

Figure 4.8 shows the storage performance of cells containing the newly synthesized dioxazolones (Figures 4.8 a), 4.8 c), 4.8 d)), compared to PDO data (Figure 4.8 b)). When no co-additives are present, 2% PDO is the best performing dioxazolone additive during storage, followed by 2% pMODO, 2% pNDO and 2% pFDO, in this order. Except for blends containing MMDS, the performance of all dioxazolone blends follow a trend. First, 2% of a dioxazolone with 2% VC is the best performing blend but it does not beat the performance of 2% VC cells.

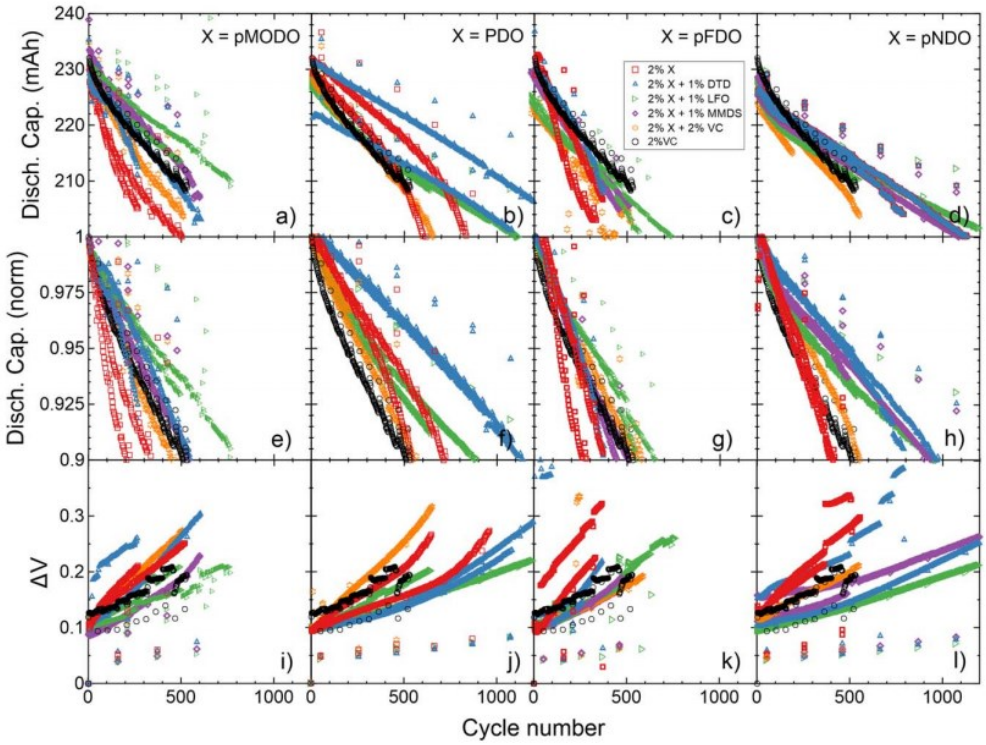

Figure 4.6: Long-term cycling data of pMODO, PDO, pFDO and pNDO alone or with a co-additive in NMC622/gr cells at 40 °C. Cells were cycled between 3.0 V and 4.3 V at C/3. The first row a) – d) shows the discharge capacity, the second row e) – h) shows the normalized discharge capacity data, while the third row i) – l) shows the ΔV data. Each column shows the data for a primary additive X: a), e), i) 2% pMODO, b), f), j) 2% PDO, c), g), k) 2% pFDO and d), h), i) 2% pNDO. Except for 2% X and 2% VC, the different colors/symbols correspond to a specific secondary additive. All cells contained 1.2 M LiPF6 EC:EMC:DMC 25:5:70 as the main component of the electrolyte, except for 2% VC, 2% PDO and the PDO blends which used 1.2 M LiPF6 EC:DMC 3:7.

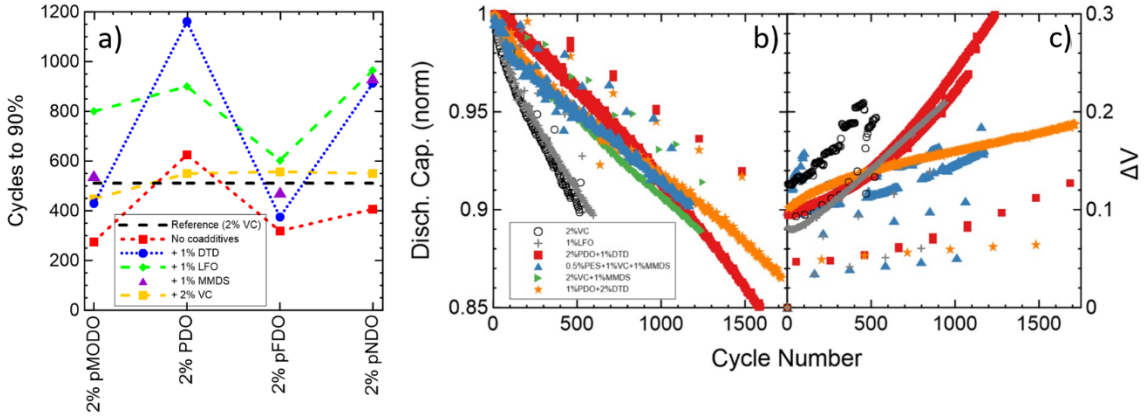

Figure 4.7: a) Summary of Figure 4.6: cycles to 90% of dioxazolones addives mixed or not with co-additives as illustrated in the legend. 2% VC is used as a reference. Lines are added to the graph to help guide the eye. b) and c) Long-term cycling data of some of the best NMC622/gr cells at 40°C: b) show normalized discharge capacity and c) show ΔV vs cycle number. Cells were charged and discharged at C/3 between 3.0 V and 4.3 V. Results for cells with 2% VC or 1% LFO are also shown as a comparison. All cells in b) and c) contained 1.2 M $LiPF_6$ EC:EMC 3:7 as the main component of the electrolyte, except for the PDO/DTD blends which used 1.2 M $LiPF_6$ EC:DMC 3:7.

Then, cells with 2% of a dioxazolone with 1% LFO, 2% of diozazolone alone and 2% of a dioxazolone with 1% DTD follows in terms of performance, in this order. MMDS performs best in cells with 2% pNDO, however MMDS was not tested in 2% PDO cells. Note from Figures 4.6 and 4.8 that 2% PDO + 1% DTD is better than 2% VC during long-term cycling, but not during high temperature storage. Why is this the case? While the performance of a cell during long-term cycling depends on how

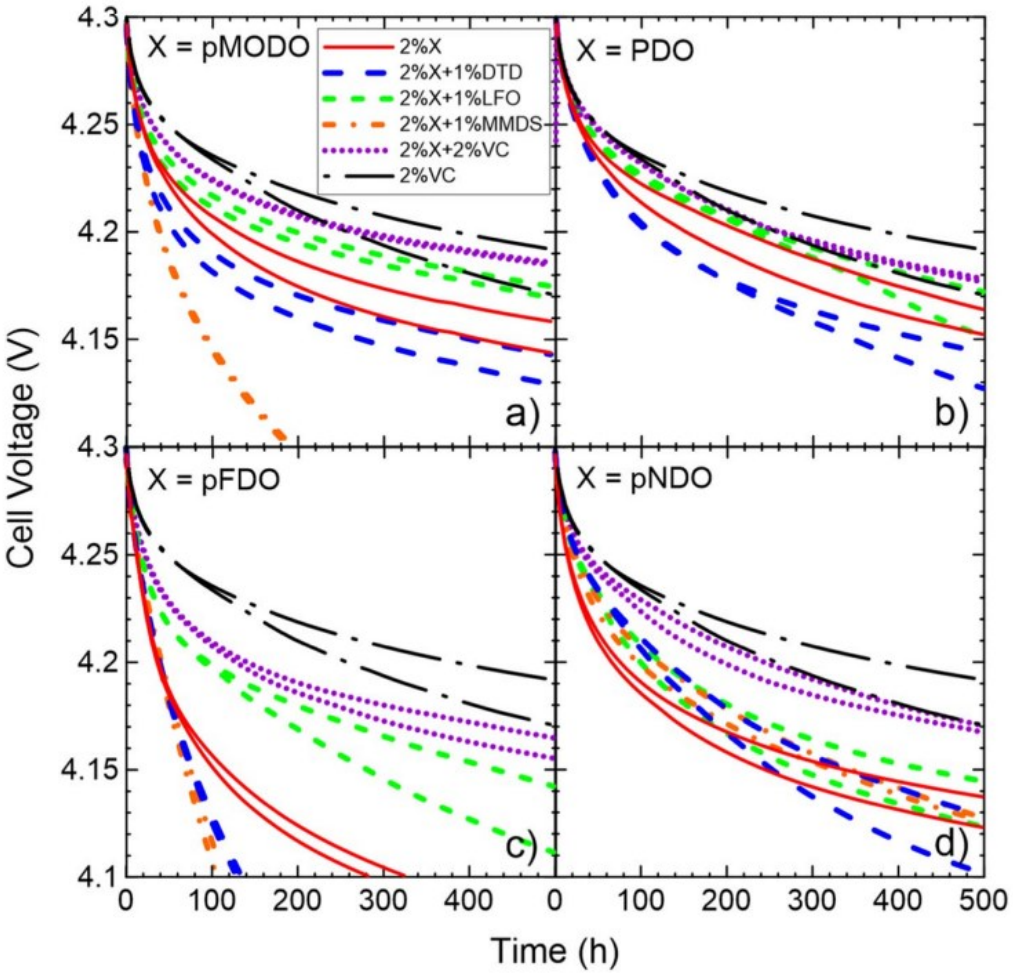

Figure 4.8: Storage data at 60°C of primary additives X: a) pMODO, b) PDO, c) pFDO and d) pNDO alone or with a co-additive in NMC622/gr cells. The cell voltages in open circuit conditions are shown as a function of time. Except for 2% X and 2% VC, different lines/colors correspond to a cell with a different secondary additive, as shown in the legend. 2% VC is shown as a comparison. All cells contained 1.2 M LiPF6 EC:EMC:DMC 25:5:70 as the main components of the electrolyte, except for 2% VC, 2% PDO and the PDO blends which used 1.2 M LiPF6 EC:DMC 3:7.

much lithium inventory loss occurs at the SEI and on how much impedance related capacity loss happens, performance of a cell during high temperature storage depends on how much oxidation of the electrolyte, how much transition metals dissolution occurs at the positive electrode or if a redox shuttle is present in the electrolyte.[98] Since the failure mechanisms

are different, the performance of cells in Figure 4.6 and 4.8 can't correlate. In the case of an electric car however, long-term cycling performance is more important if the car is charged daily or often.

4.4 GAS AND IMPEDANCE

Figure 4.9 shows in-situ gas data during formation at 40ºC for cells with electrolytes containing 2% PDO or 2% pNDO compared with control electrolyte. All three electrolytes contain 1.2M $LiPF_6$ EC:EMC:DMC 25:5:70 as the main component. Figure 4.9 a) shows the cell voltage versus time for each cell during the 250 hour in-situ gas measurement. Figure 4.9 b) shows the volume change measured as a function of time, while 4.9 c) shows it as a function of cell voltage. pNDO and control cells start producing gas around 3 V. The gases emitted by control cells during reduction contain ethylene, carbon dioxide and other gases[99], while the gas emitted by pNDO cells may be due, directly or indirectly, to lithium p-nitrobenzonitrile radicals reacting further and the products could possibly oxidize at the positive electrode. Control cells produce more gas than pNDO below 4.3 V, but pNDO cells start producing more gas than control cells above 4.3 V. pNDO cells slowly continue to create gas in open circuit conditions, and control cells start consuming gas as has been noted by Ellis et al.[100]

Control and 2% pNDO cells do not create any net change in gas volume while wetting at 1.5 V and 40°C while 2% PDO cells produced 0.6 mL of gas and consumed 54 mAh of charge during this period (see Figure A.13). An impurity in the PDO, acting as a redox

shuttle (i.e. a molecule that reduces and then oxidizes back to the original form in a loop at the negative and positive electrode.), could explain these observations. Before explaining why we think that a redox shuttle is responsible, let us add further evidence that gas is indeed produced by PDO cells during wetting. Two cells with 2% PDO in 1.2M LiPF6 EC:EMC:DMC were held on a Maccor 4000 series charger at a constant voltage of 1.5 V at 40°C. The volume of gas following 24 h of wetting was measured using the ex-situ gas apparatus as described in chapter 3 and was found to be 0.43 ± 0.03 mL. This shows that the in-situ and ex-situ gas measurements do agree.

Let us now explain why we think that a redox shuttle is present in cells that contain 2% PDO. First, the large amount of charge consumed of 54 mAh can't be explained by PDO reduction since PDO reduces at a cell voltage of 2.24 V. Second, it can't be explained by the control electrolyte since we don't see this phenomenon in control cells. This then means that it must come from the reduction or oxidation of an impurity. However, the reduction of a molecule, 2% PDO for example consumes around 3.3 mAh for a one-electron reduction (see Table A.15) assuming all the additive molecules present reduces. Since a 55/3 ~ 20 electrons reduction doesn't make sense, the only reasonable explanation is a redox shuttle. Note that benzoic acid has been detected in PDO by the chemist in our lab via NMR and it is thought that it could be the cause of this, and hydrogen could be the gas that is formed in the process.

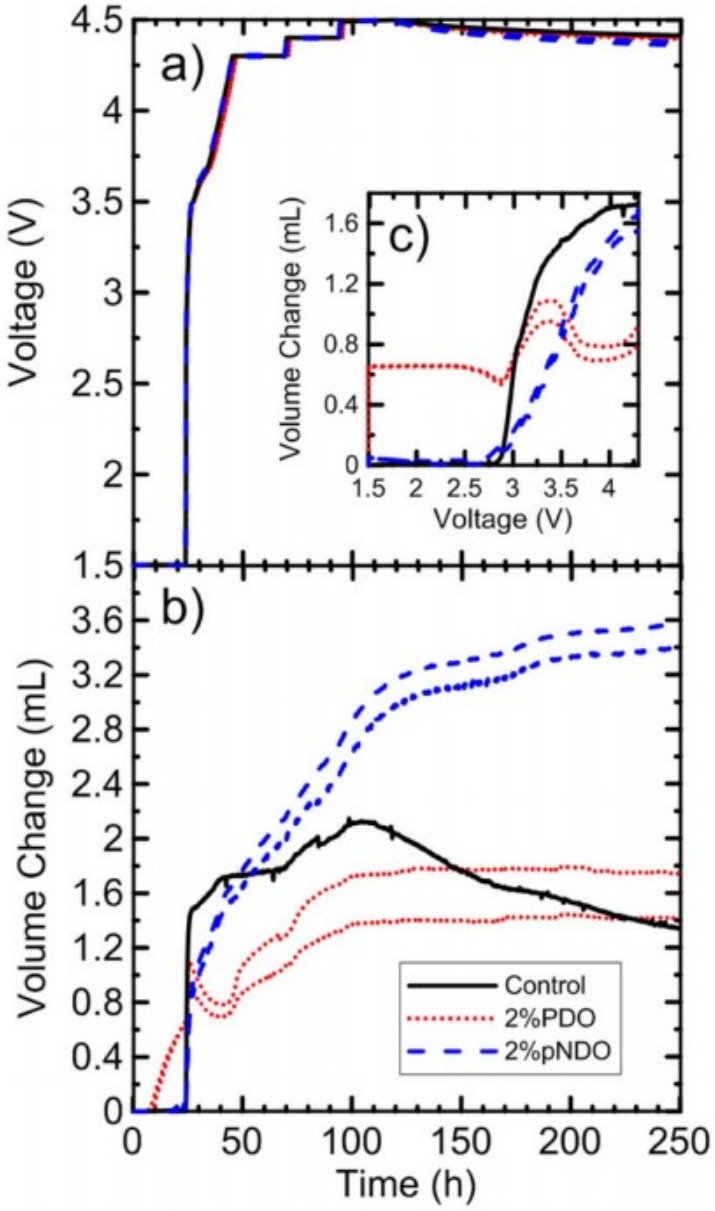

Figure 4.9: Volume change of control, 2% PDO and 2% pNDO in NMC622/gr cells during formation at 40 ± 2°C using an in situ gas apparatus. The control electrolyte used was 1.2 M $LiPF_6$ EC:EMC:DMC 25:5:70 for all three cells, to which the additives were added. The graph shows a) the voltage vs time, b) the volume change vs time and c) the volume change vs voltage of these cells.

Furthermore, Figure 4.9 c) shows that some small amount of gas consumption occurs between ~2.5 V and ~2.9 V in 2% PDO cells. At ~2.9 V, gases evolve until ~3.5 V, maybe

because of EC reduction. Then, some consumption of gas occurs until ~4 V. At 4 V, gas production due to oxidation starts for PDO cells and continues until open circuit conditions at ~100 h. Then, no gas production or consumption occur during open circuit conditions. Note that since the cells are balanced to 4.4 V (The areal capacity ratio of the negative electrode to the positive electrode is 1.1 at 4.4 V), charging these cells to 4.5 V in Figure 4.9 could have caused unwanted lithium plating. Consequently, the net gas production after 90 h could be different than that shown in Figure 4.9 if equivalent cells balanced to 4.5 V were tested similarly.

Figure 4.10 a) shows cell volume changes, due to gas production, following formation. Cells with 2% PDO produce less gas than cells with 2% of other dioxazolones during formation. This suggests that functional groups can negatively impact gas production during formation. Cells with only 2% pNDO produce the most gas during formation, an amount which is like the volume produced by control cells, in agreement with Figure 4.9. Adding a co-additive decreases the amount of gas during formation in most cases, except for pFDO with DTD. The blends that produced the least amount of gas here are 2% PDO + 1% DTD, 2% pFDO + 1% LFO and 2% pNDO + 2% VC.

Figure 4.10 b) shows R_{ct} after formation for the same cells. Adding co-additives to the dioxazolones increases R_{ct} after formation in all cases. Furthermore, it seems like more electron withdrawing functional groups on the para position of the benzene ring increase R_{ct} on average when the dioxazolones are added to a co-additive. Interestingly, 2% pNDO + 1% LFO cells perform as well as 2% PDO + 1% LFO when it comes to this measurement. This is interesting since the other pNDO blends tested here have a R_{ct} much higher than

the PDO blends. Overall, cells with 2% pMODO had the smallest R_{ct} after formation, being better than control and 2% VC. As an example, the EIS Nyquist plot of dioxazolones without and with 1% DTD of cells after formation are shown in Figures A.1 and A.3.

Figure 4.10 c) shows gas production of the same cells after storage. The first trend that can be seen is the increase in gas production as the functional group on the para position of the phenyl moiety is more electron withdrawing. For all dioxazolones, the presence of 2% VC as a co-additive or the absence of a co-additive resulted in more gas during storage, while the other blends tested produce way less gas. When a co-additive other than VC is used, the amount of gas is comparable to cells with 2%VC, except maybe for the pNDO blends which create more gas. However, cells with 2% pNDO and 2% pNDO + 2% VC produce almost as much gas as control. In terms of gas production during storage, the best cell is 2% PDO + 1% DTD.

Figure 4.10 d) shows R_{ct} after storage for the same cells. Except when VC is added, it seems like any blends of dioxazolone perform similarly in terms of R_{ct} after storage when the functional group is changed at the para position of the phenyl moiety, however PDO and its blends do perform better. In the case of dioxazolone and VC blends, R_{ct} after storage decreases as the functional group become more electron withdrawing. The best performing cells in terms of R_{ct} after storage are cells with 2% pNDO + 1% LFO and PDO cells without VC, all being better than 2% VC cells. As an example, the EIS Nyquist plot of cells containing dioxazolones without and with 1% DTD of cells after storage are shown in Figure A.2 and A.4.

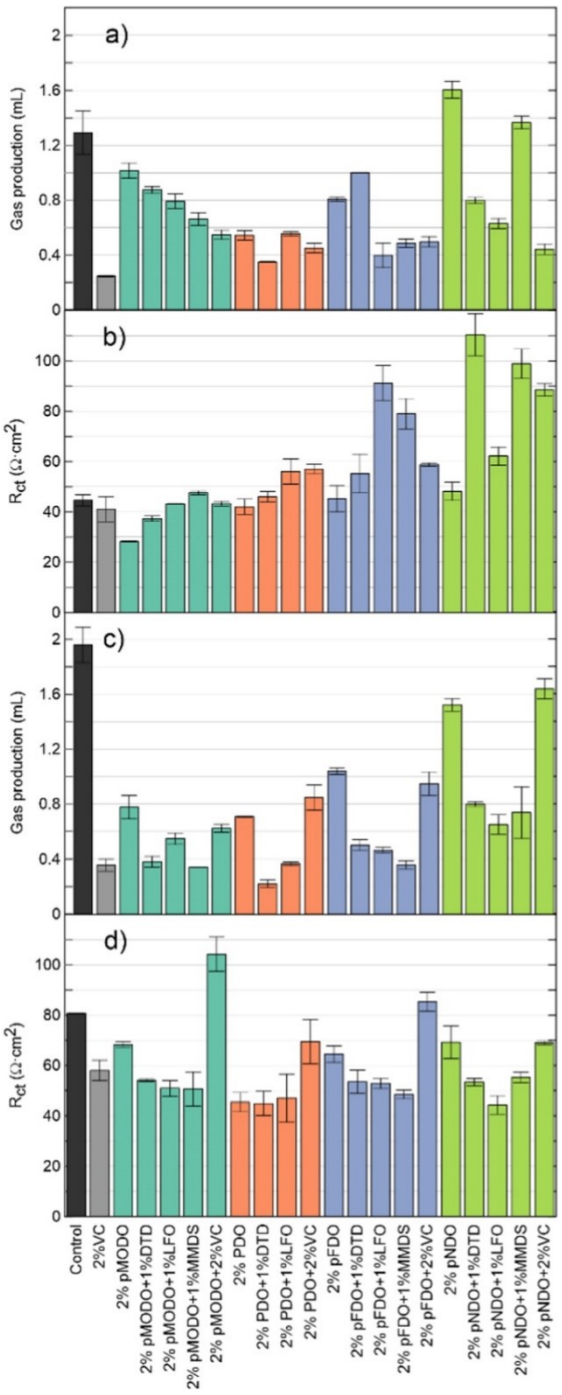

Figure 4.10: Gas production and Rct of pMODO, PDO, pFDO and pNDO in NMC622/gr cells, alone or combined with a co-additive, a), b) before storage and c), d) after storage at 60°C and 4.3 V for 500 h. Control and 2% VC are shown as a comparison. All cells contained 1.2 M LiPF6 EC:EMC:DMC 25:5:70 as the main components of the electrolyte, except for control, 2% VC, 2% PDO and the PDO blends which used 1.2 M LiPF6 EC:DMC 3:7. R_{ct} was measured at 3.8 V and 10°C.

CHAPTER 5 EFFECT OF DEPTH OF DISCHARGE ON CELL PERFORMANCE AND CELL PARAMETERS

5.1 INTRODUCTION

As the world rapidly turns to electric vehicles as a mode of transportation and to electrical energy storage systems for solar and wind power, predicting and improving the long-term performance of lithium-ion batteries is crucial. Researchers often use full charge and discharge protocols to determine and predict Li-ion cell lifetime.[13,101–103] However, since many users rarely drive long distances daily or deplete energy storage systems completely, those protocols do not represent realistic duty cycles well for battery electric vehicles (BEV) or electrical energy storage systems.[104–106] As a result, analyzing the impact of the depth of discharge (DOD) and state of charge (SOC) range on cell lifetime is important to understand cell degradation in real applications. The effect of DOD and SOC range on lifetime and other cell parameters has been studied before.[107–121] However, there are few experimental studies on a large SOC range/rate/temperature matrix of cells that also include an extensive study of the changes which have occurred to the cells after years of testing.

One of the primary causes of cell capacity fade, the growth of the negative electrode solid-electrolyte interface (SEI), which leads to lithium inventory loss, is still not well understood. Many different mechanisms have been proposed to explain the continuous growth of the SEI on the graphite electrode after formation: diffusion of the electrolyte through nanosized SEI pores, electron tunneling, electron conduction or interstitial

diffusion of neutral lithium through the SEI, “near-shore” SEI aggregation or SEI cracking.[107,122,123] A detailed study of the effect of depth of discharge and state of charge range on cell capacity loss can help researchers determine how these factors influence SEI growth.

For this study, a large matrix of cells which consisted of two different cycling temperatures (20°C and 40°C), three different cycling rates (C/10, C/5, C/3) and seven different SOC ranges (0-25, 0-50, 0-75, 0-100, 75-100, 50-100 and 25-100%) was created, for a total of 96 cells. The cells consisted of polycrystalline NMC622/natural graphite (NMC622/NG) cells with VC211 (2% vinylene carbonate (VC) + 1% methylene methane disulfonate (MMDS) + 1% tris-trimethylsilyl phosphite (TTSPi)) as an additive blend in 1.2M $LiPF_6$ EC:EMC 3:7 or 1.2M $LiPF_6$ EC:DMC 3:7 electrolyte. The VC211 additive blend was chosen because of its good performance in cells.[124] Natural graphite was used because of its irreversible expansion during cycling, which might create SEI cracking.[7] Polycrystalline NMC622 was used to study the effect of SOC range or DOD on the microcracking of the positive electrode. As a result, the cells used in this work are not intended to be as good as the ‘million-mile battery’ of Harlow et al.,[125] instead they are intended to help researchers develop a deeper understanding of the degradation of lithium-ion cells.

This research was inspired by the theoretical work of Deshpande and Bernardi, who proposed that capacity loss during cycling should be proportional to the state of lithiation swing squared. They proposed this result by assuming that lithium inventory loss is a

consequence of SEI cracking due to expansion and contraction of graphite particles during charge and discharge.[107] In order to show if this model is indeed correct, a large matrix of cells with different depth of discharge, C-rate and temperature was built as described above.

The current project intended to study cell capacity loss and impedance growth both during and after cycling. Furthermore, the thickness measurements of our cells, differential thermal analysis (DTA) of the electrolyte, ultrasonic transmission mapping and X-ray CT scans of our cells gave us insight about the reasons for capacity loss and impedance growth.

5.2 LONG-TERM CYCLING DATA

After our cells went through their formation protocol, cells were degassed and then connected to a Neware charger and tested at room temperature or in temperature boxes at 40°C. After the cells went through a couple of cycles, the exact DOD value of each cell was calculated and was found to be slightly different compared to the approximate values predicted in Tables 3.3 and 3.4. Figure 5.1 shows these exact values. For a specific DOD (e.g. ~75% DOD) one can see that the DOD values as a function of C-rate do not change more than ± 5%. Each plateau in Figure 5.1 shows the data points of cells at C/10 (red squares), at C/5 (blue circles) and at C/3 (green triangles), respectively from left to right. The LC cells have a smaller DOD than the UC cells by approximately 5%, except for the 100% DOD cells. Furthermore, all cells that permanently cycled in the 3.0 V – 4.1 V range had their DOD values set to 100% DOD for all C-rates and all cells used the 100% DOD cells at the same C-rate as a reference to calculate their DOD values. The exact DOD values

from Figure 5.1 are used in this work when needed.

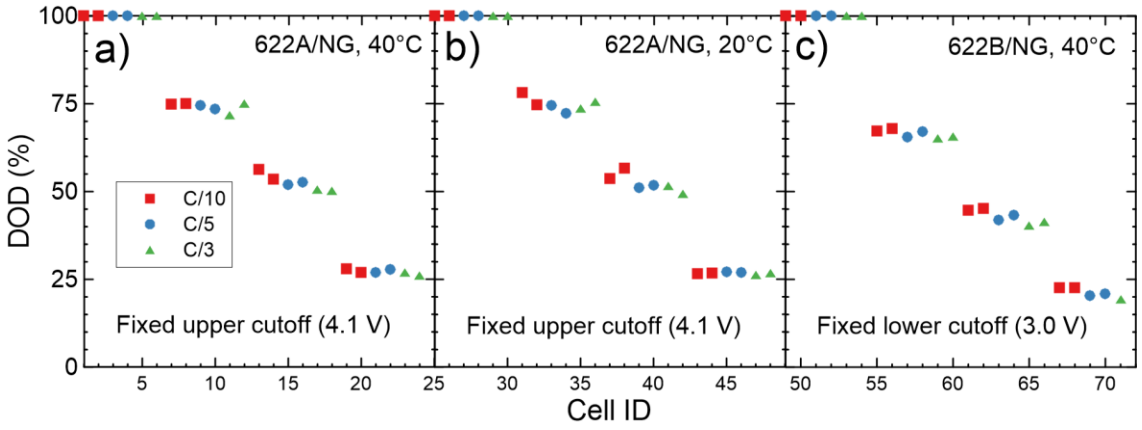

Figure 5.1: Exact initial DOD values for UC and LC cells at t ≈ 0 hour. A cell ID is used to identify each cell. For each plateau, the first two data points correspond to cells cycling at C/10 (red squares), the two in the middle to cells cycling at C/5 (blue circles) and the last two to cells cycling at C/3 (green triangles). Each DOD value is calculated using the full-range (3.0 V - 4.1 V) cells at the same rate as a 100% DOD reference. Figure 5.1 a) shows the initial DOD values for NMC622A/NG UC cells that cycled at 40°C, Figure 5.1 b) for NMC622A/NG UC cells that cycled at 20°C and Figure 5.1 c) for NMC622B/NG LC cells that cycled at 40°C.

Each cell was cycled for approximatively 20000 hours using the appropriate protocols, which are mentioned in the Experimental Methods section. Figures 5.2 to 5.4 show the discharge capacity and ΔV versus time for all these cells. The b), e), h) columns of these figures show an expanded view of the checkup cycles of these cells, which correspond to the 170-220 mAh region of the data shown in the a), d), g) columns. Each row of these three figures shows the data for a specific C-rate. Figure 5.5 shows the capacity loss that was calculated from the checkup cycles for each cell. For cells that missed some initial checkup cycles from 0 to 2000 hours, a linear or square root extrapolation to 0 hour was used to calculate the capacity loss.

Figures 5.2, 5.3 and 5.5 show that at 40ºC capacity loss increases when DOD and C-rate increase and that the slope of ΔV vs. time also increases with DOD and C-rate. Also note how cells that cycled at 25% DOD and C/3 have a capacity that is relatively constant around 50 mAh even after 20000 h. Figures 5.5 a) and 5.5 b) show that capacity losses are similar between UC and LC cells cycling at 40°C, while Figure 5.5 c) shows that capacity loss for cells cycling at 20°C is non-linear as a function of DOD because of contributions from overhang/overlap diffusion (see Figure A.17). Note that the capacity loss in Figures 5.5 a) and 5.5 b) is mostly linear versus DOD.

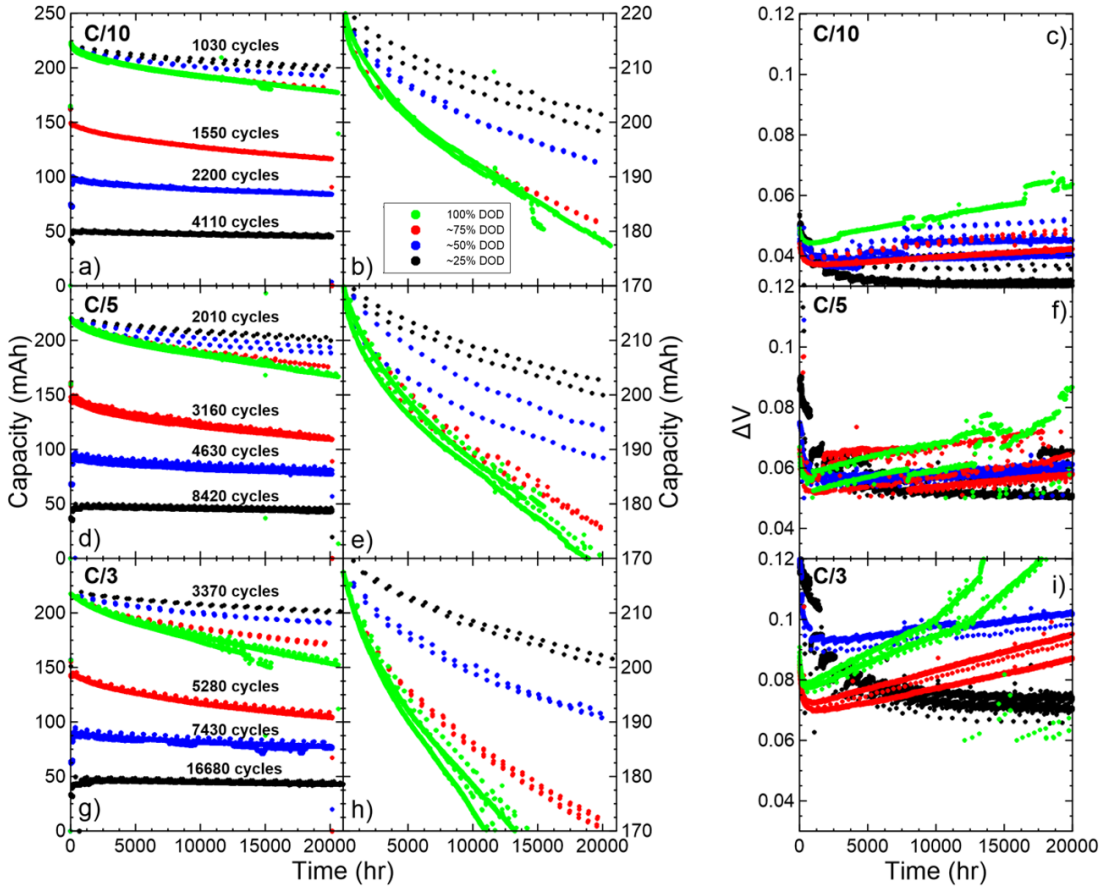

Figure 5.2: a), b), d), e), g), h) show the discharge capacity versus time and c), f), i) show ΔV versus time of LC cells that cycled at 40°C. The middle column shows an expanded view of the checkup cycles of the data in the left column. The number of total cycles is also indicated as well as the C-rate. To make the graphs cleaner, the data below 0.045 V in f) and below 0.06 V in i) where removed. This data corresponding to the ΔV values of the checkup cycles can be found in Figure A.18. Data in green, red, blue and black represent cells that cycled at 100% DOD, 75% DOD, 50% DOD and 25% DOD, respectively. Note that time and cycle numbers don't appear proportional to each other here since a low DOD cycle is shorter than a large one (capacity is proportional to time at constant current). Similarly high C-rate cycles occur faster than low C-rate cycles. They are approximately related to each other by t = 2n DOD/Crate, where t is time, n is the cycle number, while DOD and Crate are written as decimals. Note that the relationship is an approximation since it assume that there is not capacity loss.

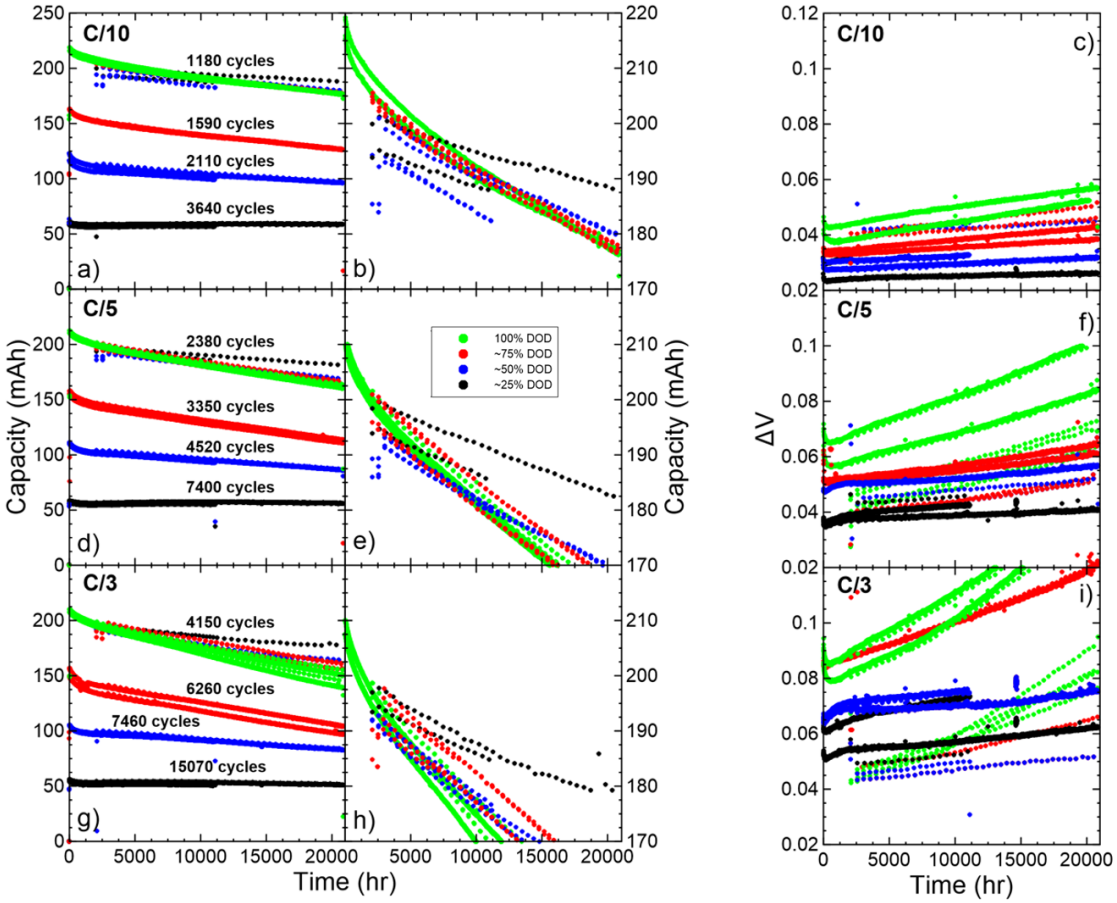

Figure 5.3: a), b), d), e), g), h) show the discharge capacity versus time and c), f), i) show ΔV versus time of UC cells that cycled at 40°C. The middle column shows an expanded view of the checkup cycles of the data in the left column. The number of total cycles is also indicated as well as the C-rate. Data in green, red, blue and black represent cells that cycled at 100% DOD, 75% DOD, 50% DOD and 25% DOD, respectively. Note that time and cycle numbers don't appear proportional to each other here since a low DOD cycle is shorter than a large one (capacity is proportional to time at constant current). Similarly high C-rate cycles occur faster than low C-rate cycles. They are related to each other by t = 2n DOD/Crate, where t is time, n is the cycle number, while DOD and Crate are written as decimals.

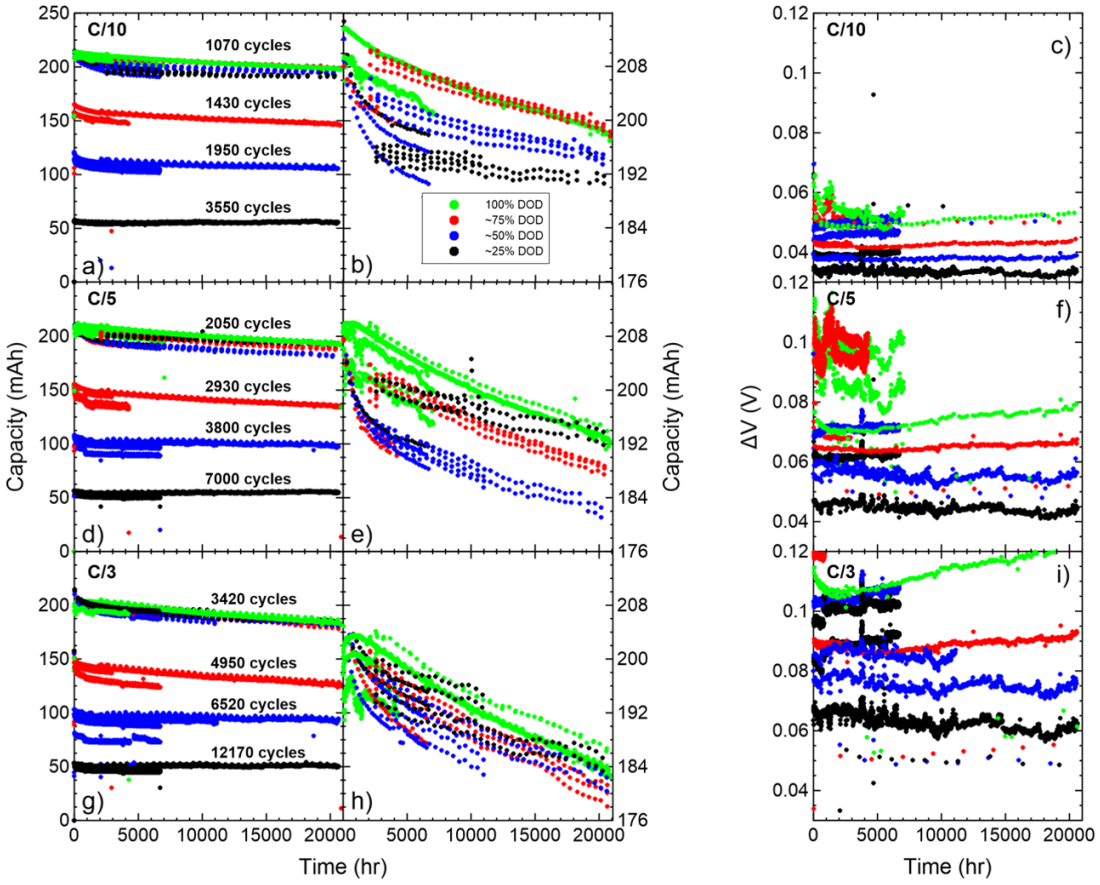

Figure 5.4: a), b), d), e), g), h) show the discharge capacity versus time and c), f), i) show ΔV versus time of UC cells that cycled at 20°C. The middle column shows an expanded view of the checkup cycles of the data in the left column. The number of total cycles is also indicated as well as the C-rate. Data in green, red, blue and black represent cells that cycled at 100% DOD, 75% DOD, 50% DOD and 25% DOD, respectively. Note that time and cycle numbers don't appear proportional to each other here since a low DOD cycle is shorter than a large one (capacity is proportional to time at constant current). Similarly high C-rate cycles occur faster than low C-rate cycles. They are related to each other by t = 2n DOD/Crate, where t is time, n is the cycle number, while DOD and Crate are written as decimals.

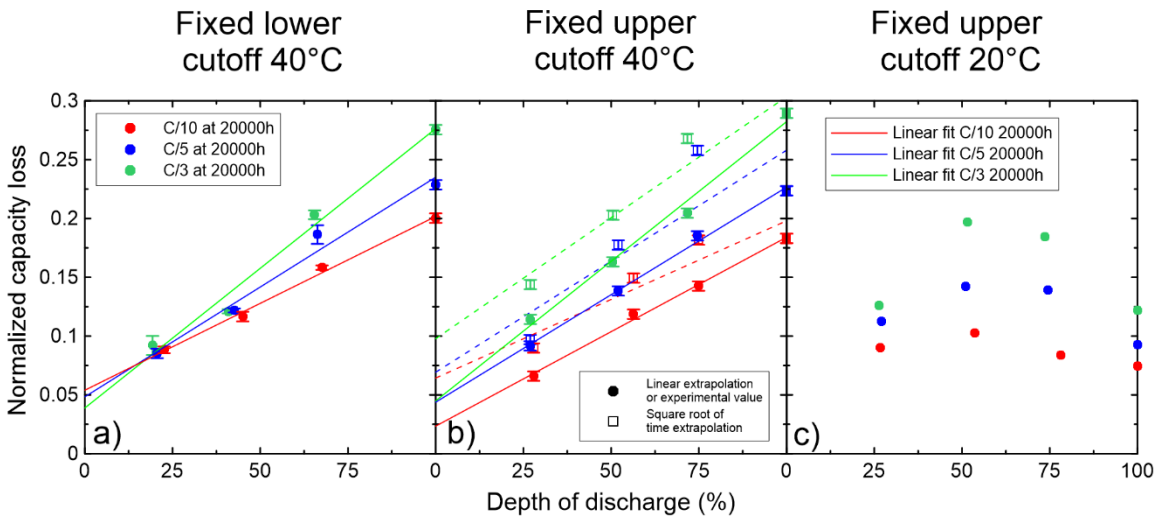

Figure 5.5: Normalized capacity loss during long-term cycling between 0 h and 20000 h of a) LC cells that cycled at 40°C, b) UC cells that cycled at 40°C and of c) UC cells that cycled at 20°C. Checkup cycles are used here to calculate capacity loss. Since UC cells are missing their initial checkup cycles, linear extrapolation (solid circles and solid lines), or square root model extrapolation (open square points and dashed lines) to 0 h was used to estimate the capacity loss of the UC cells that cycled at 40°C and a combination with new data was done for the UC cells that cycled at 20°C (see Figure A.17 for an example for C/10). Since no data were missing for LC cells, no extrapolation was needed for the data in a). Red, blue, and green data are used to show the results from different C-rates (C/10, C/5, and C/3, respectively).

Figure 5.6 shows the cycles and equivalent full cycles to 90% of the initial capacity for different SOC ranges and C-rates. The results in Figure 5.6 a) were obtained by fitting the capacity vs cycle number curves of the cells to a $Q_0(1 - \alpha\sqrt{n})$ behaviour, where Q_0 and α are fitting constants and n is the cycle number. Figures A.19 to A.24 show these fits, as well as the capacity versus cycle number data for 100% DOD cells. The results in Figure 5.6 b) were obtained by the discrete integration of the capacity versus cycle number curve (including the checkup and main cycles) and by dividing the result by the initial 100% DOD capacity (~220 mAh). For example, the 25% DOD LC cells cycling at C/10 achieved 3906 cycles to 90% initial capacity, which corresponds to 874 equivalent full cycles, while

the 100% DOD LC cells cycling at C/10 achieved 270 cycles. These values were very similar for UC cells at C/10. However, 25% DOD C/3 LC cells achieved 13372 cycles to 90%, which corresponds to 2611 equivalent full cycles while 25% DOD C/3 UC cells achieved 5917 cycles to 90%, which corresponds to 1542 equivalent full cycles. As expected, the cells that cycle at a low DOD value perform better. Figure A.25 shows that the difference between UC cells and LC cells in Figure 5.6 can be explained by impedance effects. Similar work as in Figure 5.6 has been done in the past.[126–129]

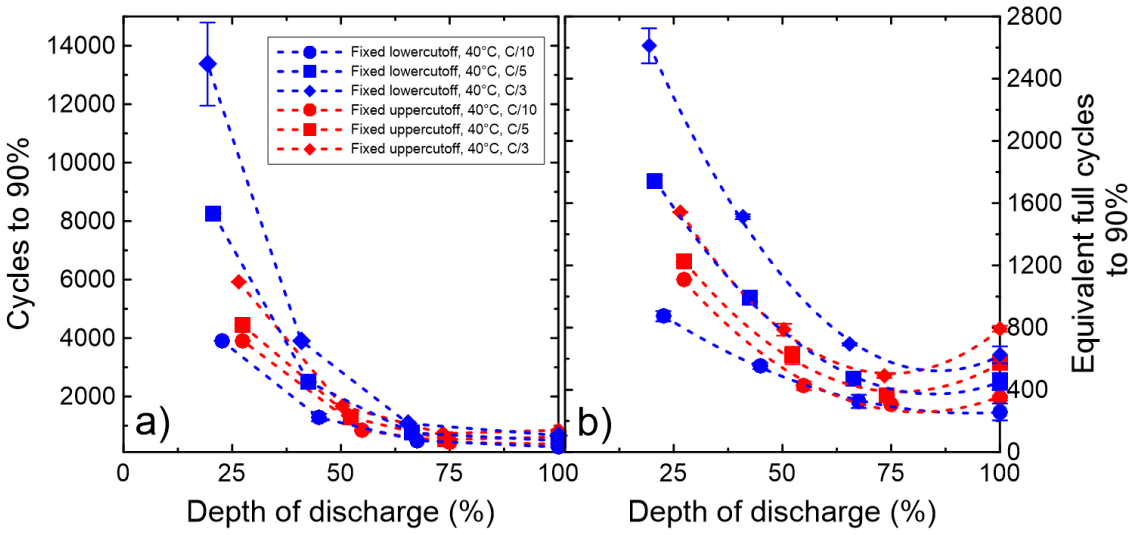

Figure 5.6: a) Number of cycles before the capacity reaches 90% of the initial capacity and b) number of equivalent full cycles before the capacity reaches 90% of the initial capacity. Blue data correspond to LC cells that cycled at 40°C, while red data correspond to UC cells that cycled at 40°C. Circles, squares or diamonds are used to show the results from different C-rates (C/10, C/5, and C/3, respectively).

5.3 ANALYSIS OF LONG-TERM CYCLING DATA

Figure 5.7 show the results of fitting ΔV vs. cycling time from the checkup cycles, for the UC and LC cells that cycled at 40°C, with a linear model of the form $\Delta V(t) = Ct + D$ (see Figures A.18 and A.26). The parameter C is plotted versus DOD and different colors are used to distinguish data for different C-rates. The results for parameter D, which are the

same for all cells, are shown in the right top corner of Figures 5.7 a) and 5.7 b). A quadratic fit matches the variation of C versus DOD quite well. Furthermore, while experimental noise is present, the value of C also seems to follow a trend versus C-rate. Since power fade depends on ΔV, understanding these trends is important to better predict the long-term performance of lithium-ion batteries. The data in Figure 5.7 can be found in Tables A.12 to A.14, so that it can be compared easily to other data, like pouch cell thickness shown later. The main cycle ΔV(t) values have also been fitted and the results can be seen in Figures A.27 to A.30.

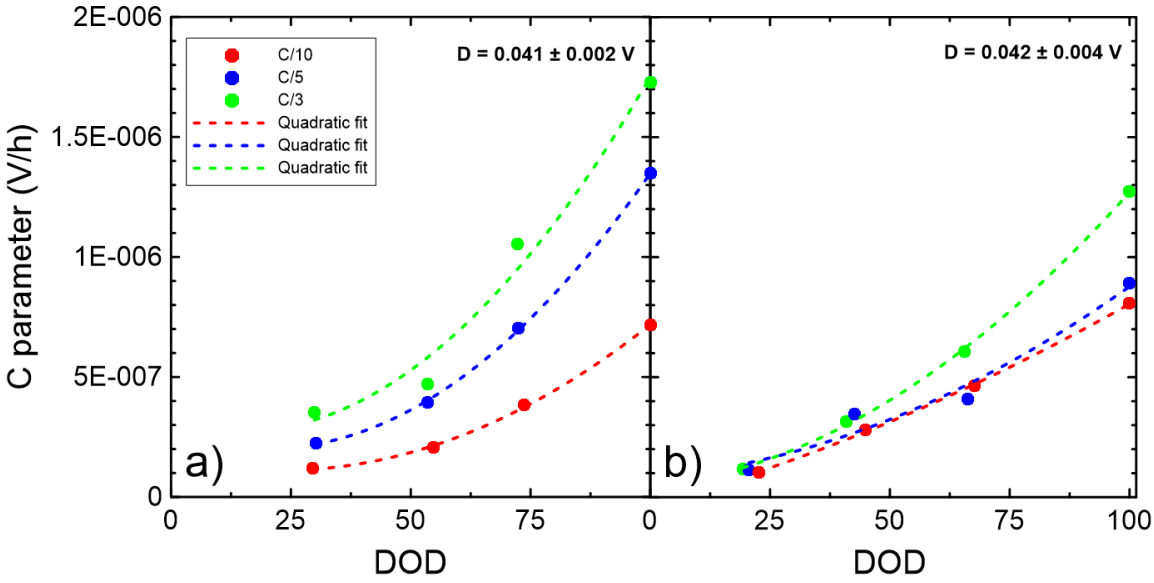

Figure 5.7: Linear fit results for C using the formula $\Delta V(t) = Ct + D$ for the a) UC cells (subfigures 5.3 c), 5.3 f), 5.3 i)) and b) LC cells (subfigures 5.2 c), 5.2 f) and 5.2 i)) at 40°C. The fits were applied to the ΔV values for the checkup cycles only.

Figures 5.8 and 5.9 show example results for automatic dV/dQ vs. Q analysis of two UC cells (25% and 100% DOD C/10 UC cells) at various cycle numbers. Figures 5.8 and 5.9 show a "heat map" of -log χ^2 for different possible positive electrode active mass m_p and relative slippage $\Delta = \delta_n - Q_p$, (See Figure 2.19). Δ is the difference in capacity between the fully lithiated positive and the fully delithiated negative electrodes (See Figure 2.19) and is used in the calculation of Li inventory loss, Q_{SEI} (see Equation 10). The χ^2 values represent the least-squares error between the experimental dV/dQ vs Q graph of a cell at a specific cycle number and a dV/dQ calculation using specific m_p and Δ values. The map therefore corresponds to a 2D dV/dQ vs Q scan where the negative electrode mass m_n and the negative electrode slippage[42] were fixed to values predetermined from a single 4D dV/dQ scan. In these specific cases, the negative electrode mass m_n was fixed to 1.025 g and the negative electrode slippage was fixed to -1 mAh. In Figures 5.8 and 5.9, the center

of the dark red ellipse (i.e. $-\log(\chi^2) = 5$) corresponds to the most likely values of Δ and m_p for that cell at that specific cycle number or time, while the blue region (i.e. $-\log(\chi^2) < 2$) corresponds to less likely values for that cell at that specific cycle number or time. Figure 5.8 shows that the 100% DOD C/10 UC cell lost ~0.2 g of its positive active mass after ~22000h of cycling, which corresponds to approximately 15% of the total initial positive active mass, while Δ increased by approximately 10 mAh. Figure 5.9 shows that the 25% DOD C/10 UC cell lost ~0.05 g of its positive active mass after ~16000h of cycling, while Δ increased by approximately 10 mAh. Most importantly, these figures can help deduce the error that is associated with this computational analysis.

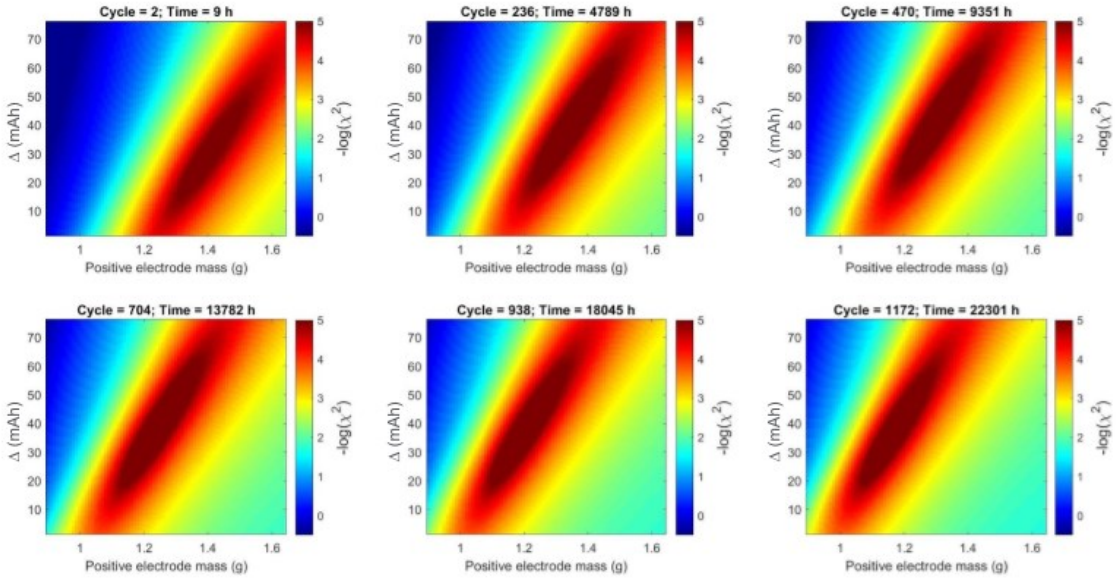

Figure 5.8: 2D dV/dQ vs Q heat maps of a 100% DOD C/10 UC cell cycled at 40°C for six different times. Multiple $-\log \chi^2$ heat maps are shown as a function of positive electrode active mass m_p and Δ. The negative electrode active mass is kept constant as a function of time.

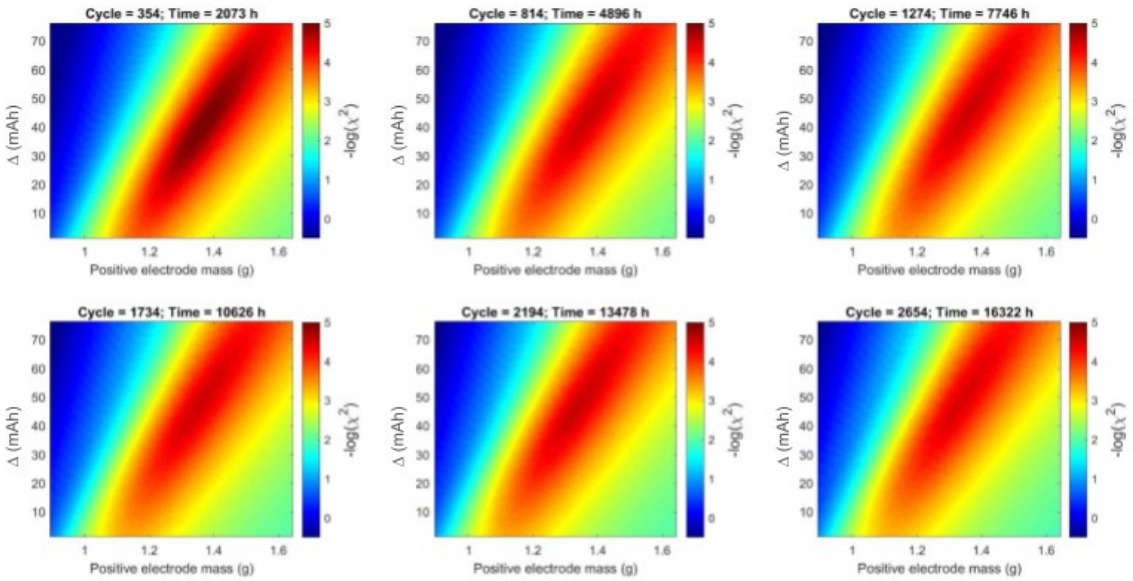

Figure 5.9: 2D dV/dQ vs Q heat maps of a 25% DOD C/10 UC cell cycled at 40°C for six different times. Multiple -log χ^2 heat maps are shown as a function of positive electrode mass m_p and Δ. The negative electrode active mass is kept constant as a function of time.

Figure 5.10 shows the result of a 4D dV/dQ vs Q scan, using the automatic dV/dQ analysis program, of UC and LC cells that cycled for ~20000h at 40°C. The positive electrode active mass and the lithium inventory loss Q_{SEI} are plotted as a function of time. Figure 5.10 shows that UC cells have a bigger positive electrode active mass loss Δm_p than LC cells at low DOD. This suggest that positive active mass loss occurs more predominantly at high voltage. At high DOD, UC and LC cells have more similar positive active mass losses. Figure 5.10 shows that the lithium inventory losses are very similar between UC and LC cells for all SOC ranges. This suggests that Q_{SEI} is independent of the average voltage of the SOC ranges, at least for the voltage ranges of the current study. One can find the results for the negative active mass m_n and slippage Δ as a function of time in Figure A.11 as well as some of the dV/dQ fits in Figures A.31 to A.36.

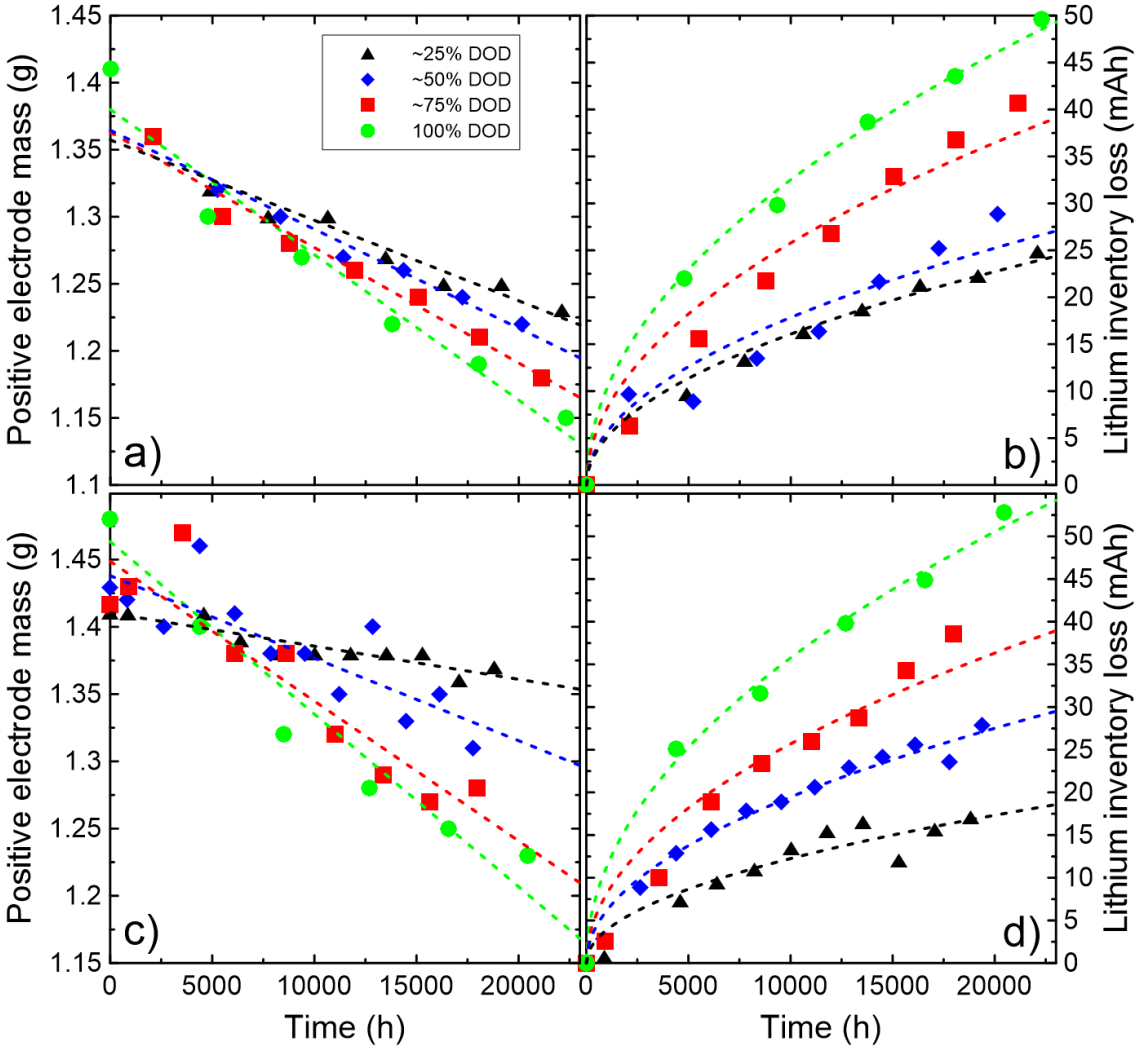

Figure 5.10: Automatic dV/dQ vs Q scan results for a), b) UC and c), d) LC cells at 40°C and C/10 as a function of cycling time. Subfigures a) and c) show positive electrode active mass results and subfigures b) and d) show lithium inventory loss results. An automatic 4D dV/dQ vs Q scan was used to get these results. Linear fits (dashed lines in panels a) and c)) and square root time fits (dashed lines in panels b) and d)) were applied to the positive electrode active mass and lithium inventory loss data, respectively, to show likely trends.

Figure 5.11 shows the positive and negative electrode V(Q) curves vs Li metal obtained from manual dV/dQ analysis on a UHPC charger data before and after long-term cycling at 40°C and C/10 for 75-100% SOC range, 50-100% SOC range, 25-100% SOC range and 0-100% SOC ranges of UC cells. Figure 5.11 shows that Q_{SEI} increases as a function of

DOD, but the cells are always anode limited even as Δm_p increases with DOD. We also see an increase in positive active mass loss as the DOD value increases.

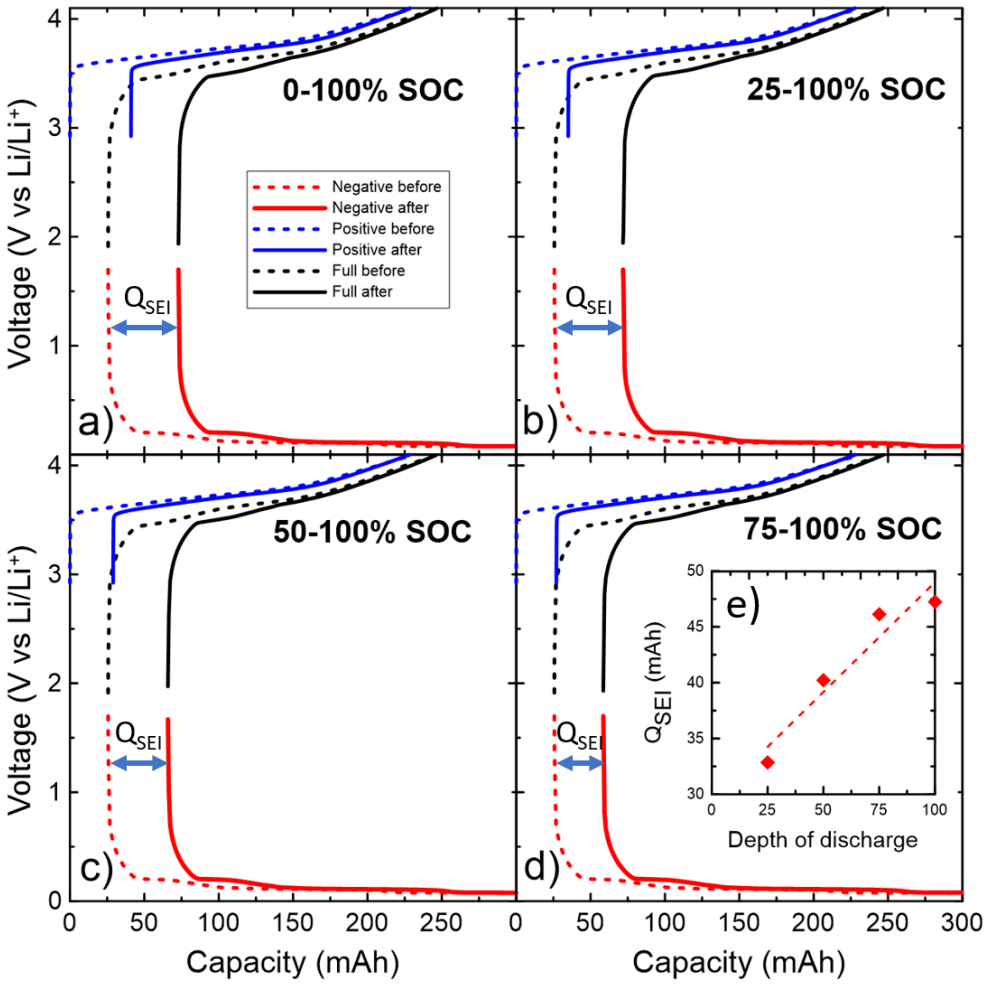

Figure 5.11: Negative and positive electrode V(Q) curves vs Li/Li^+ before and after long-term cycling (~20000h) at C/10 and 40°C of a) 0-100% SOC range, b) 25-100% SOC range, c) 50-100% SOC range and d) 75-100% SOC range for UC cells. Subfigure e) shows the lithium inventory loss versus depth of discharche taken from the data in a), b), c) and d) as well as a linear fit.

Figure 5.12 shows that Δm_p increases with SOC range for both UC and LC cells at 40°C but the positive active mass loss is much smaller at 20°C for all SOC ranges and C-rates. Also, Δm_p increase with C-rate at 100% DOD at 40°C. Again, the positive electrode active

mass loss is higher for UC cells tested at 40ºC. Similarly, Q_{SEI} increases with SOC range and C-rate for cells cycling at 40°C, while the increases in Q_{SEI} are much smaller at 20°C as the SOC range increases. The results shown in Figure 5.12, as well as additional results such as Δ and negative electrode active mass, m_n, can be found in Tables A.9 to A.14. To better understand the comparison between the lithium inventory loss data from Figures 5.12 b) and 5.12 d), the data from Figures 5.10 b) and 5.10 d) and the data in Figures 5.2 to 5.4, Figures A.37 to A.38 were made. Note that the errors for UC cells are mostly due to capacity versus time extrapolation errors. Additional errors can be caused by uncertainties in the initial positive mass m_{p0} and initial slippage Δ_0 of each cell at t = 0 hour since we only know these values for some of the cells.

For the result in Figure 5.12, the initial slippage Δ_0 and initial positive mass m_{p0} were fixed to 25 mAh and 1.42 g for all cells as an approximation. Note that the initial slippage of 25 mAh was found to be the smallest initial slippage in Figure A.11 and Figure 5.10 was used to approximate the initial positive mass. If we compare the positive active mass loss and the ΔV related parameter C, we see a linear correlation (see Figure A.39). This suggests that positive active mass loss and related electrode damage is a major cause of ΔV growth in these cells. For the interested reader, state of charge maps of our cells can be found in the Appendix (see Figures A.40 and A.41).[130]

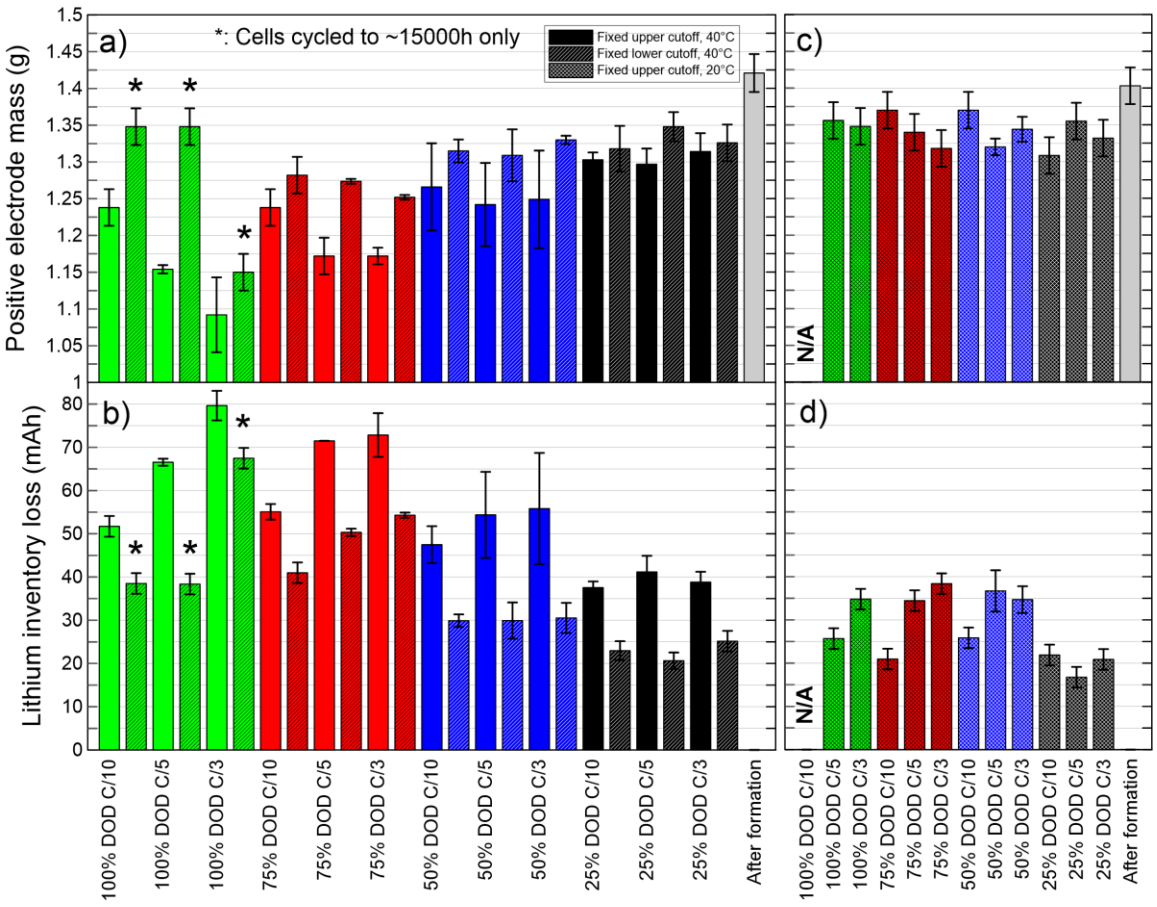

Figure 5.12: Manual dV/dQ analysis results of UC and LC cells after ~20000h of cycling, except for the indicated cells (*) which cycled only for ~15000h. Subfigures a), c) show the positive electrode mass and subfigures b), d) show the lithium inventory loss. 5.12 a) and 5.12 b) show results for cells that cycled at 40°C, while subfigures c), d) show results for cells that cycled at 20°C. The initial slippage and the initial positive electrode were both fixed at 25 mAh and 1.42 g for all cells.

Figure 5.13 shows the parameter A ($h^{-1/2}$) as a function of DOD for cells cycling at C/10 in blue, C/5 in red and C/3 in green obtained by fitting the capacity versus time curves for the checkup cycles of the cells with different models. Equation 1 was used for cells tested at C/10 and 40ºC; Equation 3, with no Q_{CV} term was used for cells tested at C/3 and C/5 at 40ºC; Equation 9, with no impedance or Q_{CV} term, was used for cells tested at 20ºC at C/10 and Equation 9 with no Q_{CV} term was used for cells tested at 20ºC at C/3 or C/5. Figures A.17 and A.43-A.44 show the quality of some of these fits.

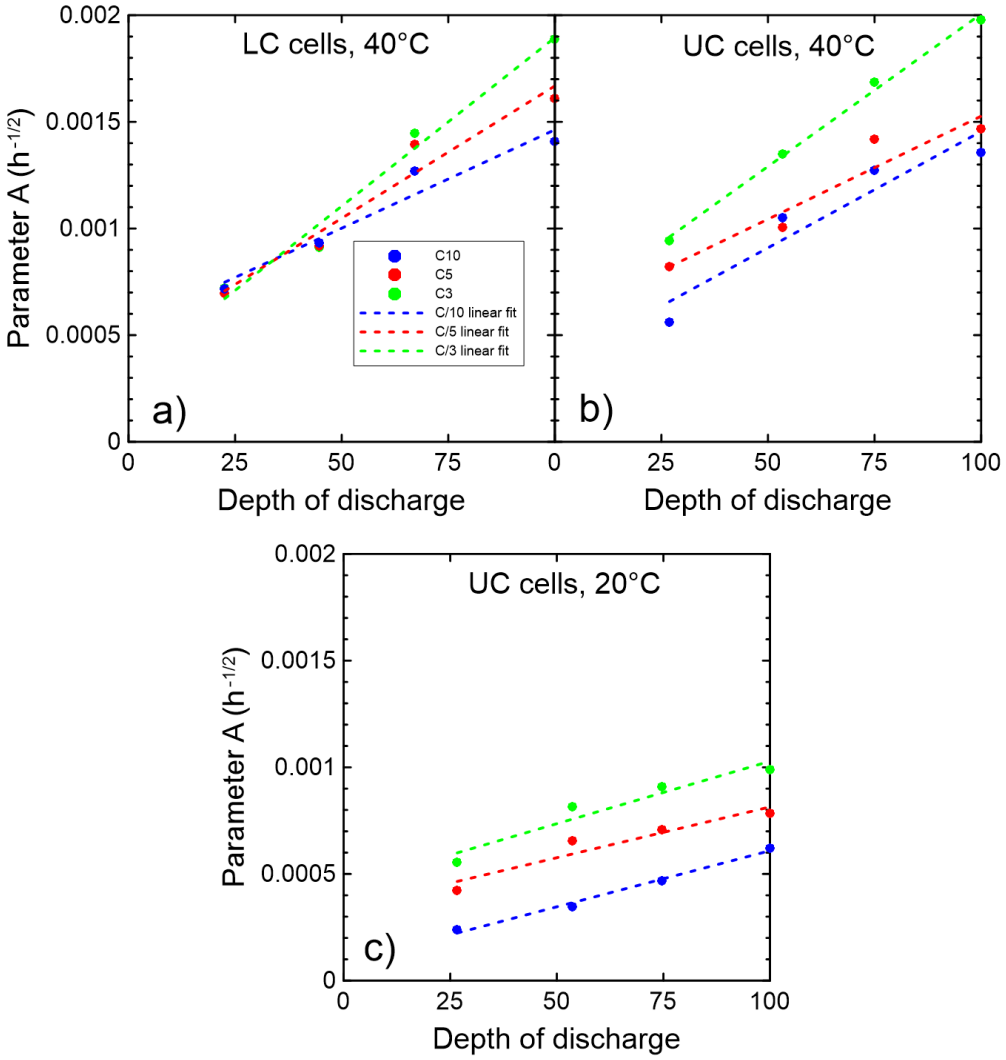

Figure 5.13: Results of fitting a) LC cells at 40°C, b) UC cells at 40°C and c) UC cells at 20°C using Equation 1, Equation 3, or Equation 9 to obtain parameter A. Equation 1 was used in a) and b) at C/10. The Q_{cv} term was neglected in every case. Equation 3 was used in subfigures a) and b) at C/5 and C/3, Equation 9 without the impedance term was used at C/10 in c) and Equation 9 with the impedance term was used in c) at C/5 and C/3. $\left.\frac{dQ}{dV}\right|_L + \left.\frac{dQ}{dV}\right|_U = 225$ mAh/V was used for all C/5 and C/3 cells. Note that the impedance term was negligible at C/10. C/10 data is in blue, C/5 data is in red and C/3 data is in green.

The A parameters of the UC and LC cells are virtually the same at 40°C and increase as the SOC range increases. At 20°C the parameter A is much smaller than at 40°C, as

expected, and increases as the SOC range increases. These results indicate that the rate of SEI thickening, and inventory loss increases with temperature, C-rate and SOC range. (See Figure A.45 for the average voltage vs. time of the UC cells that cycled at 20°C).

Figure 5.14 shows that it is possible to explain and predict the discharge capacity versus time data by fitting the first 2000, 5000 or 6000 hours with a pure lithium inventory loss model (i.e. Equation 1) or by combining the lithium inventory loss term with an impedance term (i.e. Equation 3) and then projecting the fit to the full 20000 hours of data. Since ΔV growth is small at low DOD and C-rate, one can predict the data for the 100% DOD and ~25% DOD cells at C/10 without any impedance term and very little data, as seen in Figures 5.14 a) and 5.14 b). Figures 5.14 c) and 5.14 d) show that adding an impedance term can explain most of the difference between the square root of time model (red dashed lines) and the experimental data (blue lines) for cells tested at C/5 and C/3. Table 5.1 show the parameters used in those fits. Note that the Q_{CV} term in Equation 3 was calculated from the linear fit in Figure A.15 for Figures 5.14 c) and 5.14 d) and was neglected for Figures 5.14 a) and 5.14 b). $\left.\frac{dQ}{dV}\right|_L + \left.\frac{dQ}{dV}\right|_U = 225$ mAh/V was used for Figures 5.14 c) and 5.14 d). This value can be determined from Figure 2.15 c).

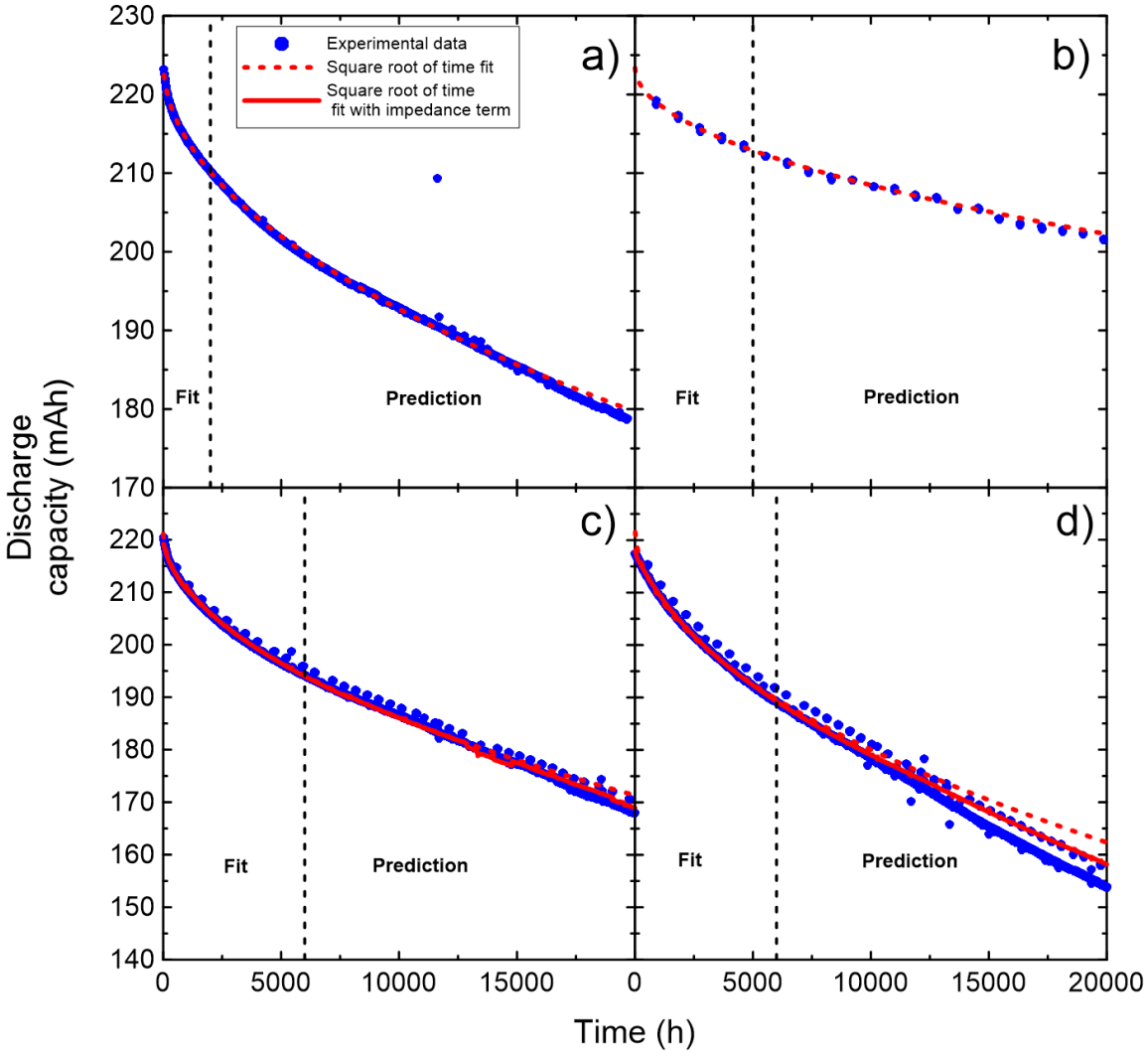

Figure 5.14: Fitting results for the capacity versus time of LC cells that cycled at 40°C. Cells with the following cycling conditions have been fitted: a) 0-100% SOC C/10, b) 0-25% SOC C/10, c) 0-100% SOC C/5 and d) 0-100% SOC C/3. Results for the square root of time model (red dashed lines) and square root of time models that include an impedance term (red lines) are included and compared to experimental data (blue line). A black vertical dashed line is used to indicate the maximum time used in the fitting of the model to experiment. The model calculation was then projected to times greater than that of the dashed vertical line.

Table 5.1: Results from the fitting of capacity versus time for LC cells at 40ºC in Figure 5.14 using Equations 1 and 3. (NI) means no impedance term was used in the fit (Equation 1) and (I) means that an impedance term was used in the fit (Equation 3).

Cell protocol and fitting type	Q_0 (mAh)	A ($h^{-1/2}$)
100% DOD C/10 (NI)	224.2	0.001404
25% DOD C/10 (NI)	223.5	0.0006718
100% DOD C/5 (NI)	221.8	0.001610
100% DOD C/5 (I)	220.0	0.001659
100% DOD C/3 (NI)	222.8	0.001918
100% DOD C/3 (I)	215.7	0.002056

Figure 5.15 shows the value of the slope of the normalized discharge capacity vs cycle number as a function of DOD at cycle 500 for LC cells that cycled at 40°C, UC cells that cycled at 40°C and UC cells that cycled at 20°C. All the data shown correspond to cells that cycled at C/10. Only the checkup cycles have been included in this analysis. Both the experimental data and the predicted theoretical curve are shown (the equation of the theoretical curve is shown in the figure, where Q_N is the unitless normalized capacity). The proof for the equation of the theoretical curve can be found in the ‘’Theoretical explanation and proofs’’ section of the Appendix. Since the derivative of the normalized capacity with respect to cycle number at time t_1 is quadratic with DOD (from Figure 5.13, parameter A is linear with DOD, so A times DOD is quadratic), our research does not contradict the Deshpande-Bernardi model.[107] In fact, we show in the ‘’Theoretical explanation and proofs’’ section of the Appendix that both our model and the Deshpande-Bernardi model

are equivalent locally, but that our model is more general (we find that a constant in their model is dependent on time). However, more research is needed to confirm that SEI cracking occurs in our cells.

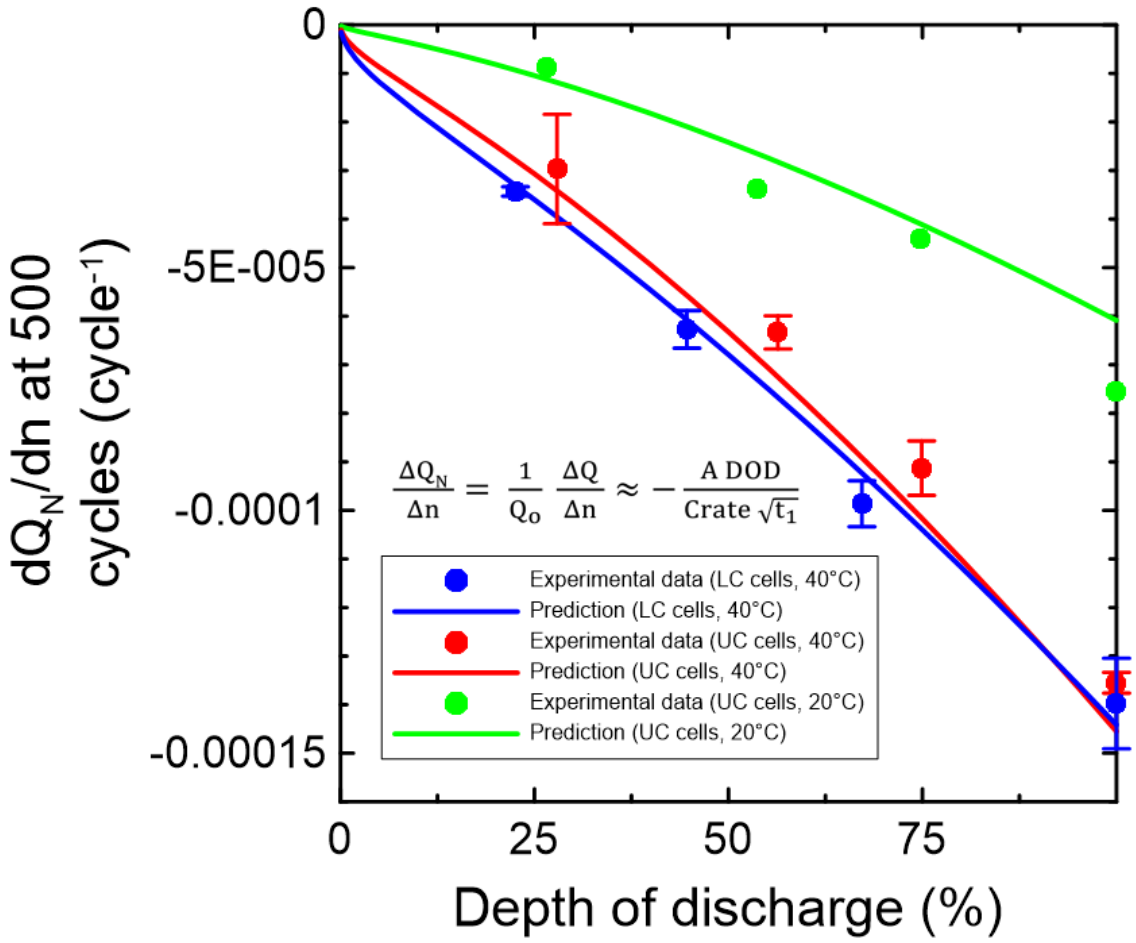

Figure 5.15: Derivative of normalized capacity with respect to cycle number at cycle number 500 as a function of the depth of discharge. The experimental data of LC at 40°C (in blue), UC cells at 40°C (in red) and UC cells at 20°C (in green) that cycled at C/10 is compared to the theoretical prediction (line of the same colors).

5.4 POST-CYCLING ANALYSIS

Figure 5.16 a) shows that the cell volume change, measured by the Archimedes method, during cycling is closely related to the thickness change, measured with the linear gage, of

the jelly roll. In fact, the experimental data closely follow the predicted volume change (black line) which was calculated by multiplying the thickness change by the area of the jelly roll (2.0 cm x 3.0 cm). Most cells showed very little, if any, gas in the gas bags which is consistent with all volume change being due to electrode stack thickness growth. Cells that cycled at 20°C seem to have a larger slope in 5.16 a) which may be due to DMC being used instead of EMC in the electrolyte of the cells tested at 20°C, which may produce more gas during cycling. Figure 5.16 b) shows that thickness increase is strongly correlated with the normalized capacity loss during long-term cycling for all types of cells.

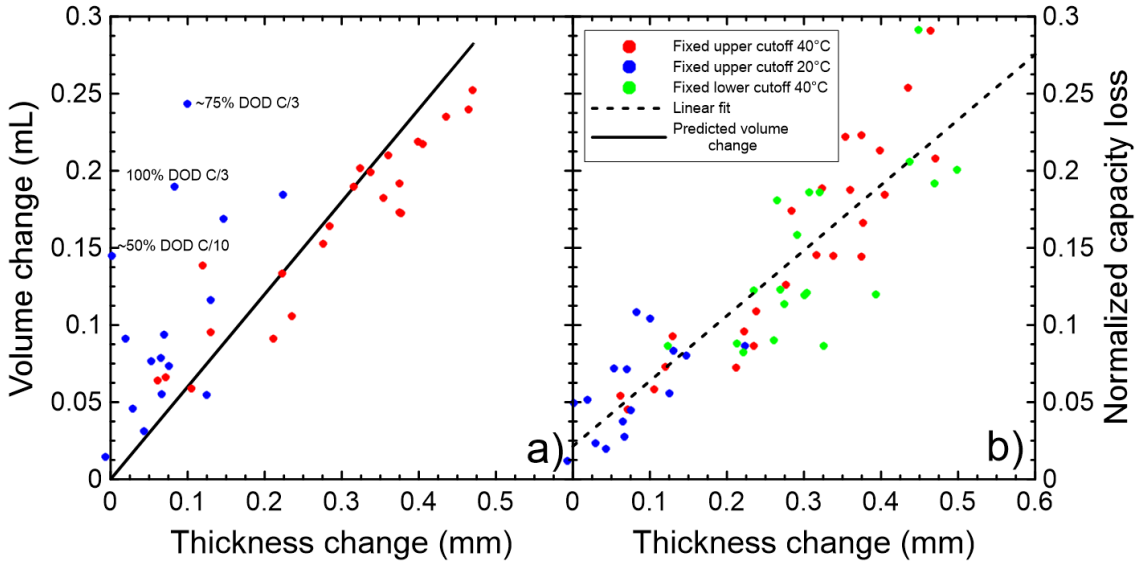

Figure 5.16: a) Volume change from Archimedes' principle and b) normalized capacity loss after ~20000h of cycling versus thickness change. Red, blue, and green dots indicate UC cells cycling at 40°C, UC cells cycling at 20°C and LC cells cycling at 40°C, respectively.

Figure 5.17 a) shows that the positive electrode active mass loss, from dV/dQ vs. Q analysis, and the thickness increase are approximately quadratically related to each other. This strongly points toward positive electrode thickness increase, which will be confirmed

later in this work by X-ray computed tomography (CT). Negative electrode mass loss also seems to be correlated with thickness increase, however the active mass loss at the negative electrode is five times less than at the positive electrode. We will also confirm, using CT scans, that the thickness of the negative electrode increases during cycling, but much less than the positive electrode. Since the cells are balanced to 4.5 V and the maximum voltage of these cells is 4.1 V, the negative electrode has a large excess of graphite and the negative electrode mass loss is too small to affect capacity loss. Since these cells are always anode limited, this can only make sense if the negative mass loss occurs in the fully contracted (delithiated) state. Then the lithium coming from the positive electrode during charge will simply find electrically connected graphite particles to intercalate within. Figures 5.16 and 5.17 should convince researchers that measuring cell thickness before and after cycling is important. The raw volume, capacity loss and thickness data can be found in Tables A.12 to A.14.

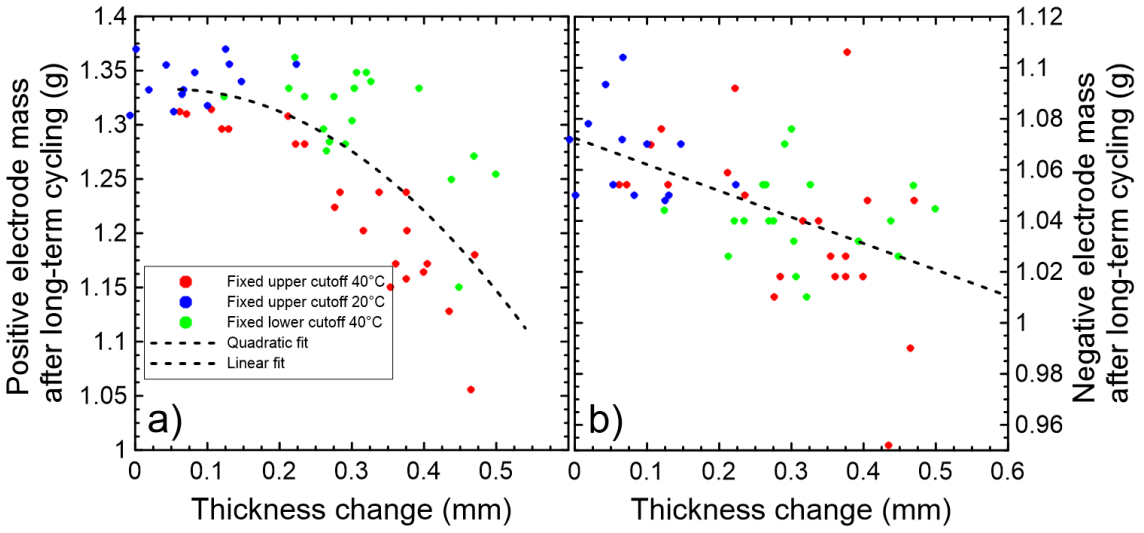

Figure 5.17: a) Positive and b) negative electrode active mass after ~20000h of cycling versus thickness change of the jelly roll for all UC and LC cells. Red, blue, and green dots indicate UC cells cycling at 40°C, UC cells cycling at 20°C and LC cells cycling at 40°C, respectively. Linear and quadratic fits are also included.

To check if the electrolyte in our cells changed after ~20000 hours of cycling, we used Li-ion differential thermal analysis (DTA).[81] Figures 5.18 to 5.20 show results from DTA on UC and LC cells. The inverse peak at the highest temperature occurs at the liquidus point of the electrolyte composition-temperature phase diagram.[81,131,132] The temperature of liquidus feature is very sensitive to the salt concentration and solvent ratios. Since the temperature of the liquidus feature does not vary for cells with the same electrolyte, it can be concluded that changes to the electrolyte are minimal as a function of DOD and C-rate. In addition, the DTA traces in Figures 5.18 and 5.19 match quite well to that of a fresh cell after formation, suggesting minimal changes to the electrolyte. There are, however, some slight changes to the DTA signals as the DOD and C-rate both increases. For example, Figures 5.18 and 5.19, show that a double peak at approximately -70°C is present at high C-rate (C/3 and C/5) and high SOC range (0-75%, 25-100% and 0-100%), which is not seen at low C-rate and lower SOC range. This change can be caused by minimal changes in salt and/or solvent concentration. Figures A.46 to A.48 show an overlap of the DTA spectra of ~25% DOD C/10, 100% DOD C/3 and the fresh cells after formation cells (Figures A.46 and A.47 only) to better see the differences between them.

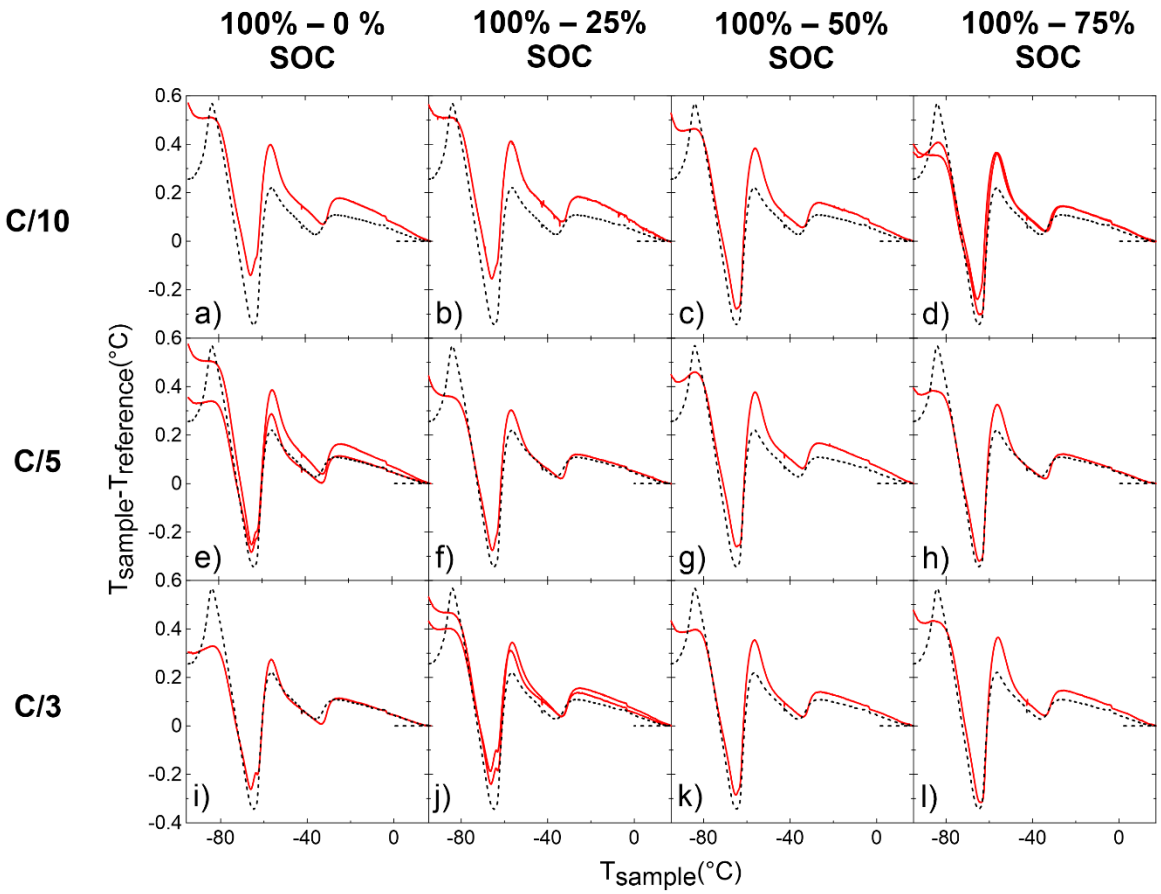

Figure 5.18: Differential thermal analysis (DTA) versus temperature for UC cells that cycled at 40°C. Columns represent cells that cycled over different SOC ranges, while rows represent cells that cycled at different C-rates. When available the result from a brother cell is shown. The electrolyte originally added to the cells was 1.2M $LiPF_6$ EC:EMC 3:7 with VC211. The red lines show the results after long-term cycling and the black dashed lines show the data of a fresh cell after formation with 1.2M $LiPF_6$ EC:EMC 3:7 with 2% VC + 1% DTD + 1% MMDS as the electrolyte. A cell filled with methyl acetate, which has a melting point of -98 °C, was used as the reference temperature here. Note that the reference temperature is increasing linearly as a function of time, as show in Figure 2.2 of M. Bauer's thesis.[133] DTA data courtesy of Michael Bauer.

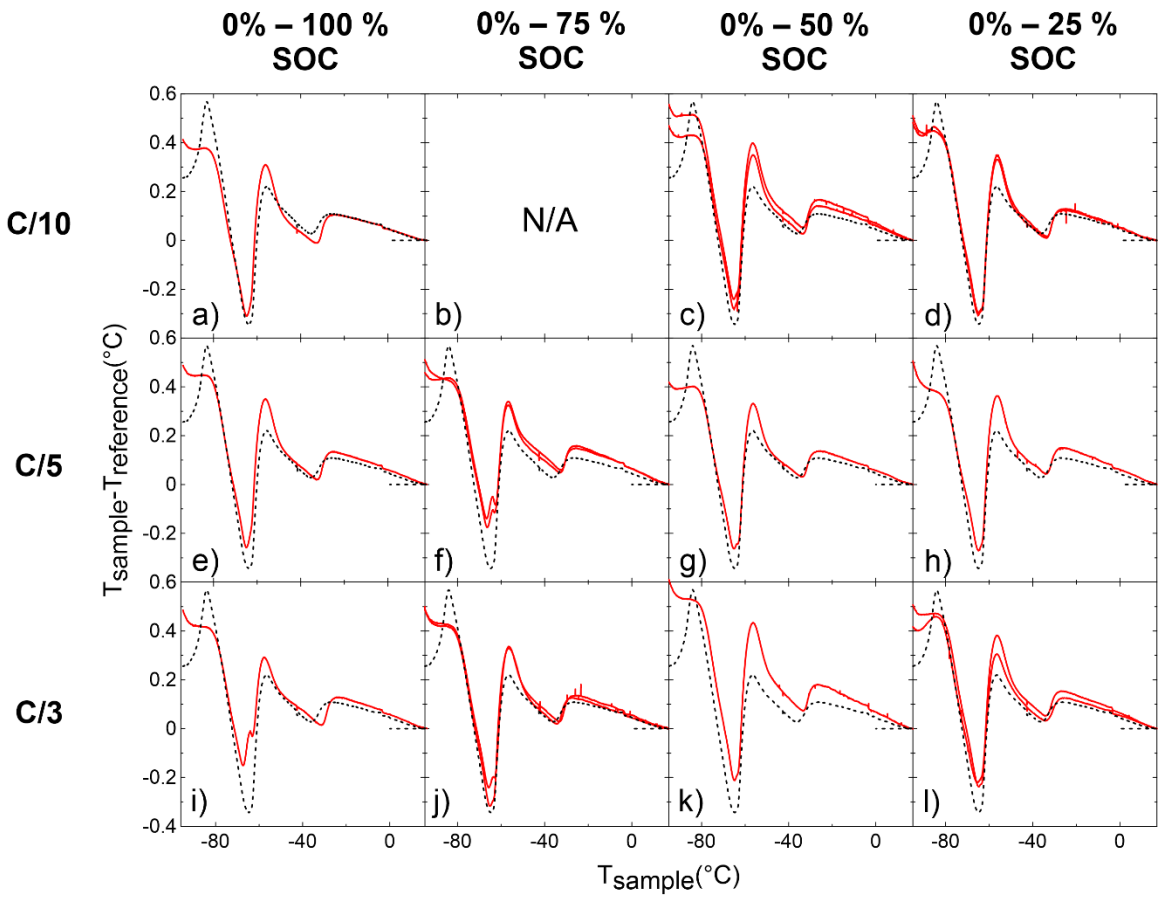

Figure 5.19: Differential thermal analysis (DTA) versus temperature for LC cells that cycled at 40°C. Columns represent cells that cycled over different SOC ranges, while rows represent cells that cycled at different C-rates. When available the result from a duplicate cell is shown. The electrolyte originally added to the cell was 1.2M $LiPF_6$ EC:EMC 3:7 with VC211. The red lines show the results after long-term cycling and the black dashed lines show the data of a fresh cell after formation with 1.2M $LiPF_6$ EC:EMC 3:7 with 2% VC + 1% DTD + 1% MMDS as the electrolyte. A cell filled with methyl acetate, which has a melting point of -98 °C, was used as the reference temperature here. Note that the reference temperature is increasing linearly as a function of time, as show in Figure 2.2 of M. Bauer's thesis.[133] DTA data courtesy of Michael Bauer.

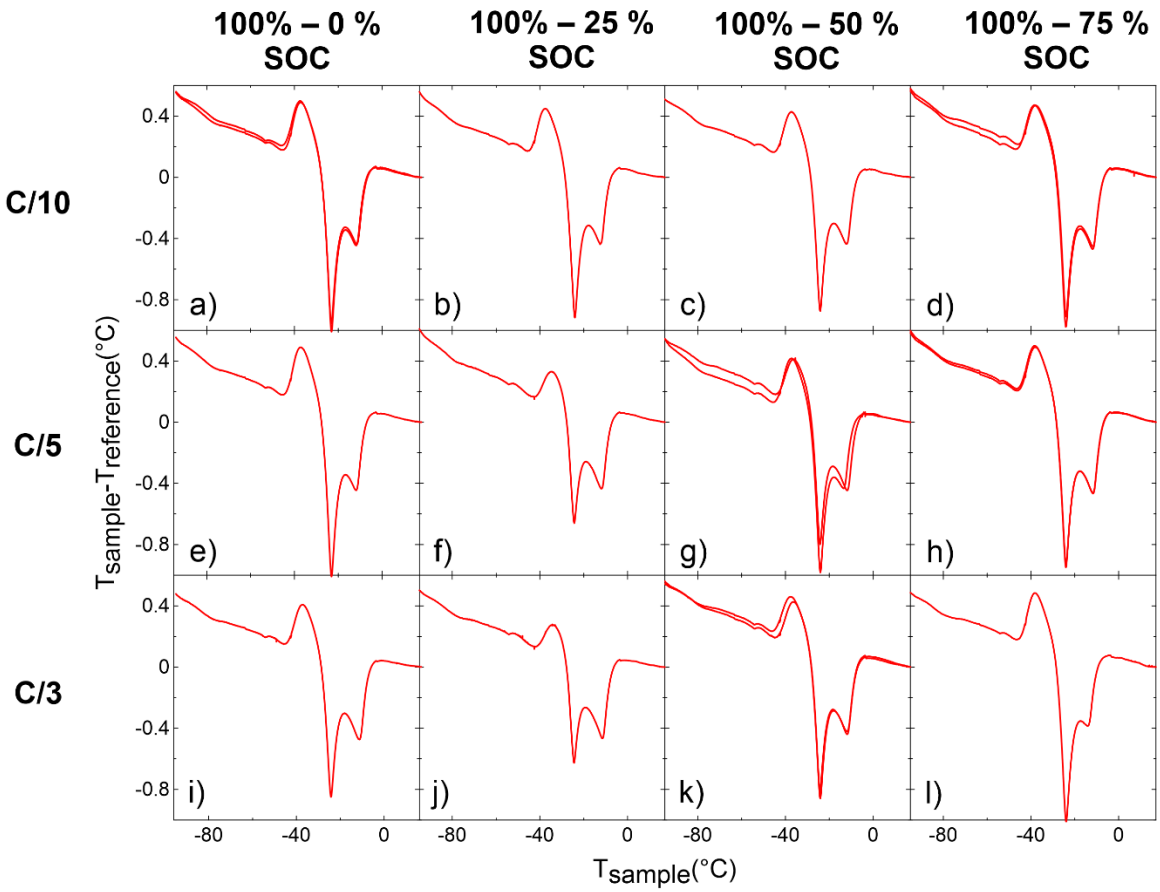

Figure 5.20: Differential thermal analysis (DTA) versus temperature for UC cells that cycled at 20°C. Columns represent cells that cycled at different SOC ranges while rows represent cells that cycled at different C-rates. When available the results from duplicate cells are shown. The electrolyte originally added to the cell was 1.2M LiPF6 EC:DMC 3:7 with VC211. A cell filled with methyl acetate, which has a melting point of -98 °C, was used as the reference temperature here. Note that the reference temperature is increasing linearly as a function of time, as show in Figure 2.2 of M. Bauer's thesis.[133] DTA data courtesy of Michael Bauer.

Figures 5.21 to 5.23 summarize data reported above for the cells tested here and also provide an ultrasonic image of most of the cells tested. Figures 5.21 to 5.23 show that cells with large thickness increase also show the poor transmission to ultrasonic waves. Since volume change and capacity loss correlate with thickness change, they also correlate with poor transmission. We also see that cells with large C-rate and large SOC range during cycling have worse transmission. While it is harder to see any correlation due to missing

data in Figure 5.23, it is thought that transmission is better at 100% DOD C/3 for cells that cycled at 20°C than at 40°C since the thickness increase is much lower. The curious reader can have a look at the impact of cell voltage on ultrasonic transmission in Figures A.49 and A.50.

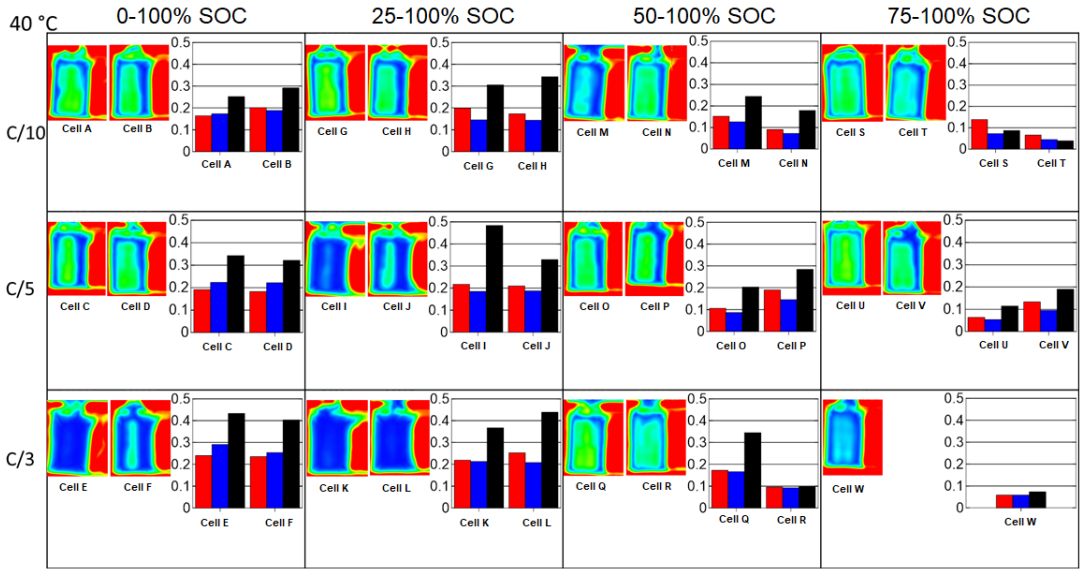

Figure 5.21: Ultrasonic transmission results for UC cells that cycled at 40°C for 20000 h. Columns represent cells that cycled over different SOC ranges, while rows represent cells that cycled at different C-rates. The bar graphs show, in order, the true volume change in mL from Archimedes principle (red), the normalized capacity loss (blue) and the change in thickness in mm (black). When available the results from duplicate cells are shown. In the Ultrasonic color maps, red represents no attenuation, green represents high transmission and blue represents low transmission. Ultrasonic transmission mapping data courtesy of Aidan Luscombe.

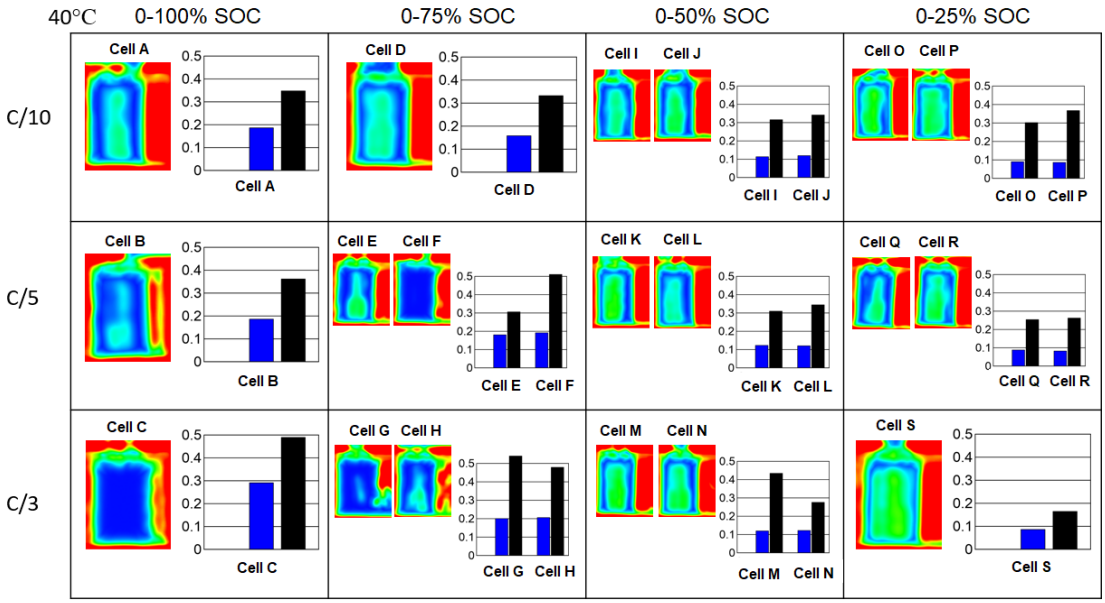

Figure 5.22: Ultrasonic transmission results for multiple LC cells that cycled at 40°C for 20000 h. Columns represent cells that cycled at different SOC ranges, while rows represent cells that cycled at different C-rates. The bar graphs show, in order, the normalized capacity loss (blue) and the change in thickness in mm (black). When available the results from duplicate cells are shown. In the Ultrasonic color maps, red represents no attenuation, green represents high transmission and blue represents low transmission. Ultrasonic transmission mapping data courtesy of Aidan Luscombe.

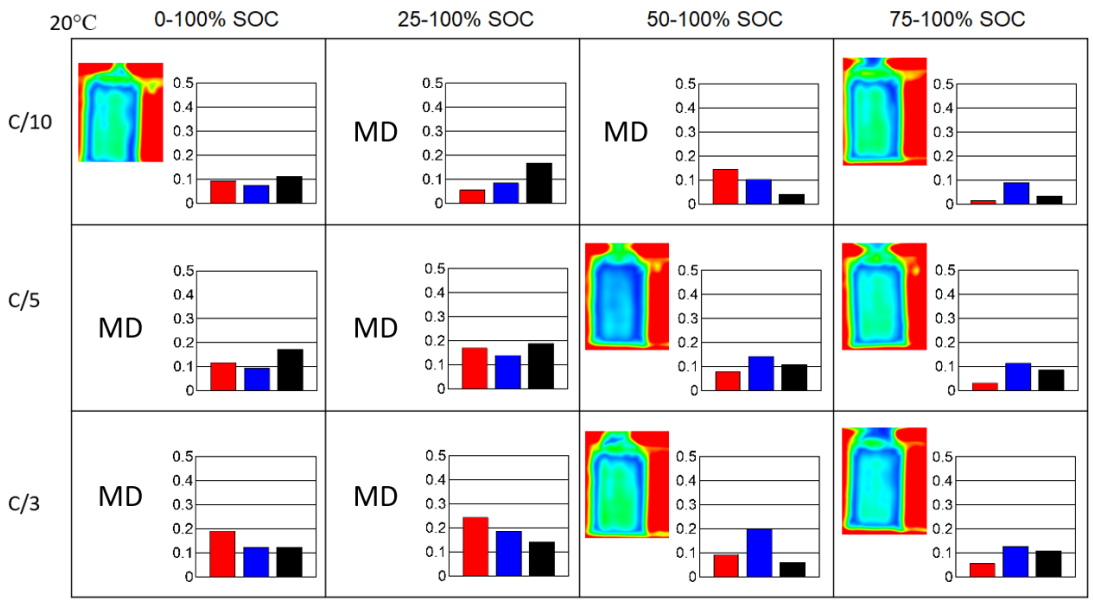

Figure 5.23: Ultrasonic transmission results for multiple UC cells that cycled at 20°C for 20000 h. Columns represent cells that cycled at different SOC ranges, while rows represent cells that cycled at different C-rates. The bar graphs show, in order, the true volume change in mL from Archimedes principle (red), the normalized capacity loss (blue) and the change in thickness in mm (black). In the Ultrasonic color maps, red represents no attenuation, green represents high transmission and blue represents low transmission. MD means Missing Data. Ultrasonic transmission mapping data courtesy of Aidan Luscombe.

The results in Figures 5.21 to 5.23 can be understood based on the work of Deng et al.[61] Cells that have a large thickness increase do not have enough electrolyte to fill the increased pore volume (as illustrated in Figure A.52). This “unwetting” leads to poor ultrasonic transmission. A careful examination of Figures 5.21 to 5.23 shows that cells which generally had a large thickness increase (length of black bar in the Figures) had poor ultrasonic transmission (Blue color).

Figure 5.24 and 5.25 show X-ray computed tomography scans of some of our cells after 20000 h of cycling (Figure 5.24 b) - e) and Figure 5.25 b) - d)) as compared to a fresh cell (Figure 5.24 a) and Figure 5.25 a)). One can have a second look at Figure 2.2 for a clear

description of the parts seen in Figures 5.24 and 5.25. Figure 5.24 shows the effect of increasing the depth of discharge and Figure 5.25 shows the effect of increasing the C-rate on the appearance of the electrodes and jelly roll. The legend of the figures describes each subfigure more in detail. The first thing that can be seen in these figures is the increase in positive electrode thickness during cycling and this increase in thickness is larger when the depth of discharge or C-rate are larger. As an example, let us compare the 75% DOD C/3 UC cell (Figure 5.24 d)) to the control cell (Figure 5.24 a)). In that case, the thickness of the positive electrode increases by 39%, while the thickness of the negative electrode increases by 10% in the flat region of the jelly roll. The increase in electrode thickness with cycling also appears to have filled in the "empty" region at the center of the jelly roll. The 75% DOD C/3 UC cell also had a large positive electrode active mass loss of 16 percent as shown in Table A.9 (assuming an initial positive active mass of 1.4 g). It is likely that the positive electrode active mass loss and positive electrode thickness expansion are related. Microcracking of the electrode particles will cause thickness increase and active mass loss. Also, notice how the thicknesses of the positive electrodes are larger in the flat (left) region of the jelly roll when compared to their thicknesses in the turn (right) region for cells that cycled at large DOD and C-rate. This effect is more easily seen, while difficult to see, in the center of the jelly roll. It is thought that this is caused by the tension that the flat region of the jelly roll exerts on the turn region as it increases in thickness. The ratio between these two thicknesses will be called the flat/turn ratio from now on.

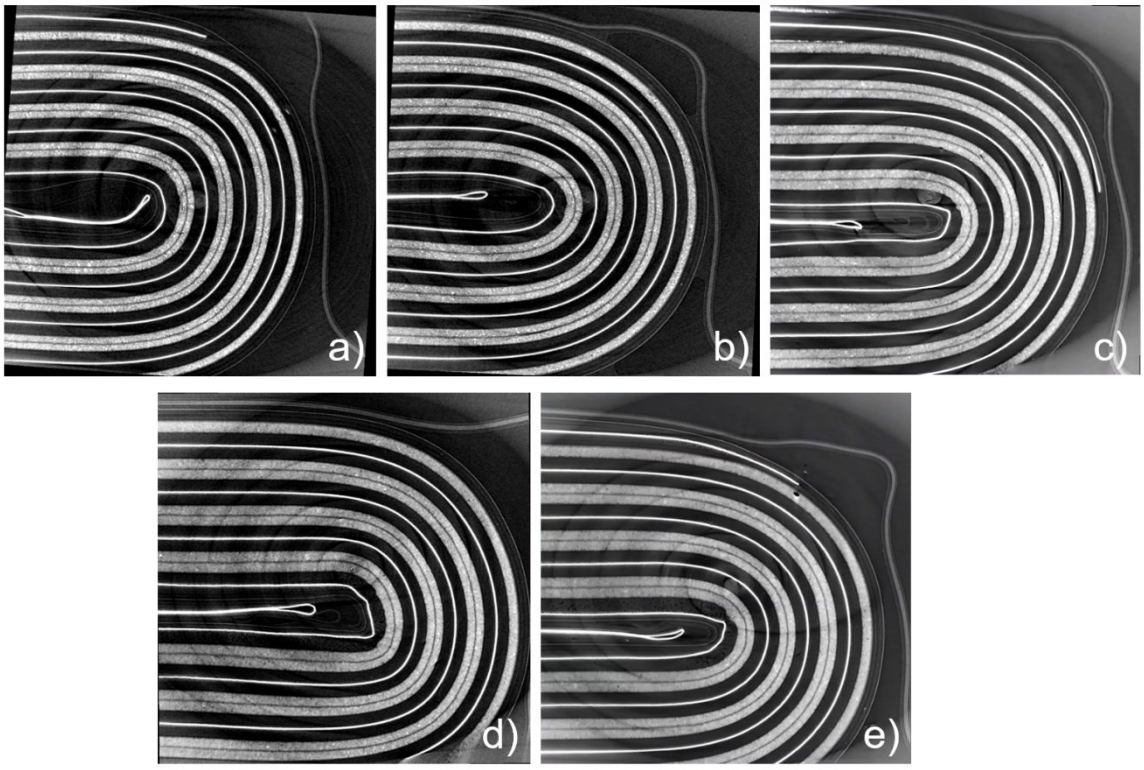

Figure 5.24: X-ray computed tomography scans of a) control (after formation) and b) 25% DOD C/10, c) 50% DOD C/10, d) 75% DOD C/3, e) 100% DOD C/3 cells that cycled for 20000 h at 40°C and with a fixed upper cutoff voltage. CT-scans courtesy of Toby Bond.

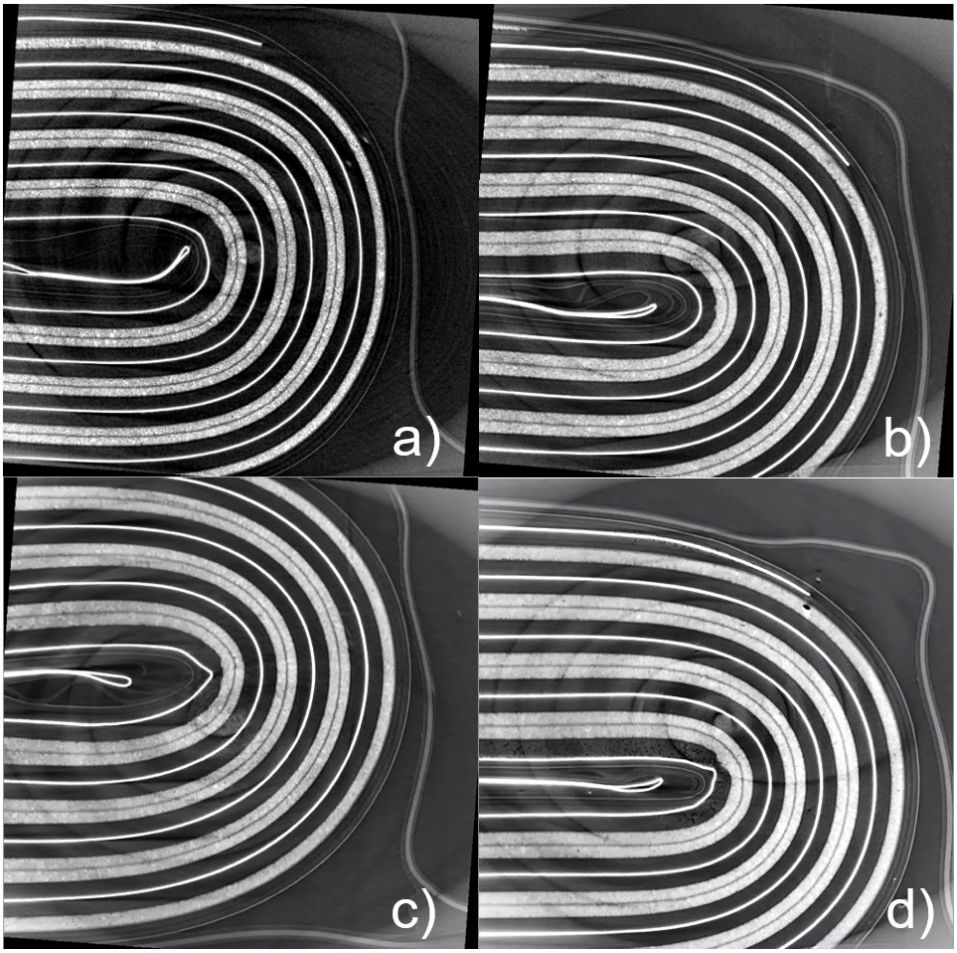

Figure 5.25: X-ray computed tomography scans of a) control (after formation) and b) C/10, c) C/5, d) C/3 cells that cycled for 20000h at 100% DOD, 40°C and with a fixed upper cutoff voltage. CT-scans courtesy of Toby Bond.

Figure 5.26 shows positive and negative electrode thickness change and flat/turn ratio as a function of depth of discharge and C-rate. We see that electrode thickness increases linearly with C-rate and the increase is larger at for the positive electrode. The electrode thickness also increases with depth of discharge but in a non-linear fashion. Again, the increase is larger at the positive electrode. Furthermore, the flat/turn ratio of the positive and negative electrode also increase linearly as a function of C-rate and non-linearly as a function of depth of discharge.

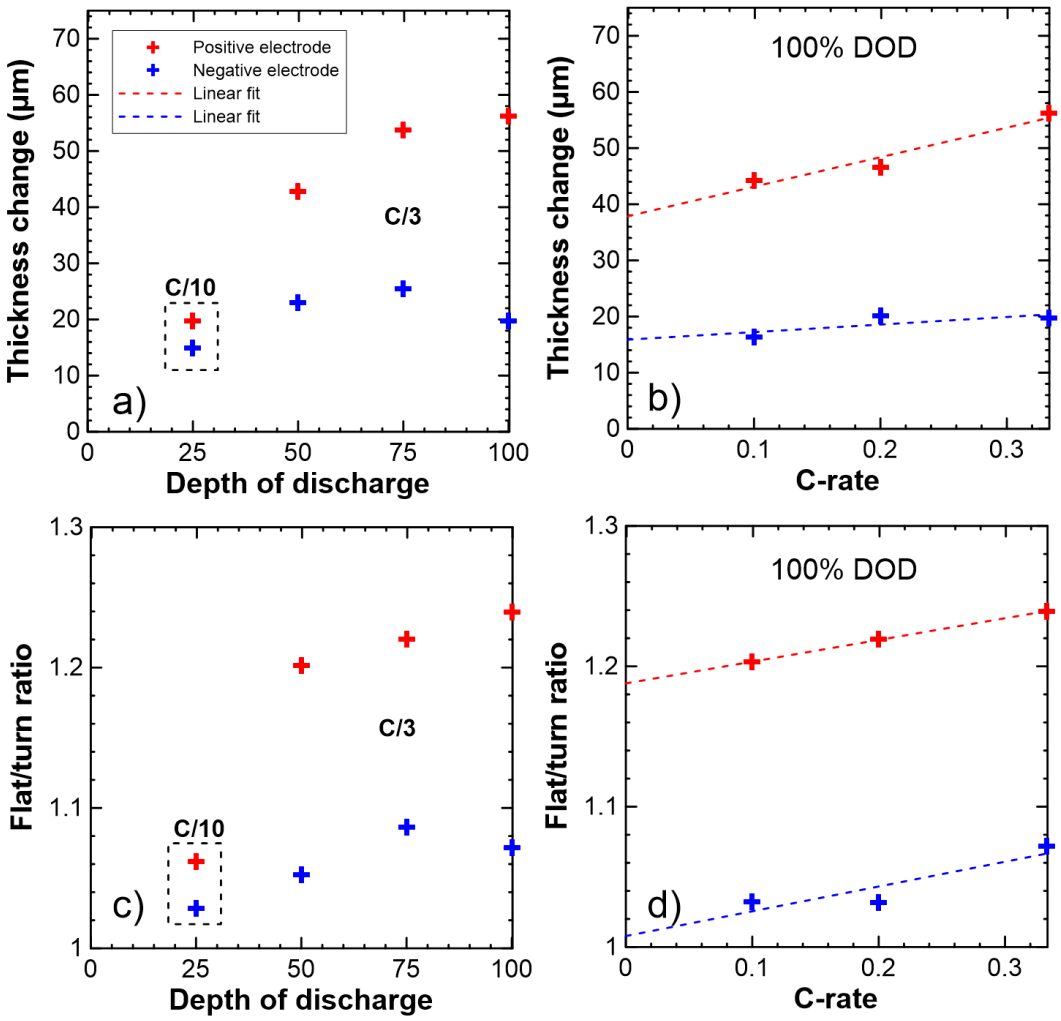

Figure 5.26: a) Electrode thickness change as a function of depth of discharge, b) electrode thickness change as function of C-rate, c) flat/turn ratio as a function of depth of discharge and d) flat/turn ratio as a function of C-rate for cells cycling at 40°C and fixed upper cutoff voltage. Data in c) and d) are for cells cycling at 100% DOD. In a) and b), the data points that are boxed are representing cells that cycled at C/10, while the data points that are not boxed represent cells that cycled at C/3. Thickness data for the positive electrode are in red and the thickness data for the negative electrode are in blue. Raw data courtesy of Toby Bond.

Figure 5.27 shows X-ray CT scans focused at the edge of the jelly roll to examine the amount of electrolyte that can be observed outside the jelly roll. Figure 5.27 shows that after cells cycle for 20000 h at 40°C over a large SOC range that no electrolyte is visible outside the jelly roll. By contrast, some electrolyte can be observed outside the jelly roll for cells cycled over a 25% SOC range where cell thickness expansion is less. This explains why the transmission of ultrasonic waves is poor for cells that cycled the most times (C/3 and C/5) over large SOC ranges at 40°C, since there may not be enough electrolyte available to fill the expanded pore spaces even though all available electrolyte has been "sucked" into the jelly roll.[61] The increase in electrode thicknesses causes the pore volume inside the electrodes to increase. The electrolyte then fills as much of the empty space inside the electrodes as possible like a sponge, explaining why no electrolyte is observed outside the jelly roll for the cells cycled over large SOC range.

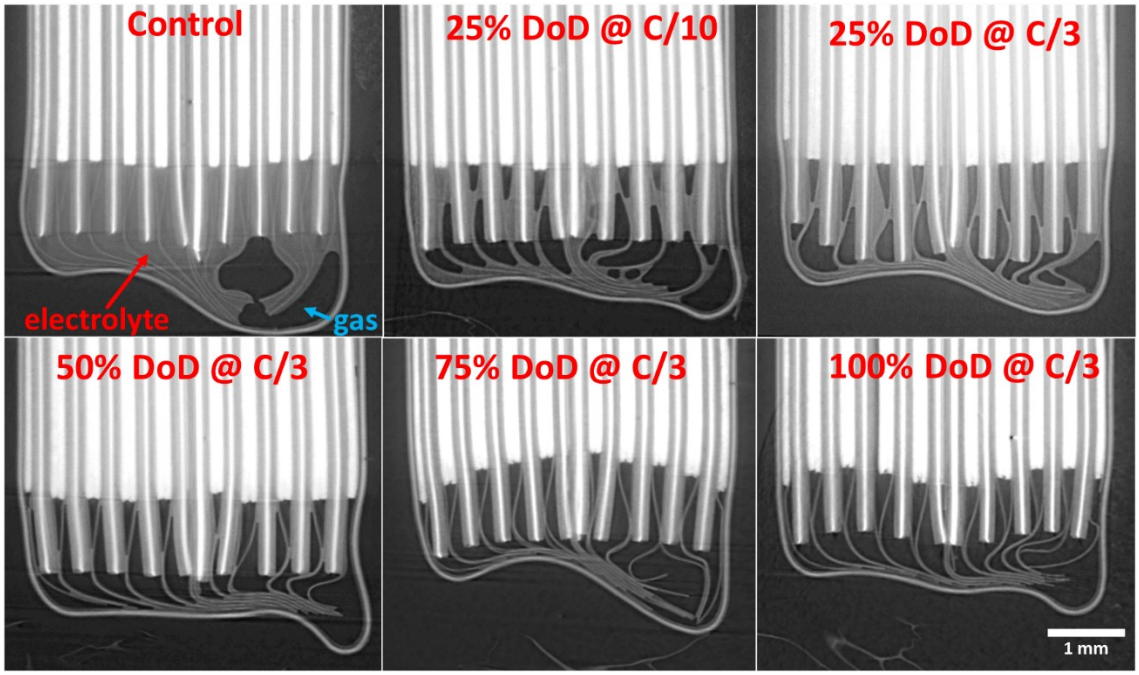

Figure 5.27: CT-scans of a control cell (immediately after formation) and UC cells that cycled at 100-75% SOC C/10, at 100-75% SOC C/3, at 100-50% SOC C/3, at 100-25% SOC C/3, 100-0% SOC C/3 that cycled for 20000h. The electrolyte appears as light gray regions outside the jelly roll and gas, or vacuum appear as black regions. The white regions represent the electrode of the cells. The plastic casing of the cells and the separators extending beyond the electrodes are also seen as light grey. CT-scans courtesy of Toby Bond.

CHAPTER 6 CONCLUSION AND FUTURE WORK

6.1 CONCLUSION

Using trial and error, a new class of additives from the dioxazolone family of molecules was studied in NMC622/gr cells. It was found, using long-term cycling, that PDO and pNDO were the best additives from the four dioxazolones tested in term of capacity retention, PDO being the best. Adding the co-additives DTD or LFO increased the performance of these dioxazolones further. In fact, 2% PDO + 1% DTD and 1% PDO + 2% DTD were the best performing blend during cycling, while 2% pNDO + 1% DTD was not far behind in term of performance. DFT results for the reduction potentials of each additive showed good agreement with experiment and more electron withdrawing groups decreased the reduction cell potentials of these additives, however further studies using NMR, DFT, GC-MS and XPS are needed to fully understand the reduction mechanisms that take place at the anode during formation for each new additive. Trends between gas production and Rct versus the electron withdrawing power of the functional groups added may exist and require further study.

Furthermore, a complete study of the effect of depth of discharge on cell performance and cell parameters was done. The main cause of capacity loss in those cells was from lithium inventory loss caused by SEI growth. At low C-rate, the capacity versus time data was fitting well to a square root of time model, while an impedance term needed to be added at high C-rate. Impedance growth of the check-up cycles was quadratic and increasing as a

function of DOD for both LC and UC cells, suggesting higher impedance at low and high SOC and low impedance around 3.6 V. It is thought that electrolyte ‘’unwetting’’ and positive active mass loss are the major cause of impedance growth in those cells. Positive active mass loss was worse at high average SOC, while lithium inventory loss was independent of the average SOC at fixed DOD, at least for the SOC range tested in this work. Even though positive electrode active mass loss was present, these cells remained anode limited so the positive active mass loss did not directly contribute to capacity fade during the 2.5 years of these tests. However, active mass loss can indirectly contribute to capacity loss through impedance growth. Also note that negative mass loss and thickness increase were minimal in those cells relative to the positive electrode. It was shown that lithium inventory loss increased as a function of SOC range and temperature. This increase is linear with depth of discharge. Furthermore, impedance, positive electrode mass loss and impedance related capacity loss were shown to be worse at high temperature and high DOD. X-ray CT demonstrated that most of the thickness increase of these cells came from the positive electrode. It was also shown that capacity loss and jelly roll thickness increase were correlated and that positive active mass loss, jelly roll thickness increase and impedance growth were correlated. The volume increase measured using Archimedes’ principle was also shown to be entirely caused by the increase in thickness of the electrodes. The increase in electrode thickness caused the pore volumes inside the electrodes to increase. The electrolyte then filled as much of the empty space inside the electrodes as possible like water in a sponge, explaining why no electrolyte was observed outside the jelly roll for the cells cycled over a large SOC range. The lower amount of electrolyte

resulting from this absorption resulted in poor ultrasonic transmission. Then, DTA showed that changes to the composition of the electrolyte in the cycled cells were minimal.

Finally, while synchrotron X-ray CT is very expensive, it can inform about the thickness of both electrodes, about unwetting of the jelly roll, and damage at high resolution. However, high-intensity X-rays may cause unwanted chemical reactions inside the cells, making the experiment chemically destructive.

Then, Ultrasonic is less expensive and non-destructive, however it can only inform about unwetting of the jelly roll at lower resolution. It needs to be coupled with linear gauge thickness measurements and dV/dQ analysis to give a similar amount of knowledge as the synchrotron.

6.2 FUTURE WORK

By studying the dQ/dV graph of cells containing PDO, pFDO and pMoDO, it was found that a peak at 2.2 V could not be explained. DFT seems to match the peaks around ~2.5 V better. Furthermore, the values of the integral of the peaks at 2.2 V are way too small compared to the peak at ~2.5 V to be caused by one of the electrolyte additives. As a result, it is possible that this peak is caused by an impurity in the dioxazolones. To understand better this peak, it will be then important to use NMR to study the PDO containing

electrolyte before and after the 2.2 V peak, while remaining well below 2.5 V. The 2.5 V peak could also be studied similarly. Furthermore, the SEI mechanism of cells containing PDO and pNDO could be studied if new dioxazolone blends with improved performance are found. This could be done by using NMR, GC-MS and XPS at different voltages (1.5V, 2.25 V, 2.6 V, 3 V, for example). Then, the effect of the functional groups could be further studied to understand their impact on gas production, impedance, electrolyte stability and lithium inventory loss. This type of functional group study could also be applied to other families of molecules. For example, esters could be an interesting family of molecules to study with different functional groups as additives.

From the depth of discharge project, it was found that capacity loss, which was mainly caused by lithium inventory loss in those cells, was linear with the depth of discharge. It would then be important to figure out what mechanism can explain this trend. Can it be proven or disproven that SEI cracking is the main degradation mechanism that explains SEI growth? What instrument(s) and/or technique(s) would need to be used to prove or disprove this mechanism? Also, is the thickness increase at the positive electrode and the capacity loss correlated by chance or is there a mechanism of cause and effect between them? Can one have better precision when measuring the negative electrode active mass loss in those cells? It would be nice to figure out exactly how the positive mass loss, impedance growth and thickness increase are correlated. Electrochemical impedance spectroscopy of symmetric cells built from full-cells that cycled at different DOD could confirm or not that the impedance growth is mostly occurring at the positive electrode in those cells.

FIB-SEM tomography (Focused ion-beam scanning electron microscopy),[134] X-ray nano-computed tomography,[135] or other imagery techniques and modeling[135] could be used to study the evolution of the morphology of the positive electrode active particles, their relative position in space during cycling and the porosity of the electrode. From experimental evidence, a 3D model of the positive electrode versus time could be developed, which could inform us better about the above correlations.

While positive electrode mass loss is much less important in commercially relevant cells that contain single crystal NMCs, due to smaller particle cracking and smaller thickness increases, it likely still occurs at a much slower pace in those cells and may eventually be the underlying cause of failure after many years of operation. While experimental evidences are needed to confirm this hypothesis, cells with polycrystalline NMCs could be used to accelerate this degradation mechanism, allowing it to be conveniently studied in the lab. This type of study may be particularly important for grid energy storage which require batteries to last for decades or for cells that must operate at very high C-rates. This degradation mechanism may also be present in LFP-based cells. As such, thickness measurements of LFP-based cells would be important as they age. Also, tomography of single crystal NMCs as a function of aging could ultimately confirm or not the above hypothesis.The same experiment could also be done on the negative electrode.

The above modeling/imaging experiment as well as the experiments described in Chapter 5 could be done on many types of cells with electrodes of different composition and

morphology (e.g., using LFP or NCA instead of NMC, by using different transition metal ratios, different primary and secondary active particle sizes, different loadings, different electrolyte additives, different salt concentration, etc). Furthermore, different cycling conditions could be studied, like different cycling temperature, different C-rates, different depth of discharge, different average state of charge, different upper voltage cutoff, etc.

More specifically, it would be interesting to study a finer grid of different depth of discharge from 0% to 100% and different average state of charge. 5% DOD would be particularly interesting at different average state of charge. This could help better understand the impact of the graphite voltage versus capacity curve on lithium inventory loss due to SEI growth. For example, what would be the impact of the stage 2 to stage 2L transition plateau of graphite on SEI growth? In fact, since the graphite lattice experience no volume change during this transition, SEI growth should be minimal if we were to cycle a cell only between stage 2 to 2L. Some cells were cycled in this region in our lab at 25% DOD, but surprisingly they showed the opposite effect. Instead of showing less degradation than UC and LC that cycled at 25% DOD, they showed more degradation. Those results were not shown in this thesis, since we need more experiments to show that they are repeatable. If they are indeed repeatable, more work would need to be done to better understand why this is the case.

Studies could be done using cells that have a lower salt concentration to intentionally decrease their lifetime. Low salt concentration (i.e., < 0.8M $LiPF_6$) with a upper cutoff voltage of 4.4 V was shown by Aiken et al. to result in early rollover failure (i.e., < 200

cycles).[136] Since depth of discharge studies like the one in this thesis require a lot of resources, intentionally decreasing the lifetime of these cells could decrease the duration of the experiments. This would make large projects, like the ones mentioned above, more practical. High temperature (70°C) could also be used to accelerate the failure of those cells, however it is important to keep in mind that new chemical reactions could appear, like the thermal decomposition of $LiPF_6$. Furthermore, loss during storage could be compared to loss during cycling to see the impact of volume change on capacity loss. This could be done on a set of polycrystalline cells and a set of single crystal cells that contain the same electrolyte.

Scanning micro x-ray fluorescence could be done on the negative electrode to quantify the amount of transition metal dissolution that happens inside those cells after long-term cycling.[137] XPS and other surface techniques could be used to study the composition and morphology of the anode SEI for different depth of discharge and temperature.

It would also be necessary to apply and likely generalize the impedance and overhang models shown in this work (equation 9) to other cells. The impedance model could be applied to cells that undergo rollover failure. It is very likely that generalisation and improvement of the model will be required. Before the cell are fitted, it would be necessary to know if the cells are anode or cathode limited. Then, it would be needed to know if those cells have any lithium plating during rollover. If lithium plating does occur, it would be required to add a term to (equation 9) for lithium plating. It is also very likely that non-linear terms would need to be added. For the overhang model, one could calculate the

capacity gain/loss from diffusion if one knows the initial state of charge of the overhang and the average state of charge of the cell during cycling. In theory, it should be possible to calculate this term. After formation, one could store the cells at a specific state of charge until equilibrium between the graphite active region and the overhang/overlap region occur (1000 hours of storage for example). After this, one can estimate the state of charge of the overhang/overlap to be similar to the state of charge of the active region of the graphite electrode. Then, the cells can be cycled at different average state of charges, different depth of discharges and temperatures. From this and the knowledge of the Q(V) curve, one can calculate the expected capacity gain/loss due to diffusion from/to the overhang/overlap and compare it to the experiment.

Then, one could wonder what would happen if a silicon-based negative electrode was used instead. To the author's best knowledge, a limited amount of capacity fade versus depth of discharge studies on silicon-based cells exists.[109,138–141] For example, Willenberg et al. undertook a depth of discharge study on these type of cells, but further studies are still required in order for researcher to better understand the mechanisms at play.[109] Since silicon-based negative electrode experience huge expansions and contractions during cycling, we would expect capacity retention to be changing dramatically with depth of discharge. This is indeed observed by Willenberg et al. at a mean state of 50%, where they show that a cell that cycled at 20% DOD does not show any sign of rollover failure during the first 1000 cycles, but cell that cycled at 75% DOD experience rollover failure at cycle number 250. Interestingly, at a mean state of charge of 10% and at 20% DOD,rollover failure occurs at cycle 250. However, at a mean state of charge of 50% and 75% and at

20% DOD,rollover failure does not occur during the first 1000 cycles. If these results are repeatable, it would be important to understand the mechanisms that are responsible for this failure. A complete study, similar to the one shown in this thesis, should be done on silicon-based cells in order to better understand how the result shown here generalize to other type of cells. The result of this study should then be compared to the result obtained for graphite-based cells.

Note that due to limited resources, it would be necessary to prioritize and decrease the size of some of the above proposed experiments.

APPENDIX A: ADDITIONAL DATA AND INFORMATION

Table A.1: Loading, parameters, and composition of the electrodes of the polycrystalline NMC622A/NG and NMC622B/NG cells used for the DOD project (Chapter 5). The values of NMC622B/NG cells are included in brackets when they are different than the NMC622A/NG values. Values for cells from the PDO project (Chapter 4) can be found in Table A.16.

	Positive electrode	**Negative electrode**
Loading (mg/cm^2)	19.3	13.6
Active area (cm^2)	78.52	87.36
Conductive additive	Carbon black	Carbon black
Binder(s)	PVDF	CMC/SBR
Mass ratio	96 : 2 : 2	95.4 : 1.3 : 1.1 : 2.2
Electrode thickness (µm)	136 [134]	200 [194]
Foil thickness (µm)	15	8
L (cm)	17.1	17
S (cm)	13.1	14.2
w (cm)	2.6	2.8

Table A.2: Parameters of the polycrystalline NMC622A/NG and NMC622B/NG cells used for the DOD project (Chapter 5).

Max. charge voltage (V)	4.5
Separator thickness (µm)	20
Cell width (mm)	20
Cell length (mm)	30
Metal bag sheet thickness (mm)	0.108

Table A.3: Electronic energies (E_{elec}), enthalpies (H) and Gibbs free energies (G) at 25°C of unreacted, singly oxidized, and singly reduced dioxazolone molecules, as well as unreacted EC and VC, calculated using B3LYP/6-311++G(2df,2pd)/IEFPCM-UFF(ε=20).

	E_{elec} (Ha)	H (Ha)	G (Ha)
pMODO$^+$	-702.790457	-702.626582	-702.677974
pMODO	-703.028076	-702.864069	-702.915116
LipMODO	-710.600560	-710.436297	-710.491842
PDO$^+$	-588.197160	-588.068955	-588.114360
PDO	-588.459185	-588.330095	-588.374951
LiPDO	-596.039045	-595.909448	-595.958244
pFDO$^+$	-687.472518	-687.351386	-687.398852
pFDO	-687.732446	-687.610838	-687.657830
LipFDO	-695.311475	-695.189510	-695.240794
pNDO$^+$	-792.755851	-792.623108	-792.676180
pNDO	-793.034346	-792.900523	-792.952329
LipNDO	-800.669257	-800.534111	-800.589238
EC	-342.539411	-342.458719	-342.493159
VC	-341.303198	-341.247488	-341.280252

Table A.4: Electronic energies (E_{elec}) at 25°C of singly reduced dioxazolone were calculated using B3LYP/6 311++G(2df,2pd)/IEFPCM-UFF(ε=20). A lithium ion was included in the calculation and the five Li+ sites in Figure 3 were tested.

	pMODO	**PDO**	**pFDO**	**pNDO**
Reduced (Ha)				
Li^+ at site 1	-710.595640	-596.034709	-695.307263	-800.653243
Li^+ at site 2	-710.595982	-596.034788	-695.307613	-800.653513
Li^+ at site 3	-710.590268	-596.029358	-695.301902	-800.647595
Li^+ at site 4	-710.600560	-596.039045	-695.311475	-800.652984
Li^+ at site 5	-710.590655	-596.024165	-695.297140	-800.669257

Table A.5: Enthalpies (H) at 25°C were calculated using B3LYP/6 311++G(2df,2pd)/IEFPCM-UFF(ε=20). A lithium ion was included in the calculation and the five Li+ sites in Figure 3 were tested.

	pMODO	PDO	pFDO	pNDO
Reduced (Ha)				
Li^+ at site 1	-710.431833	-595.905653	-695.185674	-800.518359
Li^+ at site 2	-710.432152	-595.905430	-695.186018	-800.518587
Li^+ at site 3	-710.426675	-595.900459	-695.180575	-800.512767
Li^+ at site 4	-710.436297	-595.909448	-695.189510	-800.517799
Li^+ at site 5	-710.425802	-595.895330	-695.175985	-800.534111

Table A.6: Gibbs free energies (G) at 25°C were calculated using B3LYP/6 311++G(2df,2pd)/IEFPCM-UFF(ε=20). A lithium ion was included in the calculation and the five Li+ sites in Figure 3 were tested.

	pMODO	PDO	pFDO	pNDO
Reduced (Ha)				
Li^+ at site 1	-710.488362	-595.955412	-695.237444	-800.573471
Li^+ at site 2	-710.488335	-595.953692	-695.237615	-800.573749
Li^+ at site 3	-710.483370	-595.950032	-695.232526	-800.567411
Li^+ at site 4	-710.491842	-595.958244	-695.240794	-800.572358
Li^+ at site 5	-710.479396	-595.946815	-695.228464	-800.589238

Table A.7: Electronic energies (E_{elec}), enthalpies (H) and Gibbs free energies (G) at 25°C were calculated for the case of pNDO and its reduction products using B3LYP/6-311++G(2df,2pd)/IEFPCM-UFF(ε=20). LiNBN is the acronym used for lithium p-nitrobenzonitrile.

	E_{elec} (Ha)	**H (Ha)**	**G (Ha)**
pNDO	-793.034346	-792.900523	-792.952329
LipNDO	-800.669257	-800.534111	-800.589238
Li_2pNDO	-808.273264	-808.135951	-808.190526
Li_2CO_3	-279.184470	-279.159493	-279.193970
LiNBN	-536.816458	-536.704184	-536.752661

Table A.8: Parameters obtained from the fits of UC cells of Figure A.17 that cycled at 20°C and C/10.

DOD	Q_0 (mAh)	A	Q_{OHL} (mAh)	τ (h)
1	210.95	0.000622	2.33	1518
0.75	207.97	0.000468	-2.23	1518
0.5	212.32	0.000345	-10.90	1338
0.25	214.43	0.000239	-11.93	975

Table A.9: Results of manual dV/dQ analysis after 20000 h of cycling at 40°C for fixed UC cells. Slippages **Δ** include both formation slippage and long-term cycling slippage. Lithium inventory loss does not include lithium inventory loss during formation.

DOD	C-rate	Slippage Δ (mAh) ±1.5	Neg. mass (g) ±0.02	Pos. mass (g) ±0.01	Lithium inventory loss (mAh) ±4
1	0.1	44.5	1.02	1.24	46
1	0.1	N/A	N/A	N/A	N/A
1	0.2	44.7	1.02	1.16	55
1	0.2	44.4	1.03	1.15	56
1	0.3	42.9	0.99	1.06	64
1	0.3	50.7	0.95	1.13	64
0.75	0.1	49.2	1.04	1.24	51
0.75	0.1	46.6	1.03	1.24	48
0.75	0.2	45.7	1.05	1.17	54
0.75	0.2	52.7	1.02	1.17	61
0.75	0.3	56.2	1.02	1.16	66
0.75	0.3	51.9	1.05	1.18	60
0.5	0.1	40.8	1.01	1.22	44
0.5	0.1	49.6	1.06	1.31	44
0.5	0.2	49.6	1.05	1.28	46
0.5	0.2	47.9	1.04	1.20	53
0.5	0.3	51.4	1.11	1.20	57
0.5	0.3	49.7	1.05	1.30	45
0.25	0.1	39.6	1.08	1.30	35
0.25	0.1	44.0	1.05	1.31	38
0.25	0.2	44.0	1.05	1.31	38
0.25	0.2	44.4	1.09	1.28	41
0.25	0.3	N/A	N/A	N/A	N/A
0.25	0.3	45.0	1.07	1.31	38

Table A.10: Results of manual dV/dQ analysis after 20000h of cycling at 40°C for fixed LC cells. Slippages **Δ** include both formation slippage and long-term cycling slippage. Lithium inventory loss does not include lithium inventory loss during formation.

DOD	C-rate	Slippage Δ (mAh) ±1.5	Neg. mass (g) ±0.02	Pos. mass (g) ±0.01	Lithium inventory loss (mAh) ±4
1	0.1	N/A	N/A	N/A	N/A
1	0.1	50.7	1.02	1.35	40
1	0.2	N/A	N/A	N/A	N/A
1	0.2	50.5	1.01	1.35	40
1	0.333	44.8	1.03	1.15	56
1	0.333	N/A	N/A	N/A	N/A
0.75	0.1	41.5	1.07	1.28	38
0.75	0.1	N/A	N/A	N/A	N/A
0.75	0.2	50.4	1.05	1.28	48
0.75	0.2	48.4	1.05	1.27	46
0.75	0.333	49.5	1.05	1.25	49
0.75	0.333	49.6	1.04	1.25	50
0.5	0.1	37.1	1.04	1.33	29
0.5	0.1	35.3	1.08	1.30	30
0.5	0.2	33.8	1.04	1.28	30
0.5	0.2	36.6	1.03	1.33	28
0.5	0.333	37.8	1.03	1.33	29
0.5	0.333	41.3	1.04	1.33	33
0.25	0.1	27.5	1.05	1.30	23
0.25	0.1	32.2	1.05	1.34	23
0.25	0.2	31.7	1.03	1.33	23
0.25	0.2	33.9	1.04	1.36	22
0.25	0.333	N/A	N/A	N/A	N/A
0.25	0.333	33.4	1.04	1.33	25

Table A.11: Results of manual dV/dQ analysis after 20000h of cycling at 20°C for fixed UC cells. Slippages **Δ** include both formation slippage and long-term cycling slippage. Lithium inventory loss does not include lithium inventory loss during formation.

DOD	C-rate	Slippage Δ (mAh) ±1.5	Neg. mass (g) ±0.02	Pos. mass (g) ±0.01	Lithium inventory loss (mAh) ±4
1	0.1	N/A	N/A	N/A	N/A
1	0.1	N/A	N/A	N/A	N/A
1	0.2	42.3	1.05	1.36	31
1	0.2	N/A	N/A	N/A	N/A
1	0.3	50.0	1.05	1.35	40
1	0.3	N/A	N/A	N/A	N/A
0.75	0.1	40.0	1.05	1.37	27
0.75	0.1	N/A	N/A	N/A	N/A
0.75	0.2	48.2	1.07	1.34	39
0.75	0.2	N/A	N/A	N/A	N/A
0.75	0.3	N/A	N/A	N/A	N/A
0.75	0.3	48.2	1.07	1.32	41
0.5	0.1	N/A	N/A	N/A	N/A
0.5	0.1	44.9	1.05	1.37	32
0.5	0.2	44.9	1.07	1.33	37
0.5	0.2	48.8	1.05	1.31	42
0.5	0.3	53.5	1.05	1.36	42
0.5	0.3	44.8	1.08	1.33	36
0.25	0.1	N/A	N/A	N/A	N/A
0.25	0.1	30.0	1.07	1.31	24
0.25	0.2	N/A	N/A	N/A	N/A
0.25	0.2	33.2	1.09	1.36	22
0.25	0.3	N/A	N/A	N/A	N/A
0.25	0.3	33.2	1.10	1.33	25

Table A.12: General results after 20000h of cycling at 40°C for fixed UC cells.

DOD	Crate	Thickness (mm) ±0.04	Volume change (mL) ±0.05	Normalized Capacity loss ±0.001	Absolute capacity loss (mAh) ±0.2	Rct ($\Omega \cdot cm^2$) ±0.4	C parameter (V/h) ±1E-08
1	0.1	4.41	0.16	0.174	37.4	24.0	7.2E-07
1	0.1	4.45	0.20	0.188	41.2	23.8	N/A
1	0.2	4.50	0.19	0.223	51.9	33.8	1.35E-06
1	0.2	4.48	0.18	0.222	53.5	25.9	N/A
1	0.3	4.59	0.24	0.291	69.9	34.0	1.73E-06
1	0.3	4.56	0.24	0.254	60.4	33.2	N/A
0.75	0.1	4.47	0.20	0.145	39.6	24.9	3.8E-07
0.75	0.1	4.50	0.17	0.144	38.2	24.7	N/A
0.75	0.2	4.53	0.22	0.184	49.5	N/A	7.0E-07
0.75	0.2	4.49	0.21	0.187	53.9	26.5	N/A
0.75	0.3	4.53	0.22	0.213	60.3	36.7	1.05E-06
0.75	0.3	4.60	0.25	0.208	54.9	N/A	N/A
0.5	0.1	4.40	0.15	0.126	36.5	23.6	2.1E-07
0.5	0.1	4.34	0.09	0.072	33.8	N/A	N/A
0.5	0.2	4.36	0.11	0.086	36.6	N/A	3.9E-07
0.5	0.2	4.44	0.19	0.145	47.4	24.3	N/A
0.5	0.3	4.50	0.17	0.166	52.3	23.8	4.7E-07
0.5	0.3	4.26	0.10	0.093	39.8	N/A	N/A
0.25	0.1	4.25	0.14	0.073	28.8	24.8	1.2E-07
0.25	0.1	4.20	0.07	0.045	29.4	N/A	N/A
0.25	0.2	4.19	0.06	0.054	31.7	N/A	2.2E-07
0.25	0.2	4.35	0.13	0.096	34.9	23.6	N/A
0.25	0.3	4.37	N/A	0.109	38.0	N/A	3.5E-07
0.25	0.3	4.23	0.06	0.058	32.9	N/A	N/A

Table A.13: General results after 20000h of cycling at 40°C for fixed LC cells.

DOD	Crate	Thickness (mm) ±0.04	Normalized Capacity loss ±0.001	Absolute capacity loss (mAh) ±0.2	Rct ($\Omega \cdot cm^2$) ±0.4	C parameter (V/h) ±1E-08
1	0.1	N/A	0.200	44.7	N/A	8.1E-07
1	0.1	4.43	0.186	41.3	28.7	
1	0.2	N/A	0.229	50.4	N/A	8.9E-07
1	0.2	4.45	0.186	41.1	25.8	
1	0.333	4.58	0.291	63.3	25.9	1.27E-06
1	0.333	N/A	0.276	59.9	N/A	N/A
0.75	0.1	4.42	0.158	34.2	31.5	4.6E-07
0.75	0.1	N/A	N/A	N/A	N/A	N/A
0.75	0.2	4.39	0.181	38.7	33.5	4.1E-07
0.75	0.2	4.60	0.192	41.8	33.3	N/A
0.75	0.333	4.63	0.200	43.1	32.9	6.1E-07
0.75	0.333	4.57	0.206	44.2	35.5	N/A
0.5	0.1	4.40	0.114	24.7	43.5	2.8E-07
0.5	0.1	4.43	0.119	26.1	37.3	N/A
0.5	0.2	4.40	0.123	26.4	46.0	3.5E-07
0.5	0.2	4.43	0.121	26.6	44.1	N/A
0.5	0.333	4.52	0.120	26.1	40.3	3.1E-07
0.5	0.333	4.36	0.122	26.6	39.1	N/A
0.25	0.1	4.39	0.090	19.7	51.3	1.0E-07
0.25	0.1	4.45	0.086	19.0	49.5	N/A
0.25	0.2	4.34	0.088	19.3	42.9	1.2E-07
0.25	0.2	4.35	0.082	18.2	42.2	N/A
0.25	0.333	N/A	0.098	21.6	N/A	1.2E-07
0.25	0.333	4.25	0.086	18.9	43.1	N/A

Table A.14: General results after 20000h of cycling at 20°C for fixed UC cells.

DOD	Crate	Thickness (mm) ±0.04	Volume change (mL) ±0.05	Normalized Capacity loss ±0.001	Absolute capacity loss (mAh) ±0.2	Rct ($\Omega \cdot cm^2$) ±0.4
1	0.1	N/A	N/A	0.019	4.0	N/A
1	0.1	4.20	0.09	0.072	15.3	N/A
1	0.2	4.26	0.12	0.084	17.6	14.5
1	0.2	N/A	N/A	0.016	3.4	N/A
1	0.3	4.21	0.19	0.108	22.4	16.2
1	0.3	N/A	N/A	0.018	3.6	N/A
0.75	0.1	4.25	0.06	0.056	11.7	15.1
0.75	0.1	N/A	N/A	N/A	N/A	N/A
0.75	0.2	4.28	0.17	0.080	16.5	14.4
0.75	0.2	N/A	N/A	N/A	N/A	N/A
0.75	0.3	N/A	N/A	N/A	N/A	N/A
0.75	0.3	4.23	0.24	0.104	21.1	13.7
0.5	0.1	N/A	N/A	N/A	N/A	N/A
0.5	0.1	4.13	0.15	0.050	10.1	16.5
0.5	0.2	4.19	0.08	0.038	7.3	
0.5	0.2	4.18	0.08	0.072	14.1	14.9
0.5	0.3	4.35	0.19	0.086	17.3	14.1
0.5	0.3	4.15	0.09	0.052	10.1	N/A
0.25	0.1	4.16	0.05	0.023	4.6	22.0
0.25	0.1	4.12	0.03	0.012	2.4	N/A
0.25	0.2	4.20	0.07	0.045	9.1	17.3
0.25	0.2	4.17	0.03	0.019	3.9	N/A
0.25	0.3	N/A	N/A	0.048	9.5	N/A
0.25	0.3	4.19	0.06	0.028	5.6	N/A

Table A.15: Molecular mass and total charge transferred to a 2% concentration by mass of the corresponding additive assuming 1 electron reduction and 1.0 gram of electrolyte per cell. These values assume that all the additive molecules are being reduced.

	Molecular mass (g/mol)	**Total charge transferred (mAh/e^-)**
pMoDO	193.15	2.78
PDO	163.13	3.29
pFDO	181.12	2.96
pNDO	208.13	2.58
VC	86.04	6.23

Table A.16: Loading and composition of the electrodes of the polycrystalline NMC622/gr cells used for the PDO project (Chapter 4).

	Positive electrode	**Negative electrode**
Loading (mg/cm^2)	21.1	12.8
Active area (cm^2)	69.9	78.0
Conductive additive	Carbon black	Carbon black
Binder(s)	PVDF	CMC/SBR
Mass ratio	96 : 2 : 2	95.2 : 2 : 1.4 : 1.4

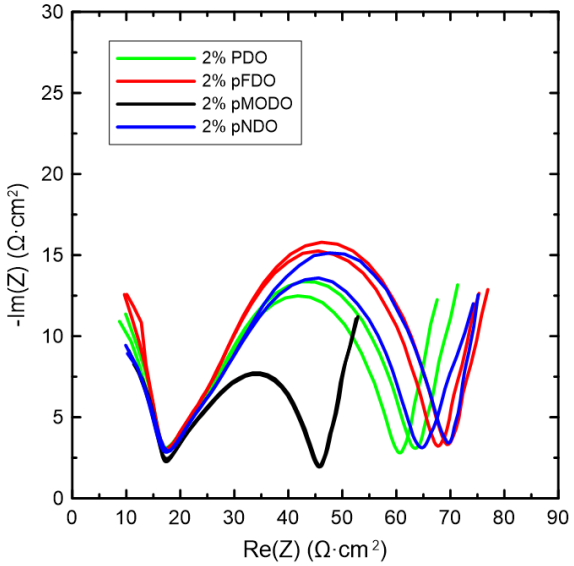

Figure A.1: Nyquist plot showing the impedance spectra of NMC622/graphite cells prepared with one of the four dioxazolone electrolyte additives studied in this work after C/20 formation at 40°C to 4.3 V. The spectra were measured after the cells were discharged to 3.8 V in a temperature box at 10°C. The electrolyte contained 1.2M $LiPF_6$ EC:EMC:DMC 25:5:70 for 2% pFDO, 2% pMODO and 2% pNDO cells, but 1.2 $LiPF_6$ EC:DMC 3:7 for the 2% PDO cell.

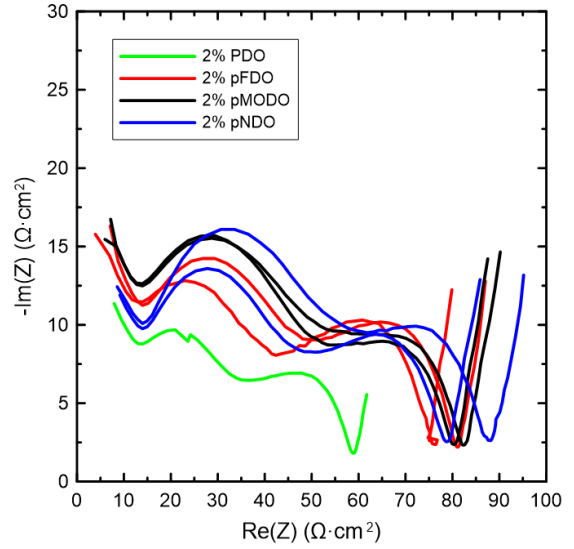

Figure A.2: Nyquist plot showing the impedance spectra of NMC622/graphite cells prepared with one of the four dioxazolone electrolyte additives studied in this work after storage at 60°C with an initial cell voltage of 4.3 V. The spectra were measured in a temperature box at 10°C after the cells were charged to 3.8 V. The electrolyte contained 1.2M $LiPF_6$ EC:EMC:DMC 25:5:70 for 2% pFDO, 2% pMODO and 2% pNDO cells, but 1.2 $LiPF_6$ EC:DMC 3:7 for the 2% PDO cell.

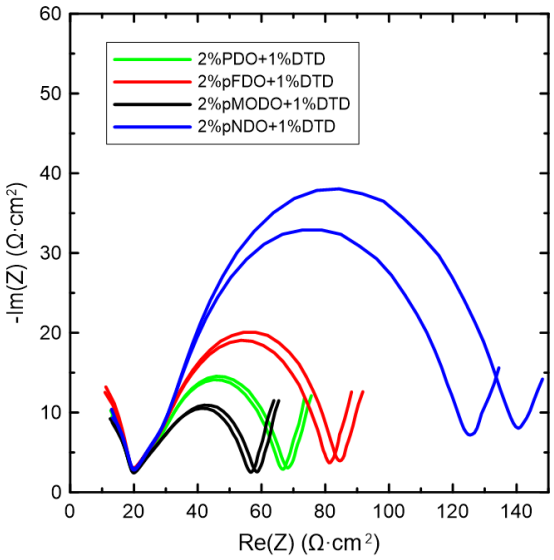

Figure A.3: Nyquist plot showing the impedance spectra of NMC622/graphite cells prepared with one of the four dioxazolone electrolyte additives studied in this work in combination with 1% DTD after C/20 formation at 40°C to 4.3 V. The spectra were measured after the cells were discharged to 3.8 V in a temperature box at 10°C. The electrolyte contained 1.2M $LiPF_6$ EC:EMC:DMC 25:5:70 for 2% pFDO + 1% DTD, 2% pMODO + 1% DTD and 2% pNDO + 1% DTD cells, but 1.2 $LiPF_6$ EC:DMC 3:7 for the 2% PDO + 1% DTD cell.

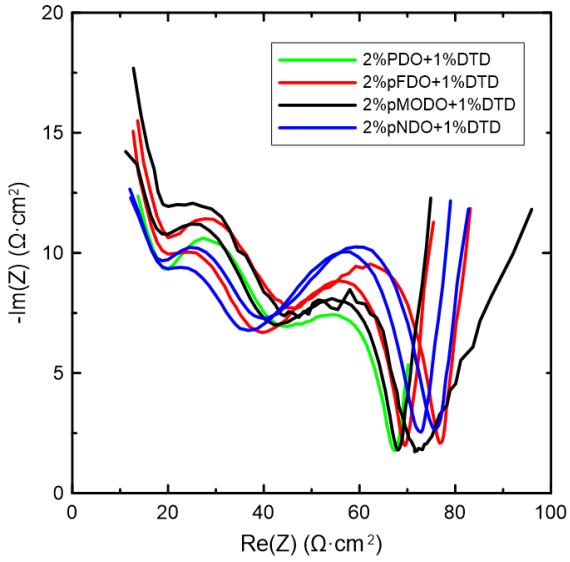

Figure A.4: Nyquist plot showing the impedance spectra of NMC622/graphite cells prepared with one of the four dioxazolone electrolyte additives studied in this work work in combination with 1% DTD after storage at 60°C with an initial cell voltage of 4.3 V. The spectra were measured in a temperature box at 10°C after the cells were charged to 3.8 V. The electrolyte contained 1.2M $LiPF_6$ EC:EMC:DMC 25:5:70 for 2% pFDO + 1% DTD, 2% pMODO + 1% DTD and 2% pNDO + 1% DTD cells, but 1.2 $LiPF_6$ EC:DMC 3:7 for the 2% PDO + 1% DTD cell.

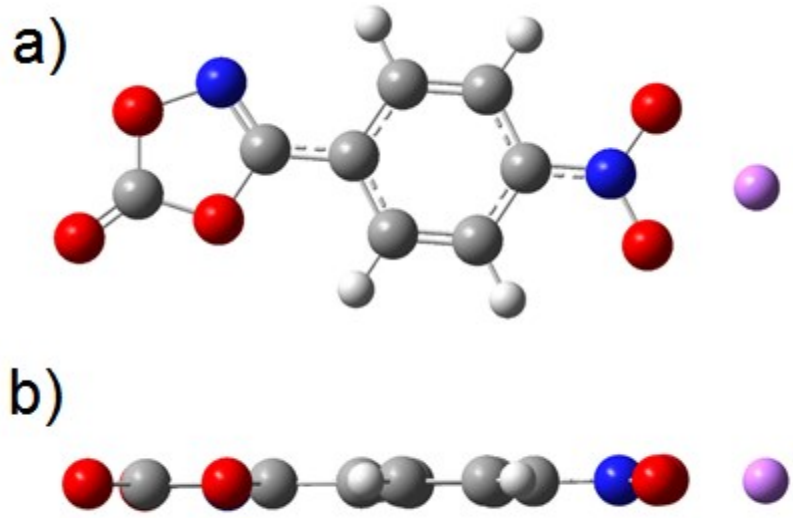

Figure A.5: Singly reduced pNDO (LipNDO) as seen from a) the top and from b) the side.

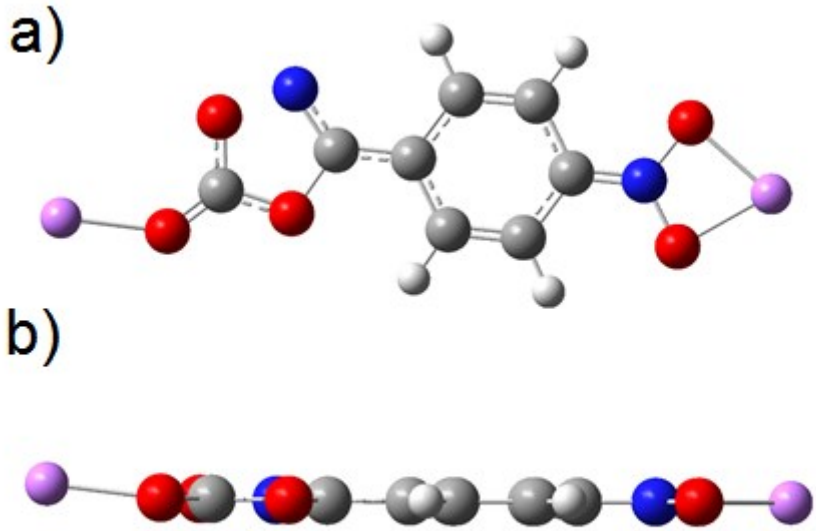

Figure A.6: Doubly reduced pNDO (Li_2pNDO) as seen from a) the top and from b) the side.

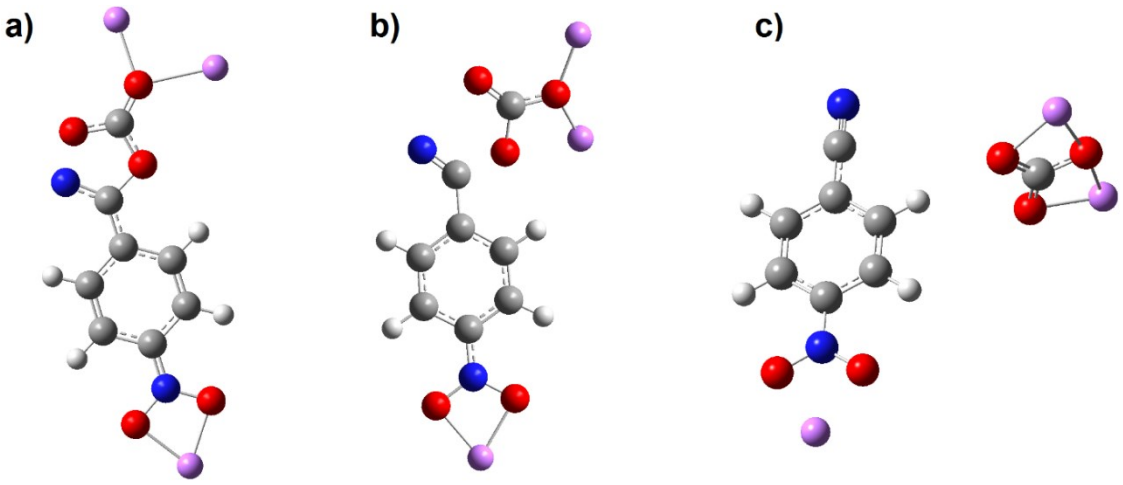

Figure A.7: Decomposition of triply reduced pNDO (Li3pNDO) during geometry optimization into lithium carbonate and lithium p-nitrobenzonitrile. A.7 a) shows the initial configuration guess of Li3pNDO before geometry optimization, A.7 b) shows step 20 of the geometry optimization and A.7 c) shows step 60 of the geometry optimization. The initial lithium positions were chosen based on the results shown in Table A.5.

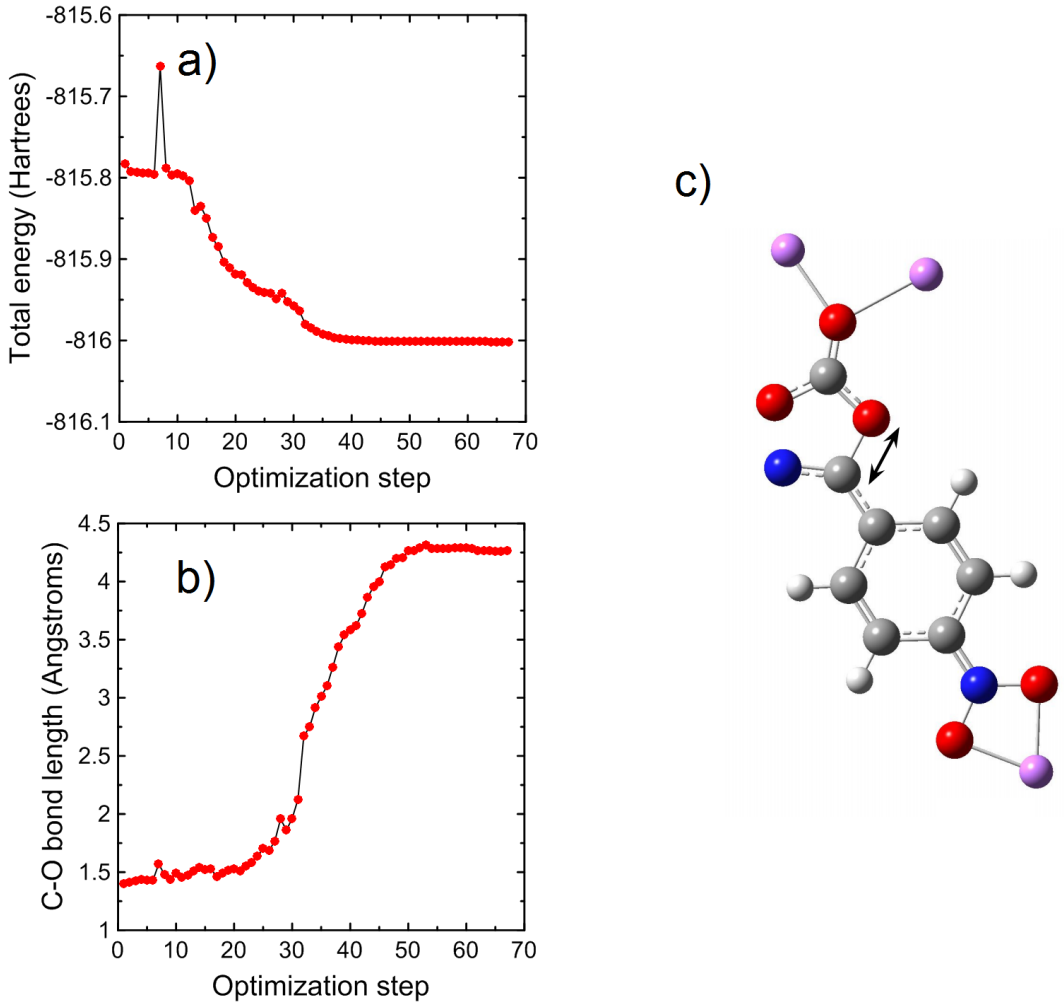

Figure A.8: a) Total energy in Hartrees and b) Carbon-Oxygen bond length (for the bond shown in c) by the double arrows) in function of the optimization step during the decomposition of triply reduced pNDO, as shown in Figure A.7.

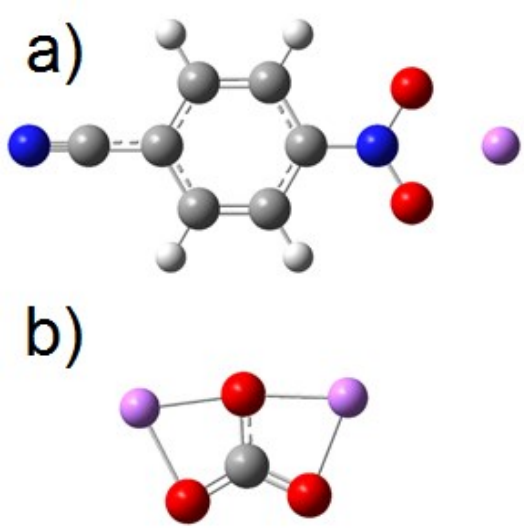

Figure A.9: Products of the third reduction of pNDO: a) lithium p-nitrobenzonitrile and b) lithium carbonate. Lithium p-nitrobenzonitrile is a radical and will react further, likely with the electrolyte. Lithium carbonate will passivate the negative electrode. Note that the geometry optimization and the Gibbs free energy of each molecule was calculated separately.

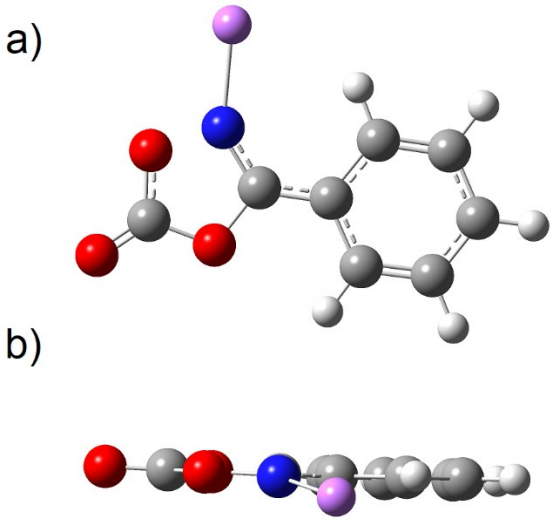

Figure A.10: Singly reduced PDO (LiPDO) as seen from a) the top and from b) the side.

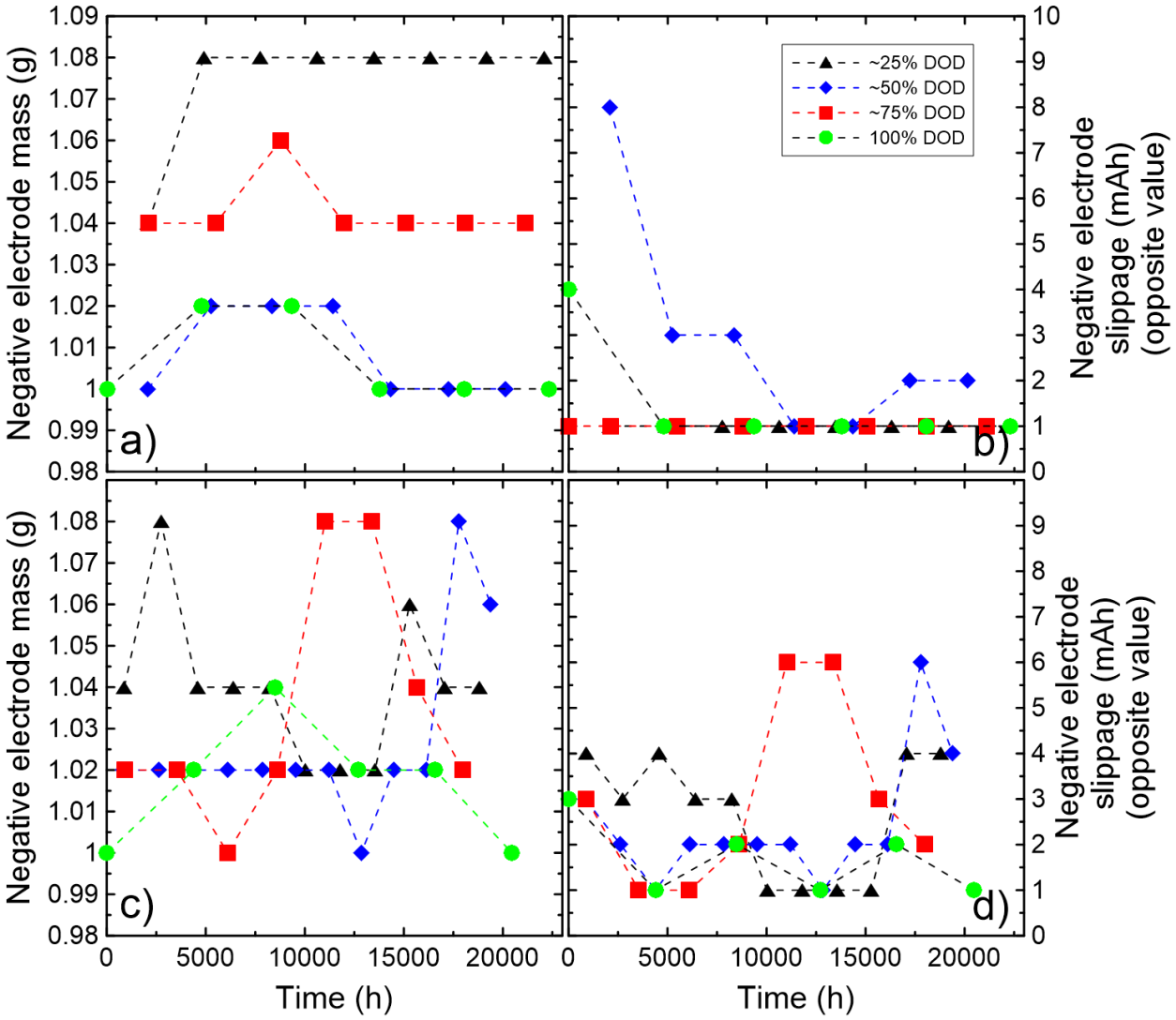

Figure A.11: a), c) Negative electrode mass m_n and b), d) negative electrode slippage δ_{nexp} of a), b) UC cells that cycled at C/10 and 40°C and c), d) LC cells that cycled at C/10 and 40°C obtained using the automatic dV/dQ analysis program and the matrix method.

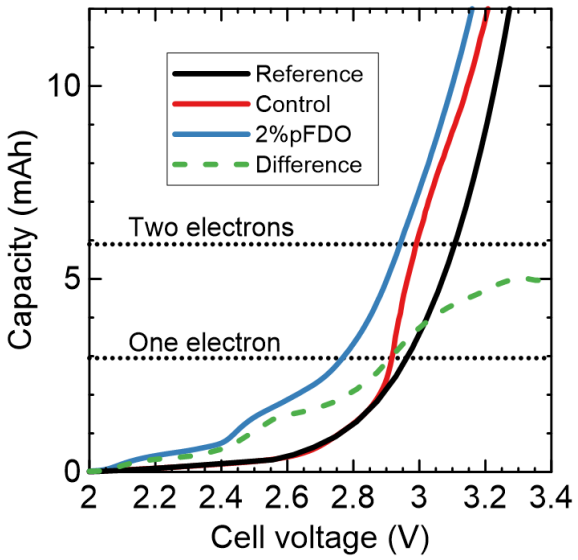

Figure A.12: Capacity as a function of cell voltage of 2% pFDO NMC622/gr pouch cell during formation at 40°C at C/3. The data is the same as Figure 4d. However, the data from 3.2 V to 3.4 V, which was not shown in Figure 4d, is added. This data adds more evidence that 2% pFDO reduces twice using two electrons per molecule. Since the maximum value of the dashed curve is not exactly 6 mAh, but 5 mAh instead, it is possible that pFDO passivates the graphite electrode before all the pFDO gets reduced in a two electrons process. Figure 2e does confirm that pFDO passivates the graphite electrode against EC reduction.

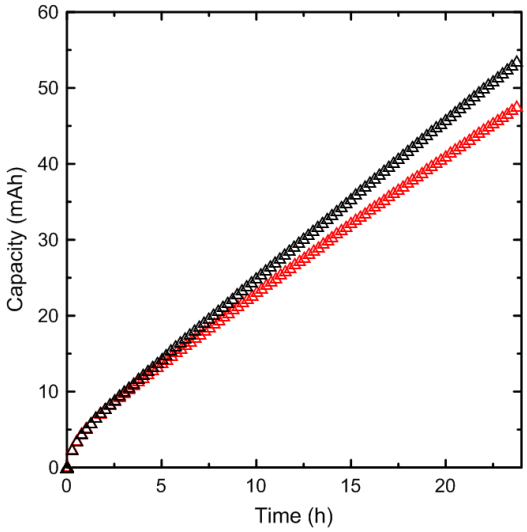

Figure A.13: Capacity versus time during 24h of wetting at 1.5 V and 40°C of 2% PDO cells. The first 30 minutes consisted of a constant current charge to 1.5 V followed by a constant voltage of 1.5 V for 24h.

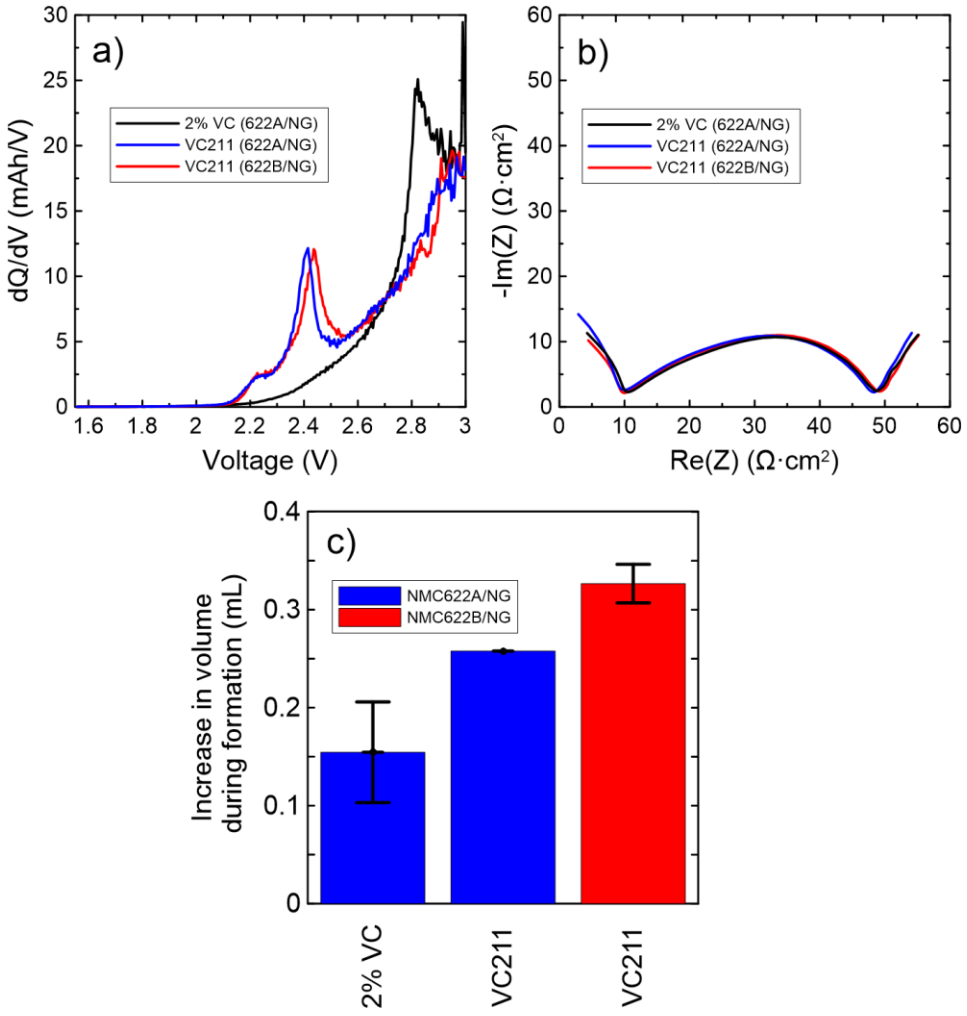

Figure A.14: a) Formation dQ/dV versus voltage data showing features related to the reduction of VC211 electrolyte versus a 2% VC electrolyte, b) EIS Nyquist plot of cells containing VC211 and 2% VC electrolyte and c) increase in volume due to gassing during formation of cells containing VC211 and 2% VC. Data for NMC622A/NG and NMC622B/NG are both shown.

Capacity gain from constant voltage part of charging

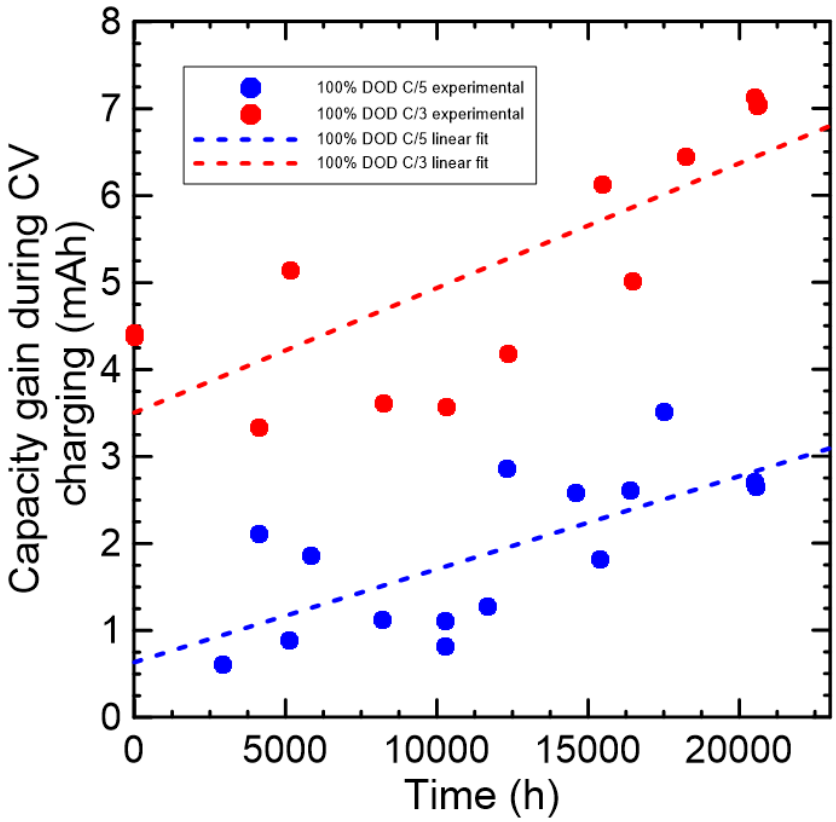

Figure A.15: Capacity gain obtained during the constant voltage (CV) step of the cycling of the 100% DOD cells from the LC cell batch at C/5 and C/3 at 40°C as a function of cycling time. The experimental data is fitted with a linear model. The fitting results are 0.0001070 t + 0.6350 and 0.0001434 t + 3.505, where t is the cycling time.

Theoretical explanation and proofs

To better understand why non-linear impedance terms need to be included in Equation 3 when ΔV' is large, let us suppose that a cell has a ΔV growth of 0.5 V during its lifetime. Figure A.16 shows what happen to the initial Q(V) curve of a NMC622/gr cell when ΔV/2 increases by ΔV'/2 = 0.5 V.

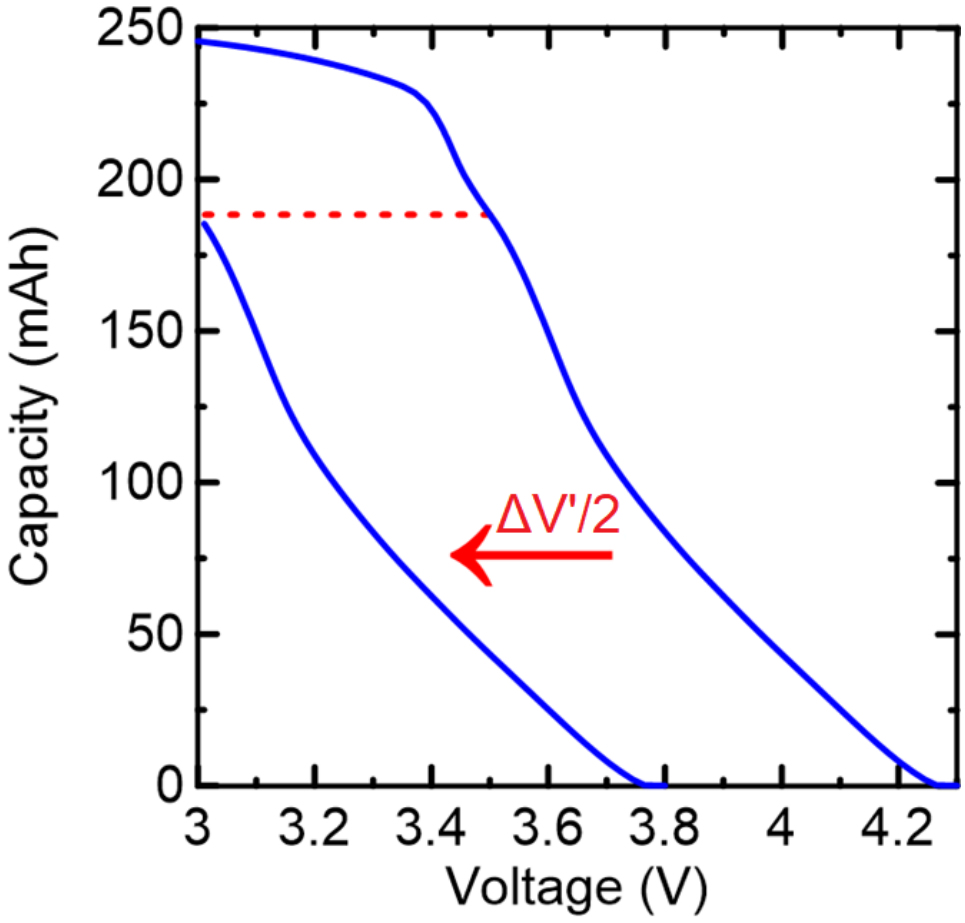

Figure A.16: Capacity versus voltage Q(V) curve before and after a ΔV increase of 1 V. The horizontal red dashed line helps to see that shifting a Q(V) curve toward the left by ΔV'/2 is equivalent to the transformation Q(V) → Q(V+ΔV'/2).

Figure A.16 show an increase in ΔV of ΔV'= ΔV – ΔV_0 = 1 V result in a reversible capacity loss of 57 mAh. This loss is in part caused by the presence of a fixed lower cutoff voltage of 3 V. One can realize that shifting the function Q(V) toward the left by ΔV'/2 is equivalent to the transformation Q(V) → Q(V+ΔV'/2). The red dashed line helps to see this in Figure A.16. As a result, the impedance related capacity loss can be calculated by a Taylor series for both the charge and discharge contribution:

$$Q(t) = Q_0\left(1 - A\sqrt{t}\right) - \sum_{n=1}^{\infty}\left(\left.\frac{d^n Q}{dV^n}\right|_L + \left.\frac{d^n Q}{dV^n}\right|_U\right)\frac{(\Delta V(t) - \Delta V_0)^n}{2^n\, n!} + Q_{CV}(t)$$

However, in practice, it is better to calculate the non-linear impedance contribution numerically by shifting the Q(V) curve manually, since multiple derivatives of experimental data can create a lot of noise. Despite of this, the equation above can help researchers have a better intuition about these non-linear contributions.

On a different note, one can wonder how our work compare to past theoretical work by Deshpande and Bernardi. While we propose a model of the form (where A depends on DOD and we also define Q(t) = Q_0 Q_N(t)):

$$Q(t) = Q_o\left(1 - A\sqrt{t}\right) = Q_o Q_N(t)$$

Deshpande and Bernardi proposed a model of the form (here simplified):

$$Q(t) = Q_o\left(1 - b\,\Delta SOL^2\, n - K\sqrt{t}\right)$$

, where ΔSOL is the state of lithiation swing of the graphite electrode, n is the number of cycles, t is the time and b, K and Q_0 are fitting constants. This equation assumes that the

state of lithiation swing is constant with time, but a more complete model exists. ΔSOL can be related to DOD by a constant c, such that $DOD = c\,\Delta SOL$. Our model and the Deshpande-Bernardi model can be compared by taking the derivative with respect to cycle number n of the first model (using $t = \frac{2\,n\,DOD}{Crate}$, which is an approximation that assume no capacity fade and $A = A_0 DOD + B_0$, which was empirically observed in Figure 5.13):

$$\frac{dQ_N}{dn} = -A\sqrt{\frac{DOD}{2\,n\,Crate}} = -\frac{A\,DOD}{Crate\,\sqrt{t}} = -\frac{A_0\,DOD^2}{Crate\,\sqrt{t}} - \frac{B_0\,DOD}{Crate\,\sqrt{t}}$$

Doing the same with the second model (where $c^2b=B$), we get:

$$Q(t) = Q_o\left(1 - B\,DOD^2\,n - K\sqrt{t}\right) = Q_o Q_N(t)$$

$$\frac{dQ_N}{dn} = -B\,DOD^2 - K\sqrt{\frac{DOD}{2\,n\,Crate}} = -B\,DOD^2 - \frac{K\,DOD}{Crate\,\sqrt{t}}$$

From this analysis, we find that the two model are equivalent if:

$$B = \frac{A_0}{Crate\,\sqrt{t}}$$

$$K = B_0$$

From which we conclude that the constant B is not really a constant and depends on cycling time.

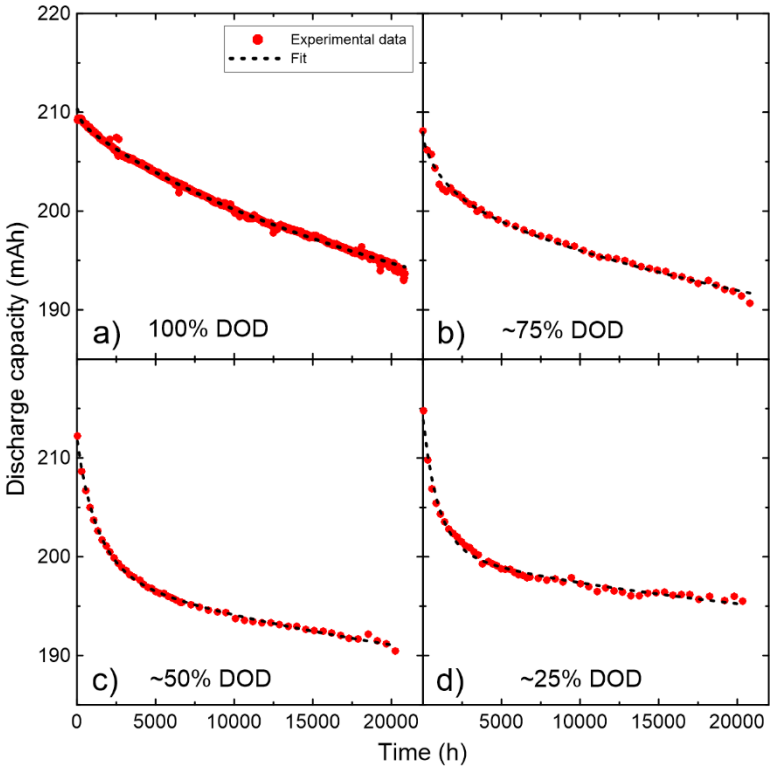

Figure A.17: Fits using a square root of time model combined with an overhang/overlap exponential term to the checkup cycles of the fixed upper cutoff cells at C/10 and 20°C for four different DOD values: a) 100% DOD, b) ~75% DOD, c) ~50% DOD and d) ~25% DOD. Equation 7 without the impedance and Q_{cv} terms was used for these fits since the impedance term is assumed negligeable at C/10. The numerical values of those fits can be found in Table A.8.

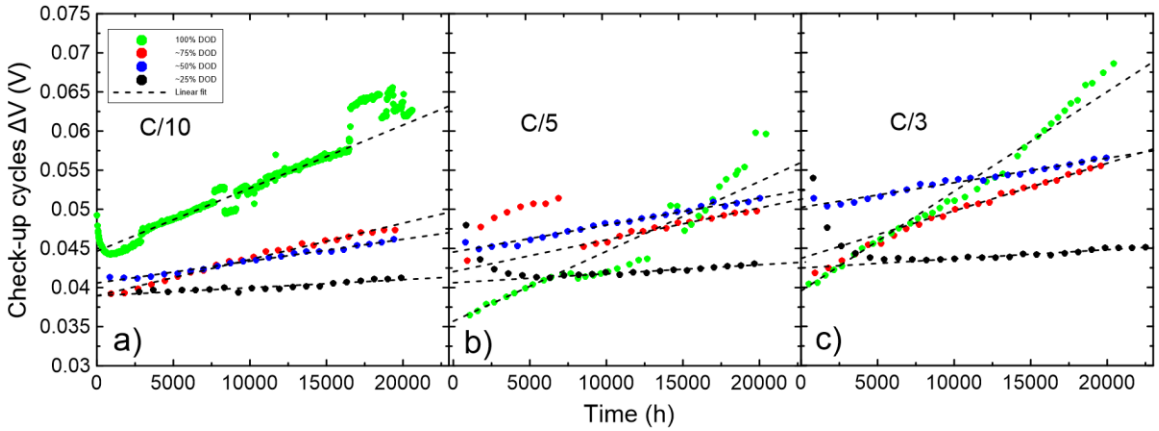

Figure A.18: ΔV versus cycle number for the checkup cycles of cells with fixed lower cutoff voltages at 40°C. Linear fits are also included.

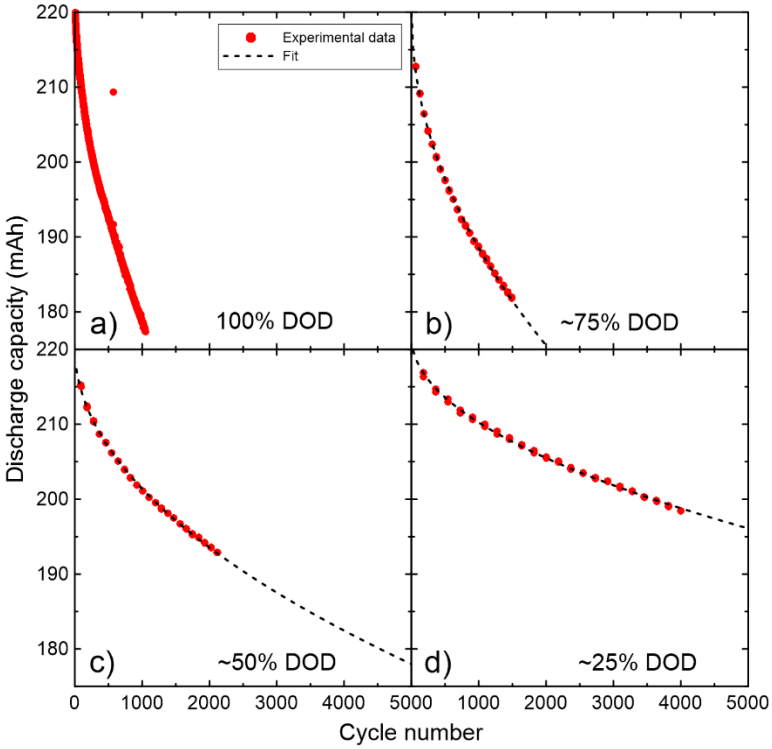

Figure A.19: Fits using a $Q_0(1 - \alpha\sqrt{n})$ model to the checkup cycles of fixed lower cutoff cells at C/10 and 40°C for three different DOD values: b) ~75% DOD, c) ~50% DOD and d) ~25% DOD. These fits were used to determine the number of cycles required to attain 90% of the initial capacity. The 100% DOD cell (panel a) did not require a fit, due to the larger density of data.

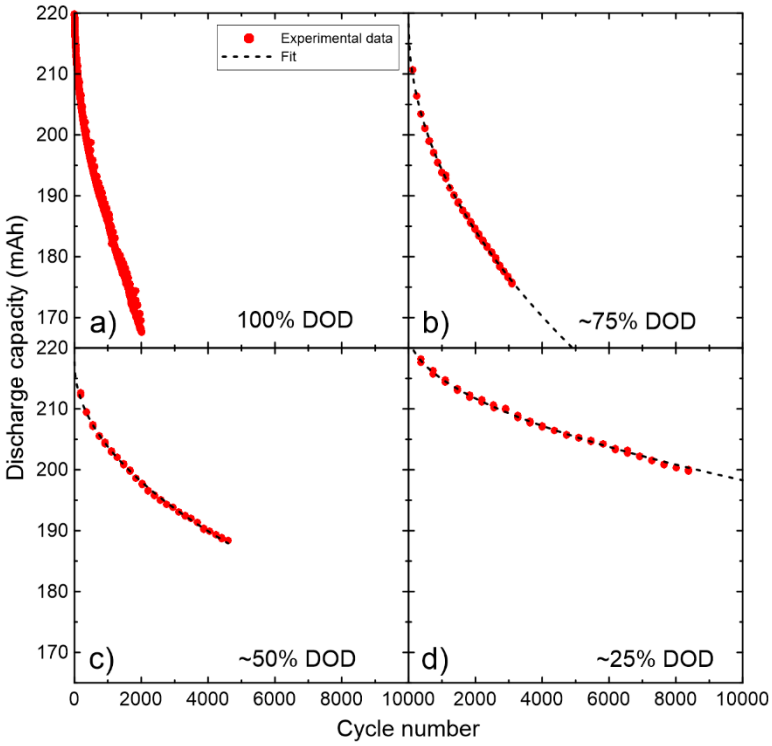

Figure A.20: Fits using a $Q_0(1 - \alpha\sqrt{n})$ model to the checkup cycles of fixed lower cutoff cells at C/5 and 40°C for three different DOD values: b) ~75% DOD, c) ~50% DOD and d) ~25% DOD. These fits were used to determine the number of cycles required to attain 90% of the initial capacity. The 100% DOD cell (panel a) did not require a fit, due to the larger density of data.

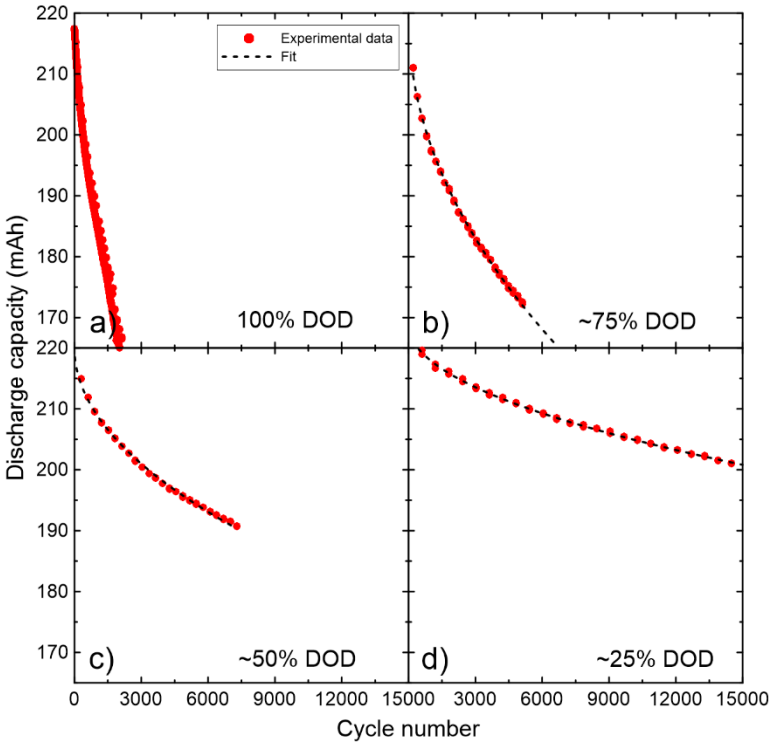

Figure A.21: Fits using a $Q_0(1 - \alpha\sqrt{n})$ model to the checkup cycles of fixed lower cutoff cells at C/3 and 40°C for three different DOD values: b) ~75% DOD, c) ~50% DOD and d) ~25% DOD. These fits were used to determine the number of cycles required to attain 90% of the initial capacity. The 100% DOD cell (panel a) did not require a fit, due to the larger density of data.

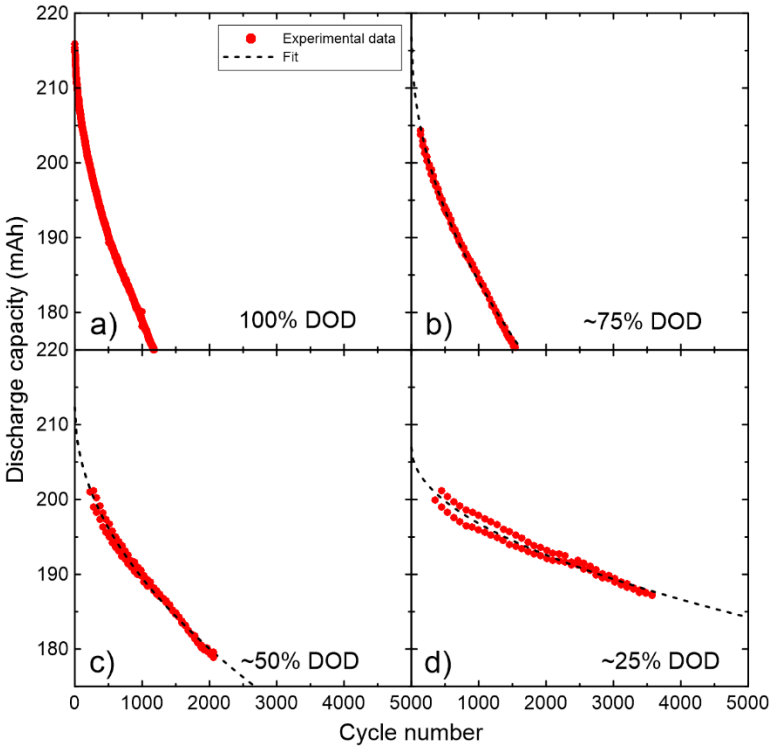

Figure A.22: Fits using a $Q_0(1 - \alpha\sqrt{n})$ model to the checkup cycles of fixed upper cutoff cells at C/10 and 40°C for three different DOD values: b) ~75% DOD, c) ~50% DOD and d) ~25% DOD. These fits were used to determine the number of cycles required to attain 90% of the initial capacity. The 100% DOD cell (panel a) did not require a fit, due to the larger density of data.

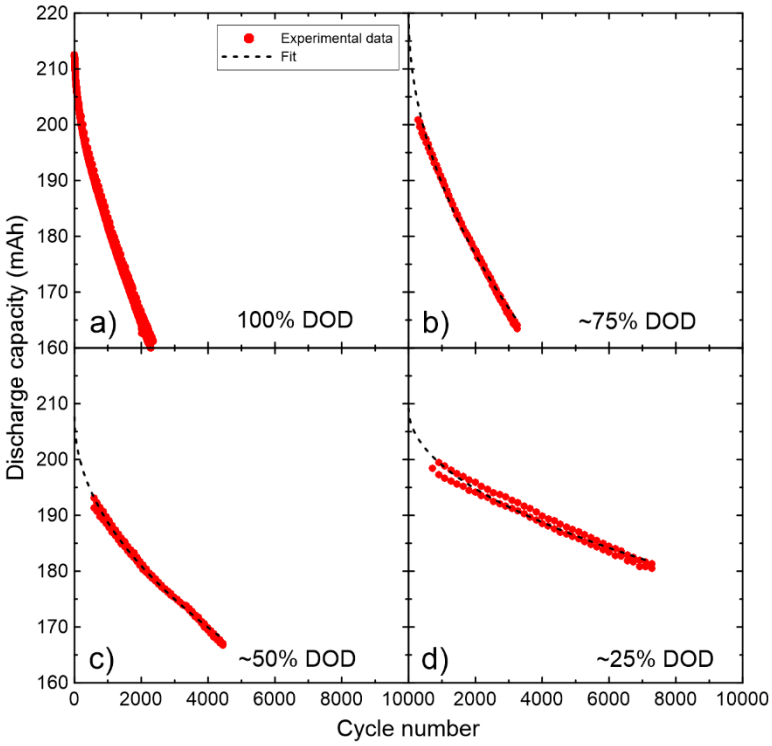

Figure A.23: Fits using a $Q_0(1 - \alpha \sqrt{n})$ model to the checkup cycles of fixed upper cutoff cells at C/5 and 40°C for three different DOD values: b) ~75% DOD, c) ~50% DOD and d) ~25% DOD. These fits were used to determine the number of cycles required to attain 90% of the initial capacity. The 100% DOD cell (panel a) did not require a fit, due to the larger density of data.

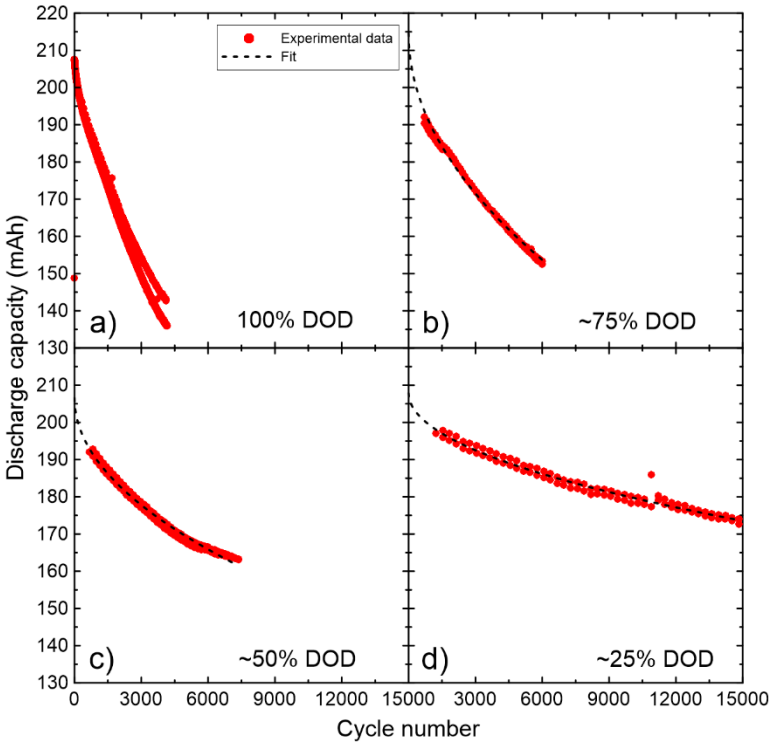

Figure A.24: Fits using a $Q_0(1 - \alpha\sqrt{n})$ model to the checkup cycles of fixed upper cutoff cells at C/3 and 40°C for three different DOD values: b) ~75% DOD, c) ~50% DOD and d) ~25% DOD. These fits were used to determine the number of cycles required to attain 90% of the initial capacity. The 100% DOD cell (panel a) did not require a fit, due to the larger density of data.

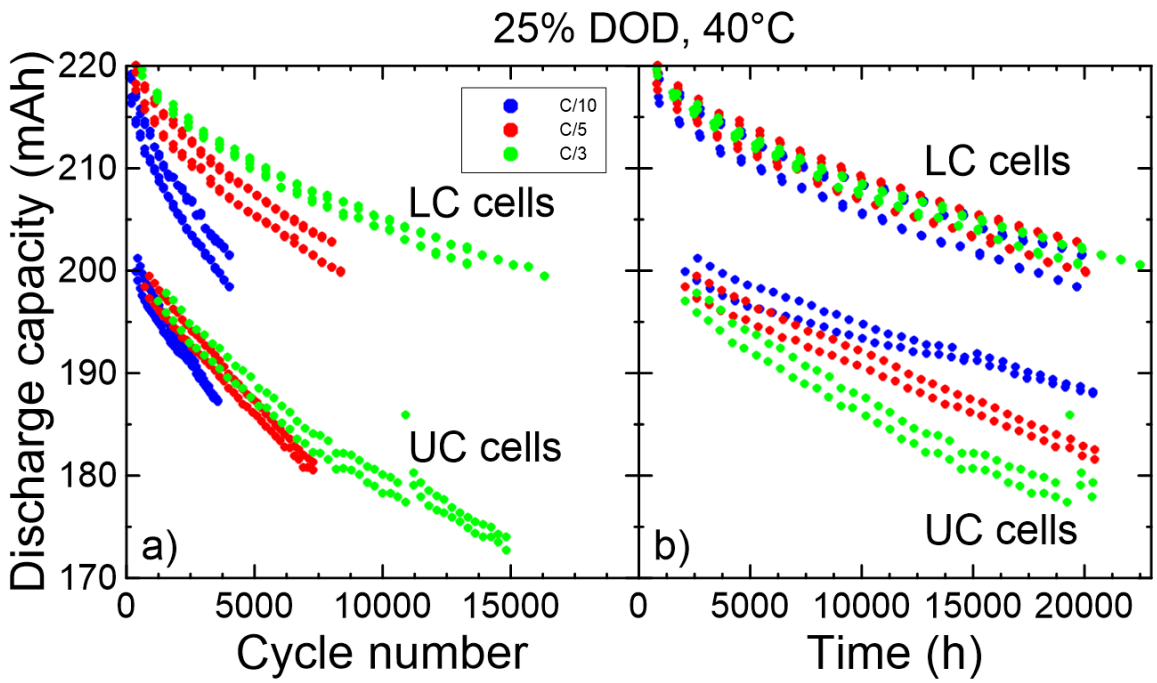

Figure A.25: a) Discharge capacity of checkup cycles versus cycle number and b) discharge capacity of checkup cycles versus time of 25% DOD cells LC (top) and UC (bottom) cells at three different C-rates. C/10 in blue, C/5 in red and C/3 in green. The UC cells at 25% DOD have larger impedance growth than the LC cells as shown in Figure A.30, and therefore the slopes of the capacity versus time curves are more negative for the UC cells in panel b.

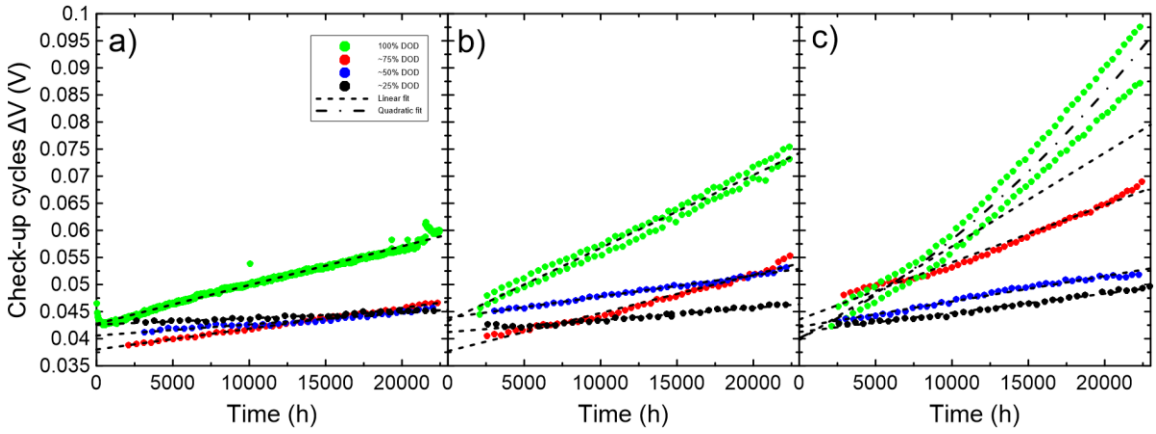

Figure A.26: ΔV versus cycle number for the checkup cycles of cells with fixed upper cutoff voltages at 40°C. Linear fits are also included.

Main cycles impedance fit versus time

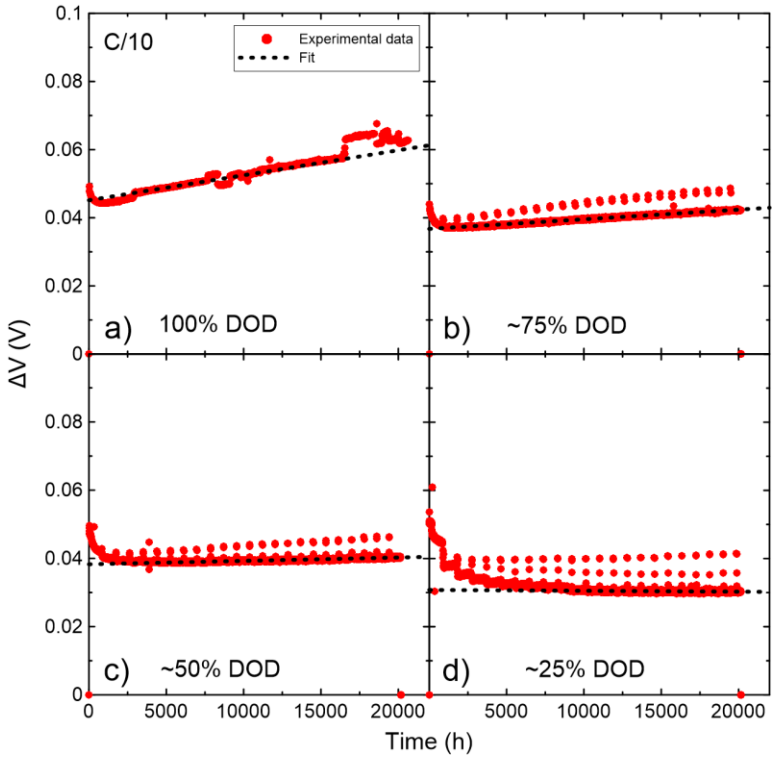

Figure A.27: Linear fit of ΔV vs time of fixed lower cutoff cells at C/10 and 40°C for four different DOD values: a) 100% DOD, b) ~75% DOD, c) ~50% DOD and d) ~25% DOD.

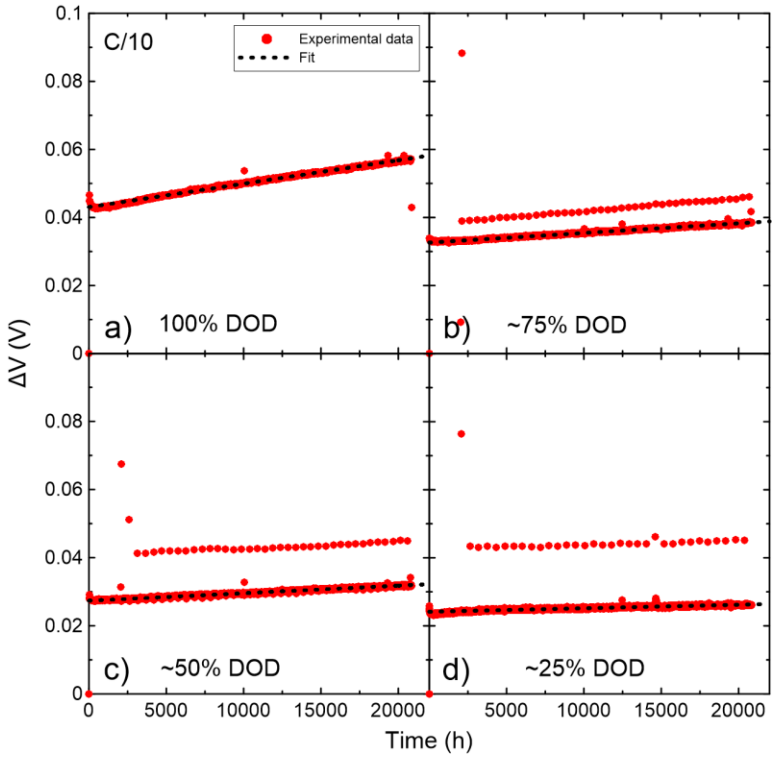

Figure A.28: Linear fit of ΔV vs time for fixed upper cutoff cells at C/10 and 40°C for four different DOD values: a) 100% DOD, b) ~75% DOD, c) ~50% DOD and d) ~25% DOD.

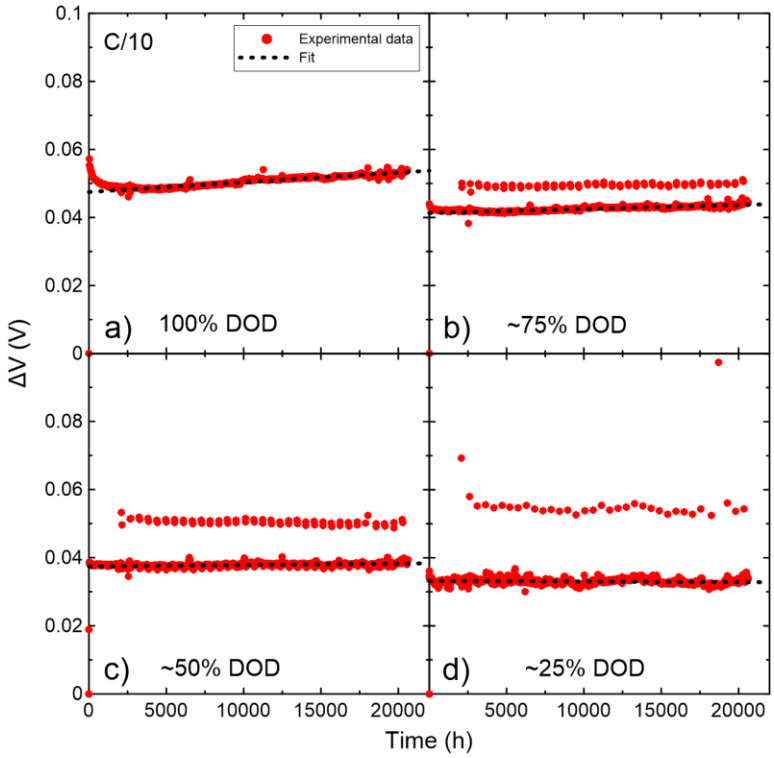

Figure A.29: Linear fit of ΔV vs time for fixed upper cutoff cells at C/10 and 20°C for four different DOD values: a) 100% DOD, b) ~75% DOD, c) ~50% DOD and d) ~25% DOD.

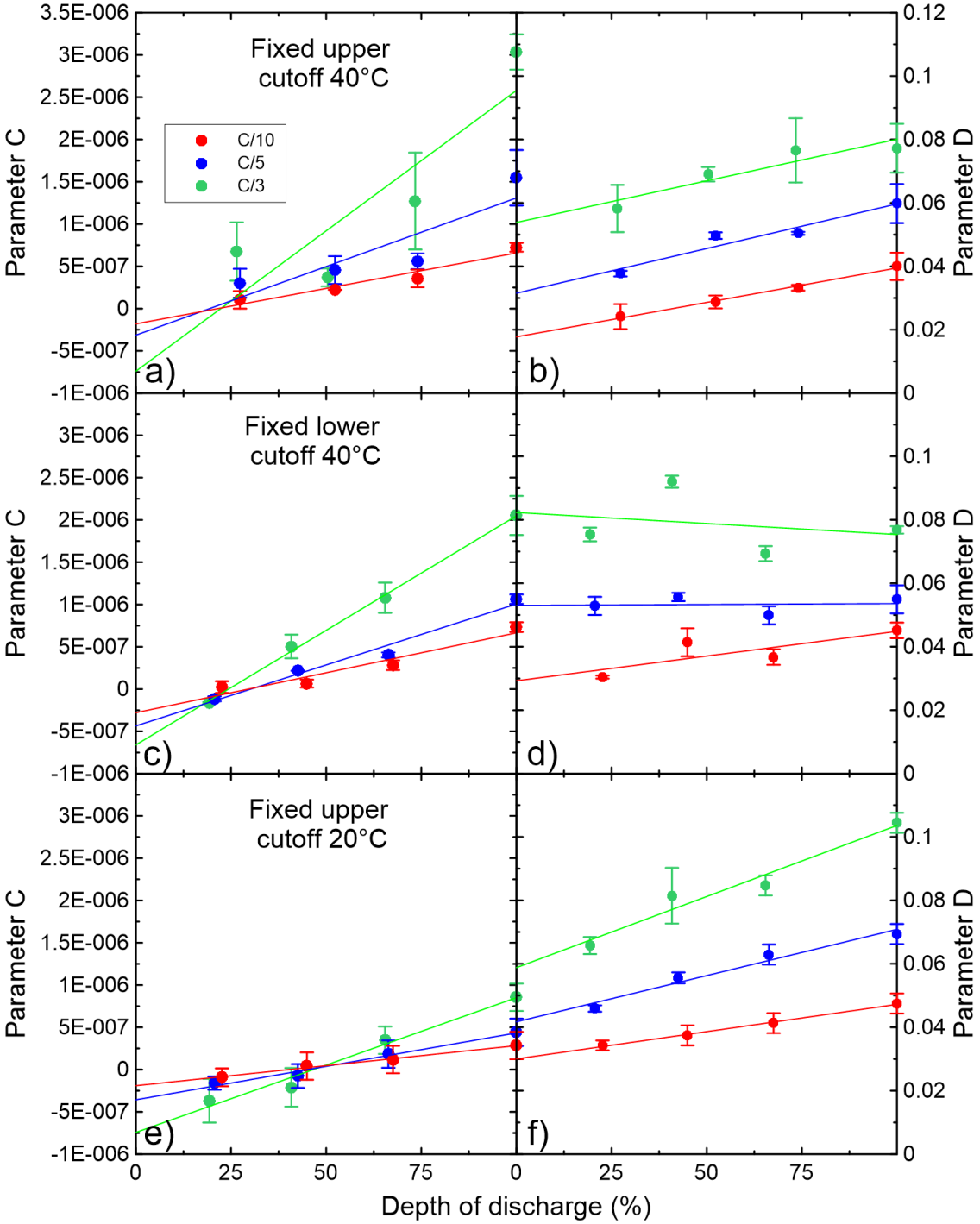

Figure A.30: Result for the parameters C and D from fitting ΔV(t) of the main cycles with a linear function of the form Ct + D.

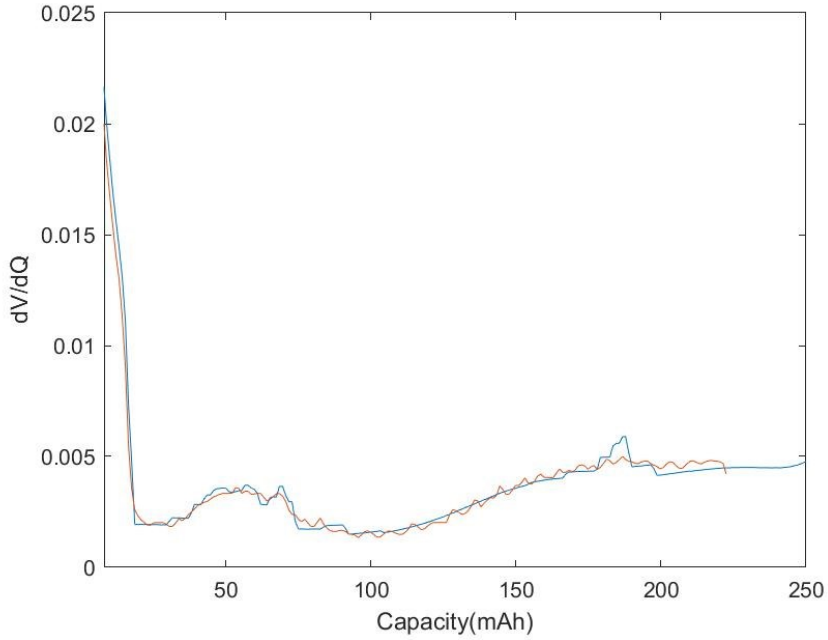

Figure A.31: dV/dQ fit of a 100% DOD C/10 cell at 40°C and cycle number 2 obtained using the automatic dV/dQ analysis program. The orange line represents experimental data and the blue line represents the theoretical fit. The units of dV/dQ are in V/mAh.

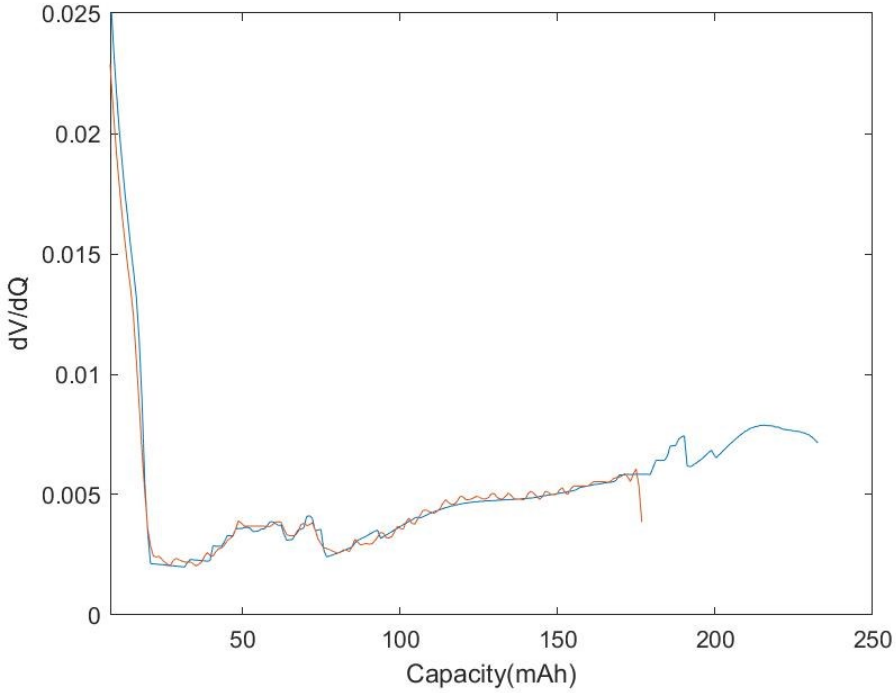

Figure A.32: dV/dQ fit of a 100% DOD C/10 cell at 40°C and cycle number 1042 obtained using the automatic dV/dQ analysis program. The orange line represents experimental data and the blue line represent the theoretical fit. The units of dV/dQ are in V/mAh.

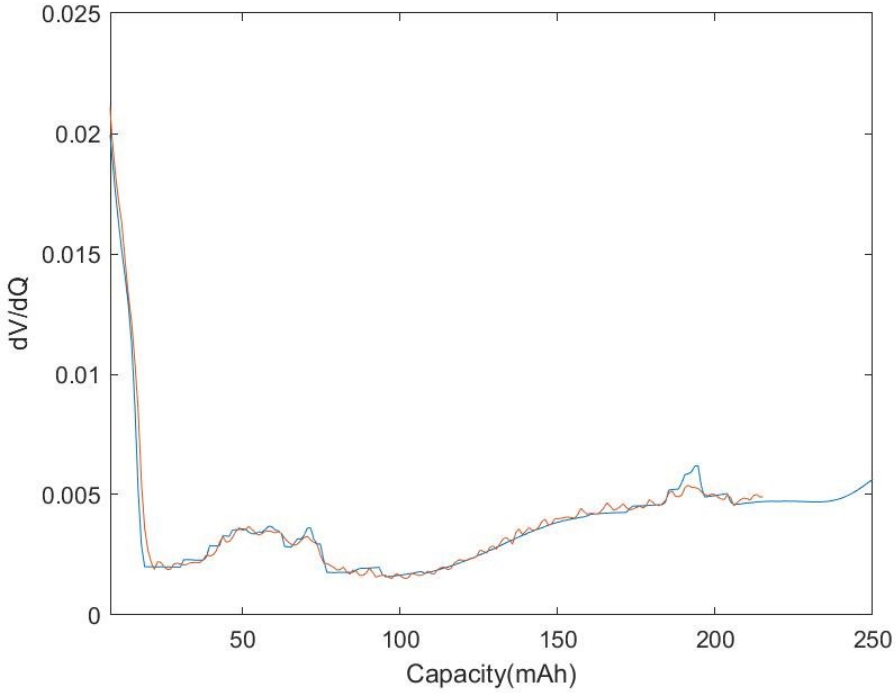

Figure A.33: dV/dQ fit of the checkup cycle a 25% DOD C/10 LC cell at 40°C at cycle number 183 obtained using the automatic dV/dQ analysis program. The orange line represents experimental data and the blue line represent the theoretical fit. The units of dV/dQ are in V/mAh.

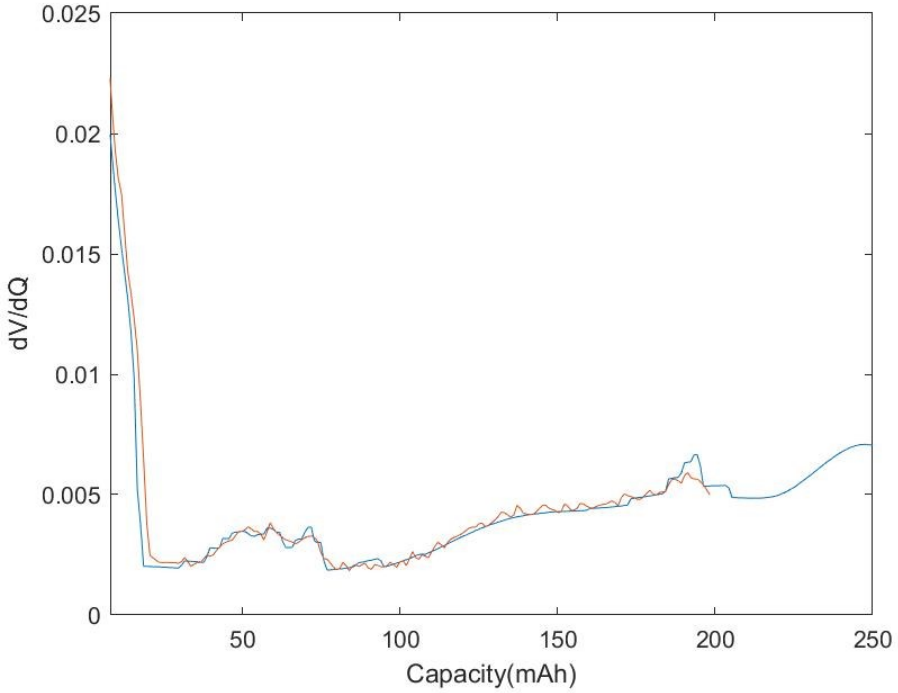

Figure A.34: dV/dQ fit of a checkup cycle from a 25% DOD C/10 LC cell at 40°C and cycle number 3823 obtained using the automatic dV/dQ analysis program. The orange line represents experimental data and the blue line represent the theoretical fit. The units of dV/dQ are in V/mAh.

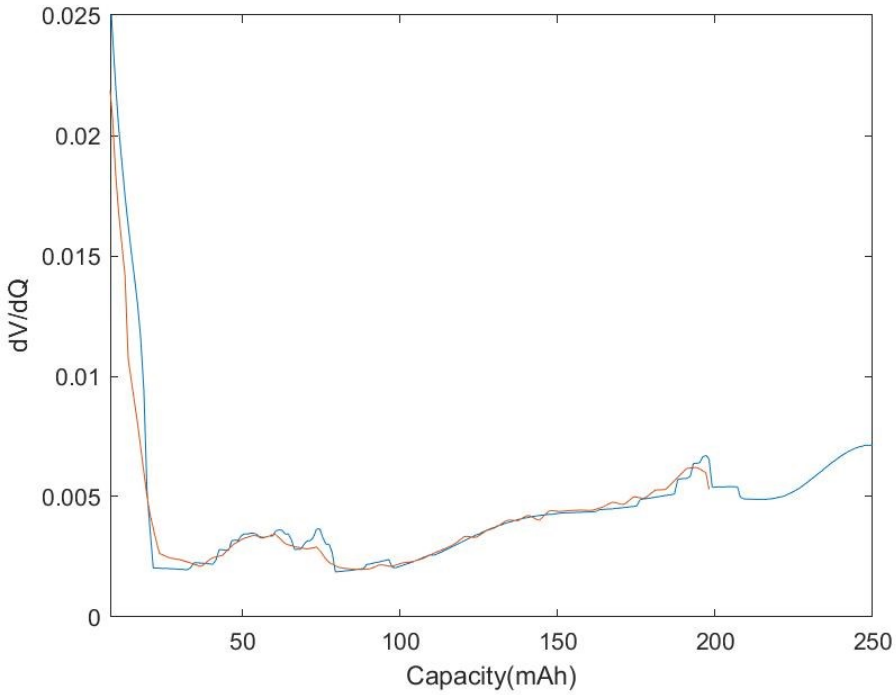

Figure A.35: dV/dQ fit of a checkup cycle from a 25% DOD C/10 UC cell at 40°C and cycle number 354 obtained using the automatic dV/dQ analysis program. The orange line represents experimental data and the blue line represent the theoretical fit. The units of dV/dQ are in V/mAh.

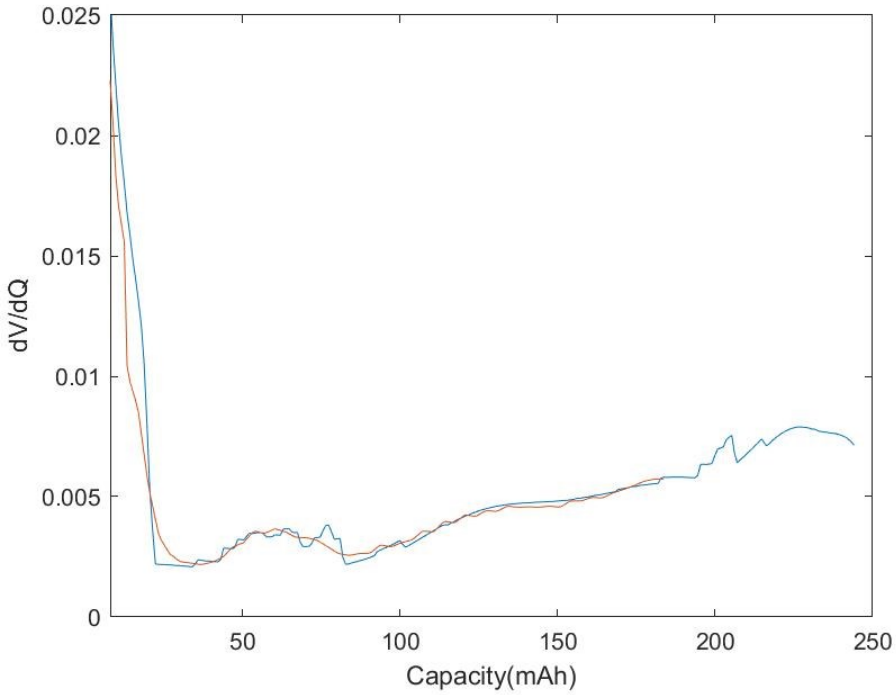

Figure A.36: dV/dQ fit of a checkup cycle from a 25% DOD C/10 UC cell at 40°C and cycle number 3574 obtained using the automatic dV/dQ analysis program. The orange line represents experimental data and the blue line represent the theoretical fit. The units of dV/dQ are in V/mAh.

Comparison between lithium inventory loss results and capacity loss

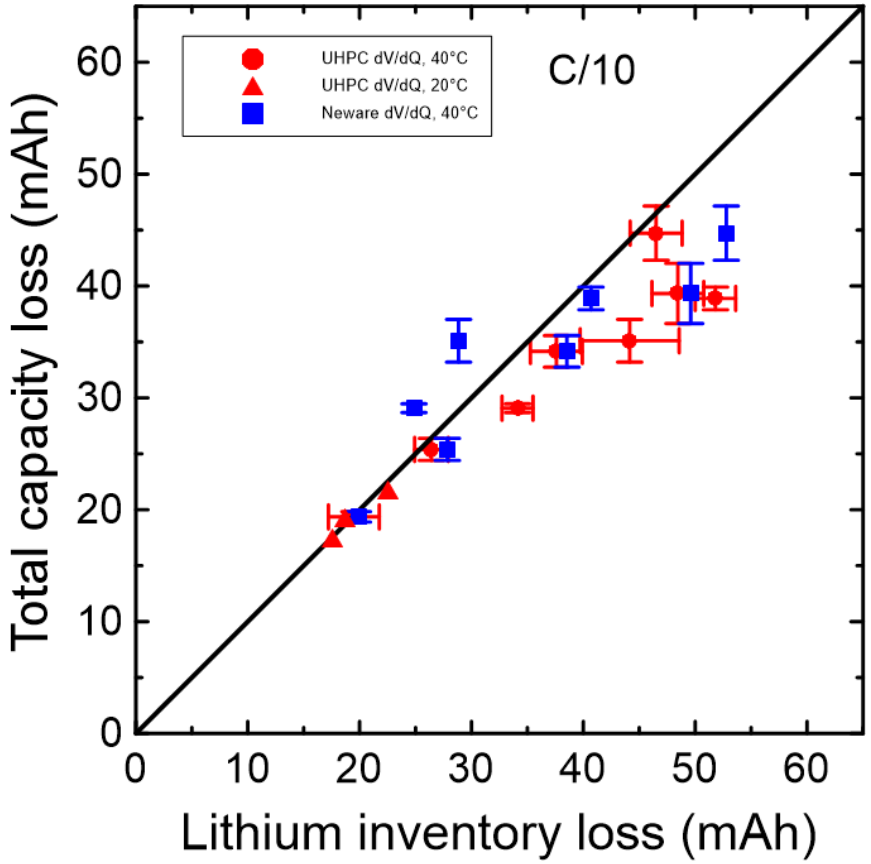

Figure A.37: Comparison of measured capacity loss and lithium inventory loss determined by dV/dQ analysis for cells tested at C/10. The circles and squares show both fixed upper cutoff and fixed lower cutoff data at 40°C, respectively while the triangles show the data for fixed upper cutoff cells at 20°C. The lithium inventory loss data at 100% DOD C/10, 20°C is not available.

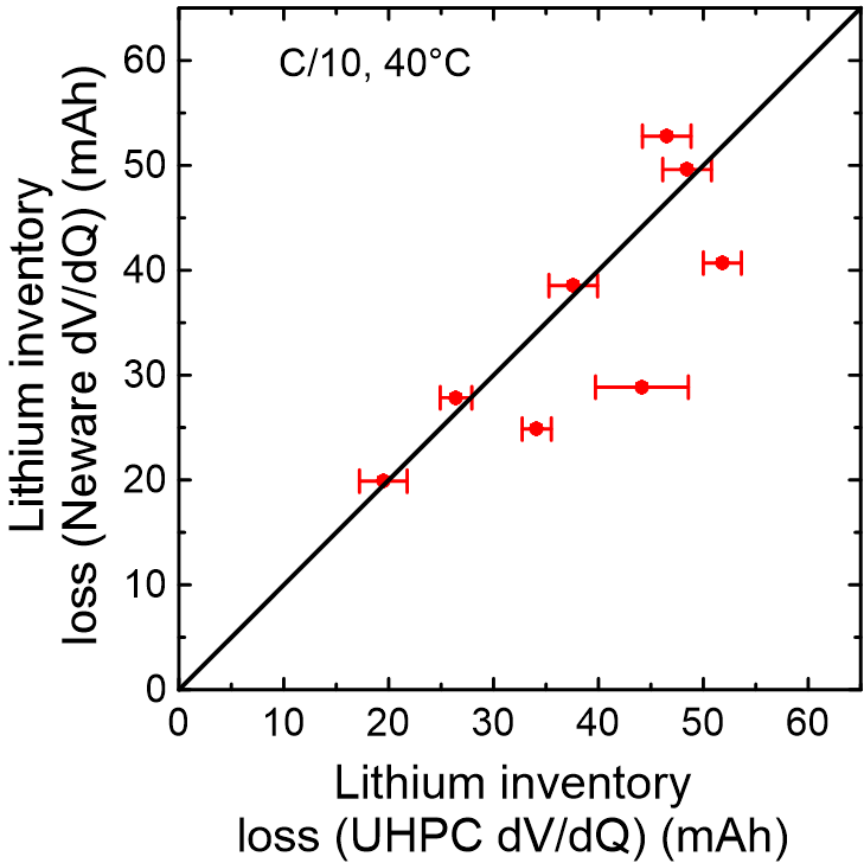

Figure A.38: Comparison of lithium inventory loss obtained from UHPC dV/dQ analysis and Neware dV/dQ analysis. All the data from cells that cycled at 40°C and C/10 are shown. Data at 20°C is not available. The error between the two methods is mostly due to the different way that the initial slippage is calculated. For the UHPC dV/dQ, the initial slippage was fixed at 25 mAh for all cells. For the Neware dV/dQ, it was possible to figure out the initial slippage of the cells using the Neware data. On average, the initial slippage value was found to be around 33 mAh (oscillating between 25 and 45 mAh). This creates an error 8 mAh on average for some cells.

Comparison between parameter C (ΔV) and positive mass loss

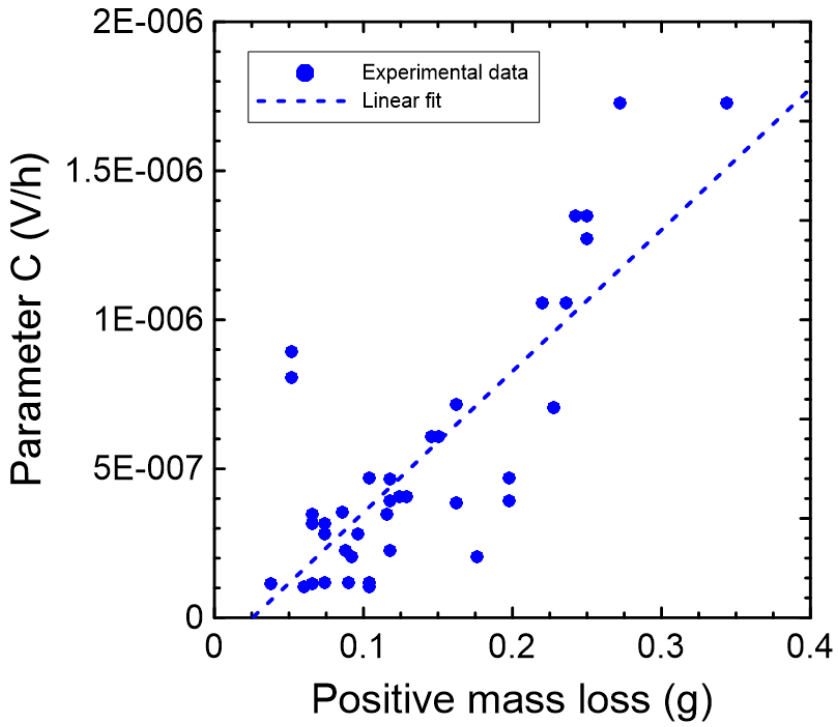

Figure A.39: The parameter C from ΔV = C t + D, plotted versus the positive electrode active mass loss. The linear fit was done on ΔV of the check-up cycles (C/10 100% DOD cycles) of LC and UC cells that cycled at 40°C as shown in Figures A.18 and A.26. The linear fit in the graph above shows that the data is mostly linear. Points that are far from the line are thought to be a result of dV/dQ fitting errors.

State of charge maps

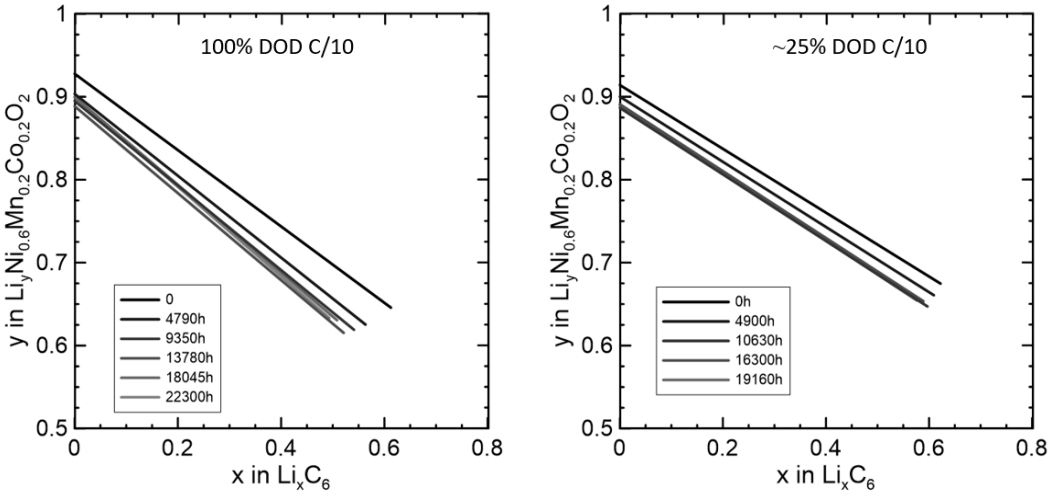

Figure A.40: State of charge map[122] of 100% DOD and ~25% DOD UC cells that cycled at 40°C and C/10.

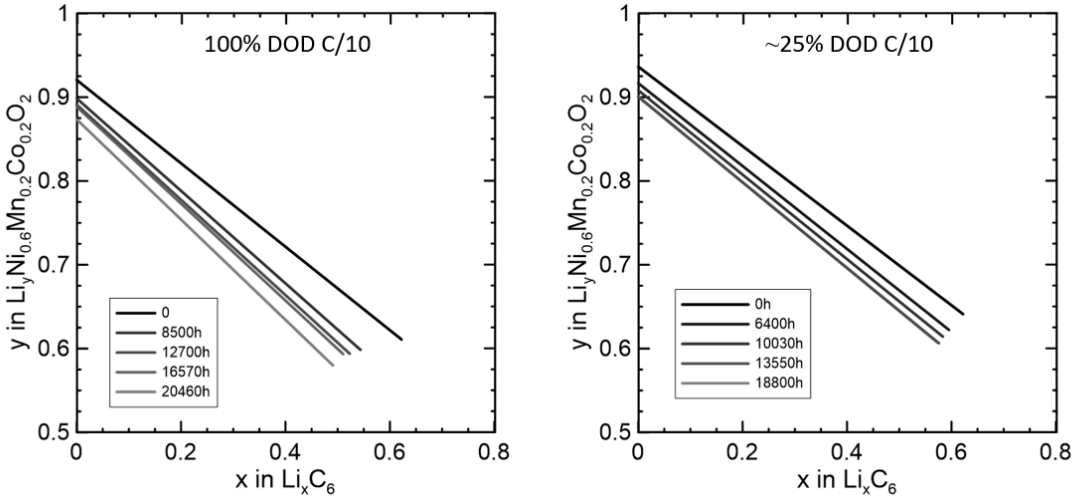

Figure A.41: State of charge map[122] of 100% DOD and ~25% DOD LC cells that cycled at 40°C and C/10.

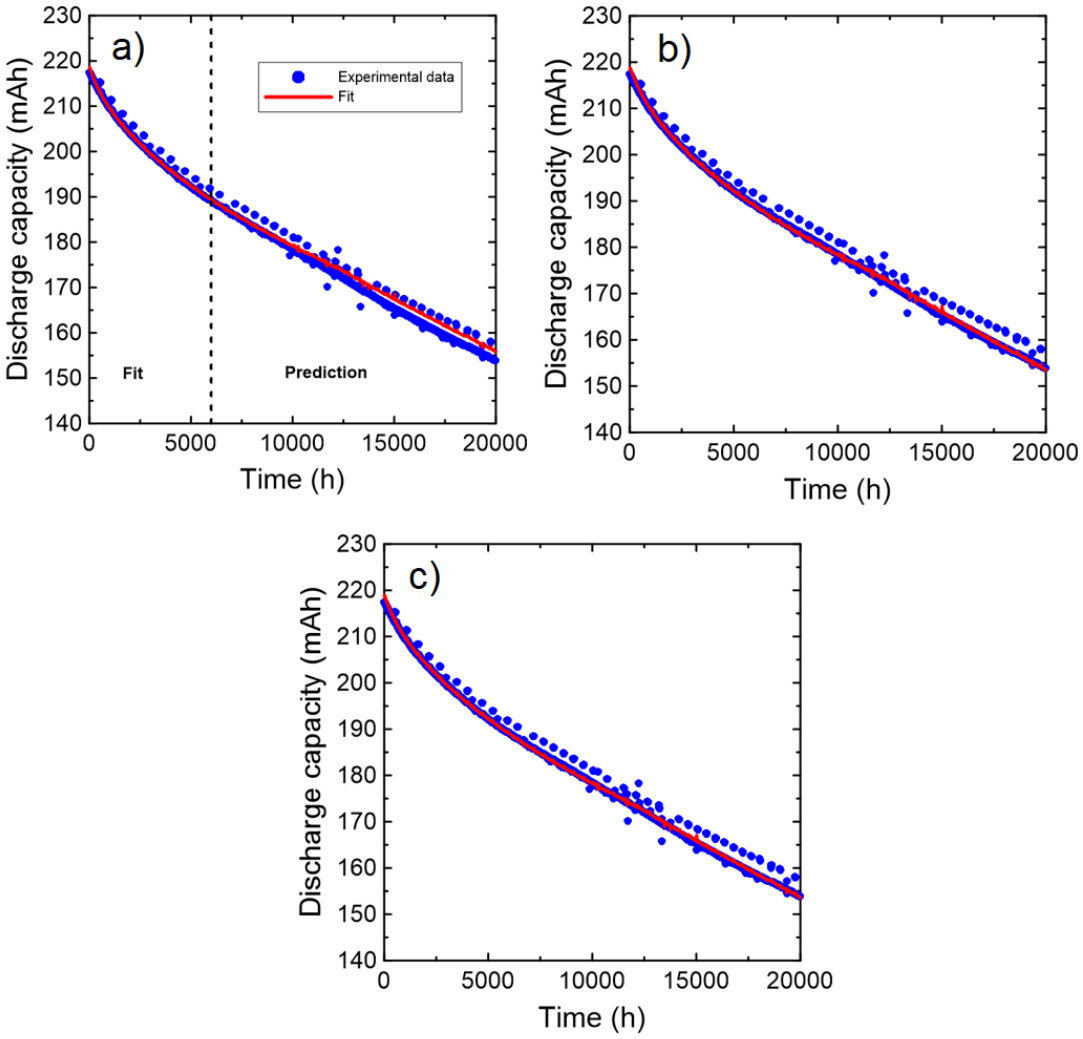

Figure A.42: Fits, using different models, of a 100% DOD C/3 LC cells that cycled at 40°C. The fit in a) used (Equation 3) to fit the data between 0 h and 6000 h, the fit in b) used (Equation 3) to fit all the data between 0 h and 20000 h and the fit in c) used (Equation 3) to fit all the data between 0 h and 20000 h but neglected the Q_{CV} term. The fitting values found were a) Q_0 = 216.3 mAh, A = 0.001886, b) Q_0 = 217.6 mAh, A = 0.001982 and c) Q_0 = 220.2 mAh, A = 0.001845. In all cases, $\left(\left.\frac{dQ}{dV}\right|_L + \left.\frac{dQ}{dV}\right|_U\right) = 225$ was used. This shows that the parameter A can be reasonably approximated by neglecting the Q_{CV} term.

Capacity and impedance fit versus time

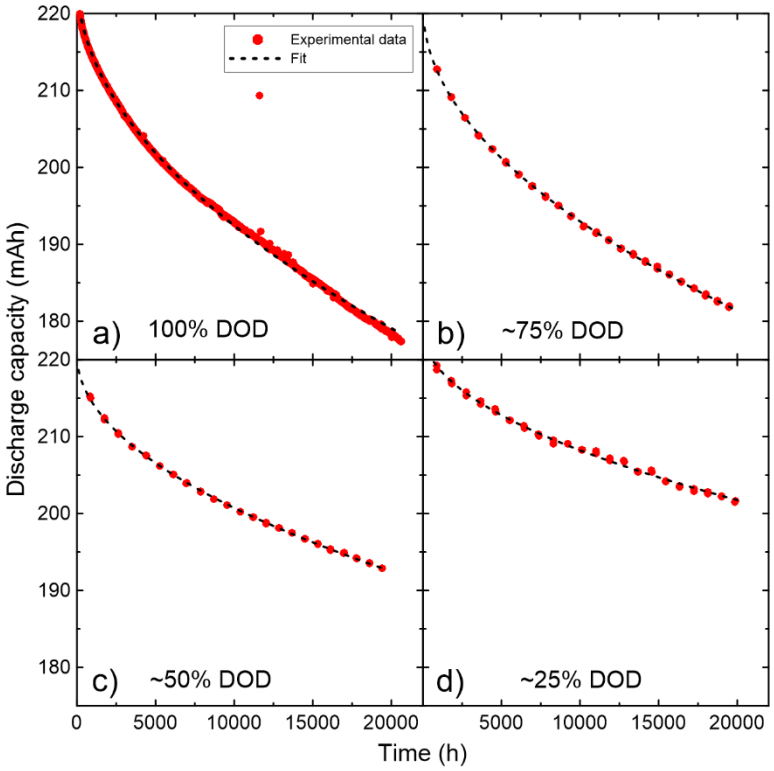

Figure A.43: Square root of time fit to the checkup cycles of the fixed lower cutoff cells at C/10 and 40°C for four different DOD values: a) 100% DOD, b) ~75% DOD, c) ~50% DOD and d) ~25% DOD. Equation 1 was used for these fits (the impedance term is assumed negligeable at C/10).

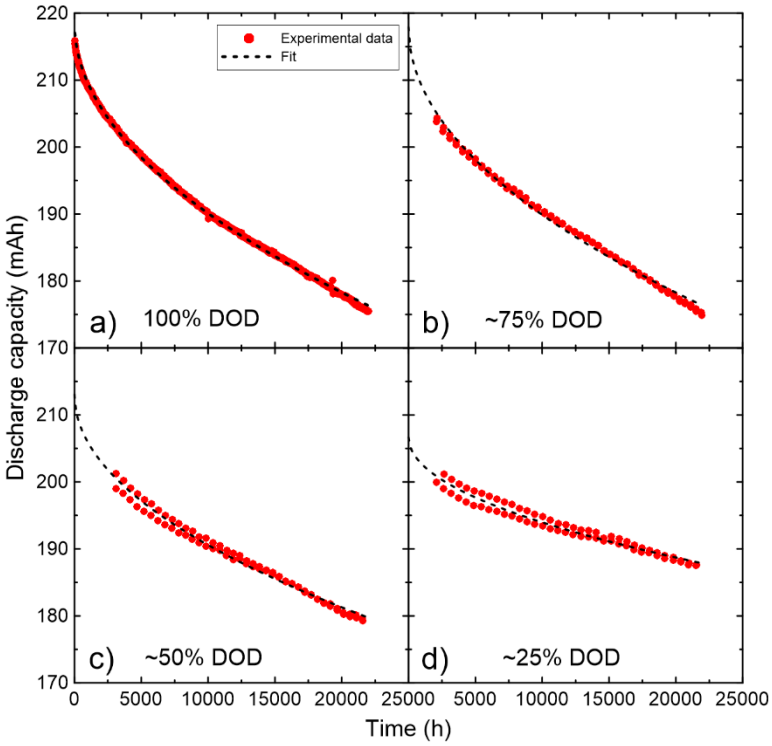

Figure A.44: Square root of time fit to the checkup cycles of the fixed upper cutoff cells at C/10 and 40°C for four different DOD values: a) 100% DOD, b) ~75% DOD, c) ~50% DOD and d) ~25% DOD. Equation 1 was used for these fits (the impedance term is assumed negligeable at C/10).

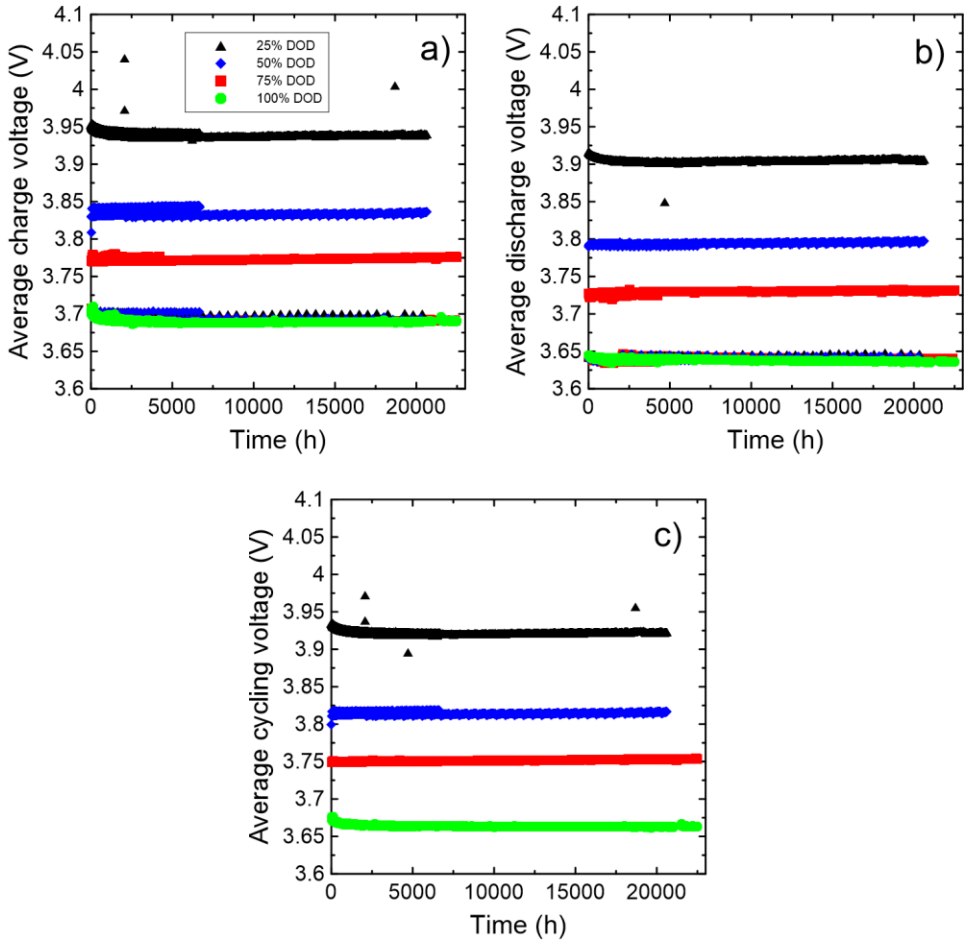

Figure A.45: a) Average charge voltage, b) average discharge voltage and c) average cycling voltage of UC cells that cycled at 20°C and C/10.

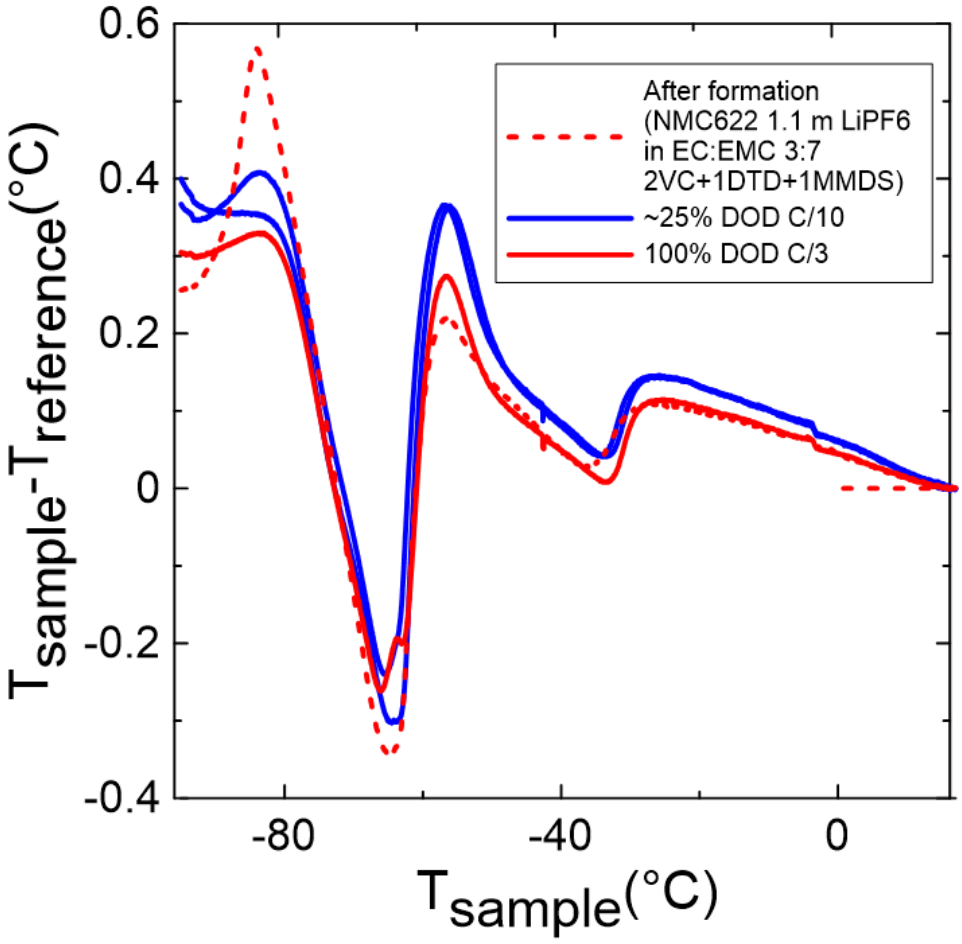

Figure A.46: Comparison between the DTA spectra of ~25% DOD C/10 and 100% DOD C/3 UC cells that cycled for ~20000 hours at 40°C with a fresh NMC622/graphite cell after formation. The fresh cell contained 1.2 M $LiPF_6$ EC:EMC 3:7 with 2% VC + 1% DTD + 1% MMDS, while the cells that cycled for ~20000 hours contained 1.2 M $LiPF_6$ EC:EMC 3:7 with 2% VC + 1% MMDS + 1% TTSPi.

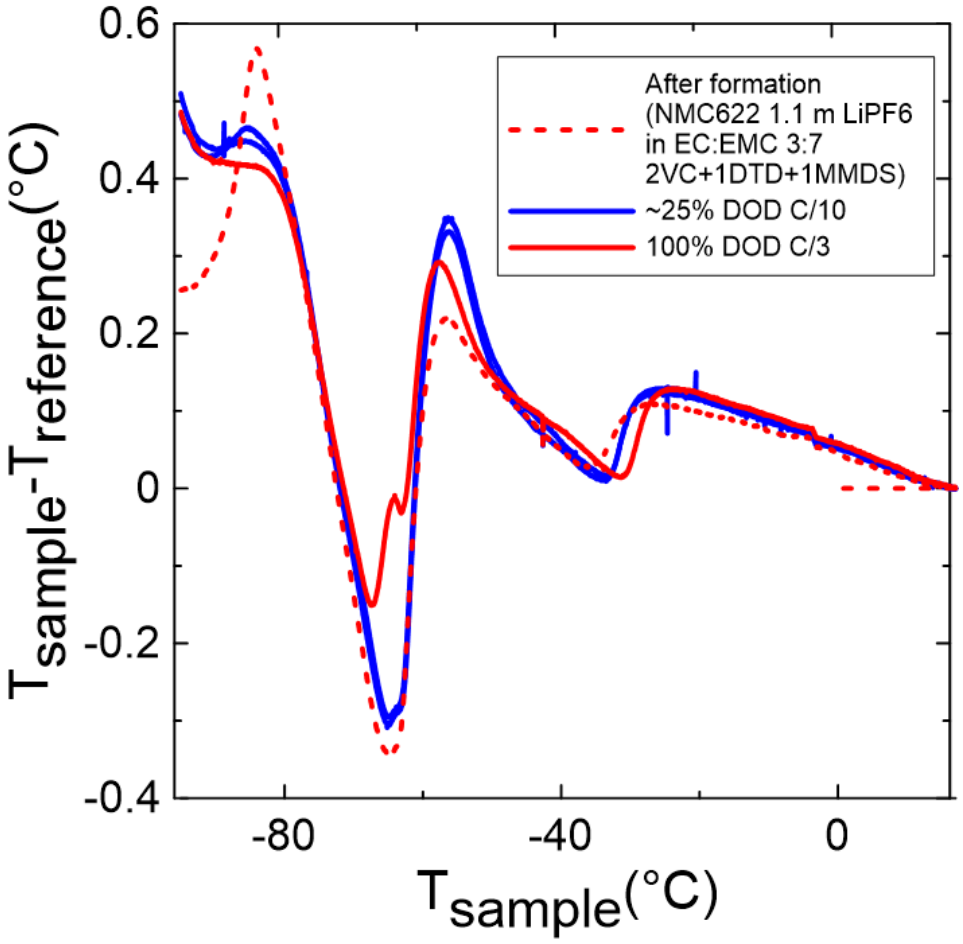

Figure A.47: Comparison between the DTA spectra of ~25% DOD C/10 and 100% DOC C/3 LC cells that cycled for ~20000 hours at 40°C with a fresh NMC622/graphite cell after formation. The fresh cell contained 1.2 M $LiPF_6$ EC:EMC 3:7 with 2% VC + 1% DTD + 1% MMDS, while the cells that cycled for ~20000 hours contained 1.2 M $LiPF_6$ EC:EMC 3:7 with 2% VC + 1% MMDS + 1% TTSPi. The shift of the liquidus peak to higher temperature and the splitting of the solidus peak for the 100% DOD C/3 cell suggests a small amount of salt loss during testing for this cell.

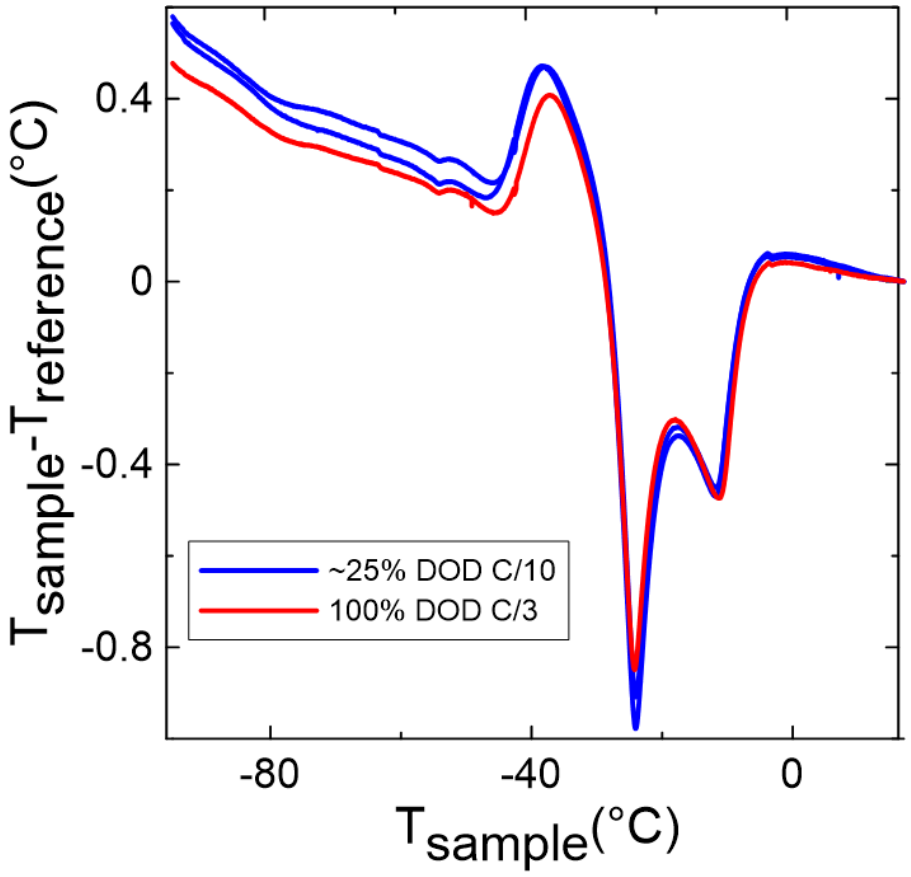

Figure A.48: Comparison between the DTA spectra of ~25% DOD C/10 and 100% DOC C/3 UC cells that cycled for ~20000 hours at 20°C. The cells contained 1.2 M $LiPF_6$ EC:DMC 3:7 with 2% VC + 1% MMDS + 1% TTSPi.

Ultrasonic transmission map of full cells versus voltage

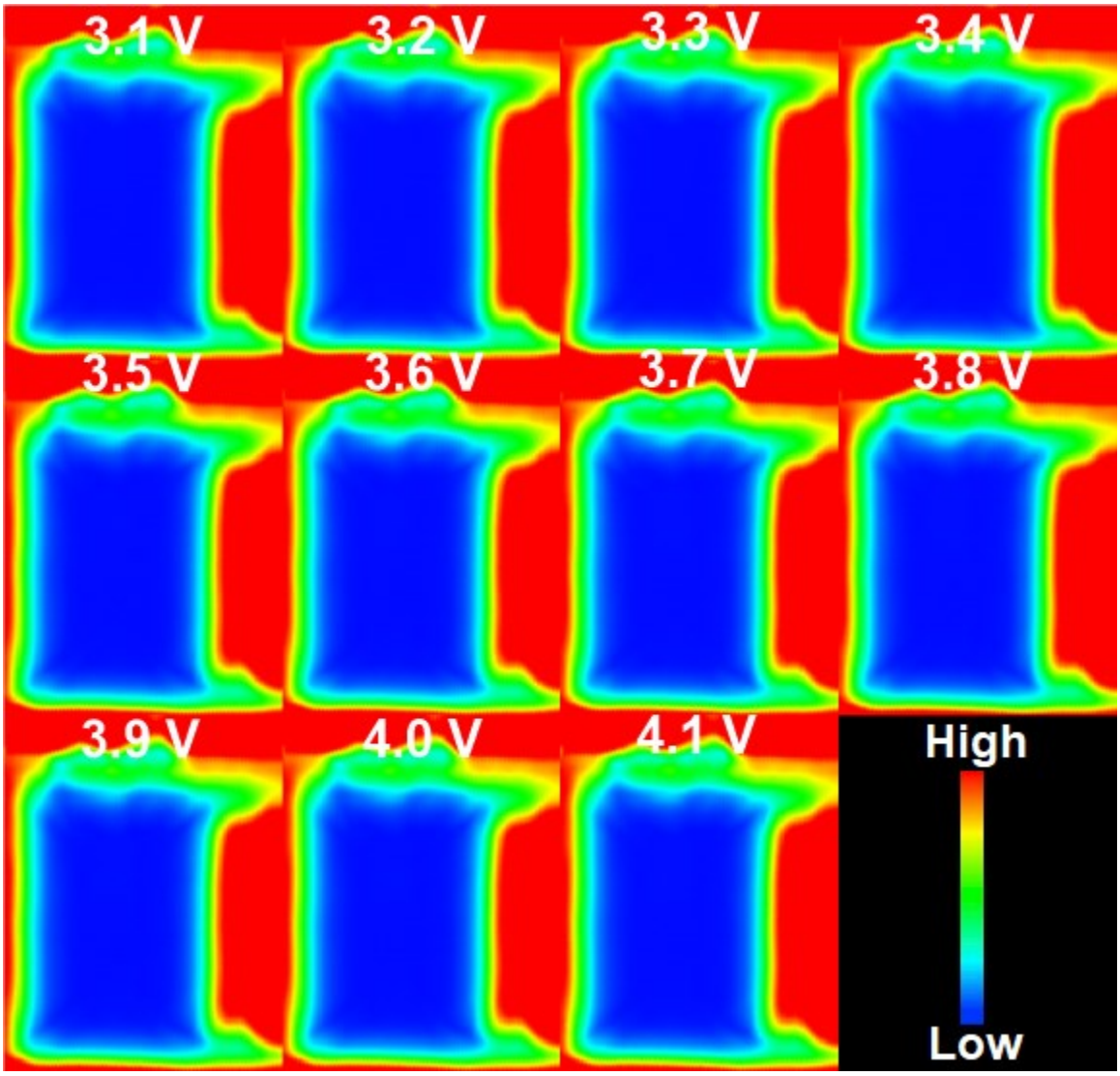

Figure A.49: Ultrasonic transmission as a function of voltage of a 75% DOD C/5 UC cell after 20000h of cycling at 40°C. Cell voltage at which the false color image was captured are indicated. The scale show that blue correspond to low transmission and red to high transmission.

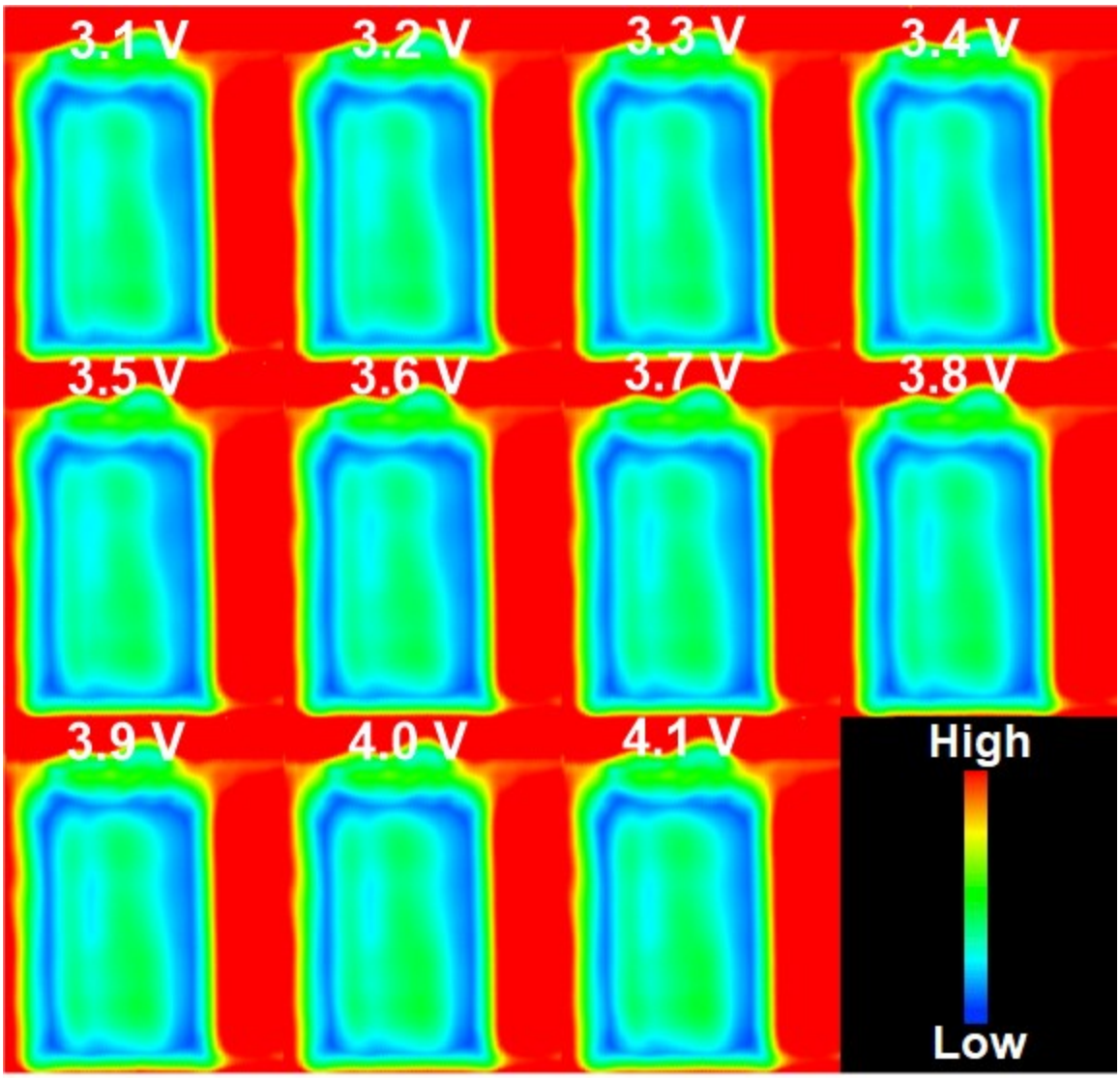

Figure A.50: Ultrasonic transmission as a function of voltage of a 25% DOD C/5 UC cell after 20000h of cycling at 40°C. Cell voltage at which the false color image was captured are indicated. The scale show that blue correspond to low transmission and red to high transmission.

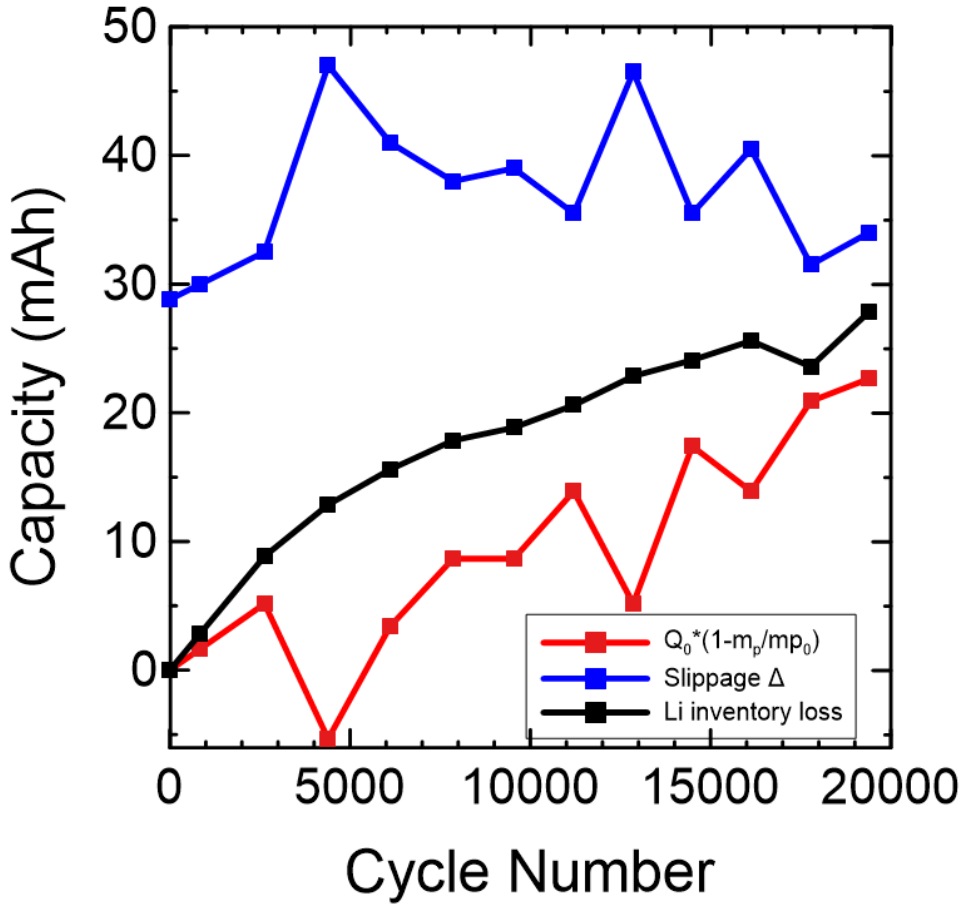

Figure A.51: Figure showing the two contributions to Equation 10: the slippage Δ (in blue) and Q_p (in red). The lithium inventory loss is in black. This Figure show that the noise in the curve of Δ is anti-correlated to the noise in the curve of Q_p. Note that the noise is no longer present in the lithium inventory loss curve. The data show is for a LC cells that cycled at 40°C, C/10 and 75% DOD.

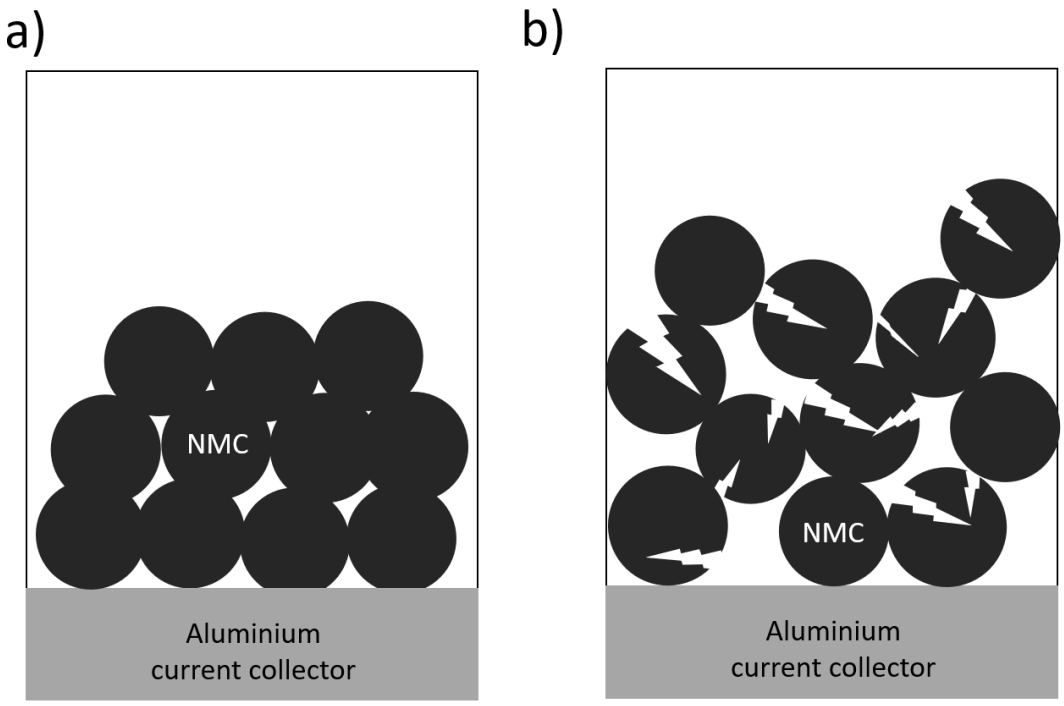

Figure A.52: a) A schematic showing a fresh electrode on a current collector with low porosity. b) A schematic of the same electrode after many charge-discharge cycles. Due to microcracking, the electrode has become thicker, and the porosity has increased. Therefore, more electrolyte would be required to fill the pores.

APPENDIX B: PERMISSIONS

2021-06-22

Impact of Functionalization and Co-Additives on Dioxazolone Electrolyte Additives

https://iopscience.iop.org/article/10.1149/1945-7111/ab8ed6

I am preparing my Ph.D. thesis for submission to the Faculty of Graduate Studies at Dalhousie University, Halifax, Nova Scotia, Canada. I am seeking your permission to include a manuscript version of the following paper(s) as a chapter in the thesis:

Impact of Functionalization and Co-Additives on Dioxazolone Electrolyte Additives, R. Gauthier, D. S. Hall, K. Lin, J. Baltazar, T. Hynes, and J. R. Dahn, J. Electrochem. Soc., 167, 080540 (2020).

Canadian graduate theses are reproduced by the Library and Archives of Canada (formerly National Library of Canada) through a non-exclusive, world-wide license to reproduce, loan, distribute, or sell theses. I am also seeking your permission for the material described above to be reproduced and distributed by the LAC(NLC). Further details about the LAC(NLC) thesis program are available on the LAC(NLC) website (www.nlc-bnc.ca).

Full publication details and a copy of this permission letter will be included in the thesis.

Yours sincerely,

Roby Gauthier, PhD candidate

Department of Physics and Atmospheric Science

Dalhousie University

Dear Roby Gauthier,

Thank you for your request to reproduce content from Journal of The Electrochemical Society.

The content you have requested was published under a CC BY licence which permits reuse for any purposes, even commercial, provided the licence terms are adhered to.

Therefore you may reuse the content without permission, so long as you reference it adequately and adhere to the terms of the CC BY licence.
Please note this does not apply to any content/figure which is credited to another source in our publication or has been obtained from a third party, which is not available under a suitable open access licence. Express permission for such content/figures must be obtained from the copyright owner.

Kind regards,

Sophie

Copyright & Permissions Team
Sophie Brittain - Rights & Permissions Assistant
Cameron Wood - Legal & Rights Adviser
Contact Details
E-mail: permissions@ioppublishing.org

REFERENCES

1. T. Marks, S. Trussler, A. J. Smith, D. Xiong, and J. R. Dahn, *J. Electrochem. Soc.*, **158**, A51–A57 (2011).

2. V. Murray, D. S. Hall, and J. R. Dahn, *J. Electrochem. Soc.*, **166**, A329–A333 (2019).

3. Q. Liu, S. Li, S. Wang, X. Zhang, S. Zhou, Y. Bai, J. Zheng, and X. Lu, *J. Phys. Chem. Lett.*, **9**, 5567–5573 (2018).

4. M. K. G. Bauer and J. R. Dahn, *J. Electrochem. Soc.*, **168**, 020501 (2021).

5. B. Gyenes, D. A. Stevens, V. L. Chevrier, and J. R. Dahn, *J. Electrochem. Soc.*, **162**, A278 (2014).

6. W. Bao, J. Wan, X. Han, X. Cai, H. Zhu, D. Kim, D. Ma, Y. Xu, J. N. Munday, H. D. Drew, M. S. Fuhrer, and L. Hu, *Nat Commun*, **5**, 4224 (2014).

7. S. L. Glazier, J. Li, A. J. Louli, J. P. Allen, and J. R. Dahn, *J. Electrochem. Soc.*, **164**, A3545 (2017).

8. W. Lee, S. Muhammad, T. Kim, H. Kim, E. Lee, M. Jeong, S. Son, J.-H. Ryou, and W.-S. Yoon, *Advanced Energy Materials*, **8**, 1701788 (2018).

9. A. J. Louli, J. Li, S. Trussler, C. R. Fell, and J. R. Dahn, *J. Electrochem. Soc.*, **164**, A2689–A2696 (2017).

10. K. Xu, *Chem. Rev.*, **104**, 4303–4418 (2004).

11. D. S. Hall, A. Eldesoky, E. R. Logan, E. M. Tonita, X. Ma, and J. R. Dahn, *J. Electrochem. Soc.*, **165**, A2365–A2373 (2018).

12. X. Ma, J. E. Harlow, J. Li, L. Ma, D. S. Hall, S. Buteau, M. Genovese, M. Cormier, and J. R. Dahn, *J. Electrochem. Soc.*, **166**, A711–A724 (2019).

13. D. S. Hall, T. Hynes, and J. R. Dahn, *J. Electrochem. Soc.*, **165**, A2961–A2967 (2018).

14. D. S. Hall, J. P. Allen, S. L. Glazier, L. D. Ellis, L. Ma, J. M. Peters, I. G. Hill, and J. R. Dahn, *J. Electrochem. Soc.*, **164**, A3445–A3453 (2017).

15. E. R. Logan, E. M. Tonita, K. L. Gering, J. Li, X. Ma, L. Y. Beaulieu, and J. R. Dahn, *J. Electrochem. Soc.*, **165**, A21–A30 (2018).

16. E. R. Logan, E. M. Tonita, K. L. Gering, L. Ma, M. K. G. Bauer, J. Li, L. Y. Beaulieu, and J. R. Dahn, *J. Electrochem. Soc.*, **165**, A705–A716 (2018).

17. S. S. Zhang, *Journal of Power Sources*, **162**, 1379–1394 (2006).

18. D. Aurbach, K. Gamolsky, B. Markovsky, Y. Gofer, M. Schmidt, and U. Heider, *Electrochimica Acta*, **47**, 1423–1439 (2002).

19. X. Li, Z. Yin, X. Li, and C. Wang, *Ionics*, **20**, 795–801 (2014).

20. J. Xia, N. N. Sinha, L. P. Chen, and J. R. Dahn, *J. Electrochem. Soc.*, **161**, A264–A274 (2014).

21. L. Madec, R. Petibon, J. Xia, J.-P. Sun, I. G. Hill, and J. R. Dahn, *J. Electrochem. Soc.*, **162**, A2635–A2645 (2015).

22. J. Xia, J. E. Harlow, R. Petibon, J. C. Burns, L. P. Chen, and J. R. Dahn, *J. Electrochem. Soc.*, **161**, A547–A553 (2014).

23. K.-E. Kim, J. Y. Jang, I. Park, M.-H. Woo, M.-H. Jeong, W. C. Shin, M. Ue, and N.-S. Choi, *Electrochemistry Communications*, **61**, 121–124 (2015).

24. D. Y. Wang, N. N. Sinha, J. C. Burns, C. P. Aiken, R. Petibon, and J. R. Dahn, *J. Electrochem. Soc.*, **161**, A467–A472 (2014).

25. A. Meazah Haregewoin, A. Sorsa Wotango, and B.-J. Hwang, *Energy & Environmental Science*, **9**, 1955–1988 (2016).

26. L. E. Ouatani, R. Dedryvère, C. Siret, P. Biensan, and D. Gonbeau, *J. Electrochem. Soc.*, **156**, A468–A477 (2009).

27. L. Madec, R. Petibon, K. Tasaki, J. Xia, J.-P. Sun, I. G. Hill, and J. R. Dahn, *Phys. Chem. Chem. Phys.*, **17**, 27062–27076 (2015).

28. L. E. Ouatani, R. Dedryvère, C. Siret, P. Biensan, S. Reynaud, P. Iratçabal, and D. Gonbeau, *J. Electrochem. Soc.*, **156**, A103–A113 (2009).

29. E. Girma Leggesse and J.-C. Jiang, *RSC Advances*, **2**, 5439–5446 (2012).

30. M. Xu, W. Li, and B. L. Lucht, *Journal of Power Sources*, **193**, 804–809 (2009).

31. B. Zhang, M. Metzger, S. Solchenbach, M. Payne, S. Meini, H. A. Gasteiger, A. Garsuch, and B. L. Lucht, *J. Phys. Chem. C*, **119**, 11337–11348 (2015).

32. B. Yang, H. Zhang, L. Yu, W. Fan, and D. Huang, *Electrochimica Acta*, **221**, 107–114 (2016).

33. G. Yang, J. Shi, C. Shen, S. Wang, L. Xia, H. Hu, H. Luo, Y. Xia, and Z. Liu, *RSC Advances*, **7**, 26052–26059 (2017).

34. Y. Jin, N.-J. H. Kneusels, L. E. Marbella, E. Castillo-Martínez, P. C. M. M. Magusin, R. S. Weatherup, E. Jónsson, T. Liu, S. Paul, and C. P. Grey, *J. Am. Chem. Soc.*, **140**, 9854–9867 (2018).

35. B. Liu, B. Li, and S. Guan, *Electrochem. Solid-State Lett.*, **15**, A77–A79 (2012).

36. R. McMillan, H. Slegr, Z. X. Shu, and W. Wang, *Journal of Power Sources*, **81–82**, 20–26 (1999).

37. N. N. Sinha, J. C. Burns, and J. R. Dahn, *J. Electrochem. Soc.*, **161**, A1084–A1089 (2014).

38. L. Ma, J. Xia, and J. R. Dahn, *J. Electrochem. Soc.*, **162**, A1170–A1174 (2015).

39. J. Xia, N. N. Sinha, L. P. Chen, G. Y. Kim, D. J. Xiong, and J. R. Dahn, *J. Electrochem. Soc.*, **161**, A84–A88 (2014).

40. S. Röser, A. Lerchen, L. Ibing, X. Cao, J. Kasnatscheew, F. Glorius, M. Winter, and R. Wagner, *Chem. Mater.*, **29**, 7733–7739 (2017).

41. X. Cheng, R. Zhang, C. Zhao, F. Wei, J. Zhang, and Q. Zhang, *Adv Sci (Weinh)*, **3**, 1500213 (2015).

42. H. M. Dahn, A. J. Smith, J. C. Burns, D. A. Stevens, and J. R. Dahn, *J. Electrochem. Soc.*, **159**, A1405–A1409 (2012).

43. P. Hohenberg and W. Kohn, *Phys. Rev.*, **136**, B864–B871 (1964).

44. W. Kohn and L. J. Sham, *Phys. Rev.*, **140**, A1133–A1138 (1965).

45. T. Ando, K. Ikeda, and Y. Suzuki, *Prog Theor Phys*, **54**, 119–133 (1975).

46. P. a. M. Dirac, *Mathematical Proceedings of the Cambridge Philosophical Society*, **26**, 376–385 (1930).

47. J. L. McDonagh, M. A. Vincent, and P. L. A. Popelier, *Chemical Physics Letters*, **662**, 228–234 (2016).

48. G. Calogero, thesis, (2015).

49. P. J. Stephens, F. J. Devlin, C. F. Chabalowski, and M. J. Frisch, *J. Phys. Chem.*, **98**, 11623–11627 (1994).

50. R. G. Parr and W. Yang, *Density-functional theory of atoms and molecules*, Oxford University Press ; Clarendon Press, New York; Oxford, Engl., (1994).

51. S. H. Vosko, L. Wilk, and M. Nusair, *Can. J. Phys.*, **58**, 1200–1211 (1980).

52. A. D. Becke, *Phys. Rev. A*, **38**, 3098–3100 (1988).

53. C. Lee, W. Yang, and R. G. Parr, *Phys. Rev. B*, **37**, 785–789 (1988).

54. https://gaussian.com/thermo/.

55. H. G. Mayfield and W. E. Bull, *J. Chem. Soc. A*, 2279–2281 (1971).

56. J. Tomasi, B. Mennucci, and R. Cammi, *Chem. Rev.*, **105**, 2999–3094 (2005).

57. J. Tomasi, B. Mennucci, and E. Cancès, *Journal of Molecular Structure: THEOCHEM*, **464**, 211–226 (1999).

58. J. Self, D. S. Hall, L. Madec, and J. R. Dahn, *Journal of Power Sources*, **298**, 369–378 (2015).

59. A. A. Isse and A. Gennaro, *J. Phys. Chem. B*, **114**, 7894–7899 (2010).

60. W. M. Haynes, editor.) Haynes William M., and T. & Francis, *CRC handbook of chemistry and physics*, Ninety Fifth edition., Boca Raton, FL : Taylor and Francis, an imprint of CRC Press, (2014) https://trove.nla.gov.au/version/215802082.

61. Z. Deng, Z. Huang, Y. Shen, Y. Huang, H. Ding, A. Luscombe, M. Johnson, J. E. Harlow, R. Gauthier, and J. R. Dahn, *Joule*, **4**, 2017–2029 (2020).

62. T. Bond, J. Zhou, and J. Cutler, *J. Electrochem. Soc.*, **164**, A6158 (2016).

63. K. R. Adair, M. N. Banis, Y. Zhao, T. Bond, R. Li, and X. Sun, *Advanced Materials*, **32**, 2002550 (2020).

64. Y. Wu, S. Saxena, Y. Xing, Y. Wang, C. Li, W. K. C. Yung, and M. Pecht, *Energies*, **11**, 925 (2018).

65. D. P. Finegan, M. Scheel, J. B. Robinson, B. Tjaden, I. Hunt, T. J. Mason, J. Millichamp, M. Di Michiel, G. J. Offer, G. Hinds, D. J. L. Brett, and P. R. Shearing, *Nat Commun*, **6**, 6924 (2015).

66. L. Willenberg, P. Dechent, G. Fuchs, M. Teuber, M. Eckert, M. Graff, N. Kürten, D. U. Sauer, and E. Figgemeier, *J. Electrochem. Soc.*, **167**, 120502 (2020).

67. A. J. Smith, H. M. Dahn, J. C. Burns, and J. R. Dahn, *J. Electrochem. Soc.*, **159**, A705–A710 (2012).

68. I. Bloom, A. N. Jansen, D. P. Abraham, J. Knuth, S. A. Jones, V. S. Battaglia, and G. L. Henriksen, *Journal of Power Sources*, **139**, 295–303 (2005).

69. I. Bloom, J. Christophersen, and K. Gering, *Journal of Power Sources*, **139**, 304–313 (2005).

70. I. Bloom, L. K. Walker, J. K. Basco, D. P. Abraham, J. P. Christophersen, and C. D. Ho, *Journal of Power Sources*, **195**, 877–882 (2010).

71. N. N. Sinha, A. J. Smith, J. C. Burns, G. Jain, K. W. Eberman, E. Scott, J. P. Gardner, and J. R. Dahn, *J. Electrochem. Soc.*, **158**, A1194–A1201 (2011).

72. T. M. Bond, J. C. Burns, D. A. Stevens, H. M. Dahn, and J. R. Dahn, *J. Electrochem. Soc.*, **160**, A521–A527 (2013).

73. M. Frisch, G. Trucks, H. Schlegel, G. Scuseria, M. Robb, J. Cheeseman, G. Scalmani, V. Barone, B. Mennucci, G. Petersson, H. Nakatsuji, M. Caricato, X. Li, H. Hratchian, A. Izmaylov, J. Bloino, G. Zheng, J. Sonnenberg, M. Hada, M. Ehara, K. Toyota, R. Fukuda, J. Hasegawa, M. Ishida, T. Nakajima, Y. Honda, O. Kitao, H. Nakai, T. Vreven, J. Montgomery, J. Peralta, F. Ogliaro, M. Bearpark, J. Heyd, E. Brothers, K. Kudin, V. Staroverov, R. Kobayashi, J. Normand, K. Raghavachari, A. Rendell, J. Burant, S. Iyengar, J. Tomasi, M. Cossi, N. Rega, J. Millam, M. Klene, J. Knox, J. Cross, V. Bakken, C. Adamo, J. Jaramillo, R. Gomperts, R. Stratmann, O. Yazyev, A. Austin, R. Cammi, C. Pomelli, J. Ochterski, R. Martin, K. Morokuma, V. Zakrzewski, G. Voth, P.

Salvador, J. Dannenberg, S. Dapprich, A. Daniels, Farkas, J. Foresman, J. Ortiz, J. Cioslowski, and D. Fox, *Gaussian 09*, Gaussian, Inc., Wallingford, CT, USA, (2009).

74. D. S. Hall, J. Self, and J. R. Dahn, *The Journal of Physical Chemistry C*, **119**, 22322–22330 (2015).

75. O. Borodin, W. Behl, and T. R. Jow, *The Journal of Physical Chemistry C*, **117**, 8661–8682 (2013).

76. O. Borodin, M. Olguin, C. E. Spear, K. W. Leiter, and J. Knap, *Nanotechnology*, **26**, 354003 (2015).

77. A. von Cresce and K. Xu, *Electrochem. Solid-State Lett.*, **14**, A154–A156 (2011).

78. S. A. Delp, O. Borodin, M. Olguin, C. G. Eisner, J. L. Allen, and T. R. Jow, *Electrochimica Acta*, **209**, 498–510 (2016).

79. C. P. Aiken, J. Xia, D. Y. Wang, D. A. Stevens, S. Trussler, and J. R. Dahn, *J. Electrochem. Soc.*, **161**, A1548–A1554 (2014).

80. MATLAB, *9.8.0.1417392 (R2020a)*, The MathWorks Inc., Natick, Massachusetts, (2020).

81. R. P. Day, J. Xia, R. Petibon, J. Rucska, H. Wang, A. T. B. Wright, and J. R. Dahn, *J. Electrochem. Soc.*, **162**, A2577 (2015).

82. T. W. Wysokinski, D. Chapman, G. Adams, M. Renier, P. Suortti, and W. Thomlinson, *Nuclear Instruments and Methods in Physics Research Section A: Accelerators, Spectrometers, Detectors and Associated Equipment*, **775**, 1–4 (2015).

83. M. Vogelgesang, T. Farago, T. F. Morgeneyer, L. Helfen, T. dos Santos Rolo, A. Myagotin, and T. Baumbach, *J Synchrotron Rad*, **23**, 1254–1263 (2016).

84. T. Hynes, D. S. Hall, A. Speed, J. D. Masuda, and J. Dahn, *Can. J. Chem.* (2020).

85. D. S. Hall, J. Li, K. Lin, N. Stakheiko, J. Baltazar, and J. R. Dahn, *J. Electrochem. Soc.*, **166**, A793–A801 (2019).

86. D. S. Hall, M. Nie, L. D. Ellis, S. L. Glazier, S. Hyatt, R. Petibon, A. Xiao, W. M. Lamanna, K. Smith, I. G. Hill, and J. R. Dahn, *J. Electrochem. Soc.*, **163**, A773–A780 (2016).

87. Y. Okamoto and Y. Kubo, *ACS Omega*, **3**, 7868–7874 (2018).

88. T. Hou, G. Yang, N. N. Rajput, J. Self, S.-W. Park, J. Nanda, and K. A. Persson, *Nano Energy*, **64**, 103881 (2019).

89. Z. Ding, X. Li, T. Wei, Z. Yin, and X. Li, *Electrochimica Acta*, **196**, 622–628 (2016).

90. D. Weingarth, I. Czekaj, Z. Fei, A. Foelske-Schmitz, P. J. Dyson, A. Wokaun, and R. Kötz, *J. Electrochem. Soc.*, **159**, H611–H615 (2012).

91. R. L. Wang, C. Buhrmester, and J. R. Dahn, *J. Electrochem. Soc.*, **153**, A445–A449 (2006).

92. R. Gauthier, D. S. Hall, T. Taskovic, and J. R. Dahn, *J. Electrochem. Soc.*, **166**, A3707–A3715 (2019).

93. D. J. Xiong, L. D. Ellis, J. Li, H. Li, T. Hynes, J. P. Allen, J. Xia, D. S. Hall, I. G. Hill, and J. R. Dahn, *J. Electrochem. Soc.*, **164**, A3025–A3037 (2017).

94. R. Jung, M. Metzger, F. Maglia, C. Stinner, and H. A. Gasteiger, *J. Electrochem. Soc.*, **164**, A1361–A1377 (2017).

95. R. Jung, M. Metzger, F. Maglia, C. Stinner, and H. A. Gasteiger, *J. Phys. Chem. Lett.*, **8**, 4820–4825 (2017).

96. D. Pritzl, S. Solchenbach, M. Wetjen, and H. A. Gasteiger, *J. Electrochem. Soc.*, **164**, A2625–A2635 (2017).

97. R. Petibon, J. Xia, J. C. Burns, and J. R. Dahn, *J. Electrochem. Soc.*, **161**, A1618–A1624 (2014).

98. N. N. Sinha, A. J. Smith, J. C. Burns, G. Jain, K. W. Eberman, E. Scott, J. P. Gardner, and J. R. Dahn, *J. Electrochem. Soc.*, **158**, A1194–A1201 (2011).

99. J. Self, C. P. Aiken, R. Petibon, and J. R. Dahn, *J. Electrochem. Soc.*, **162**, A796–A802 (2015).

100. L. D. Ellis, J. P. Allen, L. M. Thompson, J. E. Harlow, W. J. Stone, I. G. Hill, and J. R. Dahn, *J. Electrochem. Soc.*, **164**, A3518–A3528 (2017).

101. J. Xia, L. Ma, and J. R. Dahn, *Journal of Power Sources*, **287**, 377–385 (2015).

102. F. Bian, Z. Zhang, and Y. Yang, *Journal of Energy Chemistry*, **23**, 383–390 (2014).

103. K. Wang, L. Xing, Y. Zhu, X. Zheng, D. Cai, and W. Li, *Journal of Power Sources*, **342**, 677–684 (2017).

104. J. Smart, W. Powell, and S. Schey, in, p. 2013-01–1441 (2013) https://www.sae.org/content/2013-01-1441/.

105. P. Plötz, N. Jakobsson, and F. Sprei, *Transportation Research Part B: Methodological*, **101**, 213–227 (2017).

106. N. S. Pearre, W. Kempton, R. L. Guensler, and V. V. Elango, *Transportation Research Part C: Emerging Technologies*, **19**, 1171–1184 (2011).

107. R. D. Deshpande and D. M. Bernardi, *J. Electrochem. Soc.*, **164**, A461–A474 (2017).

108. Y. Preger, H. M. Barkholtz, A. Fresquez, D. L. Campbell, B. W. Juba, J. Romàn-Kustas, S. R. Ferreira, and B. Chalamala, *J. Electrochem. Soc.*, **167**, 120532 (2020).

109. L. Willenberg, P. Dechent, M. Eckert, D. Sauer, and E. Figgemeier, *Systematic Investigation of Mechanical Ageing of High Energy Lithium-Ion Batteries*, (2019).

110. X. M. Liu and C. B. Arnold, *J. Electrochem. Soc.*, **163**, A2501 (2016).

111. A. Maheshwari, M. Heck, and M. Santarelli, *Electrochimica Acta*, **273**, 335–348 (2018).

112. J. Wang, P. Liu, J. Hicks-Garner, E. Sherman, S. Soukiazian, M. Verbrugge, H. Tataria, J. Musser, and P. Finamore, *Journal of Power Sources*, **196**, 3942–3948 (2011).

113. E. Sarasketa-Zabala, I. Gandiaga, E. Martinez-Laserna, L. M. Rodriguez-Martinez, and I. Villarreal, *Journal of Power Sources*, **275**, 573–587 (2015).

114. S. Watanabe, M. Kinoshita, T. Hosokawa, K. Morigaki, and K. Nakura, *Journal of Power Sources*, **260**, 50–56 (2014).

115. J. Li, J. Harlow, N. Stakheiko, N. Zhang, J. Paulsen, and J. Dahn, *J. Electrochem. Soc.*, **165**, A2682 (2018).

116. Y. Zhang, R. Xiong, H. He, X. Qu, and M. Pecht, *Applied Energy*, **255**, 113818 (2019).

117. J. de Hoog, J.-M. Timmermans, D. Ioan-Stroe, M. Swierczynski, J. Jaguemont, S. Goutam, N. Omar, J. Van Mierlo, and P. Van Den Bossche, *Applied Energy*, **200**, 47–61 (2017).

118. Y. Gao, J. Jiang, C. Zhang, W. Zhang, and Y. Jiang, *Journal of Power Sources*, **400**, 641–651 (2018).

119. M. Lewerenz, J. Münnix, J. Schmalstieg, S. Käbitz, M. Knips, and D. U. Sauer, *Journal of Power Sources*, **345**, 254–263 (2017).

120. Y. Cui, C. Du, G. Yin, Y. Gao, L. Zhang, T. Guan, L. Yang, and F. Wang, *Journal of Power Sources*, **279**, 123–132 (2015).

121. K. Darcovich, S. Recoskie, and F. Fattal, *J Appl Electrochem*, **50**, 111–124 (2020).

122. F. Single, A. Latz, and B. Horstmann, *ChemSusChem*, **11**, 1950–1955 (2018).

123. K. Ushirogata, K. Sodeyama, Z. Futera, Y. Tateyama, and Y. Okuno, *J. Electrochem. Soc.*, **162**, A2670 (2015).

124. D. Y. Wang, J. Xia, L. Ma, K. J. Nelson, J. E. Harlow, D. Xiong, L. E. Downie, R. Petibon, J. C. Burns, A. Xiao, W. M. Lamanna, and J. R. Dahn, *J. Electrochem. Soc.*, **161**, A1818–A1827 (2014).

125. J. E. Harlow, X. Ma, J. Li, E. Logan, Y. Liu, N. Zhang, L. Ma, S. L. Glazier, M. M. E. Cormier, M. Genovese, S. Buteau, A. Cameron, J. E. Stark, and J. R. Dahn, *J. Electrochem. Soc.*, **166**, A3031–A3044 (2019).

126. M. Ecker, N. Nieto, S. Käbitz, J. Schmalstieg, H. Blanke, A. Warnecke, and D. U. Sauer, *Journal of Power Sources*, **248**, 839–851 (2014).

127. R. D. Deshpande and K. Uddin, *Journal of Energy Storage*, **33**, 101932 (2021).

128. J. Marcos, I. De la Parra, M. García, and L. Marroyo, *Energies*, **7**, 6593–6619 (2014).

129. G. Graber, V. Calderaro, V. Galdi, and A. Piccolo, *Electronics*, **9**, 939 (2020).

130. J. Christensen and J. Newman, *J. Electrochem. Soc.*, **152**, A818 (2005).

131. M. S. Ding, K. Xu, and T. R. Jow, *J. Electrochem. Soc.*, **147**, 1688 (2000).

132. M. S. Ding, K. Xu, S. Zhang, and T. R. Jow, *J. Electrochem. Soc.*, **148**, A299 (2001).

133. M. Bauer, thesis, (2018) https://DalSpace.library.dal.ca//handle/10222/74208.

134. B. Song, T. Sui, S. Ying, L. Li, L. Lu, and A. M. Korsunsky, *J. Mater. Chem. A*, **3**, 18171–18179 (2015).

135. X. Lu, A. Bertei, D. P. Finegan, C. Tan, S. R. Daemi, J. S. Weaving, K. B. O'Regan, T. M. M. Heenan, G. Hinds, E. Kendrick, D. J. L. Brett, and P. R. Shearing, *Nat Commun*, **11**, 2079 (2020).

136. C. P. Aiken, J. E. Harlow, R. Tingley, T. Hynes, E. R. Logan, S. L. Glazier, A. S. Keefe, and J. R. Dahn, *J. Electrochem. Soc.*, **167**, 130541 (2020).

137. A. Eldesoky, E. R. Logan, M. Johnson, C. McFarlane, and J. R. Dahn, *Meet. Abstr.*, **MA2020-02**, 666 (2020).

138. V. L. Chevrier, L. J. Krause, L. D. Jensen, C. Huynh, M. Triemert, E. L. Bowen, and J. Thorson, *J. Electrochem. Soc.*, **165**, A2968 (2018).

139. L. De Sutter, G. Berckmans, M. Marinaro, J. Smekens, Y. Firouz, M. Wohlfahrt-Mehrens, J. Van Mierlo, and N. Omar, *Energies*, **11**, 2948 (2018).

140. T. Kajita, R. Yuge, K. Nakahara, J. Iriyama, H. Takahashi, R. Kasahara, T. Numata, S. Serizawa, and K. Utsugi, *J. Electrochem. Soc.*, **160**, A1806 (2013).

141. K. Ogata, S. Jeon, D.-S. Ko, I. S. Jung, J. H. Kim, K. Ito, Y. Kubo, K. Takei, S. Saito, Y.-H. Cho, H. Park, J. Jang, H.-G. Kim, J.-H. Kim, Y. S. Kim, W. Choi, M. Koh, K. Uosaki, S. G. Doo, Y. Hwang, and S. Han, *Nat Commun*, **9**, 479 (2018).